Non Gaussianity of Primordial Gravitational Waves and Cosmic Density and Velocity Fields

Aniket Agrawal

München 2018

Non Gaussianity of Primordial Gravitational Waves and Cosmic Density and Velocity Fields

Aniket Agrawal

Dissertation
an der Fakultät für Physik
der Ludwig–Maximilians–Universität
München

vorgelegt von
Aniket Agrawal
aus Lucknow, Indien

München, den 14 März, 2018

Erstgutachter: Prof. Eiichiro Komatsu
Zweitgutachter: Prof. Jochen Weller
Tag der mündlichen Prüfung: 11 Mai, 2018

Contents

List of Figures

Zusammenfassung

Diese Dissertation befasst sich mit nicht-Gaussförmigen Signaturen in Gravitationswellen (GW), die während der Phase der Inflation erzeugt wurden, sowie in den gegenwärtigen Materie-, Galaxiendichte- und Geschwindigkeitsfeldern im Universum. Wir zeigen, dass die nicht-Gaussianität primordialer GW wichtige Hinweise auf ihre Entstehung liefert und dazu verwendet werden kann, den Energiedichteanteil von "spectator" Eichfeldern zu bestimmen, falls die GW durch solche erzeugt worden sind. Als Beispiel betrachten wir ein Inflationsmodell, das aus einem skalaren Inflaton, einem "spectator" Axion und SU(2) Eichfeldern besteht. Axion und Eichfelder sind durch eine Chern-Simons-ähnliche Wechselwirkung gekoppelt. Dieser Kopplung induziert eine tachyonische Instabilität der Eichfelder während der Inflation und bewirkt deren Verstärkung. Die SU(2) Eichfelder besitzen einen Tensor-Freiheitsgrad der als Quelle von helikalen GW agiert, die eine starke Skalenabhängigkeit aufweisen können. Ihre Amplitude kann die der Vakuumfluktuationen der Metrik deutlich übersteigen. In der vorliegenden Arbeit beschränken wir uns auf von diesem Modell beschriebene skalenunabhängige GW. Wir untersuchen ihr Bispektrum und stellen fest, dass sie in erster Linie durch eine Selbstinteraktion der Eichfelder produziert werden. Für $3 \lesssim m_Q \lesssim 4$ wird das Tensor Bispektrum durch Beiträge bei näherungsweise gleichseitigen Konfigurationen dominiert; m_Q ist hier die effektive dimensionlose Masse des SU(2) Eichfeldes, normalisiert durch die Hubble Expansionsrate während der inflationären Phase. Die nicht-Gaussianität der Tensormoden, beschrieben durch das Verhältnis B_h/P_h^2, ist umgekehrt proportional zum Anteil des Eichfeldes an der Energiedichte. Dieses Verhältnis kann die Größenordnung eins deutlich überschreiten, etwa dem Wert des Verhältnisses, den wir für die Vakuumfluktuationen der Metrik ermitteln. Messungen des Bispektrums sind insbesondere dazu geeignet, den Parameterraum bei großen Werten von m_Q zu untersuchen, während das Leistungsspektrum bei kleinen m_Q effektiver ist.

Durch den Einfluss von nichtlinearen gravitativen Effekten in ihrer Entwicklungsgeschichte sind gegenwärtige kosmische Dichte- und Geschwindigkeitsfelder im Universum ebenfalls hochgradig nicht-Gaussförmig. Unter der Annahme einer logarithmischen Normalverteilung für Materie- und Galaxienverteilung und für ein linear von der Materiedichte erzeugtes Geschwindigkeitsfeld zeigen wir, dass die Verteilung der paarweisen Geschwindigkeiten entlang der Sichtline von logarithmisch Normalverteilten Feldern nicht-Gaussförmig ist und qualitativ mit der von Mehrkörpersimulationen übereinstimmt. Mit diesen Vereinfachungen können die Momente der Wahrscheinlichkeitsdichtefunktion (PDF)

paarweiser Geschwindigkeiten prinzipiell analytisch berechnet werden, was eine genauere Modellierung ihrer PDF erlaubt. Wir vergleichen das Mono- und Quadrupol Leistungsspektrum unserer Simulationen im Rotverschiebungsraum mit der Vorhersage von Kaiser auf großen Skalen und finden eine gute Übereinstimmung. Wir veröffentlichen ein Computerprogramm, das dazu benutzt werden kann, logarithmisch Normalverteilte Galaxienkataloge im Rotverschiebungsraum zu erzeugen die dazu geeignet sind, die Kreuzkorrelation zwischen Galaxienpositionen und Gravitationslinseneffekten zu untersuchen, sowie Kovarianzmatrizen für Leistungs- und Bispektra im Real- und Rotverschiebungsraum zu generieren, eine nützliche Eigenschaft für zukünftige Experimente wie PFS und Euclid.

Abstract

We study non-Gaussianity of primordial gravitational waves (GWs) generated during inflation, and of present-day matter and galaxy density and velocity fields in the Universe. We show that non-Gaussianity of primordial GWs is a crucial test of their origin and can be used to constrain the energy density fraction of spectator gauge fields in the early Universe if the primordial GWs are sourced by a spectator sector. We consider a particular inflation model containing a scalar inflaton, and spectator axion and SU(2) gauge fields. The axion and the gauge fields are coupled to each other via a Chern-Simons like interaction. Because of this coupling, the gauge fields experience a tachyonic instability during inflation and get amplified. The SU(2) gauge fields have a tensor degree of freedom which linearly sources GWs that are helical, and can be strongly scale-dependent. Moreover, their amplitude can be much larger than vacuum fluctuations of the metric. In this thesis however, we focus on scale-independent GWs produced in this model. We study the bispectrum of these scale-independent GWs, and find that its production is dominated by the self-interaction of the gauge fields. The shape of the tensor bispectrum is approximately an equilateral shape for $3 \lesssim m_Q \lesssim 4$, where m_Q is an effective dimensionless mass of the SU(2) field normalised by the Hubble expansion rate during inflation. The amplitude of non-Gaussianity of the tensor modes, characterised by the ratio B_h/P_h^2, is inversely proportional to the energy density fraction of the gauge field. This ratio can be much greater than unity, whereas we show that the ratio from the vacuum fluctuation of the metric is of order unity. The bispectrum is effective at constraining large m_Q regions of the parameter space, whereas the power spectrum constrains small m_Q regions.

The present-day cosmic density and velocity fields in the Universe are also highly non-Gaussian due to non-linear gravitational evolution. By assuming the matter and galaxy density distributions to be log-normal, and the velocity field to be linearly generated from the matter density field, we show that the pairwise line-of-sight velocity distribution of log-normal fields is non-Gaussian and looks qualitatively similar to that measured from N-body simulations. The moments of the pairwise velocity PDF can in principle be analytically calculated for this simple setting, giving us a handle on modelling of the full PDF. We compare the redshift space monopole and quadrupole power spectrum for our mock catalogs, finding a good match with the Kaiser prediction on large scales. We present a public code to generate log-normal mock catalogs of galaxies in redshift space which can be used to study the cross-correlation between galaxy positions and weak lensing fields. Our code is also being used to study power spectrum and bispectrum covariance matrices

in real and redshift space, which will be useful for upcoming galaxy surveys such as PFS and Euclid.

Chapter 1

Introduction

1.1 Generating Non-Gaussianity

The observable Universe is homogeneous and isotropic on large scales. It is not only so smooth today, but was also so far back in the past. Observations of the cosmic microwave background (CMB) made by the COBE satellite (161; 26) in the 90s, and subsequently by WMAP (27) and Planck (5), have all confirmed that even when the Universe was only about 400,000 years old (the present age is almost 14 billion years), it was also smooth, in fact much smoother than today. The small inhomogeneities present at that time, grew in time by accretion of more matter, to form the structures we see around us today. We can learn about the composition of the Universe and the nature of gravity by modelling the processes that lead to amplification of initial inhomogeneities and comparing our predictions with observations of the CMB and the late time Universe. Accordingly, CMB and the large-scale structure (LSS) of the Universe serve as two of the main probes of cosmology. In this thesis, we focus on both of these probes, and explore some pieces of information that can be extracted using them.

Planck (5) has provided us with precise measurements of the CMB temperature and polarisation over the whole sky. These measurements are so precise, that we can use them to determine fluctuations of the temperature or polarisation around their mean value, even when they are $\sim 10^{-5}$ times smaller. According to our current understanding, these fluctuations represent the fluctuations in density at the time of recombination, which arose out of *quantum fluctuations* of a field in the very early Universe (124).

If quantum fluctuations did give rise to the primordial density perturbations, then these would be expected to be Gaussian. This follows directly from the observation that the ground state of a quantum harmonic oscillator is a Gaussian (147). Any quantum field in 3-dimensional space can be written as a sum of quantum harmonic oscillators (at linear order. If the field is free, i.e. its potential can be written as that of a harmonic oscillator, this is always true) (140). Because each harmonic oscillator has an amplitude which is normally distributed, their sum is also normally distributed. Thus, the amplitude of the quantum field should obey a Gaussian distribution at the lowest order. As long

as the primordial density fluctuation depends linearly on this quantum field, it should also obey a Gaussian distribution. Hence, by measuring the deviations of the primordial density fluctuations from a Gaussian distribution, we can learn about the interactions and non-linearities of the fields that seeded them during inflation.

The preceding discussion also tells us under what conditions we can expect deviations from Gaussianity (94; 92). If the quantum field has interactions, either with itself, or with other fields, such that its potential can no longer be approximated by a harmonic oscillator potential, we would expect a non-Gaussian distribution. Another way non-Gaussianity can arise is if the density fluctuations depend non-linearly on the inflaton fluctuations. Finally, because we do not observe the density fluctuations themselves but their imprint on the CMB temperature at recombination, non-Gaussianity might also arise if the temperature is a non-linear function of the density. By studying non-Gaussianity we can probe each of these possibilities. Nevertheless, the temperature fluctuations of the CMB are actually almost perfectly Gaussian (5). We will later consider in more detail how this conclusion is arrived at.

Having understood how non-Gaussianity might arise in temperature or density fluctuations at recombination, let us now consider how non-Gaussianity arises in the late-time Universe. The late-time Universe is evidently non-Gaussian. The number of regions with high densities such as galaxies, is much smaller than the number of regions with low densities, a fact confirmed by the emptiness of space. How do we get such a non-Gaussian distribution starting with the near-perfect Gaussian density distribution at recombination? The answer is gravity! The density field obeys a non-linear equation of motion under gravity. Because of this non-linearity, the initial Gaussian field gets converted to a non-Gaussian field at later times. Let us now see what kind of observables we can use to test Gaussianity.

1.2 Measuring Non-Gaussianity

A Gaussian distribution can be completely characterised by specifying its mean and dispersion. For a real-valued field $F(\boldsymbol{x})$ in configuration space, this is equivalent to specifying the mean, $\langle F(\boldsymbol{x})\rangle$, and the 2-point function, $\langle F(\boldsymbol{x}_1)F(\boldsymbol{x}_2)\rangle$. Their Fourier space equivalents are given by $\langle F(\boldsymbol{k})\rangle$ and the power spectrum, $\langle F(\boldsymbol{k})F^*(\boldsymbol{k})\rangle$. A non-Gaussian distribution is characterised using the higher order moments of the field, namely, the n-point correlation function, for $n \geq 3$. The Fourier space equivalents are called bispectrum for $n = 3$, trispectrum for $n = 4$, and so on. In particular, the bispectrum $\mathcal{B}(\boldsymbol{k}_1, \boldsymbol{k}_2, \boldsymbol{k}_3)$, is defined as

$$\langle F(\boldsymbol{k}_1)F(\boldsymbol{k}_2)F(\boldsymbol{k}_3)\rangle = (2\pi)^3\delta_D(\boldsymbol{k}_1 + \boldsymbol{k}_2 + \boldsymbol{k}_3)\mathcal{B}(\boldsymbol{k}_1, \boldsymbol{k}_2, \boldsymbol{k}_3)\,, \tag{1.1}$$

where the delta function δ_D arises from homogeneity of the Universe (see for example (28) for a detailed discussion of moments of non-Gaussian distributions and their application to LSS). The argument of the delta function ensures that the three wave vectors that enter the bispectrum form a closed triangle. Depending on the shape of this triangle, the bispectrum is assigned a "shape". The different possible shapes are shown in figure 1.1. Different

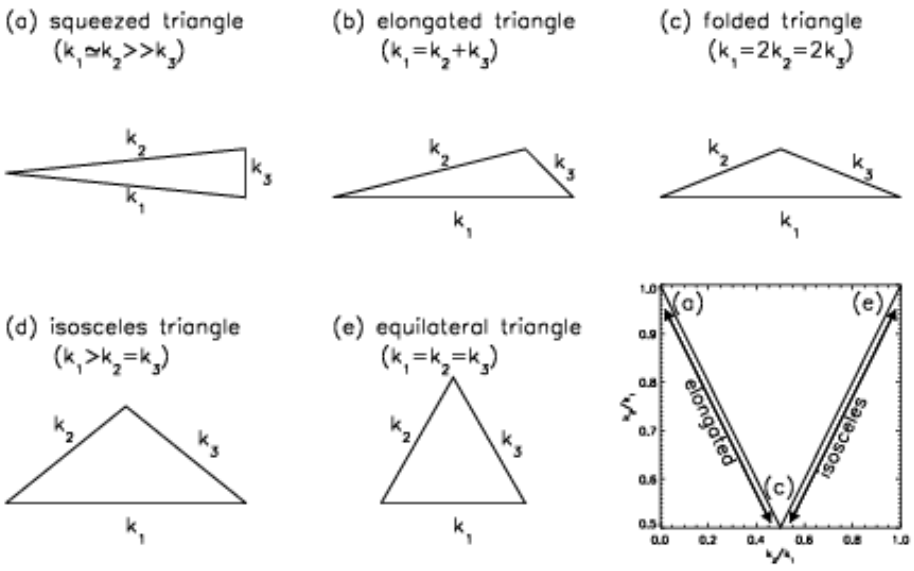

Figure 1.1: Different physical processes during inflation generate non-zero bispectrum in different shapes (93). Hence, by measuring the amplitude of the bispectrum in different shapes, we can learn about the physical processes.

shapes arise from different physical processes. For instance, local processes, such as non-linear sourcing of a field by a Gaussian field give rise to a bispectrum that is peaked in the squeezed limit (94). This is the case for vacuum fluctuations of the metric ((108; 109; 64); also chapter 2). On the other hand, processes that involve higher derivative interactions of Gaussian fields, typically produce an equilateral shape for the bispectrum, as the sources become negligible after horizon crossing (see, for example (22), for a comprehensive review on different shapes of non-Gaussianity produced in different models). Thus, the shape of the bispectrum contains information about the physics of inflation.

The bispectrum is the first non-zero moment for a non-Gaussian distribution, in the sense that if the bispectrum is non-zero the distribution is non-Gaussian. Note that the converse is not necessarily true. Thus, if we measure a non-zero bispectrum, we can be sure that the distribution is non-Gaussian. Even restricting ourselves to the bispectrum, a zero value for the bispectrum of one shape does not rule out a non-zero bispectrum for other shapes. Moreover, accounting for the triangle condition still leaves us with 3 parameters that characterise the bispectrum, corresponding to the three variables required to describe the triangle $\boldsymbol{k}_1 + \boldsymbol{k}_2 + \boldsymbol{k}_3 = \boldsymbol{0}$. If we have N bins in k for the power spectrum, we can measure $\sim N^3$ values for the bispectrum. For a CMB experiment like Planck $N \gtrsim 10^2$ while a similar number is expected for future galaxy redshift surveys such as Euclid. Thus, the full bispectrum will be characterised by $\gtrsim 10^6$ values. Therefore, measurement of the bispectrum is typically much more difficult than measuring the power spectrum. This is one reason why most of our current constraints in cosmology come from the power spectrum.

One way to simplify the measurement of bispectra is to use templates (94; 17). Tem-

plates are just approximations to the predicted bispectrum, which are separable into products of the side lengths, to enable easier numerical manipulation when going from a 3D Universe to the 2D projection of the CMB. We can "match" these templates against the observed bispectrum, to obtain the amplitude of the bispectrum. This amplitude is typically denoted by $f_{\rm NL}$ (94) and is a measure of the skewness of the distribution. For instance, the curvature perturbation generated during inflation, $\Phi(\boldsymbol{x})$ can be written as (94)

$$\Phi(\boldsymbol{x}) = \phi(\boldsymbol{x}) + f_{\rm NL}[\phi^2(\boldsymbol{x}) - \left\langle \phi^2(\boldsymbol{x}) \right\rangle] \tag{1.2}$$

where $\phi(\boldsymbol{x})$ is a Gaussian field with zero mean, typically the quantum fluctuation $\delta\phi(\boldsymbol{x})$, of the inflaton. From equation (1.2), we see that the skewness of $\Phi(\boldsymbol{x}) \equiv \langle(\Phi(\boldsymbol{x}))^3\rangle$ is $\propto f_{\rm NL}$. Template-matching works quite well for CMB observables as the perturbations are small and so tree-level perturbation theory can be used to obtain templates. For LSS, non-linear gravitational evolution means that tree-level perturbation theory must break down at some scale and so a reliable template is hard to obtain. Even when one has a tree-level prediction, there are issues such as bias (51) and redshift space distortions (80; 85; 60; 148), which complicate the matching of observations to templates.

Hence, the gold standard for analysing the non-Gaussian distribution of late-time cosmic density and velocity fields is N-body simulations (see (18; 50) for comprehensive reviews). These are simulations that trace the non-linear dynamics of dark matter particles through cosmic time, as they cluster into dark matter halos, pancakes or filaments. The starting point of such simulations is typically a Gaussian distribution of dark matter particles, as observed in the CMB, figure 1.2, with velocities set by either the linear continuity equation (equation (4.8)) (184) or by 2nd order Lagrangian Perturbation Theory (157). Figures (1.3)–(1.4) show slices through such a simulation. On large scales, the matter distribution maintains its Gaussianity because of linear evolution. On smaller scales (figures (1.3)–(1.4)), non-Gaussianity starts becoming visible, even by eye. N-body simulations have been extensively used to study properties of halo clustering and motions (30; 2; 12; 42; 58) and lensing of light as it passes through the cosmic web (2). In recent years, they have also been used to tackle the particle nature of dark matter, by exploring imprints of dark matter mass on, for instance, its clustering properties (160).

For the purposes of this thesis, the most striking feature of N-body simulations is the pronounced non-Gaussianity of the dark matter distribution. Even comparing figure 1.2 and figure 1.3 by eye, convinces one of the non-linear nature of cosmological gravity. It is instructive to also compare this to the observed distribution of galaxies from the Sloan Digital Sky Survey (SDSS) (103), figure 1.5. Although there are a bunch of caveats in inferring the dark matter distribution from a galaxy map (such as redshift space distortions which we review in chapters 2, 4 and appendix D, or bias (51)), on large scales we expect them to trace each other. We can recognise features such as big groups of galaxies, which correspond to massive halos, and extended structure corresponding to pancakes and filaments. This correspondence gives us some confidence that our basic model starting with the initial conditions set at recombination is consistent.

Having a set of N-body simulations at hand, we can now try to describe the non-Gaussianity in the dark matter/halo distrbution. Once again we can measure the bispec-

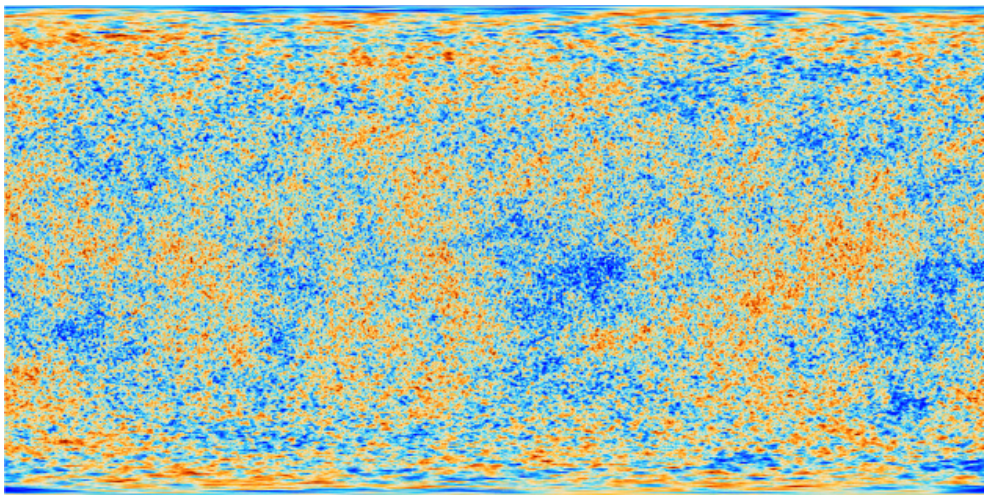

Figure 1.2: Rectangular projection of the whole CMB sky as seen by Planck. Temperature anisotropies of the CMB at recombination almost perfectly obey a Gaussian distribution (5). This can be seen in the almost equal number of hot (red) and cold (blue) spots on any scale. (Of course, any symmetric distribution would produce equal numbers of hot and cold spots. Nevertheless, this is a rudimentary check of Gaussianity).

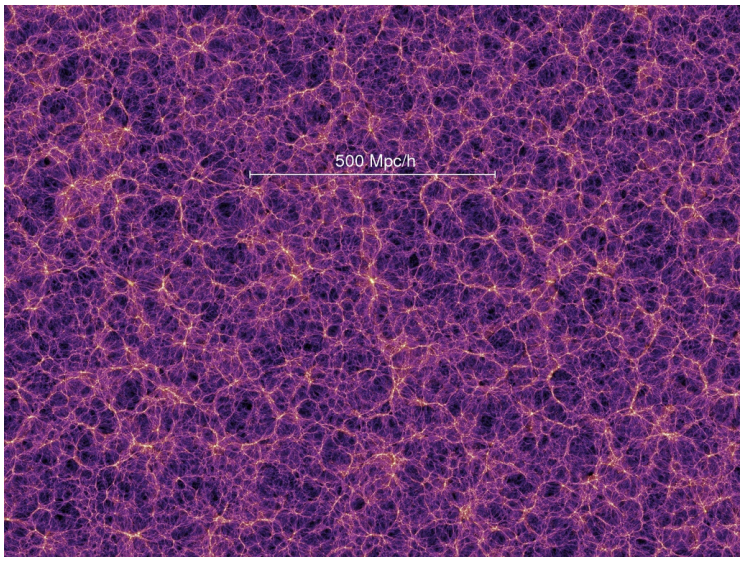

Figure 1.3: Cosmic web as output in the Millennium simulation at $z = 0$ (165), for a 1500×1125 $(\mathrm{Mpc}/h)^2$ slice. We see the non-Gaussian distribution of dark matter, in contrast to that seen in the CMB temperature map in figure 1.2.

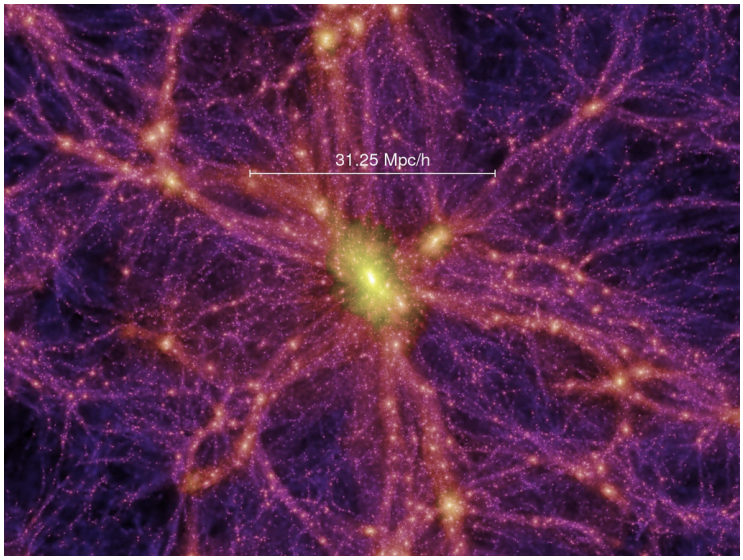

Figure 1.4: Zoom-in version of figure 1.3 (165), for a 94×70 $(\mathrm{Mpc}/h)^2$ slice. The bright central region shows a dark matter halo, while the long, extended pink lines denote filaments. We also see dark spots, which correspond to voids, or regions where matter density is less than the average density in the Universe.

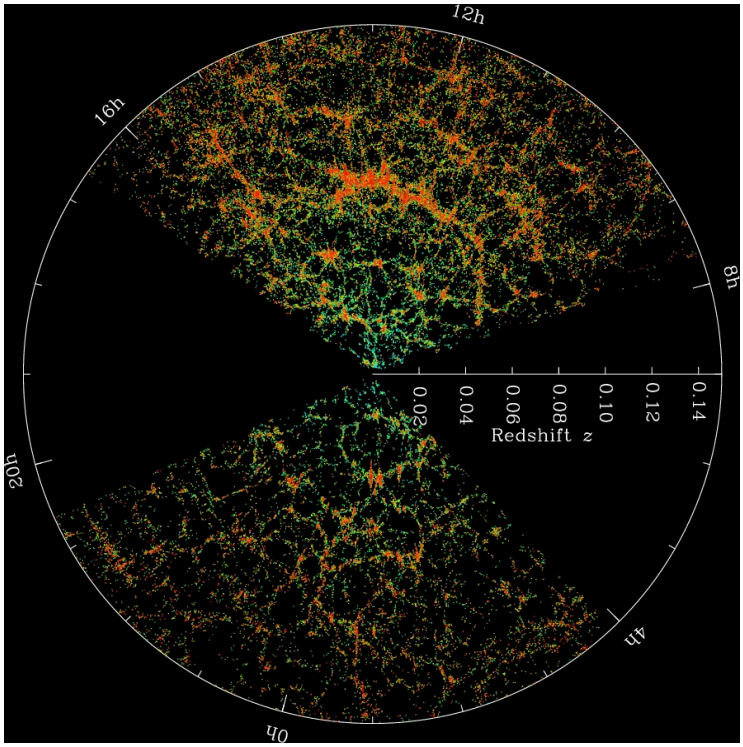

Figure 1.5: Distribution of galaxies out to $z = 0.15$ as measured by the SDSS (103). Comparing to figure 1.3 we see a qualitatively similar distribution.

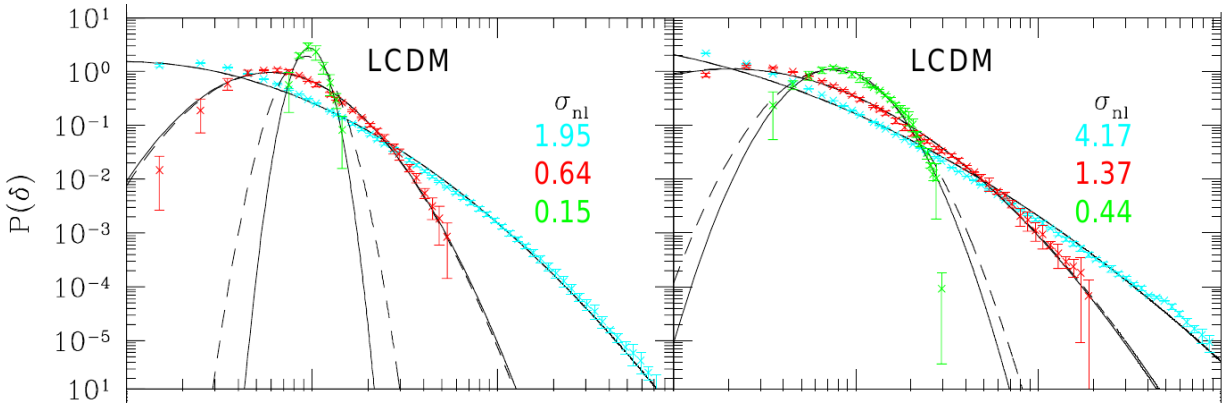

Figure 1.6: Log-normal fit (black solid) to 1-point PDF of matter density as measured from N-body simulations (points). Left panel shows a Gaussian smoothing, while right panel shows a top-hat smoothing function, applied to the density field. Different colours show different values of the smoothing radius, $R = 2\,h^{-1}$Mpc (cyan), $6\,h^{-1}$Mpc (red) and $18\,h^{-1}$Mpc (green) (88). Dashed lines show the log-normal fit using $\sigma_{\rm nl}$ predicted from a fitting formula by Peacock and Dodds (133).

trum. The dark matter and halo (galaxy) bispectrum has been measured from N-body simulations (62) (redshift surveys (66; 67; 159; 158)). However, because of the systematics mentioned above in inferring the dark matter clustering from galaxies, it is much more difficult to obtain constraints on cosmology from such measurements on observations. Also, the non-Gaussianity in matter distributions is much larger than in CMB. Consequently, the trispectrum and higher order correlation functions are also important. It might then be more useful to choose a different approach to describe the non-Gaussianity in this case. We can do this for example, by using a simple non-Gaussian distribution to characterise the density field. In chapter 4 we use a log-normal distribution. As shown in figure 1.6, this is a good description of the matter and halo density fields obtained in N-body simulations. Our choice of the log-normal distribution is also motivated by the fact that a log-normal field is quite simpy related to a Gaussian field, which is easy to simulate.

1.3 Why measure Non-Gaussianity?

Finally, let us consider why we want to measure non-Gaussianity at all. Whether from CMB or from LSS, the primary questions of interest in cosmology are - what constitutes our Universe? How did it begin? How will it end? In addition, we do not yet know what exactly caused inflation, and if in fact it did happen. An answer to these questions can be given if we can measure $f_{\rm NL} \sim 1$ and tensor-to-scalar ratio $r > 0$. Temperature measurements of the CMB have been exhausted to their cosmic variance limits in the Planck analysis (5). Once B-modes have been observed, as we show in chapter 3, it will be crucial to verify that they originate from vacuum fluctuations of the metric, if we want to claim that they were generated during single scalar field slow roll inflation.

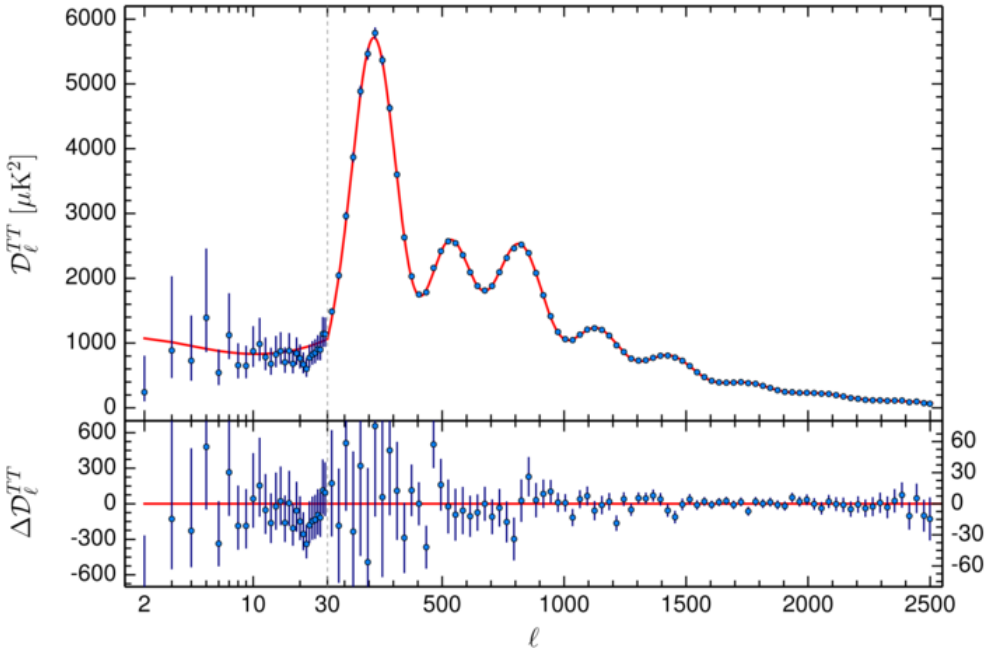

Figure 1.7: Temperature power spectrum measured by Planck (5). The overall amplitude, tilt, relative heights and locations of the peaks are used to derive constraints on cosmological parameters.

By measuring the power spectrum of temperature fluctuations in the CMB (figure 1.7), and of galaxy density fluctuations in LSS (figure 1.8), we have now arrived at what can be called a concordance model of cosmology, the ΛCDM model. According to this model, the Universe consists of about 5% baryonic matter which is what all stuff around us is made of, 27% dark matter which interacts only gravitationally and is necessary to explain galaxy rotation curves, and the rest dark energy (139; 143), which acts like "repulsive" gravity and is responsible for the present-day accelerated expansion of the Universe. However, we still do not know anything about the particle content of either dark matter or energy. One way to progress in this regard is to make more precise measurements of their properties, such as equation of state for dark energy, or mass of dark matter particles. Figure 1.9 shows the improvement in constraints obtained when using the bispectrum alone, or in combination with the power spectrum. We can see that constraints can improve by almost as large as 70%, for some parameters. This is not entirely surprising, since a 3-dimensional function should contain more information than a 1-dimensional function.

The rest of this thesis is organised as follows : in chapter 2 we lay out the basics of single field slow roll (SFSR) inflation and generation of scalar and tensor perturbations during SFSR inflation. We also describe the bispectrum of tensor modes expected from non-linear self-interactions in GR. At the end, we briefly consider the evolution of matter density and velocity fields in the late-time Universe, and elaborate on the differences between observed and true positions of galaxies due to their peculiar velocity.

Chapter 3 explores the imprint of spectator fields on tensor metric perturbations during

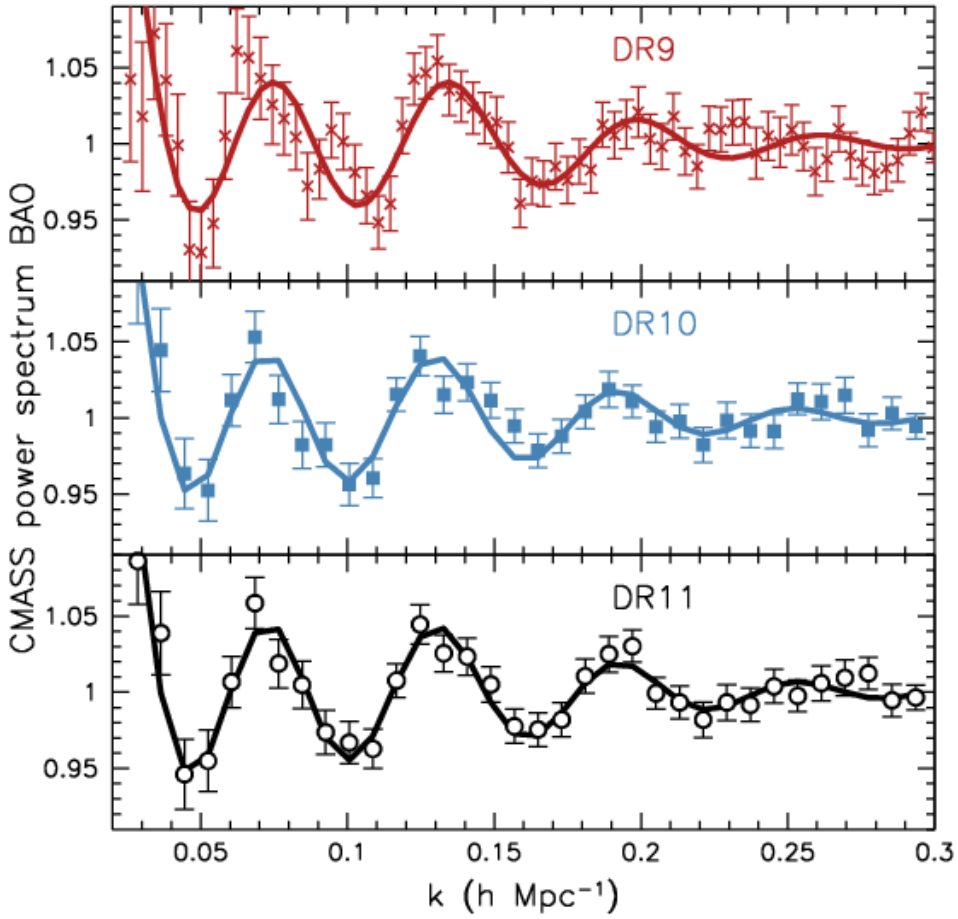

Figure 1.8: Baryon Acoustic Oscillations in the monopole of the CMASS galaxy power spectrum measured by the BOSS collaboration (16) for 3 years of analysis. The shape of the oscillatory feature is used to derive constraints on cosmological parameters.

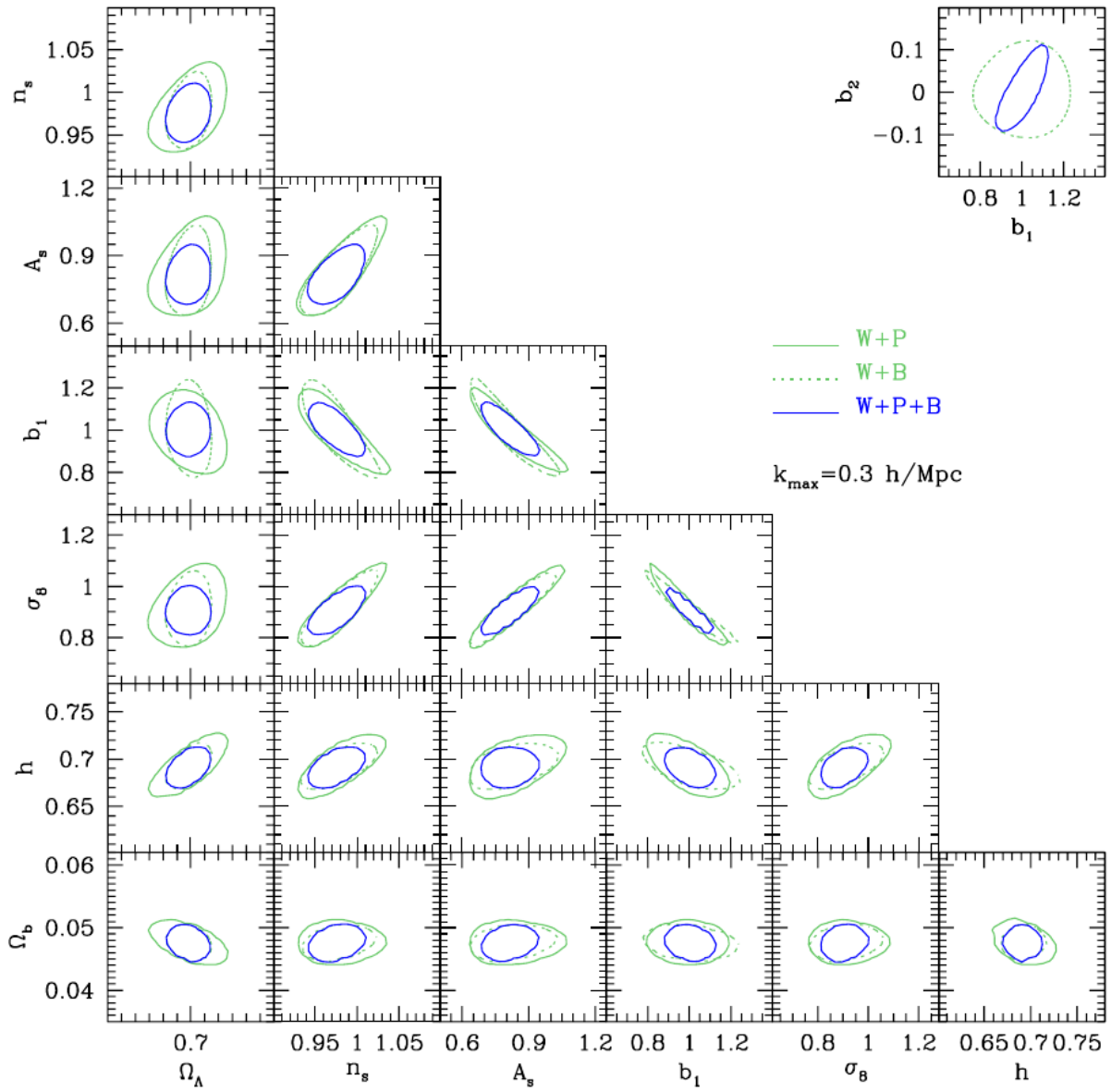

Figure 1.9: Using the bispectrum alone can also significantly improve constraints compared to using the power spectrum alone. However, combining both power spectrum and bispectrum can significantly shrink contours, for example as for $\sigma_8 - \Omega_\Lambda$, or break degeneracies, as for $b_1 - \Omega_\Lambda$. In addition, some parameters, such as the second order bias b_2, *cannot* be measured using the power spectrum alone (150).

inflation. We show that a large amplitude of helical, scale-invariant tensor modes can be generated by spectator SU(2) gauge fields during inflation in a model containing a scalar inflaton, a pseudoscalar axion and SU(2) gauge fields, at linear order. We also calculate the bispectrum of these tensor modes. A large bispectrum is generated in this model at tree-level as the gauge fields contain a tensor degree of freedom, and its production is dominated by self-coupling of the gauge fields. This is a unique feature of non-Abelian gauge theory. The shape of the tensor bispectrum is approximately an equilateral shape for $3 \lesssim m_Q \lesssim 4$, where m_Q is an effective dimensionless mass of the SU(2) field normalised by the Hubble expansion rate during inflation. The amplitude of non-Gaussianity of the tensor modes, characterised by the ratio B_h/P_h^2, is inversely proportional to the energy density fraction of the gauge field. This ratio can be much greater than unity, whereas the ratio from the vacuum fluctuation of the metric is of order unity. The bispectrum is effective at constraining large m_Q regions of the parameter space, whereas the power spectrum constrains small m_Q regions.

In chapter 4, we present a public code to generate log-normal realisations of galaxy density fields in redshift space. We draw galaxies by Poisson-sampling the log-normal field, and calculate the velocity field from the linearised continuity equation of matter fields, assuming zero vorticity. This procedure yields a PDF of the pairwise velocity fields that is qualitatively similar to that of N-body simulations. We check fidelity of the catalog, showing that the measured two-point correlation function and power spectrum in real space agree with the input precisely. We find that a linear bias relation in the power spectrum does not guarantee a linear bias relation in the density contrasts, leading to a cross-correlation coefficient of matter and galaxies deviating from unity on small scales. We also find that linearising the Jacobian of the real-to-redshift space mapping provides a poor model for the two-point statistics in redshift space. That is, non-linear redshift-space distortion is dominated by non-linearity in the Jacobian. The power spectrum in redshift space shows a damping on small scales that is qualitatively similar to that of the well-known Fingers-of-God (FoG) effect due to random velocities, except that the log-normal mock does not include random velocities. This damping is a consequence of non-linearity in the Jacobian, and thus attributing the damping of the power spectrum solely to FoG, as commonly done in the literature, is misleading.

In chapter 5 we summarize this dissertation and present the outlook.

Chapter 2

Theory

In this chapter, we will consider how inflation generates primordial fluctuations and what their observational consequences are. We first briefly review homogeneous cosmology and inflation, before moving on to generation of tensor perturbations by inflation. We also include a small section on the dynamics of perturbations of a scalar field in a de-Sitter Universe, to give an idea of how inflation stabilises quantum fluctuations. In general quantum fluctuations exist even in flat spacetime. However, they are generated and decay spontaneously. Because of the accelerated expansion of the Universe during inflation however, they can be sustained and give rise to structure in the Universe. This is what we mean by stabilisation of quantum fluctuations in this chapter. Towards the end, we discuss the present-day cosmic density and velocity fields. Most of this discussion can be found in standard textbooks on cosmology, such as (123; 23).

2.1 Homogeneous Cosmology

The field equations for gravity are given by the Einstein equation,

$$G_{\mu\nu} = \frac{T_{\mu\nu}}{M_P^2}\,, \tag{2.1}$$

where $M_P \equiv 1/\sqrt{8\pi G}$ is the reduced Planck mass and G is Newton's gravitational constant and we have set the speed of light $c = 1$. $G_{\mu\nu}$ is called the Einstein tensor, and is made up of second (and smaller) derivatives of the metric tensor $g_{\mu\nu}$. As a very rough approximation, it represents the curvature of spacetime. The energy-momentum $T_{\mu\nu}$ of a system acts as a source for the gravitational field. We also need to know how particles move on a curved spacetime. This information is also encoded in equation (2.1). From the Bianchi identities, we know that $G_{\mu\nu;\nu} = 0$. The semi-colon here denotes the covariant derivative, and repeated indices need to be summer over. This implies $T_{\mu\nu;\nu} = 0$, which is just a statement about conservation of energy-momentum and leads to the geodesic equation for particles. Equation (2.1) then says that the energy-momentum of a system curves spacetime which determines how particles move on it and in turn modify the energy-momentum. This

equation can be obtained by varying the action S

$$S = \int d^4x\sqrt{-g}\Big[\frac{M_P^2}{2}R + \mathcal{L}_m\Big] \tag{2.2}$$

where g is the determinant of the metric tensor which is required to make the volume element $\sqrt{-g}\,d^4x$ co-ordinate invariant, and $\mathcal{L}_m$ denotes the Lagrangian density of matter and R is the Ricci scalar.

For a homogeneous and isotropic Universe, the spacetime interval between two events can be written as

$$ds^2 = -dt^2 + a^2(t)\delta_{ij}dx^i dx^j \tag{2.3}$$

where $a(t)$ represents the scale factor, and describes the expansion or contraction of spatial hypersurfaces. For such a Universe, there's only one variable in the Ricci scalar, $a(t)$. For the matter part of the Lagrangian density, we can approximate matter as a perfect fluid on large scales. In this case, it can be characterised using its energy density ρ, pressure p, and its 4-velocity, u^μ. The energy-momentum tensor of a perfect fluid is written as

$$T^\mu_\nu = (\rho + p)u^\mu u_\nu - p\delta^\mu_\nu \tag{2.4}$$

where the equation of state $w = p(\rho)/\rho$ depends on the properties of matter and must be specified separately. For instance for radiation $w = 1/3$ while for matter $w \approx 0$ as the energy density of matter (which consists of the rest-mass energy too) is much larger than its pressure. Again, for a homogeneous and isotropic Universe, $\rho = \rho(t)$ is a function of time only and does not depend on position. Thus, varying equation (2.1) w.r.t. the scale factor a and the energy density ρ we arrive at the Friedmann equations,

$$\Big(\frac{\dot{a}}{a}\Big)^2 + \frac{K}{a^2} = \frac{\rho(t)}{3M_P^2}\,, \tag{2.5}$$

$$\dot{\rho}(t) = -3\frac{\dot{a}}{a}(\rho(t) + p(t))\,, \tag{2.6}$$

where $\frac{\dot{a}}{a} \equiv H(t)$ is called the Hubble parameter, and K is a constant proportional to the curvature of spatial hypersurfaces. It's value is very close to 0 today, indicating a flat Universe. We set it to 0 for the rest of this thesis.

For a homogeneous background, these equations are sufficient to describe the evolution of the Universe, once we set the initial conditions. This is typically done, by setting the present day value of the scale factor $a(t_0) = 1$, where a '0' in the subscript denotes quantities evaluated at the current epoch. We can also measure the present value of $H(t_0) \equiv H_0 = 100\,h$ km s^{-1}Mpc^{-1}, with $h \sim 0.7$ at present. Since the Universe is currently expanding and $H_0 > 0$, $a(t)$ must have been smaller in the past. If the equation of state w is a constant, one can solve the equations (2.5)–(2.6) to arrive at

$$\rho(t) \propto a(t)^{-3(1+w)}\,, \tag{2.7}$$

from which we conclude that the energy density of radiation falls off as $\rho_\gamma \propto a^{-4}$ while that of matter falls off as $\rho_m \propto a^{-3}$. Consequently, if we look back far enough into the past, the Universe is dominated by radiation.

Before concluding this section, let us also briefly define the notion of horizons. We will frequently use the notion of the *Hubble horizon* or just *horizon*. This is given simply by $1/H(t)$, and is a measure of the curvature scale of the whole Universe. Processes that happen on length scales much smaller than this scale are not affected by general relativistic effects and so can be treated in a Newtonian approximation. We will make frequent use of this scale later on. Another horizon is the (comoving) *particle horizon*. This represents the maximum distance that a photon can travel between an initial time t_i and final time t_f. It is given as, $\Delta r = \int_{t_i}^{t_f} dt/a(t)$. If we choose $t_i = 0$, i.e. at the beginning of the Universe, this distance represents the maximum distance that a photon could have travelled till the time t_f. Thus, it is a measure of the length scales up to which causal processes can operate in the Universe.

2.2 Inflation

The theory of inflation arose out of attempts to solve the so-called *horizon* and *flatness* problems among some others (71; 166; 102; 13). Let us briefly look at these problems.

Equations (2.5)–(2.6) imply that the rate at which the scale factor changes in a homogeneous Universe is given as

$$\frac{\ddot{a}}{a} = \dot{H} + H^2 = -\frac{1}{6M_P^2}(\rho + 3p). \tag{2.8}$$

If the Universe consists of matter/radiation for which w is always $> -1/3$, then $\rho + 3p > 0$, and $\dot{a}$ is always decreasing in time. The *horizon* problem arises from causality considerations of the CMB. As remarked in chapter 1, the CMB appears to be isotropic on scales of the size of the observable Universe ($\sim 3000\,h^{-1}$ Mpc), and shows non-zero correlations even on such large scales. Why might this be a problem? The size of the (comoving) particle horizon at recombination is given as

$$\Delta r_{\rm rec} = \int_0^{t_{\rm rec}} \frac{dt}{a(t)} = \int_0^{a_{\rm rec}} \frac{da}{a(aH)} \tag{2.9}$$

where $(aH)^{-1} \propto a^{(1+3w)/2}$ for a Universe dominated by a fluid with equation of state w and $a_{\rm rec}$ is the scale factor of the Universe at recombination. Using this, we find that $\Delta r_{\rm rec} = \frac{2}{1+3w} a_{\rm rec}^{(3w+1)/2} r_{\rm homo}$, where $r_{\rm homo} \equiv c/H_0$ is the (comoving) size of the homogeneous region at recombination, needed to produce the homogeneous region of the size we see today (which stays constant and so, is just the size of the Universe today). From observations of the CMB we know that $a_{\rm rec} \approx 1/1100$ and so the size of the particle horizon at recombination is always smaller than the required homogeneous region at recombination, as long as $w \gg -1/3$. Therefore, it is not possible to have any causal contact at recombination between the

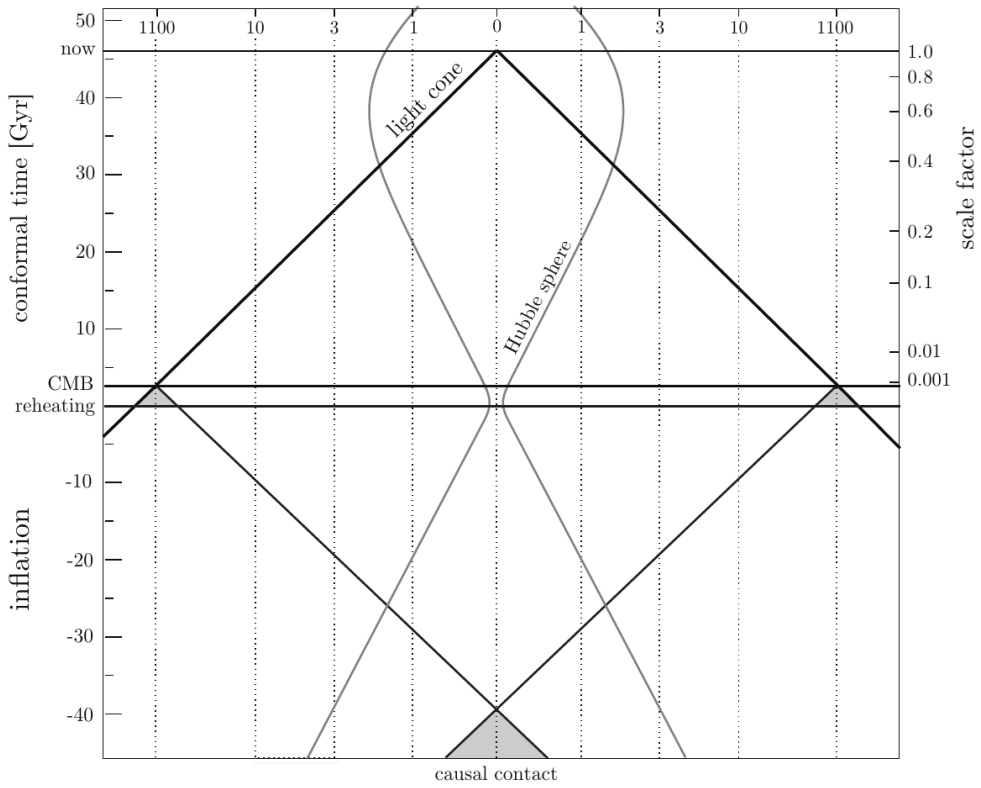

Figure 2.1: The horizon problem and its inflationary solution (23). Without inflation, light cones for different patches on the CMB sky do not intersect in the past. With an inflationary stage, the comoving Hubble horizon expands going back in past, bringing the two light cones in contact.

regions which appear to us at the same temperature today. This is also illustrated in figure 2.1, which also gives us a hint of how to solve the horizon problem. We will see below that inflation increases the size of the particle horizon long before recombination, so that even points which were not in causal contact at recombination, were still causally connected earlier on.

Next we have the *flatness* problem. From the Friedmann equation, equation (2.5) we can write the spatial curvature constant as

$$K = a^2 H^2 \Big[\frac{\rho}{3H^2 M_P^2} - 1 \Big] \equiv \dot{a}^2 [\Omega_T - 1], \tag{2.10}$$

where we have defined Ω_T as the ratio of the total energy density of the Universe to the critical energy density, $\rho_{\rm cr} = 3H^2 M_P^2$. Because K is a constant, we can use the above equation to get $|\Omega_T - 1|_0 = \frac{\dot{a}(t)^2}{\dot{a}_0^2} |\Omega_T(t) - 1|$. We also know from equation (2.8) that $\dot{a}$ is decreasing in time if $w > -1/3$. In this case, any deviation from flatness grows with time. However, observations show that the Universe is almost exactly flat today and $\Omega_K \equiv 1 - \Omega_T = 0.000 \pm 0.005$ (95%, *Planck*TT+low P+lensing+BAO) (5). This

implies that the early Universe must have been very flat in order to see the current level of curvature. The flatness problem is then, what caused the early Universe to be this flat?

It is evident from the above discussion that all these problems can be alleviated if we have a dominant energy component in the Universe for which $w < -1/3$. If this is the case, we also see from equation (2.8) that the Universe actually undergoes an accelerated expansion. This stage of accelerated expansion is called *inflation*. If $w < -1/3$ then $\Delta r_{\rm rec} = 2a_{\rm rec}^{(3w+1)/2}/(1+3w)r_{\rm homo}$ can be equal to or greater than $r_{\rm homo}$, thus solving the horizon problem. Also, in this case, $\dot{a}$ can increase in time and so even if we start off with a non-zero curvature of the Universe, we can end up with a flat Universe as $\dot{a}(t)/\dot{a}_0$ might be $\ll 1$. The conditions that the horizon and flatness be successfully resolved lead to conditions on the length of a phase of accelerated expansion of the Universe. It can be shown that inflation must last more than 60 e-folds, i.e. the Universe gets expanded by a factor of e^{60} during inflation. One of the most interesting features of inflation is that it also provides a natural mechanism to generate primordial perturbations in the Universe (124).

We can anticipate that if there are some density perturbations in the Universe, gravity will cause them to get amplified as overdense regions will attract matter causing them to become more overdense with regard to the average Universe. Thus, once perturbations are laid down, they get amplified and can give rise to all the structure in the Universe via gravitational evolution. Inflation helps in this regard by providing a mechanism for quantum fluctuations of the metric to become stable and thus seed the structure of matter in the Universe. We will study those in more detail in the next section.

2.2.1 Single Scalar Field Slow-Roll Inflation

Let us briefly understand how a state of accelerated expansion can be achieved. In the most common models, it is achieved using a scalar field, called the *inflaton* and which we denote by $\phi(t, \boldsymbol{x})$. We can write the inflaton field as $\phi(t, \boldsymbol{x}) = \bar{\phi}(t) + \delta\phi(t, \boldsymbol{x})$, where $\bar{\phi}(t)$ is the background value which is only dependent on time, and $\delta\phi$ is a small perturbation around the background value, which is a function of both time and position. This perturbation will be assumed to be of quantum origin. Assuming a potential $V(\phi)$ for the inflaton, we can write the action as

$$S = \int d^4x\sqrt{-g}\Big[\frac{M_P^2}{2}R - \frac{1}{2}g_{\mu\nu}\partial^\mu\phi\partial^\nu\phi - V(\phi)\Big] \tag{2.11}$$

from which we find the equation of motion for ϕ as

$$\Box\bar{\phi} = V_{,\phi} \quad \Rightarrow \quad \ddot{\bar{\phi}}(t) + 3H\dot{\bar{\phi}} + V_{,\phi} = 0 \tag{2.12}$$

which is just the Klein-Gordon equation for a time-dependent (only) scalar field, written in an expanding spacetime. Here $V_{,\phi} \equiv \frac{dV(\bar{\phi})}{d\phi}$. This represents the equation of a damped harmonic oscillator, with the damping term proportional to H. The expansion of the Universe acts as a "frictional" force acting against the "velocity" of the field, or opposing change in

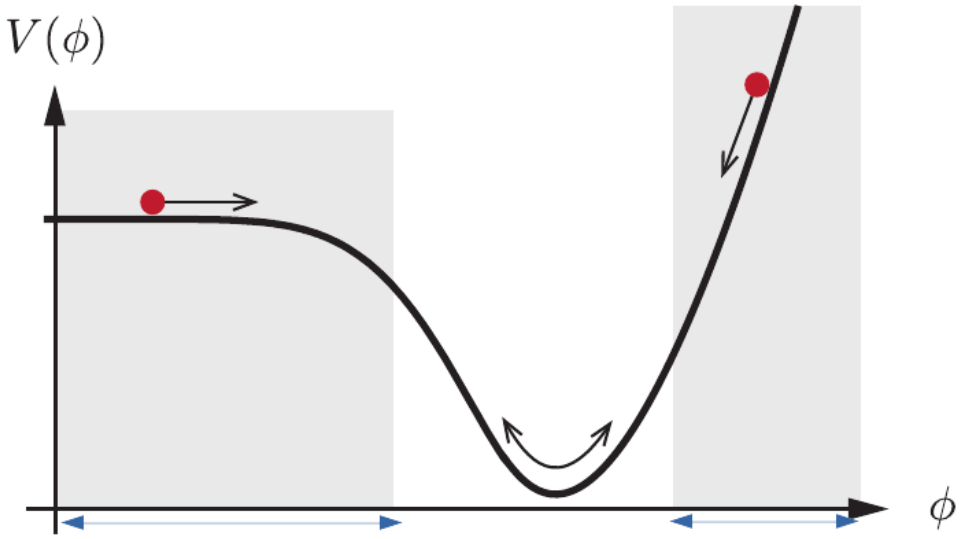

Figure 2.2: The inflaton field (red) rolls down its potential (23). A period of inflation can be realised in either of the two regions shown by arrows under the x-axis, where the potential energy is $\gg$ than the kinetic energy of the inflaton. The flatness of the potential controls the duration of inflation. A flatter potential allows for a longer duration, resulting in a flatter Universe, and a bigger causal region at the beginning of inflation, needed to solve the horizon and flatness problems.

the value of the field. It is this feature that also stabilises the quantum fluctuations of the field. But more on that in the next section.

Figure 2.2 shows a schematic representation of the inflaton as it "rolls" down its potential. The energy-momentum tensor for a field ϕ is given by

$$T^{\mu}_{\nu} = \frac{\partial \mathcal{L}}{\partial(\partial_{\mu}\phi)}\partial_{\nu}\phi - \mathcal{L}\delta^{\mu}_{\nu} \tag{2.13}$$

which for a homogeneous and isotropic scalar field, reduces to the energy-momentum tensor of a perfect fluid with pressure p_{ϕ} and energy density ρ_{ϕ} given as,

$$p_{\phi} = \frac{\dot{\phi}^2}{2} - V(\phi)\,, \qquad \rho_{\phi} = \frac{\dot{\phi}^2}{2} + V(\phi)\,, \tag{2.14}$$

so that the equation of state

$$w_{\phi} = \frac{\frac{\dot{\phi}^2}{2} - V(\phi)}{\frac{\dot{\phi}^2}{2} + V(\phi)}. \tag{2.15}$$

If the inflaton is slowly-rolling, then $\dot{\phi}^2/2 \ll V(\phi)$, and $w_{\phi} \to -1$, which leads to the accelerated expansion of the Universe. In figure 2.2, the regions shown by arrows under the x-axis correspond to epochs where this condition is satisfied, and inflation happens. We will assume throughout that the inflaton is slowly-rolling and dominates the energy

density of the Universe. In the next chapter, we consider the observational consequences of spectator gauge fields present in the Universe during inflation. There we will not specify the form of the potential $V(\phi)$ but assume that a scalar inflaton exists and drives the accelerated expansion of the Universe.

2.3 Quantum Fluctuations during Inflation

The study of quantum fluctuations during inflation can be most easily divided into study of three components - scalar, vector and tensor fluctuations. These are defined by their transformation properties under rotations on a 3-dimensional spatial hypersurface. Because of the decomposition theorem, these three types are completely decoupled from each other at the linear level (or first order). Thus, scalar fluctuations are only sourced by the scalar part of the energy-momentum tensor, tensor fluctuations by the tensor part and so on. In general however, if no source exists, vector perturbations decay as $1/a(t)$ because of the expansion of the Universe and so we can neglect them. In this section we closely follow the treatment laid out in (22).

2.3.1 Scalar Fluctuations

A thorough study of scalar fluctuations is fascinating but tedious. Also, in this thesis we do not consider the details of scalar perturbations at all, so we only explore the dynamics of scalar field fluctuations on a de-Sitter background briefly, to understand how an accelerating Universe stabilises quantum fluctuations.

We first introduce the new perturbation variable $\tilde{\delta\phi} \equiv a\delta\phi$, which is the canonical degree of freedom in an FRW background. If the perturbation $\tilde{\delta\phi}$ represents quantum fluctuations, we need to promote this variable to an operator and decompose it into its Fourier components, defined on the comoving background,

$$\hat{\tilde{\delta\phi}}(\eta, \boldsymbol{x}) = \int \frac{d^3k}{(2\pi)^{3/2}} [u_k(\eta)\hat{a}_{\boldsymbol{k}} e^{i\boldsymbol{k}\cdot\boldsymbol{x}} + u_k^*(\eta)\hat{a}^\dagger_{-k} e^{-i\boldsymbol{k}\cdot\boldsymbol{x}}] \tag{2.16}$$

where η is conformal time and $\hat{a}_{\boldsymbol{k}}$, $\hat{a}^\dagger_{\boldsymbol{k}}$ are the annihilation and creation operators for a mode $\boldsymbol{k}$, which satisfy the commutation relations $[\hat{a}_{\boldsymbol{k}}, \hat{a}^\dagger_{\boldsymbol{k'}}] = \delta^{(3)}(\boldsymbol{k} - \boldsymbol{k'})$, $[\hat{a}_{\boldsymbol{k}}, \hat{a}_{\boldsymbol{k'}}] = 0$. u_k are called mode functions of the field $\tilde{\delta\phi}$.

At first order in the perturbations, the Klein-Gordon equation (equation (2.12)) remains a linear equation in $\delta\phi$, so we can just write,

$$\Box\delta\phi(t, \boldsymbol{x}) = \frac{\partial^2 V}{\partial\delta\phi^2} \tag{2.17}$$

from which we get

$$u_k'' + \left(k^2 - \frac{a''}{a} + m_\phi^2 a^2\right) u_k = 0 \tag{2.18}$$

where $m_\phi^2 \equiv \partial^2 V/\partial\phi^2$ is the effective mass of the inflaton and $'$ denotes derivative w.r.t. the conformal time η. For a de-Sitter background, the Hubble parameter H is exactly constant, so that $a(\eta) = -1/H\eta$, and

$$\frac{a''}{a} - m_\phi^2 a^2 = \frac{2}{\eta^2}\left(1 - \frac{1}{2}\frac{m_\phi^2}{H^2}\right). \tag{2.19}$$

Using this in equation (2.18), we get

$$u_k'' + \left(k^2 - \frac{\nu_\phi^2 - 1/4}{\eta^2}\right)u_k = 0 \tag{2.20}$$

where we have introduced $\nu_\phi^2 \equiv \left(\frac{9}{4} - \frac{m_\phi^2}{H^2}\right)$. If ν_ϕ is constant in time, which is expected for a flat enough potential, equation (2.20) is a Bessel equation, whose general solution for *real* ν_ϕ reads

$$u_k(\eta) = \sqrt{-\eta}\,[c_1(k)H_{\nu_\phi}^{(1)}(-k\eta) + c_2(k)H_{\nu_\phi}^{(2)}(-k\eta)] \tag{2.21}$$

where $H_{\nu_\phi}^{(1)}$ and $H_{\nu_\phi}^{(2)}$ are Hankel functions of the first and second kind respectively, and $c_1(k)$ and $c_2(k)$ are functions set by the initial conditions.

The initial conditions are set by requiring that far enough in the past the mode functions have a very short wavelength, i.e. $k/aH \to \infty$, and so do not "see" the curvature of the spacetime, essentially behaving as vacuum fluctuations in a Minkowski spacetime. We know that these should look like

$$u_k(\eta) = \frac{1}{\sqrt{2k}}e^{-ik\eta}\,, \tag{2.22}$$

so that $c_2(k) = 0$ and $c_1(k) = \sqrt{\pi}/2\, e^{i(\nu_\phi+1/2)\pi/2}$. Thus the full solution for the mode function becomes

$$u_k(\eta) = \frac{\sqrt{\pi}}{2}e^{i(\nu_\phi+1/2)\pi/2}\sqrt{-\eta}H_{\nu_\phi}^{(1)}(-k\eta)\,. \tag{2.23}$$

From this we can write the power spectrum of the scalar field fluctuations in the super-horizon limit ($k\eta \to 0$) as

$$\mathcal{P}_u = 2^{(2\nu_\phi-3)}\left[\frac{\Gamma(\nu_\phi)}{\Gamma(3/2)}\right]^2\frac{1}{4\pi^2}\left(\frac{k}{aH}\right)^{(3-2\nu_\phi)}, \tag{2.24}$$

where $\Gamma(x)$ is the gamma function at x, and $\mathcal{P}_u$ is the dimensionless power spectrum of u_k. Equation (2.24) shows that the power spectrum of quantum fluctuations has a power law dependence on wavenumber, and a blue tilt - namely, fluctuations with a large wavenumber have larger amplitude and vice versa. This solution only holds when $m_\phi \leq 3H/2$. When the inflaton is heavier than (3/2 times) the Hubble scale, the power spectrum gets exponentially suppressed by a factor $e^{-2m_\phi^2/H^2}$, and quantum fluctuations are not amplified. Thus, if $H = 0$ we cannot have amplification of quantum fluctuations (of massive particles).

Although we obtained a blue tilt in this section, this result does not hold during inflation because the Hubble parameter H is not exactly constant during inflation and metric perturbations are not exactly 0. What do we get when we allow for non-zero values for the time variation of both of these? It turns out that in this case the effective mass of the scalar field becomes negative due to its gravitational interactions with the background and the metric fluctuation (92; 125), $m^2_{\rm eff}(\eta) = -\frac{H}{\dot\phi}\frac{d^2(\dot\phi/H)}{d\eta^2} \simeq \left(\frac{d^2V(\phi)}{d\phi^2} + 9\frac{dH}{dt}\right)$. Using the slow-roll condition, we obtain $dH/dt \approx -1/6V(dV/d\phi)^2 = -m^2_\phi/3$. Thus the effective mass of the scalar field fluctuations becomes $m^2_{\rm eff} = -2m^2_\phi$. The tilt of the spectrum is controlled by the sign of $m^2_{\rm eff}$, and so becomes negative too, with the magnitude being controlled by the intrinsic mass of the scalar field. This is what is observed in the CMB, and the scalar spectral index $n_s = 0.96$ (5). A spectral index of 0.96 was predicted already in the 1980s (124) and its discovery constitutes one of the strongest proofs of a quantum origin of the Universe.

2.3.2 Tensor Fluctuations

Now we consider tensor fluctuations during inflation. Quantum fluctuations of the scalar inflaton cannot source tensor perturbations of the metric at first order. They do source them at second order, but their magnitude is quite small (25). In this section we will just consider the quantum mechanical generation of tensor metric perturbations, and their properties. To study the generation of primordial GWs from inflation, we first start with a perturbed metric in a Cartesian co-ordinate system,

$$ds^2 = -dt^2 + a(t)^2[\delta_{ij} + h_{ij}(t, \boldsymbol{x})]dx^i dx^j \tag{2.25}$$

where h_{ij} denotes the perturbation to the spatial part of the metric. In general, for a symmetric metric, h_{ij} contains 6 independent components. However, the irreducible tensor perturbations are transverse, $h_{ij,i} = h_{ij,j} = 0$ and traceless, $\delta^{ij}h_{ij} = h_{ii} = 0$. By using these conditions, we can eliminate 4 of the 6 components in h_{ij} to get 2 independent components. It is these perturbations that we observe as GWs. By homogeneity and isotropy of the Universe, we can choose to orient our axes such that the GWs always propagate in the z-direction. In this case, the 3x3 tensor has elements $h_{zz} = 1$, $h_{xz} = h_{yz} = 0$, so that it has only 4 independent components which, by transversality and tracelessness, reduce to 2 independent components. These two components represent the two polarisations of GWs. These polarisations produce different squeezing and stretching actions on a ring of particles, arranged perpendicular to their propagation, as shown in figure 2.3.

Substituting the above metric into the Einstein equation, it can be shown that the metric perturbation h_{ij} obeys the following equation of motion in Fourier space,

$$h''_{ij}(\eta, \boldsymbol{x}) + 2\mathcal{H}(\eta)h'_{ij}(\eta, \boldsymbol{x}) - \nabla^2 h_{ij}(\eta, \boldsymbol{x}) = 0 \tag{2.26}$$

where $\mathcal{H} \equiv a'/a$ and $h_{ij} \equiv h_{ij}(k, \eta)$ and the Laplacian is w.r.t. the comoving co-ordinates. We can decompose the tensor perturbations into a left- and right-handed polarisation as

$$h_{ij}(\eta, \boldsymbol{x}) = \int \frac{d^3k}{(2\pi)^3}\, e^{i\boldsymbol{k}\cdot\boldsymbol{x}}[h_L(\eta, \boldsymbol{k})e^L_{ij}(\boldsymbol{k}) + h_R(\eta, \boldsymbol{k})e^R_{ij}(\boldsymbol{k})] \tag{2.27}$$

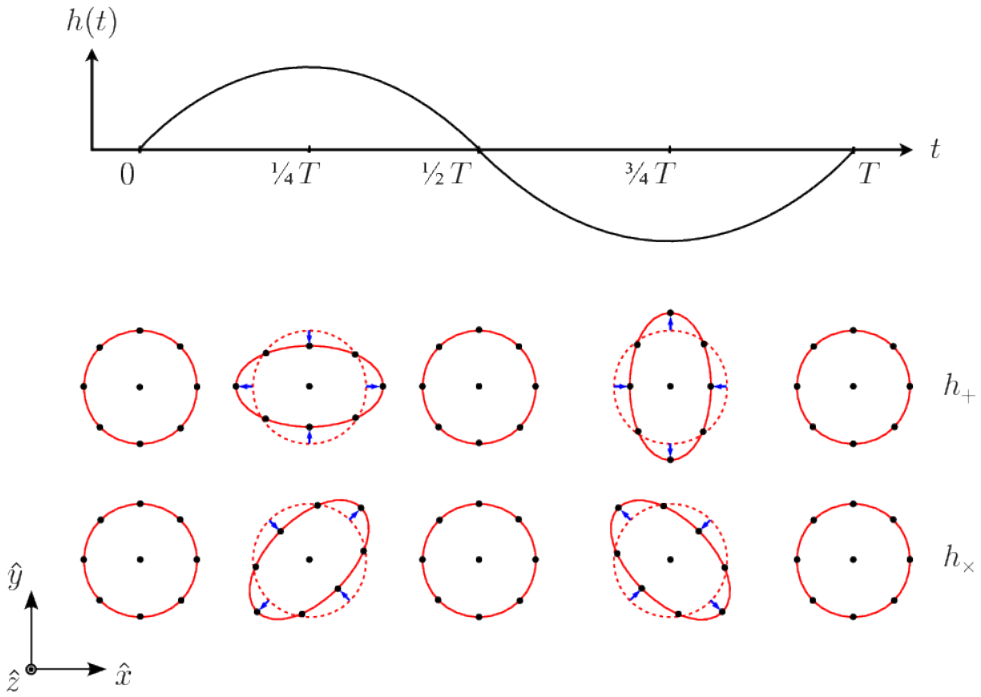

Figure 2.3: Gravitational waves come in two polarisations. They are distinguished by their action on a ring of particles as they pass perpendicular to the plane of the ring. The '+' (plus) polarisation (top) causes stretching and squeezing of the ring in the '+' direction, while the 'x' (cross) polarisation (bottom) deforms it in the 'x' direction (99).

where $e_{ij}^{L/R}(\boldsymbol{k})$ are time-independent polarisation tensors in the direction $\hat{k}$, whose properties are summarised in appendix B. Using this decomposition in equation (2.26) we find that each of the modes obeys it independently. If these modes correspond to quantum fluctuations, we can once again promote them to operators as before, and write $\hat{h}_\alpha(\eta, \boldsymbol{k}) = (2/aM_P)[\psi_k^\alpha(\eta)\hat{a}_{\boldsymbol{k}} + \psi_k^{*\alpha}(\eta)\hat{a}_{-\boldsymbol{k}}^\dagger]$, where $\alpha = L/R$ and the pre-factor arises from requiring a correct normalisation of the mode functions. Substituting this in equation (2.26), we find

$$\psi_\alpha'' + \left(k^2 - \frac{a''}{a}\right)\psi_\alpha = 0 \tag{2.28}$$

which is once again the equation of a harmonic oscillator. The rest of the analysis is parallel to that of the scalar field (section 2.3.1) , with $m_\phi = 0$, as GWs are massless in GR. In particular, the mode functions are given as (the mode functions are the same for both polarisations - vacuum fluctuations generate parity-invariant GWs)

$$\psi_\alpha(\eta, \boldsymbol{k}) = \frac{e^{-ik\eta}}{\sqrt{2k}}\left[1 - \frac{i}{k\eta}\right] \tag{2.29}$$

and accounting for both polarisations, the power spectrum of GWs is given as

$$\mathcal{P}_\psi = \frac{(aH)^2}{4\pi^2}. \tag{2.30}$$

From equation (2.30) we see that the power spectrum of GWs from vacuum fluctuations is exactly scale-independent in a de-Sitter Universe, and its amplitude gives us a measure of H, the Hubble parameter during inflation. Thus, once the scalar power spectrum is measured, measurement of the tensor-to-scalar ratio gives us a measure of the energy scale of inflation, provided the GWs originate from vacuum fluctuations of the metric. Again, if H decreases slowly, the power spectrum actually takes on a slightly red tilt.

2.3.3 Bispectrum of GWs in GR

In this thesis we use the Green's function method to calculate tensor bispectra in all the chapters. Alternatively, one can use the in-in formalism. The results derived in this section have been derived previously using the in-in formalism in (109; 108; 64). To calculate the bispectrum, we need to expand the action (equation (2.11)) to third order in h_{ij} or equivalently $\psi_{ij} \equiv aM_P h_{ij}/2$. The action, third order in ψ_{ij}, is given as,

$$S^{(3)} = \int d^4x \, \frac{2}{aM_P}\left[\psi_{ik,l}\psi_{jl}\psi_{ij,k} - \frac{1}{2}\psi_{ij,l}\psi_{kl}\psi_{ij,k}\right], \tag{2.31}$$

which can be derived by a simple but lengthy calculation. Because the Euler-Lagrange equation is linear in $\mathcal{L}$, we can just add the equation of motion following from the third-order action to the one from second-order action, equation (2.28), to get

$$\psi_{pq}'' + \left(-\nabla^2 - \frac{a''}{a}\right)\psi_{pq} = -\frac{2}{aM_P}\left[\psi_{pj,qr}\psi_{jr} + \psi_{pr,l}\psi_{ql,r} - \psi_{pq,lr}\psi_{lr} - \psi_{ik,q}\psi_{ip,k} + \frac{1}{2}\psi_{ij,q}\psi_{ij,p}\right], \tag{2.32}$$

where all the ψs are functions of $(\eta, \boldsymbol{x})$. Following the same method as laid out in detail in chapter 3, for the right-handed polarisation we find

$$\hat{\psi}_2^R(\tau, \boldsymbol{k}) = \int_{-\infty}^{\tau} d\eta\, G_\psi^{(2)}(\tau, \eta, k) \hat{S}_{pq}(\eta, \boldsymbol{k}) e_{pq}^L(\boldsymbol{k}) \tag{2.33}$$

where $G_\psi^{(2)}(\tau, \eta, k)$ is the Green's function for the second order perturbation and is the same as given in equation (3.27), $\hat{S}_{pq}$ is a function of two first order tensor perturbations, $\hat{\psi}$,

$$\hat{S}_{pq}(\eta, \boldsymbol{k}) = -\int \frac{d^3p_1 d^3p_2}{(2\pi)^6} \delta_D(\boldsymbol{p}_1 + \boldsymbol{p}_2 - \boldsymbol{k}) \frac{2H}{M_P} \eta \hat{\psi}_{p_1}(\eta) \hat{\psi}_{p_2}(\eta) Q_{pq}(\boldsymbol{p}_1, \boldsymbol{p}_2)\,, \tag{2.34}$$

with

$$\begin{aligned} Q_{pq}(\boldsymbol{p}_1, \boldsymbol{p}_2) \equiv & -e_{pl}^R(p_1) e_{lr}^R(p_2) p_{1q} p_{1r} - e_{pr}^R(p_1) e_{ql}^R(p_2) p_{1l} p_{2r} \\ & + e_{pq}^R(p_1) e_{lr}^R(p_2) p_{1l} p_{1r} + e_{lr}^R(p_1) e_{lp}^R(p_2) p_{1q} p_{2r} - \frac{1}{2} e_{rl}^R(p_1) e_{rl}^R(p_2) p_{1p} p_{2q}\,. \end{aligned} \tag{2.35}$$

The tree-level bispectrum of right-handed tensor modes is then given by

$$\begin{aligned} \left\langle \hat{\psi}^R(\tau, \boldsymbol{k}_1) \hat{\psi}^R(\tau, \boldsymbol{k}_2) \hat{\psi}^R(\tau, \boldsymbol{k}_3) \right\rangle = & \left\langle \hat{\psi}_1^R(\tau, \boldsymbol{k}_1) \hat{\psi}_1^R(\tau, \boldsymbol{k}_2) \hat{\psi}_2^R(\tau, \boldsymbol{k}_3) \right\rangle \\ & + \left\langle \hat{\psi}_1^R(\tau, \boldsymbol{k}_1) \hat{\psi}_2^R(\tau, \boldsymbol{k}_2) \hat{\psi}_1^R(\tau, \boldsymbol{k}_3) \right\rangle + \left\langle \hat{\psi}_2^R(\tau, \boldsymbol{k}_1) \hat{\psi}_1^R(\tau, \boldsymbol{k}_2) \hat{\psi}_1^R(\tau, \boldsymbol{k}_3) \right\rangle\,. \end{aligned} \tag{2.36}$$

Let us work out one of these terms in detail. Using equation (2.33), we find

$$\begin{aligned} \left\langle \hat{\psi}_1^R(\tau, \boldsymbol{k}_1) \hat{\psi}_1^R(\tau, \boldsymbol{k}_2) \hat{\psi}_2^R(\tau, \boldsymbol{k}_3) \right\rangle = & \frac{H}{M_P} \int_{-\infty}^{0} d\eta\, \eta\, G_\psi^{(2)}(\tau, \eta, k_3) \int \frac{d^3p_1 d^3p_2}{(2\pi)^6} \\ & \delta_D(\boldsymbol{p}_1 + \boldsymbol{p}_2 - \boldsymbol{k}_3)\; Q_{pq}^{RR}(\boldsymbol{p}_1, \boldsymbol{p}_2) e_{pq}^L(\boldsymbol{k}_3) \left\langle \hat{\psi}_1^R(\tau, \boldsymbol{k}_1) \hat{\psi}_1^R(\tau, \boldsymbol{k}_2) \hat{\psi}_1^R(\eta, \boldsymbol{p}_1) \hat{\psi}_1^R(\eta, \boldsymbol{p}_2) \right\rangle\,, \end{aligned} \tag{2.37}$$

where we only use Q_{pq}^{RR} because there are only right-handed first-order operators in the expectation value (see appendix A for more details). The expectation value is calculated as

$$\begin{aligned} \left\langle \hat{\psi}_1^R(\tau, \boldsymbol{k}_1) \hat{\psi}_1^R(\tau, \boldsymbol{k}_2) \hat{\psi}_1^R(\eta, \boldsymbol{p}_1) \hat{\psi}_1^R(\eta, \boldsymbol{p}_2) \right\rangle = & \left\langle \hat{a}_{\boldsymbol{k}_1}^R \hat{a}_{\boldsymbol{k}_2}^R \hat{a}_{-\boldsymbol{p}_1}^{R\dagger} \hat{a}_{-\boldsymbol{p}_2}^{R\dagger} \right\rangle \\ & \Psi_1^R(\tau, \boldsymbol{k}_1) \Psi_1^R(\tau, \boldsymbol{k}_2) \Psi_1^{*R}(\eta, \boldsymbol{p}_1) \Psi_1^{*R}(\eta, \boldsymbol{p}_2) \end{aligned} \tag{2.38}$$

$$\begin{aligned} & = (2\pi)^6 \Big[\delta_{\boldsymbol{k}_1 \boldsymbol{p}_1} \delta_{\boldsymbol{k}_2 \boldsymbol{p}_2} + \delta_{\boldsymbol{k}_2 \boldsymbol{p}_1} \delta_{\boldsymbol{k}_2 \boldsymbol{p}_1} \Big] \\ & \Psi_1^R(\tau, \boldsymbol{k}_1) \Psi_1^R(\tau, \boldsymbol{k}_2) \Psi_1^{*R}(\eta, \boldsymbol{p}_1) \Psi_1^{*R}(\eta, \boldsymbol{p}_2)\,, \end{aligned} \tag{2.39}$$

where we have defined $\delta_{\boldsymbol{k}_1\boldsymbol{p}_1} \equiv \delta_D(\boldsymbol{k}_1 + \boldsymbol{p}_1)$. Substituting this expectation value in equation (2.37) and integrating over the delta functions, we get

$$\left\langle \hat{\psi}_1^R(\tau,\boldsymbol{k}_1)\hat{\psi}_1^R(\tau,\boldsymbol{k}_2)\hat{\psi}_2^R(\tau,\boldsymbol{k}_3)\right\rangle = (2\pi)^3\delta_D(\boldsymbol{k}_1+\boldsymbol{k}_2+\boldsymbol{k}_3)\frac{H}{M_P} \int_{-\infty}^{0} d\eta\,\eta\,G_\psi^{(2)}(\tau,\eta,k_3)\Big[e_{pq}^L(\boldsymbol{k}_3)Q_{pq}^{RR}(-\boldsymbol{k}_1,-\boldsymbol{k}_2)+e_{pq}^L(\boldsymbol{k}_3)Q_{pq}^{RR}(-\boldsymbol{k}_2,-\boldsymbol{k}_1)\Big] \Psi_1^R(\tau,\boldsymbol{k}_1)\Psi_1^R(\tau,\boldsymbol{k}_2)\Psi_1^{*R}(\eta,-\boldsymbol{k}_1)\Psi_1^{*R}(\eta,-\boldsymbol{k}_2)\,. \quad (2.40)$$

The contraction of the polarisation tensors is given by (appendix A)

$$\Big[e_{pq}^L(\boldsymbol{k}_3)Q_{pq}^{RR}(-\boldsymbol{k}_1,-\boldsymbol{k}_2)+e_{pq}^L(\boldsymbol{k}_3)Q_{pq}^{RR}(-\boldsymbol{k}_2,-\boldsymbol{k}_1)\Big] = k_1^2\,\tilde{\Xi}^2\,\Xi\,, \quad (2.41)$$

where

$$\tilde{\Xi} = 1+r_2+r_3\,, \quad \Xi = \frac{(1+r_2+r_3)^3}{64r_2^2r_3^2}(r_2+r_3-1)(r_2-r_3+1)(-r_2+r_3+1)\,, \quad (2.42)$$

with $r_2 \equiv k_2/k_1$ and $r_3 = k_3/k_1$ (11). We find that this contraction remains the same regardless of the order in which the different $\boldsymbol{k}$'s appear, and so is common to all three contributions to the bispectrum in equation (2.36). Note that it is also independent of the conformal time, so we can take it out of the η integral. This gives us

$$\left\langle \hat{\psi}_1^R(\tau,\boldsymbol{k}_1)\hat{\psi}_1^R(\tau,\boldsymbol{k}_2)\hat{\psi}_2^R(\tau,\boldsymbol{k}_3)\right\rangle = (2\pi)^3\delta_D(\boldsymbol{k}_1+\boldsymbol{k}_2+\boldsymbol{k}_3)\frac{H}{M_P}k_1^2\,\tilde{\Xi}^2\,\Xi \Psi_1^R(\tau,\boldsymbol{k}_1)\Psi_1^R(\tau,\boldsymbol{k}_2)\int_{-\infty}^{0} d\eta\,\eta\,G_\psi^{(2)}(\tau,\eta,k_3)\Psi_1^{*R}(\eta,-\boldsymbol{k}_1)\Psi_1^{*R}(\eta,-\boldsymbol{k}_2)\,. \quad (2.43)$$

We now substitute the first-order mode functions, equation (2.29), into the above equation to get

$$\Psi_1^R(\tau,\boldsymbol{k}_1)\Psi_1^R(\tau,\boldsymbol{k}_2)\int_{-\infty}^{0} d\eta\,\eta\,G_\psi^{(2)}(\tau,\eta,k_3)\Psi_1^{*R}(\eta,-\boldsymbol{k}_1)\Psi_1^{*R}(\eta,-\boldsymbol{k}_2) = \frac{e^{-ik_1\tau}}{\sqrt{2k_1}}\Big[1-\frac{i}{k_1\tau}\Big]\frac{e^{-ik_2\tau}}{\sqrt{2k_2}}\Big[1-\frac{i}{k_2\tau}\Big]\int_{-\infty}^{0} d\eta\,\eta\,G_\psi^{(2)}(\tau,\eta,k_3)\frac{e^{ik_1\eta}}{\sqrt{2k_1}}\Big[1+\frac{i}{k_1\eta}\Big]\frac{e^{ik_2\eta}}{\sqrt{2k_2}}\Big[1+\frac{i}{k_2\eta}\Big]\,. \quad (2.44)$$

Taking $-i/k_j\tau$ and $-i/k_j\eta$ out from the mode functions we get

$$\Psi_1^R(\tau,\boldsymbol{k}_1)\Psi_1^R(\tau,\boldsymbol{k}_2)\int_{-\infty}^{0} d\eta\,\eta\,G_\psi^{(2)}(\tau,\eta,k_3)\Psi_1^{*R}(\eta,-\boldsymbol{k}_1)\Psi_1^{*R}(\eta,-\boldsymbol{k}_2) = \frac{e^{-i(k_1+k_2)\tau}}{4(k_1k_2)^3\tau^2}[1+ik_1\tau][1+ik_2\tau]\int_{-\infty}^{0} d\eta\,\eta\,G_\psi^{(2)}(\tau,\eta,k_3)\frac{e^{i(k_1+k_2)\eta}}{\eta^2}[1-ik_1\eta][1-ik_2\eta]\,. \quad (2.45)$$

Using equation (3.27), we can substitute Green's function,

$$\Psi_1^R(\tau,\boldsymbol{k}_1)\Psi_1^R(\tau,\boldsymbol{k}_2)\int_{-\infty}^{0} d\eta\,\eta\,G_\psi^{(2)}(\tau,\eta,k_3)\Psi_1^{*R}(\eta,-\boldsymbol{k}_1)\Psi_1^{*R}(\eta,-\boldsymbol{k}_2) =$$
$$\frac{e^{-i(k_1+k_2)\tau}}{4(k_1k_2k_3)^3\tau^3}[1+ik_1\tau][1+ik_2\tau]\int_{-\infty}^{0}\frac{d\eta}{\eta^2}\,\tilde{G}_\psi^{(2)}(\tau,\eta,k_3)\frac{e^{i(k_1+k_2)\eta}}{\eta^2}[1-ik_1\eta][1-ik_2\eta]\,. \quad (2.46)$$

Then the bispectrum of GWs is given as

$$\left\langle\hat{h}_1^R(\tau,\boldsymbol{k}_1)\hat{h}_1^R(\tau,\boldsymbol{k}_2)\hat{h}_2^R(\tau,\boldsymbol{k}_3)\right\rangle = (2\pi)^3\delta_D(\boldsymbol{k}_1+\boldsymbol{k}_2+\boldsymbol{k}_3)\left(\frac{H}{M_P}\right)^4 k_1^2\,\tilde{\Xi}^2\,\Xi$$
$$\frac{2\,e^{-i(k_1+k_2)\tau}}{(k_1k_2k_3)^3}[1+ik_1\tau][1+ik_2\tau]\int_{-\infty}^{0}\frac{d\eta}{\eta^2}\,\tilde{G}_\psi^{(2)}(\tau,\eta,k_3)e^{i(k_1+k_2)\eta}[1-ik_1\eta][1-ik_2\eta]\,, \quad (2.47)$$

where we have used $\psi_{ij}(\tau,\boldsymbol{k}) \equiv aM_Ph_{ij}(\tau,\boldsymbol{k})/2$. Equation (2.47) is valid for any time τ. However, to make contact with observations we need to take the super-horizon limit, $k_i\tau \to 0$, for all three modes. The function $\tilde{G}_\psi$ in this limit becomes (equation (3.27))

$$\tilde{G}_\psi^{(2)}(0,\eta,k) = \Theta(-\eta)[k\eta\cos(k\eta)-\sin(k\eta)]\,, \quad (2.48)$$

which we can re-write as

$$\tilde{G}_\psi^{(2)}(0,\eta,k) = \frac{i\Theta(-\eta)}{2}\Big[e^{ik\eta}(1-ik\eta)-e^{-ik\eta}(1+ik\eta)\Big]\,. \quad (2.49)$$

Taking the super-horizon limit, $k_i\tau \to 0$, of equation (2.47) and substituting equation (2.49) in it, the bispectrum becomes

$$\left\langle\hat{h}_1^R(\tau,\boldsymbol{k}_1)\hat{h}_1^R(\tau,\boldsymbol{k}_2)\hat{h}_2^R(\tau,\boldsymbol{k}_3)\right\rangle = (2\pi)^3\delta_D(\boldsymbol{k}_1+\boldsymbol{k}_2+\boldsymbol{k}_3)\left(\frac{H}{M_P}\right)^4 k_1^2\,\tilde{\Xi}^2\,\Xi\frac{2}{(k_1k_2k_3)^3}$$
$$\int_{-\infty}^{0}\frac{d\eta}{\eta^2}\,\frac{i}{2}\Big[e^{ik_3\eta}(1-ik_3\eta)-e^{-ik_3\eta}(1+ik_3\eta)]e^{i(k_1+k_2)\eta}[1-ik_1\eta][1-ik_2\eta]\,. \quad (2.50)$$

Following the same procedure as above, we find for the other two terms in equation (2.36)

$$\left\langle\hat{h}_1^R(\tau,\boldsymbol{k}_1)\hat{h}_2^R(\tau,\boldsymbol{k}_2)\hat{h}_1^R(\tau,\boldsymbol{k}_3)\right\rangle = (2\pi)^3\delta_D(\boldsymbol{k}_1+\boldsymbol{k}_2+\boldsymbol{k}_3)\left(\frac{H}{M_P}\right)^4 k_1^2\,\tilde{\Xi}^2\,\Xi\frac{2}{(k_1k_2k_3)^3}$$
$$\int_{-\infty}^{0}\frac{d\eta}{\eta^2}\,\frac{i}{2}\Big[e^{ik_2\eta}(1-ik_2\eta)-e^{-ik_2\eta}(1+ik_2\eta)]e^{i(k_1-k_3)\eta}[1-ik_1\eta][1+ik_3\eta]\,, \quad (2.51)$$

and

$$\left\langle\hat{h}_2^R(\tau,\boldsymbol{k}_1)\hat{h}_1^R(\tau,\boldsymbol{k}_2)\hat{h}_1^R(\tau,\boldsymbol{k}_3)\right\rangle = (2\pi)^3\delta_D(\boldsymbol{k}_1+\boldsymbol{k}_2+\boldsymbol{k}_3)\left(\frac{H}{M_P}\right)^4 k_1^2\,\tilde{\Xi}^2\,\Xi\frac{2}{(k_1k_2k_3)^3}$$
$$\int_{-\infty}^{0}\frac{d\eta}{\eta^2}\,\frac{i}{2}\Big[e^{ik_1\eta}(1-ik_1\eta)-e^{-ik_1\eta}(1+ik_1\eta)]e^{-i(k_2+k_3)\eta}[1+ik_2\eta][1+ik_3\eta]\,. \quad (2.52)$$

Adding equations (2.50)–(2.52), the first term of equation (2.51) is cancelled by the second term of equation (2.50) while the second term is cancelled by the first term in equation (2.52) so that we find

$$\left\langle \hat{h}^R(\tau,\boldsymbol{k}_1)\hat{h}^R(\tau,\boldsymbol{k}_2)\hat{h}^R(\tau,\boldsymbol{k}_3)\right\rangle = (2\pi)^3\delta_D(\boldsymbol{k}_1+\boldsymbol{k}_2+\boldsymbol{k}_3)\left(\frac{H}{M_P}\right)^4 k_1^2\,\tilde{\Xi}^2\,\Xi \\ \frac{2}{(k_1k_2k_3)^3}\int_{-\infty}^{0}\frac{d\eta}{\eta^2}\left[\frac{i}{2}e^{i(k_1+k_2+k_3)\eta}(1-ik_1\eta)(1-ik_2\eta)(1-ik_3\eta)+c.c.\right], \quad (2.53)$$

which we can simplify to get

$$B_h^{RRR}(k_1,k_2,k_3) = (2\pi)^3\delta_D(\boldsymbol{k}_1+\boldsymbol{k}_2+\boldsymbol{k}_3)\left(\frac{H}{M_P}\right)^4 k_1^2\,\tilde{\Xi}^2\,\Xi \\ \frac{2}{(k_1k_2k_3)^3}\mathrm{Re}\left[\int_{-\infty}^{0} i\,\frac{d\eta}{\eta^2}\,e^{i(k_1+k_2+k_3)\eta}(1-ik_1\eta)(1-ik_2\eta)(1-ik_3\eta)\right], \quad (2.54)$$

where Re$[z]$ denotes the real part of the complex number z. This is the same result as obtained via the in-in formalism (108; 109; 64). The integral can be evaluated by choosing the integration contour to go from $-\infty(1+i\epsilon)$ to 0, with $\epsilon \ll 1$, to get a convergent result (108; 109; 64),

$$(k_1k_2k_3)^2 B_h^{RRR}(k_1,k_2,k_3) = (2\pi)^3\delta_D(\boldsymbol{k}_1+\boldsymbol{k}_2+\boldsymbol{k}_3)\left(\frac{H}{M_P}\right)^4 \frac{2\,\tilde{\Xi}^2\,\Xi}{r_2r_3}\left[\tilde{\Xi}-\frac{\sum_{i>j}r_ir_j}{\tilde{\Xi}}-\frac{r_2r_3}{\tilde{\Xi}^2}\right], \quad (2.55)$$

where $r_i \equiv k_i/k_1$. Note that this choice of the integration contour corresponds to projecting the vacuum of the interacting theory on to that of the free theory in the in-in formalism (108; 180). The same choice needs to be made also in the Green's function approach. In retrospect, this is not surprising.

In our approach, the time evolution is carried entirely by the second-order operator, equation (2.33), while states remain stationary. So, the expectation value in equation (2.36) needs to be evaluated in the vacuum of the interacting theory, the so-called "in" state. On the other hand, the creation and annihilation operators, $\hat{a}^p_{\boldsymbol{k}}$ and $\hat{a}^{\dagger p}_{\boldsymbol{k}}$, are defined in the vacuum of the free theory, where the higher order source terms (S_{pq} with powers of $\psi \geq 2$) in the equation of motion for ψ_{pq} are 0 over all of spacetime. As a result, when evaluating the expectation values using $\hat{a}^p_{\boldsymbol{k}}$ and $\hat{a}^{\dagger p}_{\boldsymbol{k}}$ in equation (2.38), we need to project the "in" state on to the vacuum of the free theory. How do we achieve that? Looking at equation (2.33) and considering the Heaviside function $\Theta(\tau-\eta)$ in Green's function (equation (3.27)), we see that as $\tau \to -\infty$ the second-order operator $\to 0$ (which is equivalent to the interaction Hamiltonian $\to 0$ in the in-in formalism). Thus, at past infinity the vacuum of the interacting theory is essentially that of the free theory, and the projection prescription then follows from that of the in-in formalism (108; 180).

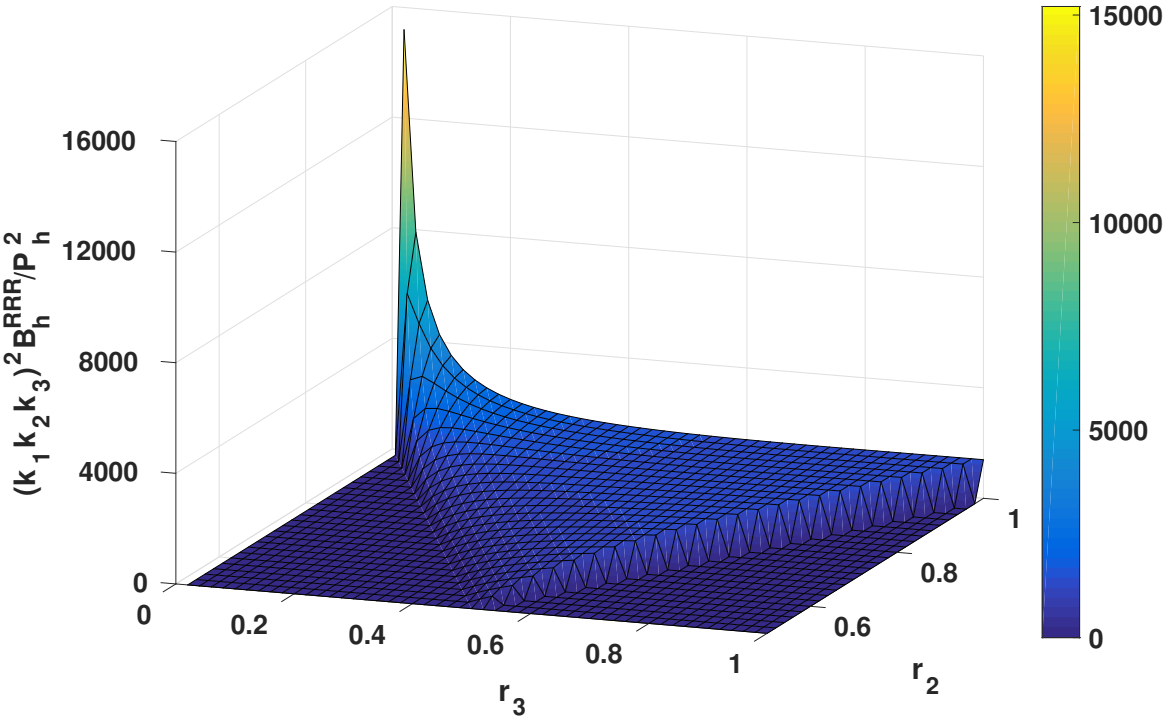

Figure 2.4: 3D plot of $(k_1k_2k_3)^2 B_h^{RRR}/(\mathcal{P}_h^R)^2$ for right-handed vacuum fluctuations of the metric. We only show $r_3 \leq r_2$ and the triangle condition implies that the bispectrum is non-zero only for $r_2 + r_3 \geq 1$.

In refs. (10; 11) right-handed tensor perturbations are chirally amplified by tachyonic instability of an SU(2) gauge field, which leads to highly non-Gaussian GWs. There, non-Gaussianity is characterised using the ratio $B_h^{RRR}(k,k,k)/(P_h^R(k))^2$. We can now evaluate the same ratio for the case of vacuum fluctuations,

$$\frac{B_{h,\mathrm{vac}}^{RRR}(k,k,k)}{(P_{h,\mathrm{vac}}^R(k))^2} = 3.586\,, \tag{2.56}$$

which is of order unity and much smaller than that generated in models with spectator gauge fields (10; 11; 47; 19). Figure 2.4 shows the shape of the tensor bispectrum, equation (2.55), normalised by the square of the dimensionless power spectrum, $(k_1k_2k_3)^2 B_h^{RRR}/(\mathcal{P}_h^R)^2$, as a function of r_2 and r_3. We find that it peaks in the squeezed limit, $r_3 \ll r_2 \approx 1$, and it is zero in the folded limit, $r_2 + r_3 = 1$.

2.3.4 Mixed Bispectrum of Right- and Left-Handed Vacuum Fluctuations

Parity invariance means that $B_h^{RRR} = B_h^{LLL}$, $B_h^{RRL} = B_h^{LLR}$, $B_h^{RLR} = B_h^{LRL}$, and $B_h^{LRR} = B_h^{RLL}$, so that one only needs to calculate 4 out of 8 possible bispectra. As a concrete illustration, let us now explicitly evaluate $B_h^{RRL}(k_1, k_2, k_3)$ using Green's functions. We have, analogous to equation (2.36),

$$\left\langle \hat{\psi}^R(\tau, \boldsymbol{k}_1)\hat{\psi}^R(\tau, \boldsymbol{k}_2)\hat{\psi}^L(\tau, \boldsymbol{k}_3)\right\rangle = \left\langle \hat{\psi}_1^R(\tau, \boldsymbol{k}_1)\hat{\psi}_1^R(\tau, \boldsymbol{k}_2)\hat{\psi}_2^L(\tau, \boldsymbol{k}_3)\right\rangle + \left\langle \hat{\psi}_1^R(\tau, \boldsymbol{k}_1)\hat{\psi}_2^R(\tau, \boldsymbol{k}_2)\hat{\psi}_1^L(\tau, \boldsymbol{k}_3)\right\rangle + \left\langle \hat{\psi}_2^R(\tau, \boldsymbol{k}_1)\hat{\psi}_1^R(\tau, \boldsymbol{k}_2)\hat{\psi}_1^L(\tau, \boldsymbol{k}_3)\right\rangle . \quad (2.57)$$

Now we need to evaluate all three terms separately. The calculation proceeds exactly as before

$$\left\langle \hat{\psi}_1^R(\tau, \boldsymbol{k}_1)\hat{\psi}_1^R(\tau, \boldsymbol{k}_2)\hat{\psi}_2^L(\tau, \boldsymbol{k}_3)\right\rangle = \frac{H}{M_P}\int_{-\infty}^{0} d\eta\, \eta\, G_\psi^{(2)}(\tau, \eta, k_3) \int \frac{d^3p_1 d^3p_2}{(2\pi)^6} \delta_D(\boldsymbol{p}_1 + \boldsymbol{p}_2 - \boldsymbol{k}_3)\; Q_{pq}^{RR}(\boldsymbol{p}_1, \boldsymbol{p}_2) e_{pq}^R(\boldsymbol{k}_3) \left\langle \hat{\psi}_1^R(\tau, \boldsymbol{k}_1)\hat{\psi}_1^R(\tau, \boldsymbol{k}_2)\hat{\psi}_1^R(\eta, \boldsymbol{p}_1)\hat{\psi}_1^R(\eta, \boldsymbol{p}_2)\right\rangle , \quad (2.58)$$

where we only needed Q_{pq}^{RR} because we have two right-handed operators at first-order in the bispectrum. Note that we now use $e_{pq}^R(\mathbf{k})$ to calculate the second-order operator for the left-handed polarisation. The expectation value of the first-order fields is given by equation (2.38). Using that we can write

$$\left\langle \hat{\psi}_1^R(\tau, \boldsymbol{k}_1)\hat{\psi}_1^R(\tau, \boldsymbol{k}_2)\hat{\psi}_2^L(\tau, \boldsymbol{k}_3)\right\rangle = \frac{H}{M_P}(2\pi)^3\delta_D(\boldsymbol{k}_1 + \boldsymbol{k}_2 + \boldsymbol{k}_3) \Big[e_{pq}^R(\boldsymbol{k}_3)Q_{pq}^{RR}(-\boldsymbol{k}_1, -\boldsymbol{k}_2) + e_{pq}^R(\boldsymbol{k}_3)Q_{pq}^{RR}(-\boldsymbol{k}_2, -\boldsymbol{k}_1)\Big]\Psi_1^R(\tau, \boldsymbol{k}_1)\Psi_1^R(\tau, \boldsymbol{k}_2) \int_{-\infty}^{0} d\eta\, \eta\, G_\psi^{(2)}(\tau, \eta, k_3)\Psi_1^{*R}(\eta, -\boldsymbol{k}_1)\Psi_1^{*R}(\eta, -\boldsymbol{k}_2) . \quad (2.59)$$

For the second term in equation (2.57) we have

$$\left\langle \hat{\psi}_1^R(\tau, \boldsymbol{k}_1)\hat{\psi}_2^R(\tau, \boldsymbol{k}_2)\hat{\psi}_1^L(\tau, \boldsymbol{k}_3)\right\rangle = \frac{H}{M_P}\int_{-\infty}^{0} d\eta\, \eta\, G_\psi^{(2)}(\tau, \eta, k_2) \int \frac{d^3p_1 d^3p_2}{(2\pi)^6} \delta_D(\boldsymbol{p}_1 + \boldsymbol{p}_2 - \boldsymbol{k}_2)\; e_{pq}^L(\boldsymbol{k}_2) \Big\langle \hat{\psi}_1^R(\tau, \boldsymbol{k}_1)\Big[Q_{pq}^{LR}(\boldsymbol{p}_1, \boldsymbol{p}_2)\hat{\psi}_1^L(\eta, \boldsymbol{p}_1)\hat{\psi}_1^R(\eta, \boldsymbol{p}_2) + Q_{pq}^{RL}(\boldsymbol{p}_1, \boldsymbol{p}_2)\hat{\psi}_1^R(\eta, \boldsymbol{p}_1)\hat{\psi}_1^L(\eta, \boldsymbol{p}_2)\Big]\hat{\psi}_1^L(\tau, \boldsymbol{k}_3)\Big\rangle , \quad (2.60)$$

where we now use terms containing Q_{pq}^{LR} and Q_{pq}^{RL} in the source function (appendix A) as we have one right-handed and one left-handed mode in our bispectrum. This can be

simplified using $\left\langle \hat{\psi}_1^L \hat{\psi}_1^R \right\rangle = \left\langle \hat{\psi}_1^R \hat{\psi}_1^L \right\rangle = 0$ to get

$$\left\langle \hat{\psi}_1^R(\tau, \boldsymbol{k}_1)\hat{\psi}_2^R(\tau, \boldsymbol{k}_2)\hat{\psi}_1^L(\tau, \boldsymbol{k}_3) \right\rangle = \frac{H}{M_P}(2\pi)^3\delta_D(\boldsymbol{k}_1 + \boldsymbol{k}_2 + \boldsymbol{k}_3) \\ e^L_{pq}(\boldsymbol{k}_2)\Big[Q^{LR}_{pq}(-\boldsymbol{k}_3, -\boldsymbol{k}_1) + Q^{RL}_{pq}(-\boldsymbol{k}_1, -\boldsymbol{k}_3)\Big]\Psi_1^R(\tau, \boldsymbol{k}_1)\Psi_1^{*L}(\tau, -\boldsymbol{k}_3) \\ \int_{-\infty}^{0} d\eta\, \eta\, G^{(2)}_{\psi}(\tau, \eta, k_2)\, \Psi_1^{*R}(\eta, -\boldsymbol{k}_1)\Psi_1^L(\eta, -\boldsymbol{k}_3)\,. \quad (2.61)$$

Similarly, for the third term in equation (2.57) we get

$$\left\langle \hat{\psi}_2^R(\tau, \boldsymbol{k}_1)\hat{\psi}_1^R(\tau, \boldsymbol{k}_2)\hat{\psi}_1^L(\tau, \boldsymbol{k}_3) \right\rangle = \frac{H}{M_P}\int_{-\infty}^{0} d\eta\, \eta\, G^{(2)}_{\psi}(\tau, \eta, k_2) \int \frac{d^3p_1 d^3p_2}{(2\pi)^6} \\ \delta_D(\boldsymbol{p}_1 + \boldsymbol{p}_2 - \boldsymbol{k}_2)\; e^L_{pq}(\boldsymbol{k}_1)\Big\langle \Big[Q^{LR}_{pq}(\boldsymbol{p}_1, \boldsymbol{p}_2)\hat{\psi}_1^L(\eta, \boldsymbol{p}_1)\hat{\psi}_1^R(\eta, \boldsymbol{p}_2) \\ + Q^{RL}_{pq}(\boldsymbol{p}_1, \boldsymbol{p}_2)\hat{\psi}_1^R(\eta, \boldsymbol{p}_1)\hat{\psi}_1^L(\eta, \boldsymbol{p}_2)\Big]\hat{\psi}_1^R(\tau, \boldsymbol{k}_2)\hat{\psi}_1^L(\tau, \boldsymbol{k}_3)\Big\rangle\,, \quad (2.62)$$

where again we need Q^{LR}_{pq} and Q^{RL}_{pq}. This can be simplified to get

$$\left\langle \hat{\psi}_2^R(\tau, \boldsymbol{k}_1)\hat{\psi}_1^R(\tau, \boldsymbol{k}_2)\hat{\psi}_1^L(\tau, \boldsymbol{k}_3) \right\rangle = \frac{H}{M_P}(2\pi)^3\delta_D(\boldsymbol{k}_1 + \boldsymbol{k}_2 + \boldsymbol{k}_3) \\ e^L_{pq}(\boldsymbol{k}_1)\Big[Q^{LR}_{pq}(-\boldsymbol{k}_3, -\boldsymbol{k}_2) + Q^{RL}_{pq}(-\boldsymbol{k}_2, -\boldsymbol{k}_3)\Big]\Psi_1^{*R}(\tau, -\boldsymbol{k}_2)\Psi_1^{*L}(\tau, -\boldsymbol{k}_3) \\ \int_{-\infty}^{0} d\eta\, \eta\, G^{(2)}_{\psi}(\tau, \eta, k_2)\, \Psi_1^R(\eta, \boldsymbol{k}_2)\Psi_1^L(\eta, \boldsymbol{k}_3)\,. \quad (2.63)$$

The contraction of polarisation tensors is again found to be the same for all three terms, and is given by

$$k_1^2 \frac{\Xi}{\tilde{\Xi}^2}(1 + r_2 - r_3)^4\,, \quad (2.64)$$

which can be taken out of all the three terms. The minus sign in front of r_3 reflects the breaking of the symmetry inherent in equation (2.57). Then, note that the remaining terms containing the first order mode functions are *exactly* the same as in section 3.3, since the first-order mode functions are the same for left- and right-handed polarisations. Thus, we obtain

$$B_h^{RRL}(k_1, k_2, k_3) = (2\pi)^3\delta_D(\boldsymbol{k}_1 + \boldsymbol{k}_2 + \boldsymbol{k}_3)\left(\frac{H}{M_P}\right)^4 k_1^2\, \frac{\Xi}{\tilde{\Xi}^2}(1 + r_2 - r_3)^4 \\ \frac{2}{(k_1k_2k_3)^3}\mathrm{Re}\left[\int_{-\infty}^{0} i\,\frac{d\eta}{\eta^2}\, e^{i(k_1+k_2+k_3)\eta}(1 - ik_1\eta)(1 - ik_2\eta)(1 - ik_3\eta)\right], \quad (2.65)$$

which, after evaluating the integral, yields

$$(k_1k_2k_3)^2 B_h^{RRL}(k_1,k_2,k_3) = (2\pi)^3\delta_D(\boldsymbol{k}_1+\boldsymbol{k}_2+\boldsymbol{k}_3)\left(\frac{H}{M_P}\right)^4 \frac{2\,\Xi}{\tilde{\Xi}^2}\frac{(1+r_2-r_3)^4}{r_2r_3}\left[\frac{\tilde{\Xi}}{\Xi} - \frac{\sum_{i>j} r_ir_j}{\tilde{\Xi}} - \frac{r_2r_3}{\tilde{\Xi}^2}\right], \quad (2.66)$$

which is again the same as that in the in-in formalism (108; 109; 64). Figure 2.5 shows the shape of the mixed bispectrum, equation (2.66), normalised by the power spectrum, as in figure 2.4. Note that we show the full range of $0 \leq r_2 \leq 1$ because the bispectrum is no longer symmetric in r_2 and r_3. While the bispectrum of three right-handed modes has large values over most of the $r_3 - r_2$ plane, the mixed bispectrum is much closer to zero for most of the plane, and has a rather sharp peak in the squeezed limit. The ratio of the mixed bispectrum to the "pure" one can also be calculated (equation (2.66) and equation (2.55))

$$\frac{B_h^{RRL}(k_1,k_2,k_3)}{B_h^{RRR}(k_1,k_2,k_3)} = \frac{(1+r_2-r_3)^4}{\tilde{\Xi}^4} = \frac{(1+r_2-r_3)^4}{(1+r_2+r_3)^4}\,, \quad (2.67)$$

which in the equilateral configuration, $r_2 = r_3 = 1$, evaluates to $1/81$, and approaches 1 in the squeezed limit, $r_3 \ll r_2 \approx 1$ (64). Note however, that in the opposite squeezed limit, $r_2 \ll r_3 \approx 1$, the bispectrum approaches 0. This is because when the left-handed mode has a wavelength much larger than the other two, the bispectrum is essentially produced by small-scale self-interactions between two right-handed modes, which are highly correlated. In the other limit, the bispectrum arises from interactions between a left- and right-handed mode, which are much less correlated. We also note that this ratio is close to 0 for the whole plane in models with spectator gauge fields (19; 47; 127; 10; 11), where tensor fluctuations are dominated by sourced modes of a single helicity, in contrast to vacuum fluctuations.

2.4 Large Scale Structure of the Universe

Once inflation ends, the inflaton settles into the bottom of its potential well, and starts oscillating about its minimum, losing energy to other fields, giving rise to the standard matter we see around us today. This phase is known as *reheating*, but we do not consider it in further detail here. At the end of reheating, the Universe enters a radiation dominated phase, and it experiences decelerated expansion. In this phase, the scale factor grows as $a(t) \propto t^{1/2}$ so that the comoving horizon starts growing as $(aH)^{-1} \propto t^{1/2}$. As a result, modes that exit the horizon during inflation, start re-entering and start accreting matter via gravitational attraction. However, the Universe is still sufficiently hot that the photons and baryons are tightly coupled to each other via electromagnetic interactions. Dark matter, on the other hand, is at most weakly coupled to the rest of the primordial fluid, and can start clustering as soon it becomes non-relativistic. When recombination occurs, and the

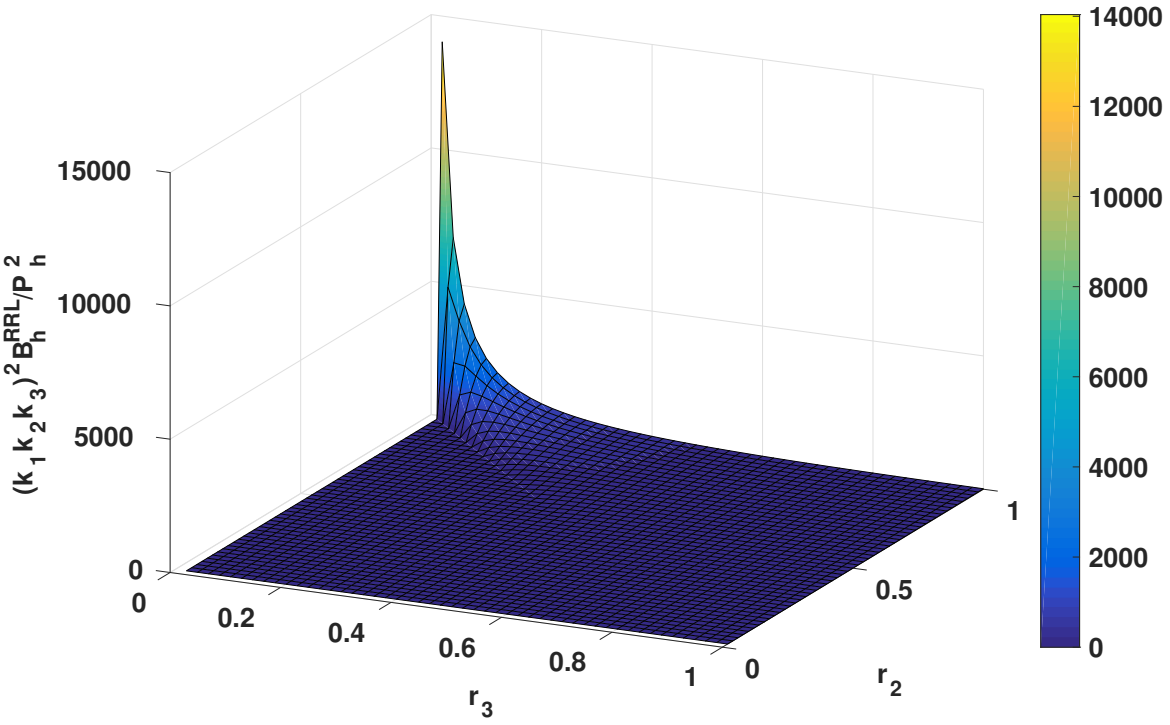

Figure 2.5: 3D plot of $(k_1k_2k_3)^2 B_h^{RRL}/(\mathcal{P}_h^R)^2$. We do not restrict to $r_3 \leq r_2$ as the bispectrum is not symmetric in r_2 and r_3. The tensor bispectrum has a sharp peak in the squeezed limit, $r_3 \ll r_2 \approx 1$, but is quite small for most of the $r_3 - r_2$ plane.

baryons decouple from radiation, they cluster into the dark matter potential wells which are by now sufficiently amplified. In the rest of this section, we consider the equations describing the process of clustering of dark matter, ignoring effects of radiation or baryons. This is a reasonably good approximation on large scales (see (56) and references therein).

To describe the dynamics of dark matter, we make use of its distribution function, $f(\boldsymbol{x}, \boldsymbol{p}, \eta)$, which represents the number density of dark matter particles at (comoving) position $\boldsymbol{x}$, moving with a (comoving) momentum $\boldsymbol{p}$ at some (conformal) time η, and assume that it is collisionless (this is a good approximation on large scales. However, collisional dark matter might resolve some small-scale inconsistencies in the ΛCDM paradigm (164; 172; 183)). In this regime, phase-space conservation implies (28),

$$\frac{\partial f}{\partial \eta} + \frac{\boldsymbol{p}}{ma} \cdot \nabla f - ma \nabla \Phi \frac{\partial f}{\partial \boldsymbol{p}} = 0 \tag{2.68}$$

where m denotes the mass of dark matter particles, and Φ is the gravitational potential at $\boldsymbol{x}$. This equation is also called the Valsov equation. In general, this equation is quite difficult to solve as it is a non-linear equation, because Φ is sourced by the density which is the integral of the distribution function over momentum. One way to make progress is using the moments of the distribution function.

The moments of the distribution function are defined by integrals over momentum,

$$\mathcal{D}_{i,j,k,\ldots} \equiv \int \frac{d^3p_i d^3p_j d^3p_k \ldots}{(2\pi)^{3n}} \frac{p_i}{ma} \frac{p_j}{ma} \frac{p_k}{ma} \ldots f(\boldsymbol{x}, \boldsymbol{p}, \eta) \tag{2.69}$$

where n denotes the number of momentum variables integrated over. In particular, the integral of the distribution function over momentum, without any factors of p/ma gives the local mass density of the particles, $\rho(\boldsymbol{x}, \eta) \equiv \bar{\rho}(\eta)[1+\delta(\eta, \boldsymbol{x})]$, which we decompose into the sum of a homogeneous background value and an inhomogeneous component; $n = 1$ ($\rho(\boldsymbol{x}, \eta) v_i(\boldsymbol{x}, \eta)$) defines the peculiar velocity, $v_i(\boldsymbol{x}, \eta)$, and $n = 2$ ($\rho(\boldsymbol{x}, \eta) v_i(\boldsymbol{x}, \eta) v_j(\boldsymbol{x}, \eta) + \Pi_{ij}(\boldsymbol{x}, \eta)$) defines the anisotropic or shear stress, $\Pi_{ij}(\boldsymbol{x}, \eta)$. The full distribution is then characterised in principle by an infinite hierarchy of moments, called the Boltzmann hierarchy. On large scales, dark matter can be treated as a perfect fluid. A perfect fluid is characterised only by its rest frame mass density, and isotropic pressure. In particular, the shear stresses in the fluid, described by, $\Pi_{ij}(\boldsymbol{x}, \boldsymbol{p}, \eta) = 0$.

Taking moments of the Vlasov equation (equation (2.68)), we find that the equations for the zeroth and first order moments are given as

$$\frac{\partial \delta(\boldsymbol{x}, \eta)}{\partial \eta} + \nabla \cdot [(1 + \delta(\boldsymbol{x}, \eta)) \boldsymbol{v}(\boldsymbol{x}, \eta)] = 0, \tag{2.70}$$

$$\begin{aligned} &\frac{\partial \boldsymbol{v}(\boldsymbol{x}, \eta)}{\partial \eta} + \mathcal{H}(\eta) \boldsymbol{v}(\boldsymbol{x}, \eta) + \boldsymbol{v}(\boldsymbol{x}, \eta) \cdot \nabla \boldsymbol{v}(\boldsymbol{x}, \eta) \\ &= -\nabla \Phi(\boldsymbol{x}, \eta) - \frac{1}{\rho(\boldsymbol{x}, \eta)} \nabla_j (\rho(\boldsymbol{x}, \eta) \Pi_{ij}(\boldsymbol{x}, \eta)) \end{aligned} \tag{2.71}$$

which are the familiar *continuity* and *Euler* equations representing conservation of mass and momentum respectively. Note that in general, the equation for any moment depends on the next higher moment. For dark matter however, as long as shell-crossing does not occur, $\Pi_{ij} \approx 0$, and so we can close this system of equations already at this point. The gravitational potential $\Phi(\boldsymbol{x}, \eta)$ is provided by the Poisson equation,

$$\nabla^2\Phi(\boldsymbol{x}, \eta) = \frac{3}{2}\Omega_m(\eta)\mathcal{H}(\eta)^2\delta(\boldsymbol{x}, \eta). \tag{2.72}$$

The set of equations (2.70)–(2.72) then allows us to solve for the evolution of dark matter density and velocity, and the gravitational potential, once initial conditions are specified. For initial conditions, we use the fact that at recombination, density fluctuations were of the order of $\delta \sim 10^{-5}$, and that they were normally distributed (as set by inflation).

From equation (2.70) and equation (2.71), we see that the density and velocity fields actually obey non-linear equations. As a result, the initial Gaussian field gets transformed to a non-Gaussian field as time goes by. In particular, the present day density and velocity fields are highly non-Gaussian, with locations such as inside galaxies, where the overdensity is extremely large being much fewer than regions where the overdensity is close to zero or lesser. From a mathematical point of view as well, we do not expect the distribution of overdensities to remain Gaussian at all times, as by its definition the overdensity is constrained to be ≥ -1, while there is no upper limit to it.

What then is the distribution of δ today? To get some hint, let us re-write equation (2.70) as (43)

$$\frac{\partial[1 + \delta(\boldsymbol{x}, \eta)]}{\partial\eta} + \boldsymbol{v} \cdot \nabla[1 + \delta(\boldsymbol{x}, \eta)] + [1 + \delta(\boldsymbol{x}, \eta)]\nabla \cdot \boldsymbol{v}(\boldsymbol{x}, \eta) = 0. \tag{2.73}$$

We can write the partial derivative w.r.t. η as a total derivative to get

$$\frac{d[1 + \delta(\boldsymbol{x}, \eta)]}{d\eta} + [1 + \delta(\boldsymbol{x}, \eta)]\nabla \cdot \boldsymbol{v}(\boldsymbol{x}, \eta) = 0. \tag{2.74}$$

Now if the velocity divergence, $\nabla \cdot \boldsymbol{v}(\boldsymbol{x}, \eta)$ is assumed to be a Gaussian field, it follows that the density field $\rho(\boldsymbol{x}, \eta)$ will be a log-normal field. In fact, as we show in chapter 4, this turns out to be a pretty good approximation for the density fields obtained in N-body simulations, which solve the full non-linear equations for δ and $\boldsymbol{v}$. Note that although we have shown that if the velocity divergence is Gaussian the density will be log-normal, the converse is not necessarily true. That is, if the density distribution is log-normal this does not imply that the velocity divergence will be Gaussian. In fact, the velocity divergence is not Gaussian.

Figure 2.6 shows the 1-point disribution of (volume-weighted) dark matter velocity divergence measured from an N-body simulation at $z = 0$ in red (72). We can see clearly that it is not Gaussian. This is again a signature of the non-linear evolution. It also means that the density distribution is not likely to be perfectly log-normal. Nevertheless, when smoothed over sufficiently large scales, the observed galaxy distribution is found to

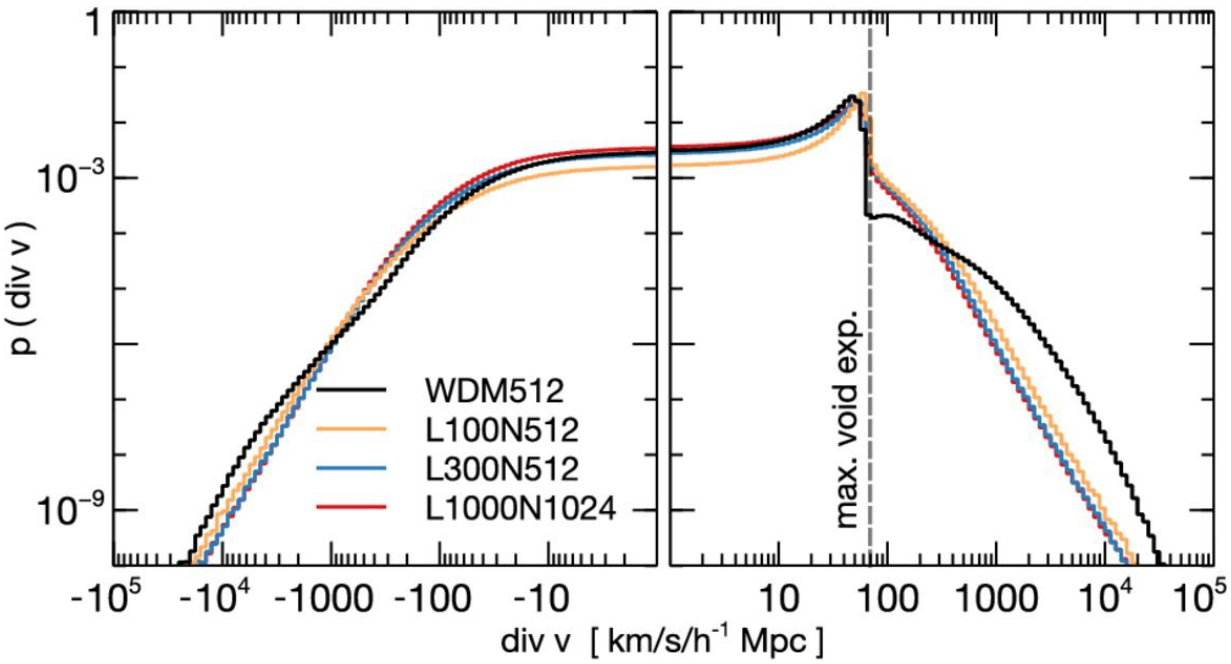

Figure 2.6: 1-point PDF of velocity divergence measured from N-body simulations, with different box lengths ('L'), resolutions ('N') and dark matter models ('W' for warm), indicated by different colours (72). The velocity divergence attains its expected maximum value (dashed) for a void with $\delta = -1$, as it is negative of the overdensity δ in linear theory. Higher values are signatures of non-linearities.

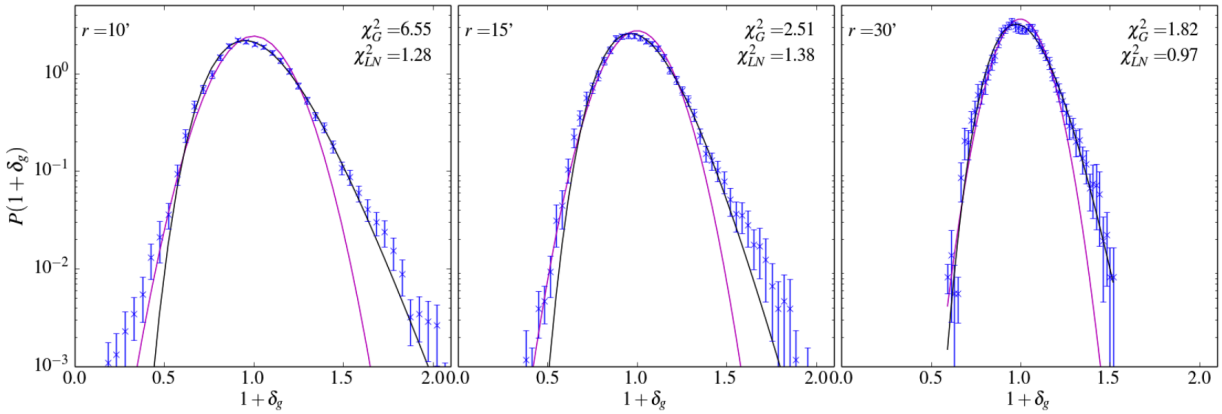

Figure 2.7: Count-in-cell of galaxies measured in the DES Science Verification data (blue points) (41), for different smoothing radii (increasing from left to right), along with their log-normal (black solid) and Gaussian (magenta) fits. As the smoothing radius increases, the distribution becomes more Gaussian (cf. figures (1.3)–(1.4)).

be log-normal, as shown in figure 2.7. This is expected because when smoothed over large scales, the velocity divergence becomes closer to Gaussian, as a consequence of the central limit theorem.

2.5 Real and Redshift Space

Galaxy redshift surveys, mapping the three-dimensional distribution of galaxies, have been one of the most powerful tools in modern cosmology (see, for example, (137)). Specifically, measurements of the galaxy two-point correlation function or its Fourier counterpart, power spectrum, allow us to extract cosmological information via, e.g., baryon acoustic oscillations and the redshift-space distortion.

However, the observed galaxy correlation function is not equal to the underlying one, because of the peculiar motion of galaxies. We observe galaxies using the light emitted by them. The redshift information from the spectrum of this light can be used to infer the relative velocity of the galaxy along the line of sight (l.o.s.). This velocity is a sum of two components - the Hubble velocity from the homogeneous and istotropic expansion of the Universe and the peculiar velocity, from local gravitational attraction.

Figure 2.8 shows the apparent distribution of a quartet of galaxies to an observer. We see that galaxies that move perpendicular to the l.o.s. appear in their actual location, but those that move parallel to the l.o.s. appear shifted depending on the magnitude of their peculiar velocities. Consequently, the observed clustering of galaxies changes along the l.o.s. and we use "redshift space" to denote the space where galaxies occupy their observed positions. In chapter 4, we consider the redshift space 2-point correlation function of log-normal galaxy distributions, that source peculiar velocities linearly and show the pairwise velocity PDFs for such a distribution. But before that, in the next chapter, we consider

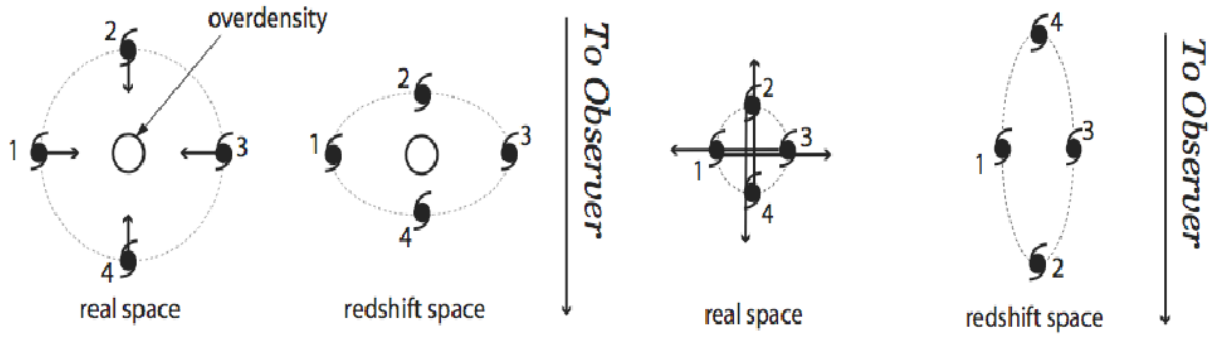

Figure 2.8: Redshift space distortion of a system of galaxies as apparent to an observer (credits: Donghui Jeong). Galaxies '1' and '3' move perpendicular to the line-of-sight (l.o.s.) and so do not affect their observed redshift. Galaxies '2' and '4' move parallel to the l.o.s. changing their observed redshift. This makes the isotropic distribution in real space, anisotropic in redshift space. Depending on the magnitude of velocities, the distribution appears to be either squashed along the l.o.s. in redshift space (left, Kaiser effect (85)) or elongated (right, Finger-of-God effect (80)).

the imprints of spectator fields during inflation, on CMB polarisation.

Chapter 3

Tensor Non-Gaussianity from Axion-Gauge-Fields Dynamics

3.1 Model Setup

The simplest (and most widely studied) models of inflation rely on a scalar field called the inflaton to achieve a state of accelerated expansion of the Universe. These models have been extremely successful in predicting CMB temperature and polarisation anisotropies (5; 6; 95; 78). However, the observable Universe contains only one known scalar field - the Higgs field. The Higgs field can act as the inflaton, but it needs to be either non-minimally coupled to gravity (31), or its parameters need to be extremely fine tuned (107), to achieve the level of inhomogeneity observed in the CMB. Thus, for almost all models of inflation, the primordial Universe cannot consist of an isolated scalar field. These other fields, which do not participate in inflation (owing to their sub-dominant contribution to the homogeneous energy density), are called spectator fields. It is natural to ask what happens to spectator fields as the Universe inflates, and if one can learn something about them via their imprint on observables. In this chapter, we consider one such field set up, containing a scalar inflaton field, and spectator axion and SU(2) gauge fields (52). This model was inspired by the Chromo-Natural Inflation (CNI) model (9).

Chromo-Natural inflation attempts to solve the η-problem in inflation. Homogeneity and isotropy constraints from the CMB require that the inflaton potential be extremely flat ($|\eta| \sim |V''/V| \ll 1$, being the slow-roll parameter), for a long period of the field's excursion. If one considers a scalar field that drives inflation, the flatness of the potential is not protected against quantum corrections (which are necessary to explain the CMB anisotropies), due to lack of any symmetries. *Natural* inflation (61) was proposed as a mechanism to overcome this problem by driving inflation with an axion, which naturally has a flat potential. But reconciling natural inflation with CMB observations requires a Planckian decay constant of the axion. In Chromo-Natural inflation (9), the inflating axion is additionally coupled to non-Abelian gauge fields, which allows for a smaller decay constant of the axion. However, owing to this five-dimensional coupling between gauge

fields and the inflating axion, CNI is unable to simultaneously satisfy the bounds on the scalar spectral index n_s, and tensor-to-scalar ratio r, from Planck (7). On the other hand, if the inflaton is only coupled to an axion and gauge fields via gravity, it can be shown that the resulting system does not violate the constraints on the scalar spectral index, n_s, and r (52). In ref. (10), the tensor bispectrum was calculated in such a setup, proposed by Dimastrogiovanni, Fasiello and Fujita (52), using a particular set of model parameters. In this chapter we give more detailed derivations of the bispectrum and present the results for wider parameter space. The rest of the chapter is organised as follows : in section 3.1 we present details of the model that we consider. In section 3.2 we present the second-order Lagrangian for the tensor perturbations in our model and their imprint on the B-mode power spectrum. The third-order Lagrangian is presented in section 3.3 and is used to calculate the bispectrum of metric fluctuations. A detailed discussion of the deviation of the bispectrum from the equilateral shape is given in section 3.4. In section 3.5 we explore parameter regions of the model, which can be potentially observed in upcoming CMB missions. We conclude in section 3.7.

In the model of ref. (52), inflation is driven by a scalar inflaton ϕ, which is only minimally coupled to a pseudoscalar axion χ and SU(2) gauge fields, A^a_μ. The SU(2) gauge fields and the axion have negligible energy densities compared to the inflaton, and thus are called "spectator fields". They are coupled to each other by a Chern-Simons like interaction $\chi F\tilde{F}$. The Lagrangian is then given as,

$$\mathcal{L} = \mathcal{L}_{\rm GR} + \mathcal{L}_\phi + \mathcal{L}_{\rm spec}, \tag{3.1}$$

$$\mathcal{L}_{\rm spec} = -\frac{1}{2}(\partial\chi)^2 - V(\chi) - \frac{1}{4}F^a_{\mu\nu}F^{a\mu\nu} + \frac{\lambda\,\chi}{4f}F^a_{\mu\nu}\tilde{F}^{a\mu\nu}, \tag{3.2}$$

where Einstein gravity $\mathcal{L}_{\rm GR} = M_{\rm Pl}^2 R/2$ is assumed, the Lagrangian of the inflaton $\mathcal{L}_\phi$ is not specified, and $\mathcal{L}_{\rm spec}$ denotes the Lagrangian of the spectator fields. $V(\chi)$ is the potential of the axion field with the canonical kinetic term $-(\partial\chi)^2/2$, the gauge field strength tensor $F^a_{\mu\nu}$ is written in terms of the gauge fields as $F^a_{\mu\nu} = \partial_\mu A^a_\nu - \partial_\nu A^a_\mu - g\epsilon^{abc}A^b_\mu A^c_\nu$ with g being the self-coupling constant, a dimensionless parameter λ controls the strength of the Chern-Simons interaction, f is a decay constant of the axion field, and $\tilde{F}^{a\mu\nu} \equiv \epsilon^{\mu\nu\rho\sigma}F^a_{\rho\sigma}/(2\sqrt{-g})$ is the dual of $F^a_{\mu\nu}$. In the rest of this section, we discuss the background dynamics, while perturbations will be studied in the following sections.

In this chapter, we do not solve for the inflaton $\phi(t)$, but consider dynamics of the spectator fields in a de Sitter universe, where the Hubble expansion rate is constant. We also leave the axion potential $V(\chi)$ unspecified by assuming that it supports slow-roll of the background axion $\chi_0(t)$ with the aid of the coupling to the SU(2) fields. While these assumptions are far from generic, they still capture the essence of physics of generation of non-Gaussianity, and are observationally relevant because they produce scale-invariant GWs.

As shown in (9; 111), while the background axion slowly evolves, the homogeneous background component of the gauge fields has an attractor configuration which respects isotropy of the universe,

$$A^a_0 = 0\,, \quad A^a_i = \delta^a_i a(t)Q(t), \tag{3.3}$$

where $a(t)$ is the scale factor. Then we decompose these spectator fields into the background and the perturbation components as

$$\chi(t,\boldsymbol{x}) = \chi_0(t) + \delta\chi(t,\boldsymbol{x}), \qquad A_i^a(t,\boldsymbol{x}) = \delta_i^a a(t)Q(t) + \delta A_i^a(t,\boldsymbol{x}). \tag{3.4}$$

There also exist non-dynamical components δA_0^a that we integrate out. The equations of motion (EoM) for the background fields are given by

$$\ddot{\chi}_0 + 3H\dot{\chi}_0 + \partial_\chi V(\chi_0) = -\frac{3g\lambda}{f}Q^2\left(\dot{Q} + HQ\right), \tag{3.5}$$

$$\ddot{Q} + 3H\dot{Q} + \left(\dot{H} + 2H^2\right)Q + 2g^2Q^3 = \frac{g\lambda}{f}Q^2\dot{\chi}_0, \tag{3.6}$$

where the dots denote cosmic time derivatives ∂_t and $H \equiv \dot{a}/a$ is the Hubble expansion rate. The terms on the right hand side of eq. (3.5) slow down the time evolution of $\chi_0(t)$ in addition to the Hubble friction term $3H\dot{\chi}_0$, because a non-zero background value $Q(t)$ is sustained by energy transfer from the kinetic energy of χ_0 through the coupling. Here we introduce two dimensionless parameters;

$$m_Q(t) \equiv \frac{gQ}{H}, \qquad \Lambda(t) \equiv \frac{\lambda Q}{f}. \tag{3.7}$$

Here, m_Q is the effective mass of the SU(2) field around its vacuum expectation value (vev) normalized by the Hubble scale, and Λ characterizes the coupling strength between χ_0 and Q. Note that the right hand side of eqs. (3.5) and (3.6) are proportional to $m_Q\Lambda$. We consider the slow-roll regime, $m_Q \gtrsim 1$ and $\Lambda \gg 1$, in which Q is stabilized by its effective mass and χ_0 is significantly slowed down by the coupling. We can then drop all the terms with time derivatives in the EoMs except for the r.h.s. of eq. (3.6) and find (9)

$$m_Q \simeq \left(\frac{-g^2 f\partial_\chi V(\chi_0)}{3\lambda H^4}\right)^{\frac{1}{3}}, \tag{3.8}$$

$$\xi \equiv \frac{\lambda\dot{\chi}_0}{2fH} \simeq m_Q + m_Q^{-1}. \tag{3.9}$$

The Einstein equations at the background yield

$$3M_{\rm Pl}^2H^2 = \rho_\phi + \frac{1}{2}\dot{\chi}_0 + V(\chi_0) + \frac{3}{2}(\dot{Q} + HQ)^2 + \frac{3}{2}g^2Q^4, \tag{3.10}$$

$$-\frac{\dot{H}}{H^2} = \epsilon_\phi + \epsilon_\chi + \epsilon_B + \epsilon_E, \tag{3.11}$$

where ρ_ϕ is the energy density of the inflaton and the slow-roll parameters are defined as $\epsilon_\phi \equiv -\dot{\rho}_\phi/6M_{\rm Pl}^2H^3$, $\epsilon_\chi = \dot{\chi}^2/2M_{\rm Pl}^2H^2$, $\epsilon_E \equiv (\dot{Q} + HQ)^2/M_{\rm Pl}^2H^2$, and $\epsilon_B \equiv g^2Q^4/M_{\rm Pl}^2H^2$. We shall assume that ρ_ϕ dominates in eq. (3.10). In the slow-roll regime, $\dot{Q} \ll HQ$, one finds

$$\epsilon_E \simeq \frac{\epsilon_B}{m_Q^2}. \tag{3.12}$$

The background fields appear only through H, m_Q, ξ, ϵ_E and ϵ_B in the EoMs for the perturbations. Using the relationships, eqs. (3.9) and (3.12), one can eliminate ξ and ϵ_E. Furthermore, in the slow-roll regime, one can disregard the time variations of H, m_Q and ϵ_B in the leading order approximation. Therefore we have three relevant background parameters H, m_Q and ϵ_B which are approximated to be constant in this chapter.[1]

3.2 Amplification of Gravitational Waves

In this section, we study the tensor perturbations at linear level. Only the tensor perturbations are amplified due to tachyonic instability, while scalar and vector perturbations are not amplified for $m_Q > \sqrt{2}$ in this model (53). Although the scalar perturbations of χ and A_i^a are generated from the vacuum fluctuations, their contribution to the curvature perturbation ζ is negligible, unless the energy density of χ becomes comparable to that of the inflaton after inflation (52).[2] The vector perturbations decay on super-horizon scales in any case. Therefore in this chapter, we assume that the observed curvature perturbation was produced from the inflaton fluctuation $\delta\phi$ and concentrate on the tensor perturbations from the gauge fields.

To calculate the power spectrum and bispectrum of GWs we need to expand the action, equation (3.1), up to second and third order in perturbations, respectively. We write the tensor perturbations of the metric and the SU(2) gauge field (53; 8) as:

$$g_{ij} = -a^2(\delta_{ij} + h_{ij})\,, \qquad \delta A_i^a = t_{ai} + \cdots\,, \tag{3.13}$$

where $\cdots$ represents the scalar and vector perturbations of the SU(2) gauge fields which we neglect in this chapter. We have imposed the transverse and traceless conditions on h_{ij} and t_{ij}, $\delta^{ij}\mathcal{T}_{ij} = \partial_i\mathcal{T}_{ij} = \partial_j\mathcal{T}_{ij} = 0$ ($\mathcal{T} = h$ and t). The inverse metric is given by $g^{ij} = -a^{-2}(\delta^{ij} - h^{ij} + h^{ik}h^{kj} + \mathcal{O}(h^3))$. For later convenience, we redefine h_{ij} as

$$\psi_{ij} = \frac{1}{2}aM_{\rm Pl}h_{ij}. \tag{3.14}$$

Precisely speaking t_{ai} is not a tensor, since the index a is not a spatial index but the label of SU(2) gauge. Nonetheless, under the background configuration of eq. (3.3), t_{ai} transforms as a tensor in practice, because the gauge index a is identified with a spatial index.

[1] In ref. (52), the background dynamics is numerically solved, and the perturbations are also solved with the time varying background quantities, $m_Q(t), \epsilon_B(t)$ and $H(t)$. They find that $m_Q, \epsilon_B, H \approx const.$ is a very good approximation for a sufficiently strong coupling, especially when one is interested in the range of wavenumbers observable by CMB.

[2] The scalar perturbations of χ and A_i^a directly contribute to ζ through the density perturbation (e.g. $\delta\rho_\chi \simeq \partial_\chi V\delta\chi$). This channel is negligible, for instance, if χ reaches its potential minimum (i.e. $V(\chi), \partial_\chi V(\chi) \to 0$) during inflation. If χ_0 acquires a non-negligible energy fraction after inflation, however, the contribution to ζ from $\delta\chi$ may be relevant. This implies that the spectator sector can produce ζ in a way similar to the curvaton mechanism (106; 105). We leave this intriguing possibility for future work.

Substituting these in equation (3.1), and expanding up to third order, we obtain the Lagrangian of the tensor perturbations as

$$S_{\rm tensor} = \int {\rm d}\tau {\rm d}^3x\sqrt{-g}\left[L_2 + L_3^{(i)} + L_3^{(ii)} + L_3^{(iii)}\right], \tag{3.15}$$

with (129)

$$L_2 = \frac{1}{2}\psi'_{ij}\psi'_{ij} - \frac{1}{2}\partial_k\psi_{ij}\partial_k\psi_{ij} + \frac{1}{\tau^2}\psi_{ij}\psi_{ij} + \frac{1}{2}t'_{ij}t'_{ij} - \frac{1}{2}\partial_l t_{ij}\partial_l t_{ij} + \frac{2m_Q + m_Q^{-1}}{\tau}\epsilon^{ijk}t_{il}\partial_j t_{kl} - \frac{m_Q^2+1}{\tau^2}t_{ij}t_{ij} + \frac{2\sqrt{\epsilon_B}}{\tau}\left[\frac{1}{m_Q}\psi_{ij}t'_{ij} - \psi_{jm}\epsilon_{aij}\partial_i t_{am} + \frac{m_Q}{\tau}\psi_{ij}t_{ij}\right], \tag{3.16}$$

where $\tau \simeq -1/aH$ is the conformal time, prime denotes the derivative with respect to τ and we neglect terms suppressed by slow-roll parameters. The cubic Lagrangian L_3 will be discussed in the next section.

From the quadratic Lagrangian above, we obtain the following EoMs for GWs $\psi_{ij}(\tau, \boldsymbol{x})$ and tensor perturbations of the SU(2) gauge field $t_{ij}(\tau, \boldsymbol{x})$,

$$\psi''_{ij} - \partial_k^2\psi_{ij} - \frac{2}{\tau^2}\psi_{ij} = \frac{2\sqrt{\epsilon_B}}{m_Q\tau}t'_{ij} + \frac{2\sqrt{\epsilon_B}}{\tau}\epsilon^{api}\partial_p t_{aj} + \frac{2\sqrt{\epsilon_B}m_Q}{\tau^2}t_{ij}\,, \tag{3.17}$$

$$t''_{ij} - \partial_k^2 t_{ij} + \frac{2(2m_Q + m_Q^{-1})}{\tau}\epsilon^{lkj}\partial_k t_{il} + \frac{2(m_Q^2+1)}{\tau^2}t_{ij} = \mathcal{O}(\psi_{ij})\,. \tag{3.18}$$

Although terms linear in ψ_{ij} also source the gauge field t_{ij}, ψ_{ij} is not as substantially amplified as t_{ij} (8; 7; 110; 52), and so we ignore its contribution as a source for t_{ij}. To solve the dynamics of ψ_{ij} and t_{ij}, it is useful to decompose them with the circular polarisation tensors,

$$X_{ij}(\tau, \boldsymbol{x}) = \int \frac{{\rm d}^3k}{(2\pi)^3}e^{i\boldsymbol{k}\cdot\boldsymbol{x}}\left[e_{ij}^R(\boldsymbol{k})X_{\boldsymbol{k}}^R(\tau) + e_{ij}^L(\boldsymbol{k})X_{\boldsymbol{k}}^L(\tau)\right], \tag{3.19}$$

where $X = \psi, t$ and the properties of the polarisation tensors are summarized in appendix. B. Note that we normalize e_{ij}^p such that $e_{ij}^R(\boldsymbol{k})e_{ij}^R(-\boldsymbol{k}) = e_{ij}^L(\boldsymbol{k})e_{ij}^L(-\boldsymbol{k}) = 1$.

To proceed further, we quantize ψ and t and expand them in a perturbative series as (149)

$$\hat{X}_{\boldsymbol{k}}^p(\tau) = \hat{X}_1^p(\tau, \boldsymbol{k}) + \hat{X}_2^p(\tau, \boldsymbol{k}) + \dots\,. \tag{3.20}$$

The first order components are written as

$$\hat{t}_1^p(\tau, \boldsymbol{k}) = T_1^p(\tau, k)\,\hat{a}_{\boldsymbol{k}}^p + T_1^{p*}(\tau, k)\,\hat{a}_{-\boldsymbol{k}}^{p\dagger}, \tag{3.21}$$

$$\hat{\psi}_1^p(\tau, \boldsymbol{k}) = \Psi_1^p(\tau, k)\,\hat{a}_{\boldsymbol{k}}^p + \Psi_1^{p*}(\tau, k)\,\hat{a}_{-\boldsymbol{k}}^{p\dagger}, \tag{3.22}$$

with the creation/annihilation operators, $\hat{a}_{\boldsymbol{k}}^p$ and $\hat{a}_{\boldsymbol{k}}^{p\dagger}$, satisfying $[\hat{a}_{\boldsymbol{k}}^p, \hat{a}_{-\boldsymbol{k}'}^{q\dagger}] = (2\pi)^3\delta^{pq}\delta(\boldsymbol{k} + \boldsymbol{k}')$. We only consider GWs sourced by the gauge field in this chapter, and assign $\hat{\psi}_1$ the

same quantum operator as $\hat{t}_1$. The mode functions of $\hat{X}_1^p$ satisfy linearised EoMs and their solutions induce the second order fields $\hat{X}_2^p$ through non-linear terms in the EoMs.

In Fourier space the EoMs for the linear mode functions can be written as,

$$\partial_x^2 T_1^{R/L} + \left[1 \mp \frac{2(2m_Q + m_Q^{-1})}{x} + \frac{2(m_Q^2+1)}{x^2}\right] T_1^{R/L} = \mathcal{O}\left(\Psi_1^{R/L}\right), \tag{3.23}$$

$$\partial_x^2 \Psi_1^{R/L} + \left[1 - \frac{2}{x^2}\right] \Psi_1^{R/L} = \frac{2\sqrt{\epsilon_B}}{m_Q x}\partial_x T_1^{R/L} \mp \frac{2\sqrt{\epsilon_B}}{x} T_1^{R/L} + \frac{2\sqrt{\epsilon_B} m_Q}{x^2} T_1^{R/L}, \tag{3.24}$$

where $x \equiv -k\tau$. The minus and plus signs are for right- (R) and left-handed (L) modes, respectively. Only T_1^R undergoes an instability and it sources only Ψ_1^R (110; 112; 7; 9), provided that m_Q is positive. Therefore, we only consider the right-handed polarisation in the rest of the chapter. The homogeneous solution for T_1^R can be analytically calculated and is expressed in terms of the Whittaker function $W_{\beta,\alpha}(z)$ as

$$T_1^R(\tau, k) = \frac{1}{\sqrt{2k}} e^{\frac{\pi}{2}(2m_Q + m_Q^{-1})} W_{\beta,\alpha}(2ik\tau)\,, \tag{3.25}$$

where $\alpha \equiv -i\sqrt{2m_Q^2 + 7/4}$ and $\beta \equiv -i(2m_Q + m_Q^{-1})$ (112; 8; 52). Ψ_1^R can then be calculated using Green's function method,

$$\Psi_1^R(\tau, \boldsymbol{k}) = \int_{-\infty}^{\infty} d\eta\, G_\psi(\tau, \eta, k) \mathcal{D}(\eta, k) T_1^R(\eta, k), \tag{3.26}$$

with

$$G_\psi(\tau, \eta, k) = \frac{\Theta(\tau - \eta)}{k^3 \tau \eta}\left[k(\eta - \tau)\cos\big(k(\tau - \eta)\big) + (1 + k^2\tau\eta)\sin\big(k(\tau - \eta)\big)\right], \tag{3.27}$$

$$\mathcal{D}(\eta, k) = \frac{2\sqrt{\epsilon_B}}{m_Q \eta}\partial_\eta + \frac{2\sqrt{\epsilon_B}}{\eta^2}(m_Q + k\eta)\,, \tag{3.28}$$

where $\Theta(x)$ is the unit Heaviside function of x. In figure 3.1, we plot T_1^R, the source term $\mathcal{D}T_1^R$, Green's function G_ψ in the super-horizon limit and the sourced gravitational wave Ψ_1^R. The time integral of the source term $\mathcal{D}T_1^R$ multiplied by G_ψ yields Ψ_1^R. The source term $\mathcal{D}T_1^R$ peaks around the horizon crossing and Green's function stops oscillating there. As a result, Ψ_1^R is mainly produced around the horizon crossing as well, as seen in the right panel.

Equation (3.26) can also be analytically solved and in the super-horizon limit we obtain,

$$\lim_{|k\tau| \to\, 0} \Psi_1^R(\tau, \boldsymbol{k}) = \frac{\sqrt{\epsilon_B}}{\sqrt{2k}k\tau}\mathcal{F}(m_Q)\,, \tag{3.29}$$

from which we obtain the power spectrum of h in the super-horizon limit (52)

$$\frac{k^3}{2\pi^2} P_h^{\text{sourced}} = \frac{\epsilon_B H^2}{\pi^2 M_P^2} \left|\mathcal{F}(m_Q)\right|^2\,, \tag{3.30}$$

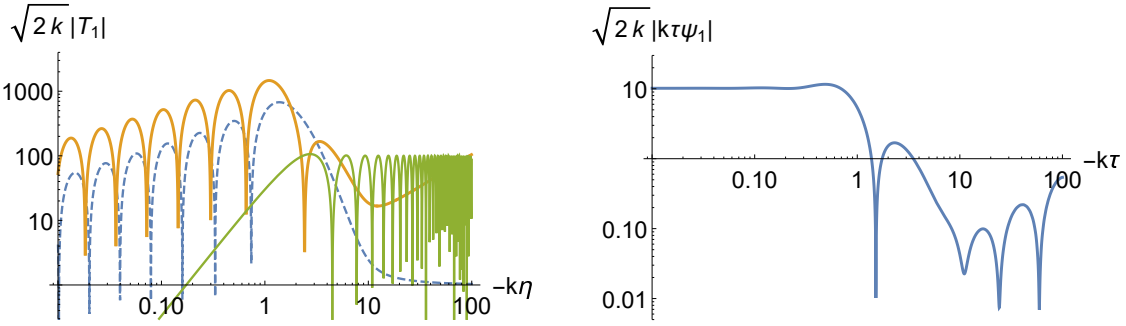

Figure 3.1: **(Left panel)** We plot the linear gauge tensor mode function $\sqrt{2k}|T_1^R(\eta,k)|$ (blue dashed), the source terms $\sqrt{2k}|m_Q^{-1}\eta\partial_\eta T_1+(m_Q+k\eta)T_1|$ (yellow solid) and $10|k\eta\cos(k\eta)-\sin(k\eta)|$ which is proportional to Green's function $G_\psi(\tau,\eta,k)$ in the super-horizon limit, $-k\tau\to 0$, multiplied by 10 for illustrative purpose (green solid). **(Right panel)** The sourced linear gravitational wave $\sqrt{2k}\,|k\tau\Psi_1^R(\tau,k)|$ is shown. $|\Psi_1^R|$ grows significantly around the horizon-crossing ($-k\tau\sim 1$) and stays constant on super-horizon scales. In both panels, we set $m_Q=3.15$ and $\epsilon_B=3\times10^{-4}$.

where $\mathcal{F}$ is a function of m_Q, whose exact expression is given in (52) ($\mathcal{F}(m_Q)$ here is $\mathcal{F}_B+\mathcal{F}_E/m_Q$ there). Note that eq. (3.30) is derived under the assumption of $(m_Q,\epsilon_B,H)=const.$ However, as long as the time variations of these background quantities are slow, eq. (3.30) with $m_Q(t),\epsilon_B(t),H(t)$ at the horizon crossing time $k=a(t)H(t)$ gives a good approximation of $P_h^{\rm sourced}(k)$. It should be also noted that only the right-handed polarisation modes contribute to the above $P_h^{\rm sourced}(k)$.

3.3 Bispectrum of Gravitational Waves

In this section, we calculate the tensor bispectrum of the right-handed GWs, B_h^{RRR}, in the super-horizon limit:

$$\begin{aligned}(2\pi)^3\delta\left(\boldsymbol{k}_1+\boldsymbol{k}_2+\boldsymbol{k}_3\right)B_h^{RRR}(k_1,k_2,k_3)&=\lim_{\tau\to0}\left\langle\hat{h}^R(\tau,\boldsymbol{k}_1)\hat{h}^R(\tau,\boldsymbol{k}_2)\hat{h}^R(\tau,\boldsymbol{k}_3)\right\rangle,\\&=\lim_{\tau\to0}\left(\frac{2}{aM_{\rm Pl}}\right)^3\left\langle\hat{\psi}^R(\tau,\boldsymbol{k}_1)\hat{\psi}^R(\tau,\boldsymbol{k}_2)\hat{\psi}^R(\tau,\boldsymbol{k}_3)\right\rangle.\end{aligned}\tag{3.31}$$

The three-point correlator of the right-handed GWs $\hat{\psi}^R=\hat{\psi}_1^R+\hat{\psi}_2^R$ can be written as

$$\begin{aligned}\left\langle\hat{\psi}^R(\tau,\boldsymbol{k}_1)\hat{\psi}^R(\tau,\boldsymbol{k}_2)\hat{\psi}^R(\tau,\boldsymbol{k}_3)\right\rangle&=\left\langle\hat{\psi}_1^R(\tau,\boldsymbol{k}_1)\hat{\psi}_1^R(\tau,\boldsymbol{k}_2)\hat{\psi}_2^R(\tau,\boldsymbol{k}_3)\right\rangle\\&+\left\langle\hat{\psi}_1^R(\tau,\boldsymbol{k}_1)\hat{\psi}_2^R(\tau,\boldsymbol{k}_2)\hat{\psi}_1^R(\tau,\boldsymbol{k}_3)\right\rangle+\left\langle\hat{\psi}_2^R(\tau,\boldsymbol{k}_1)\hat{\psi}_1^R(\tau,\boldsymbol{k}_2)\hat{\psi}_1^R(\tau,\boldsymbol{k}_3)\right\rangle,\end{aligned}\tag{3.32}$$

because $\hat{\psi}_1^R$ satisfies Gaussian statistics. We calculate $\hat{\psi}_2$ using the second order EoMs for the tensor perturbations which are derived from the cubic Lagrangian.

The cubic tensor Lagrangians introduced in eq. (3.15) are given by

$$L_3^{(i)} = c^{(i)}\left[\epsilon^{abc}t_{ai}t_{bj}\left(\partial_i t_{cj} - \frac{m_Q^2+1}{3m_Q\tau}\epsilon^{ijk}t_{ck}\right) - \frac{m_Q}{\tau}t_{ij}t_{jl}t_{li}\right], \tag{3.33}$$

$$L_3^{(ii)} = c^{(ii)}\psi_{ij}\left[\frac{\tau}{2m_Q}\left\{t'_{il}t'_{jl} - \partial_i t_{kl}(\partial_j t_{kl} - 2\partial_k t_{jl}) - \partial_k t_{il}\partial_k t_{jl}\right\}\right.$$
$$\left. - \epsilon^{iab}t_{al}\left(\partial_j t_{bl} - \partial_l t_{bj}\right) - \epsilon^{lab}t_{ai}\partial_l t_{bj} - \frac{3m_Q}{2\tau}t_{il}t_{jl}\right], \tag{3.34}$$

$$L_3^{(iii)} = c^{(iii)}\psi_{ij}\left[\frac{1}{m_Q}\psi_{jk}t'_{ik} + \epsilon^{ajm}\psi_{lm}\partial_i t_{al} - \psi_{jk}\epsilon^{akl}\partial_l t_{ai}\right], \tag{3.35}$$

where we organize terms such that $L_3^{(i)} = \mathcal{O}(t^3), L_3^{(ii)} = \mathcal{O}(\psi t^2)$ and $L_3^{(iii)} = \mathcal{O}(\psi^2 t)$ and we neglect the $\mathcal{O}(\psi^3)$ terms. The coefficients of the cubic Lagrangians are

$$c^{(i)} = g = \frac{m_Q^2 H}{\sqrt{\epsilon_B}M_{\rm Pl}}, \quad c^{(ii)} = \frac{2m_Q H}{M_{\rm Pl}}, \quad c^{(iii)} = \frac{4\sqrt{\epsilon_B}H}{M_{\rm Pl}}. \tag{3.36}$$

They satisfy a hierarchical relationship,

$$\frac{c^{(ii)}}{c^{(i)}} = \frac{c^{(iii)}}{c^{(ii)}} = \frac{2\sqrt{\epsilon_B}}{m_Q} \ll 1. \tag{3.37}$$

The tree-level contributions from $L_3^{(i)}, L_3^{(ii)}$ and $L_3^{(iii)}$ to the tensor bispectrum are illustrated as Feynman diagrams in figure 3.2. As we see below, the contributions from the three diagrams to the gravitational wave bispectrum are also hierarchical, $(i) > (ii) \gg (iii)$.[3] In what follows, we calculate these three contributions in order. When we show plots in this section, we use the following parameters as an example,

$$H = 8\times 10^{12}\text{GeV}, \quad m_Q = 3.15, \quad \epsilon_B = 3\times 10^{-4}. \tag{3.38}$$

The viable parameter space will be explored in section. 3.5.

3.3.1 Diagram (i)

This diagram arises from the self-interaction of the SU(2) gauge field, and thus is absent in Abelian theory. Here, the second order gravitational wave $\hat{\psi}_2^R$ is sourced linearly by $\hat{t}_2^R$, but the second order gauge field perturbation $\hat{t}_2^R$ is produced by $\hat{t}_1^R$ via non-linearity. The cubic Lagrangian $L_3^{(i)}$ gives the source term $\mathcal{S}_{ij}^{(i)}$ in the EoM for the second order gauge

[3]The diagram (ii) includes only two circled crosses which carry a small parameter $\sqrt{\epsilon_B}$, while the diagram (i) includes three. Hence, in spite of the hierarchical vertex coefficients $c^{(i)} \gg c^{(ii)}$, their contributions are comparable.

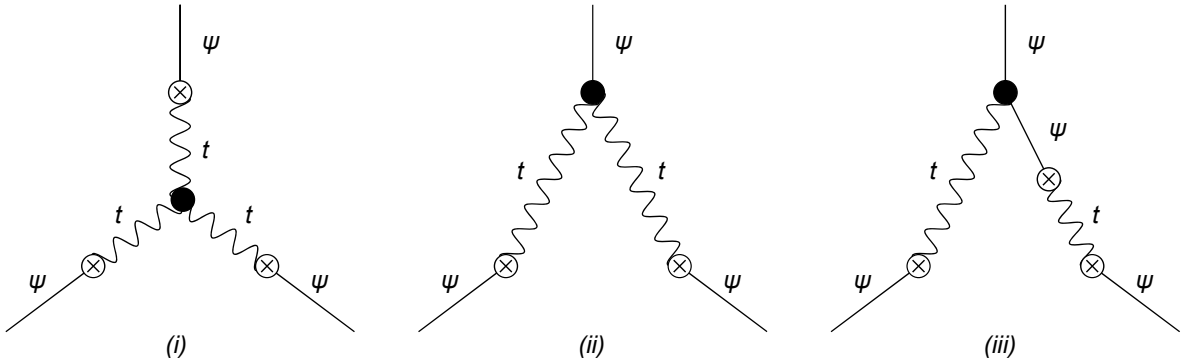

Figure 3.2: Feynman diagrams illustrating the tree-level contributions from the cubic interactions $L_3^{(i)}, L_3^{(ii)}$ and $L_3^{(iii)}$ to the bispectrum of GWs. The straight and wavy lines show ψ_{ij} and t_{ij}, respectively. The black dots show the vertices of the three-point interactions, while the circled crosses show the mixing between ψ_{ij} and t_{ij} (the last term in Eq. (3.16)).

field perturbation,

$$t''_{ij}(\tau,\boldsymbol{x}) - \partial_k^2 t_{ij}(\tau,\boldsymbol{x}) + \frac{2(2m_Q + m_Q^{-1})}{\tau}\epsilon^{lkj}\partial_k t_{il}(\tau,\boldsymbol{x}) + \frac{2(m_Q^2 + m_Q^{-1})}{\tau^2} t_{ij}(\tau,\boldsymbol{x}) = \mathcal{S}_{ij}^{(i)}\,, \tag{3.39}$$

$$\mathcal{S}_{ij}^{(i)} = \frac{\delta L_3^{(i)}}{\delta t_{ij}} = 2g\epsilon^{aic} t_{al}\partial_l t_{cj} - g\epsilon^{aic} t_{al}\partial_j t_{cl} - \frac{3gm_Q}{\tau} t_{ip}t_{pj} - \frac{g\xi}{\tau}\epsilon^{ibc}\epsilon^{jmn} t_{bm}t_{cn}\,, \tag{3.40}$$

where the source term $\mathcal{S}_{ij}^{(i)}$ is evaluated with the first order solution $\hat{t}_1^R(\tau,\boldsymbol{k})$. Although in second order it is no longer true that the right-handed polarisation is sourced only by the right-handed tensors, the exponential amplification of the right-handed modes ensures that terms containing the left-handed modes are exponentially smaller. Thus we only use the right-handed polarisation of the gauge field perturbation to evaluate the source term. Note that this source term contains g explicitly because of the non-Abelian nature of the vertex.

Expanding the tensor perturbation with the tensor polarisation as before, one finds the EoM in Fourier space as

$$\hat{t}_2''^R(\tau,\boldsymbol{k}) + \left(1 + \frac{2(m_Q^2 + m_Q^{-1})}{\tau^2} + 2k\frac{2m_Q + m_Q^{-1}}{\tau}\right)\hat{t}_2^R(\tau,\boldsymbol{k}) = \\ ge_{ij}^L(\boldsymbol{k})\int\!\!\int \frac{d^3q_1}{(2\pi)^3}\frac{d^3q_2}{(2\pi)^3}\,\delta_D(\boldsymbol{q}_1+\boldsymbol{q}_2-\boldsymbol{k})Q_{ij}^{(i)}(\boldsymbol{q}_1,\boldsymbol{q}_2,\tau)\hat{t}_1^R(\boldsymbol{q}_1,\tau)\hat{t}_1^R(\boldsymbol{q}_2,\tau)\,, \tag{3.41}$$

where we have substituted $[e_{ij}^R(\boldsymbol{k})]^{-1} = e_{ij}^L(\boldsymbol{k})$ and

$$Q_{ij}^{(i)}(\boldsymbol{q}_1,\boldsymbol{q}_2,\tau) = 2i\epsilon^{aic}e_{al}^R(\boldsymbol{q}_1)e_{cj}^R(\boldsymbol{q}_2)q_{2l} - i\epsilon^{aic}e_{al}^R(\boldsymbol{q}_1)e_{cl}^R(\boldsymbol{q}_2)q_{2j} \\ - \frac{3m_Q}{\tau}e_{ik}^R(\boldsymbol{q}_1)e_{kj}^R(\boldsymbol{q}_2) - \frac{m_Q + m_Q^{-1}}{\tau}\epsilon^{ibc}\epsilon^{jmn}e_{bm}^R(\boldsymbol{q}_1)e_{cn}^R(\boldsymbol{q}_2). \tag{3.42}$$

Using the homogeneous solution, equation (3.25), Green's function for equation (3.41) can be written as (149),

$$G_t(\tau,\eta,k) = i\Theta(\tau-\eta)\big[T_1^R(\tau,\boldsymbol{k})T_1^{*R}(\eta,\boldsymbol{k}) - T_1^{*R}(\tau,\boldsymbol{k})T_1^R(\eta,\boldsymbol{k})\big], \tag{3.43}$$

$$= \frac{1}{k}\Theta(\tau-\eta)e^{\pi(2m_Q+m_Q^{-1})}\mathrm{Im}[W^*_{\beta,\alpha}(2ik\tau)W_{\beta,\alpha}(2ik\eta)]\,, \tag{3.44}$$

where $\mathrm{Im}(z)$ denotes an imaginary part of a complex number z. Dependence of Green's function on the homogeneous solution also ensures that the second order left-handed polarisation of the gauge field is sub-dominant, even if sourced by the first order right-handed polarisation.

Then, the second order gauge field is given as

$$\hat{t}_2^R(\tau,\boldsymbol{k}) = g e_{ij}^L(\boldsymbol{k})\int_{-\infty}^{\infty} d\eta\, G_t(\tau,\eta,k) \times \int \frac{d^3q_1\, d^3q_2}{(2\pi)^6}\,\delta_D(\boldsymbol{q}_1+\boldsymbol{q}_2-\boldsymbol{k})Q_{ij}^{(i)}(\boldsymbol{q}_1,\boldsymbol{q}_2,\eta)\hat{t}_1^R(\eta,\boldsymbol{q}_1)\hat{t}_1^R(\eta,\boldsymbol{q}_2)\,, \tag{3.45}$$

which yields the second order sourced metric perturbation (c.f. equation (3.20)) as

$$\hat{\psi}_2^R(\tau,\boldsymbol{k}) = \int_{-\infty}^{\infty} d\eta\, G_\psi(\tau,\eta,k)\mathcal{D}(\eta,k)\hat{t}_2^R(\eta,k)\,. \tag{3.46}$$

Substituting $\hat{\psi}_1^R$ and the above expression for $\hat{\psi}_2^R$ into eq. (3.32), we obtain

$$\begin{aligned}
&\Big\langle \hat{\psi}_1^R(\tau,\boldsymbol{k}_1)\hat{\psi}_1^R(\tau,\boldsymbol{k}_2)\hat{\psi}_2^R(\tau,\boldsymbol{k}_3)\Big\rangle = \\
&= \int\prod_{i=1}^{3}\Big(d\eta_i G_\psi(\tau,\eta_i,k_i)\mathcal{D}(\eta_i,k_i)\Big)\left\langle \hat{t}_1^R(\eta_1,\boldsymbol{k}_1)\hat{t}_1^R(\eta_2,\boldsymbol{k}_2)\hat{t}_2^R(\eta_3,\boldsymbol{k}_3)\right\rangle\,, \\
&= \int\prod_{i=1}^{3}\Big(d\eta_i G_\psi(\tau,\eta_i,k_i)\mathcal{D}(\eta_i,k_i)\Big)\, T_1^R(\eta_1,k_1)T_1^R(\eta_2,k_2)g e_{jl}^L(\boldsymbol{k}_3)\int d\eta\, G_t(\eta_3,\eta,k_3) \\
&\times \int \frac{d^3q_1\, d^3q_2}{(2\pi)^6}\,\delta_D(\boldsymbol{q}_1+\boldsymbol{q}_2-\boldsymbol{k}_3)Q_{jl}(\boldsymbol{q}_1,\boldsymbol{q}_2,\eta_3)T_1^{*R}(\eta,q_1)T_1^{*R}(\eta,q_2)\left\langle \hat{a}^R_{\boldsymbol{k}_1}\hat{a}^R_{\boldsymbol{k}_2}\hat{a}^{R\dagger}_{-\boldsymbol{q}_1}\hat{a}^{R\dagger}_{-\boldsymbol{q}_2}\right\rangle\,, \\
&= (2\pi)^3\delta_D(\boldsymbol{k}_1+\boldsymbol{k}_2+\boldsymbol{k}_3)\, g\,\Psi_1^R(\tau,k_1)\Psi_1^R(\tau,k_2)\int d\eta_3\, G_\psi(\tau,\eta_3,k_3)\mathcal{D}(\eta_3,k_3) \\
&\times \int d\eta\, G_t(\eta_3,\eta,k_3)e_{ij}^L(\boldsymbol{k}_3)\Big[Q_{ij}(-\boldsymbol{k}_1,-\boldsymbol{k}_2,\eta)+Q_{ij}(-\boldsymbol{k}_2,-\boldsymbol{k}_1,\eta)\Big]T_1^{*R}(\eta,k_1)T_1^{*R}(\eta,k_2)\,.
\end{aligned} \tag{3.47}$$

As discussed in appendix. B, contraction of the polarisation tensors is calculated as

$$e_{ij}^L(\boldsymbol{k}_3)\Big[Q_{ij}^{(i)}(-\boldsymbol{k}_1,-\boldsymbol{k}_2,\eta)+Q_{ij}^{(i)}(-\boldsymbol{k}_2,-\boldsymbol{k}_1,\eta)\Big] = -2k_1\Xi\Big[\tilde{\Xi}+(3m_Q+2\xi)/\eta\Big], \tag{3.48}$$

where we have defined

$$\tilde{\Xi} = 1 + r_2 + r_3\,, \quad \Xi = \frac{(1+r_2+r_3)^3}{64 r_2^2 r_3^2}(r_2+r_3-1)(r_2-r_3+1)(-r_2+r_3+1)\,, \tag{3.49}$$

with $r_2 \equiv k_2/k_1$ and $r_3 = k_3/k_1$. Using this, we obtain

$$\left\langle \hat{\psi}_1^R(\tau,\boldsymbol{k}_1)\hat{\psi}_1^R(\tau,\boldsymbol{k}_2)\hat{\psi}_2^R(\tau,\boldsymbol{k}_3)\right\rangle = (2\pi)^3\delta_D(\boldsymbol{k}_1+\boldsymbol{k}_2+\boldsymbol{k}_3)\,(-2g\Xi k_1)\,\Psi_1^R(\tau,k_1)\Psi_1^R(\tau,k_2)$$
$$\times \int d\eta_3\, G_\psi(\tau,\eta_3,k_3)\mathcal{D}(\eta_3,k_3)\int d\eta\, G_t(\eta_3,\eta,k_3)\Big[\tilde{\Xi}+\frac{(5m_Q+2m_Q^{-1})}{k_1\eta}\Big]T_1^{*R}(\eta,k_1)T_1^{*R}(\eta,k_2)\,. \tag{3.50}$$

Since we are interested in the bispectrum in the super-horizon limit $k\tau \to 0$, Green's function $G_\psi(\tau,\eta_3,k_3)$ can be reduced. By changing the integration variables from η_3 and η to $y \equiv -k_1\eta_3$ and $z \equiv -k_1\eta$, we obtain

$$\lim_{|k_3\tau|\to 0}\int d\eta_3\, G_\psi(\tau,\eta_3,k_3)\mathcal{D}(\eta_3,k_3)\int d\eta\, G_t(\eta_3,\eta,k_3)\Big[\tilde{\Xi}+\frac{(3m_Q+2\xi)}{k_1\eta}\Big]T_1^{*R}(\eta,k_1)T_1^{*R}(\eta,k_2)$$
$$= \frac{\sqrt{\epsilon_B}e^{2\pi(2m_Q+m_Q^{-1})}}{\sqrt{r_2}r_3^4k_1^4\tau}\int_0^{x_{\rm max}}\frac{dy}{y^2}\Big[r_3y\cos(r_3y)-\sin(r_3y)\Big]\left(m_Q^{-1}\partial_y+\frac{m_Q}{y}-r_3\right)$$
$$\times\int_y^{x_{\rm max}} dz\,{\rm Im}\Big[W^*_{\beta,\alpha}(-2ir_3y)W_{\beta,\alpha}(-2ir_3z)\Big]\left(\tilde{\Xi}-\frac{(5m_Q+2m_Q^{-1})}{z}\right)W^*_{\beta,\alpha}(-2iz)W^*_{\beta,\alpha}(-2ir_2z),$$
$$\equiv \frac{\sqrt{\epsilon_B}e^{2\pi(2m_Q+m_Q^{-1})}}{\sqrt{r_2}r_3^4k_1^4\tau}\mathcal{N}_3, \tag{3.51}$$

where we have introduced the UV cutoff $x_{\rm max} \equiv 2m_Q + m_Q^{-1} + \sqrt{2m_Q^2+2+m_Q^{-2}}$, at which t_1^R starts undergoing a tachyonic instability, to avoid incorporating unphysical vacuum contributions. The integration result is not sensitive to the precise value of the cutoff. Using the super horizon solution for Ψ_1^R, equation (3.29), and $\psi_{ij} = aM_Ph_{ij}/2$ we finally obtain

$$\left\langle \hat{h}_1^R(\tau,\boldsymbol{k}_1)\hat{h}_1^R(\tau,\boldsymbol{k}_2)\hat{h}_2^R(\tau,\boldsymbol{k}_3)\right\rangle = (2\pi)^3\delta_D(\boldsymbol{k}_1+\boldsymbol{k}_2+\boldsymbol{k}_3)\frac{8g\Xi\epsilon_B^{3/2}}{k_1^2k_2^2k_3^2}\left(\frac{H}{M_{\rm Pl}}\right)^3 r_3^{-2}\mathcal{F}^2\mathcal{N}_3\,. \tag{3.52}$$

The factor of $\delta_D(\boldsymbol{k}_1+\boldsymbol{k}_2+\boldsymbol{k}_3)$ ensures the triangle condition, namely that the three wave vectors $\boldsymbol{k}_1$, $\boldsymbol{k}_2$, and $\boldsymbol{k}_3$ form a closed triangle. This is a consequence of homogeneity and isotropy of the Universe. In the same way, the other two terms in eq. (3.32) can be calculated. Combining them, we obtain the contribution from the diagram (i) as (10),

$$B_h^{(i)}(k_1,k_2,k_3) = \frac{8m_Q^2\Xi\epsilon_B}{k_1^2k_2^2k_3^2}e^{2\pi(2m_Q+m_Q^{-1})}\left(\frac{H}{M_{\rm Pl}}\right)^4\Big[\mathcal{F}^{*2}\mathcal{N}_1 + r_2^{-2}|\mathcal{F}|^2\mathcal{N}_2 + r_3^{-2}\mathcal{F}^2\mathcal{N}_3\Big], \tag{3.53}$$

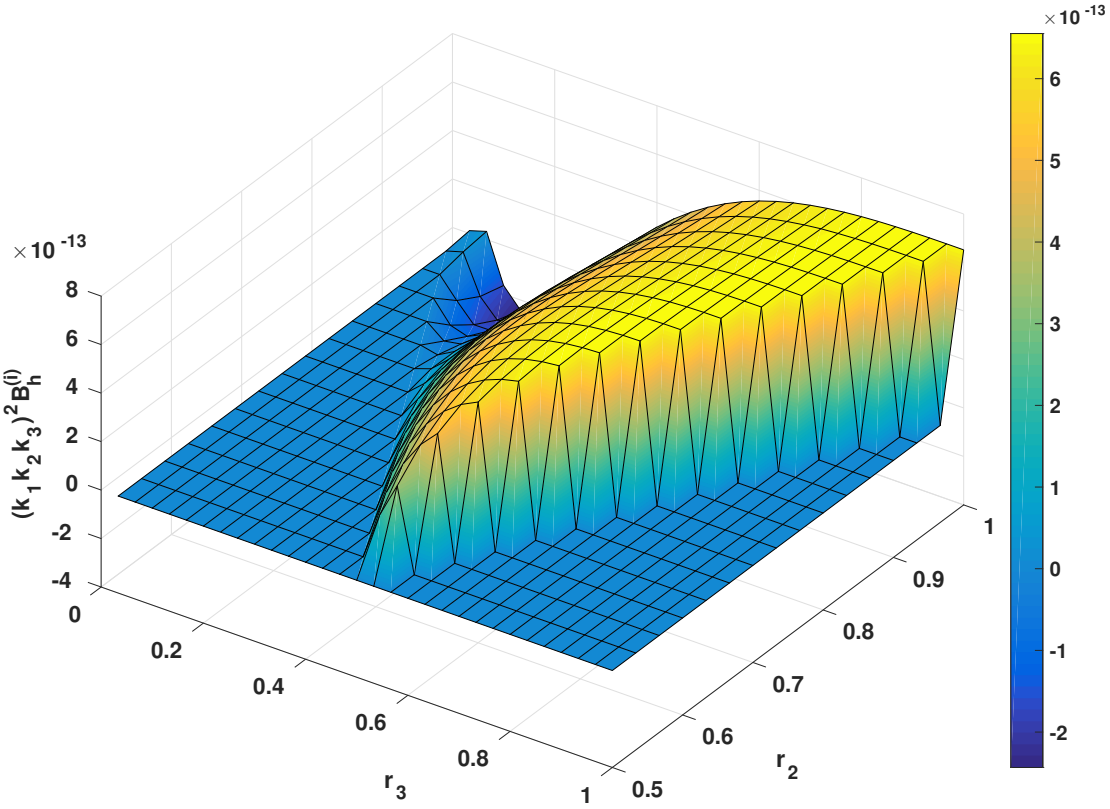

Figure 3.3: 3D plot of $(k_1k_2k_3)^2B_h^{(i)}$ contributed by the diagram (i). We show only $r_3 \leq r_2$ and the triangle condition implies a bispectrum is non-zero only for $r_2 + r_3 \geq 1$. This shape has a plateau around $0.6 \lesssim r_2 \simeq r_3 \leq 1$. The parameters are $H = 8 \times 10^{12}$GeV, $m_Q = 3.15$, and $\epsilon_B = 3 \times 10^{-4}$.

with

$$\mathcal{N}_i \equiv \int_0^{x_{\rm max}} \frac{dy}{y^2} \left[r_i y \cos(r_i y) - \sin(r_i y)\right] \left(m_Q^{-1}\partial_y + m_Q y^{-1} - r_i\right) \times \int_y^{x_{\rm max}} dz\, {\rm Im}[W^*_{\beta,\alpha}(-2ir_i y) W_{\beta,\alpha}(-2ir_i z)] \left(1 + r_2 + r_3 - \frac{5m_Q + 2m_Q^{-1}}{z}\right) \mathcal{W}_i(z), \tag{3.54}$$

where $\mathcal{W}_1(z) = W_{\beta,\alpha}(-2ir_2z)W_{\beta,\alpha}(-2ir_3z)$, $\mathcal{W}_2(z) = W^*_{\beta,\alpha}(-2iz)W_{\beta,\alpha}(-2ir_3z)$, and $\mathcal{W}_3(z) = W^*_{\beta,\alpha}(-2ir_2z)W^*_{\beta,\alpha}(-2iz)$.

Figure 3.3 shows the tensor bispectrum from the diagram (i). We shall discuss the shape of the bispectrum in detail in section 3.4.

3.3.2 Diagram (ii)

The bispectrum from the diagram (ii) is generated by a non-linear sourcing of the gravitational wave via the $\mathcal{O}(\psi tt)$ terms in the Lagrangian, $L_3^{(ii)}$. The EoM for the second order gravitational wave with the corresponding source terms in Fourier space is given by

$$\left[\partial_\tau^2 + k^2 - \frac{2}{\tau^2}\right] \hat{\psi}_2^R(\tau, \boldsymbol{k}) = \frac{H}{M_{\rm Pl}} [e_{ij}^R(\boldsymbol{k})]^{-1} S_{ij}^{(ii)}(\tau, \boldsymbol{k}) \,, \tag{3.55}$$

where the source term is written as the sum of two parts,

$$\begin{aligned} \mathcal{S}_{ij}^{(ii)}(\tau, \boldsymbol{k}) &\equiv \int \mathrm{d}^3x \, e^{-i\boldsymbol{k}\cdot\boldsymbol{x}} \, \frac{\delta L_3^{(ii)}}{\delta \psi_{ij}(\tau, \boldsymbol{x})}, \\ &= \int \frac{d^3q_1 d^3q_2}{(2\pi)^6} \delta_D(\boldsymbol{q}_1 + \boldsymbol{q}_2 - \boldsymbol{k}) \left[\mathcal{S}_{1ij}^{(ii)}(\tau, \boldsymbol{q}_1, \boldsymbol{q}_2) + \mathcal{S}_{2ij}^{(ii)}(\tau, \boldsymbol{q}_1, \boldsymbol{q}_2)\right]. \end{aligned} \tag{3.56}$$

$\mathcal{S}_{1ij}^{(ii)}$ has terms without time derivatives,

$$\begin{aligned} \mathcal{S}_{1ij}^{(ii)}(\tau, \boldsymbol{q}_1, \boldsymbol{q}_2) = \Bigg[& \frac{3m_Q^2}{\tau} e_{ci}^R(\boldsymbol{q}_1) e_{cj}^R(\boldsymbol{q}_2) - 2m_Q \Big\{ \epsilon^{acp} e_{pj}^R(\boldsymbol{q}_1) e_{ai}^R(\boldsymbol{q}_2) i q_{2c} \\ & + \epsilon^{apj} e_{pc}^R(\boldsymbol{q}_1) e_{ai}^R(\boldsymbol{q}_2) i q_{2c} - \epsilon^{apj} e_{pc}^R(\boldsymbol{q}_1) e_{ac}^R(\boldsymbol{q}_2) i q_{2i} \Big\} + \tau \Big\{ e_{ai}^R(\boldsymbol{q}_1) e_{aj}^R(\boldsymbol{q}_2) q_{1c} q_{2c} \\ & + e_{ac}^R(\boldsymbol{q}_1) e_{ac}^R(\boldsymbol{q}_2) q_{1i} q_{2j} - 2 e_{ai}^R(\boldsymbol{q}_1) e_{ac}^R(\boldsymbol{q}_2) q_{1c} q_{2j} \Big\} \Bigg] \hat{t}_1^R(\tau, \boldsymbol{q}_1) \hat{t}_1^R(\tau, \boldsymbol{q}_2) \\ & \equiv Q_{1ij}^{(ii)}(\tau, \boldsymbol{q}_1, \boldsymbol{q}_2) \hat{t}_1^R(\tau, \boldsymbol{q}_1) \hat{t}_1^R(\tau, \boldsymbol{q}_2) \,, \end{aligned} \tag{3.57}$$

whereas $\mathcal{S}_{2ij}^{(ii)}$ comes from time derivatives of $\hat{t}_1^R$,

$$\begin{aligned} \mathcal{S}_{2ij}^{(ii)}(\tau, \boldsymbol{q}_1, \boldsymbol{q}_2) =& \tau e_{ai}^R(\boldsymbol{q}_1) e_{aj}^R(\boldsymbol{q}_2) \hat{t}_1^{\prime R}(\tau, \boldsymbol{q}_1) \hat{t}_1^{\prime R}(\tau, \boldsymbol{q}_2) \\ \equiv& Q_{2ij}^{(ii)}(\tau, \boldsymbol{q}_1, \boldsymbol{q}_2) \hat{t}_1^{\prime R}(\tau, \boldsymbol{q}_1) \hat{t}_1^{\prime R}(\tau, \boldsymbol{q}_2) \,. \end{aligned} \tag{3.58}$$

The second order gravitational wave is given using Green's function,

$$\begin{aligned} \hat{\psi}_2^R(\tau, \boldsymbol{k}) = & \frac{H}{M_{\rm Pl}} \int_{-\infty}^{\infty} d\eta \, G_\psi(\tau, \eta, k) \int \frac{d^3q_1 d^3q_2}{(2\pi)^6} \delta_D(\boldsymbol{q}_1 + \boldsymbol{q}_2 - \boldsymbol{k}) \\ & \times e_{ij}^L(\boldsymbol{k}) \Big[Q_{1ij}^{(ii)}(\eta, \boldsymbol{q}_1, \boldsymbol{q}_2) \hat{t}_1^R(\eta, \boldsymbol{q}_1) \hat{t}_1^R(\eta, \boldsymbol{q}_2) + Q_{2ij}^{(ii)}(\eta, \boldsymbol{q}_1, \boldsymbol{q}_2) \hat{t}_1^{\prime R}(\eta, \boldsymbol{q}_1) \hat{t}_1^{\prime R}(\eta, \boldsymbol{q}_2) \Big] . \end{aligned} \tag{3.59}$$

We can now compute the first term in eq. (3.32) produced via the diagram (ii) as

$$\begin{aligned}
&\left\langle \hat{\psi}_1^R(\tau,\boldsymbol{k}_1)\hat{\psi}_1^R(\tau,\boldsymbol{k}_2)\hat{\psi}_2^R(\tau,\boldsymbol{k}_3)\right\rangle = \\
&\frac{H}{M_{\rm Pl}}\int\prod_{i=1}^{2}\left(\mathrm{d}\eta_i\, G_\psi(\tau,\eta_i,k_i)\mathcal{D}(\eta_i,k_i)\right)\int \mathrm{d}\eta_3\, G_\psi(\tau,\eta_3,k_3)\int\frac{d^3q_1 d^3q_2}{(2\pi)^6}\delta_D(\boldsymbol{q}_1+\boldsymbol{q}_2-\boldsymbol{k}_3)\\
&\quad\times e^L_{jl}(\boldsymbol{k})\Big[\left\langle \hat{t}_1^R(\eta_1,\boldsymbol{k}_1)\hat{t}_1^R(\eta_2,\boldsymbol{k}_2)\hat{t}_1^R(\eta_3,\boldsymbol{q}_1)\hat{t}_1^R(\eta_3,\boldsymbol{q}_2)\right\rangle Q^{(ii)}_{1jl}(\eta_3,\boldsymbol{q}_1,\boldsymbol{q}_2)\\
&\qquad+\left\langle \hat{t}_1^R(\eta_1,\boldsymbol{k}_1)\hat{t}_1^R(\eta_2,\boldsymbol{k}_2)\hat{t}_1^{\prime R}(\eta_3,\boldsymbol{q}_1)\hat{t}_1^{\prime R}(\eta_3,\boldsymbol{q}_2)\right\rangle Q^{(ii)}_{2jl}(\eta_3,\boldsymbol{q}_1,\boldsymbol{q}_2)\Big]\,.
\end{aligned}\tag{3.60}$$

The expectation values of the 4-point functions are given by

$$\begin{aligned}
&\left\langle \hat{t}_1^R(\eta_1,\boldsymbol{k}_1)\hat{t}_1^R(\eta_2,\boldsymbol{k}_2)\hat{t}_1^R(\eta_3,\boldsymbol{q}_1)\hat{t}_1^R(\eta_3,\boldsymbol{q}_2)\right\rangle\\
&\quad=(2\pi)^6(\delta_{\boldsymbol{k}_1\boldsymbol{q}_1}\delta_{\boldsymbol{k}_2\boldsymbol{q}_2}+\delta_{\boldsymbol{k}_1\boldsymbol{q}_2}\delta_{\boldsymbol{k}_2\boldsymbol{q}_1})T_1^R(\eta_1,k_1)T_1^R(\eta_2,k_2)T_1^{*R}(\eta_3,q_1)T_1^{*R}(\eta_3,q_2)\,,
\end{aligned}\tag{3.61}$$

$$\begin{aligned}
&\left\langle \hat{t}_1^R(\eta_1,\boldsymbol{k}_1)\hat{t}_1^R(\eta_2,\boldsymbol{k}_2)\hat{t}_1^{\prime R}(\eta_3,\boldsymbol{q}_1)\hat{t}_1^{\prime R}(\eta_3,\boldsymbol{q}_2)\right\rangle\\
&\quad=(2\pi)^6(\delta_{\boldsymbol{k}_1\boldsymbol{q}_1}\delta_{\boldsymbol{k}_2\boldsymbol{q}_2}+\delta_{\boldsymbol{k}_1\boldsymbol{q}_2}\delta_{\boldsymbol{k}_2\boldsymbol{q}_1})T_1^R(\eta_1,k_1)T_1^R(\eta_2,k_2)T_1^{\prime *R}(\eta_3,q_1)T_1^{\prime *R}(\eta_3,q_2)\,,
\end{aligned}\tag{3.62}$$

where $\delta_{\boldsymbol{k}_1\boldsymbol{q}_1}\equiv\delta_D(\boldsymbol{k}_1+\boldsymbol{q}_1)$. Note that these functions are invariant under interchange of $q_1\leftrightarrow q_2$. As a result, upon integrating the Dirac delta functions, the polarisation factors in equation (3.60) yield

$$e^L_{ij}(\boldsymbol{k}_3)\Big[Q^{(ii)}_{1ij}(\eta_3,-\boldsymbol{k}_1,-\boldsymbol{k}_2)+Q^{(ii)}_{1ij}(\eta_3,-\boldsymbol{k}_2,-\boldsymbol{k}_1)\Big]=2\,\Xi\left[\frac{3m_Q^2}{\eta_3}+k_1^2 r_2\eta_3+m_Q k_1(1+r_2)\right],\tag{3.63}$$

$$e^L_{ij}(\boldsymbol{k}_3)\Big[Q^{(ii)}_{2ij}(\eta_3,-\boldsymbol{k}_1,-\boldsymbol{k}_2)+Q^{(ii)}_{2ij}(\eta_3,-\boldsymbol{k}_2,-\boldsymbol{k}_1)\Big]=2\,\Xi\,\eta_3\,,\tag{3.64}$$

where $\Xi\equiv\Xi(r_2,r_3)$ has been defined in equation (3.49). Substituting this in equation (3.60), we obtain

$$\begin{aligned}
&\left\langle \hat{\psi}_1^R(\tau,\boldsymbol{k}_1)\hat{\psi}_1^R(\tau,\boldsymbol{k}_2)\hat{\psi}_2^R(\tau,\boldsymbol{k}_3)\right\rangle=(2\pi)^3\delta_D(\boldsymbol{k}_1+\boldsymbol{k}_2+\boldsymbol{k}_3)\\
&\quad\times 2\,\Xi\,\Psi_1^R(\tau,\boldsymbol{k}_1)\Psi_1^R(\tau,\boldsymbol{k}_2)\frac{H}{M_{\rm Pl}}\int d\eta_3\, G_\psi(\tau,\eta_3,k_3)\Bigg[\eta_3 T_1^{\prime *R}(\eta_3,k_1)T_1^{\prime *R}(\eta_3,k_2)\\
&\qquad+\left\{r_2k_1^2\eta_3+m_Qk_1(1+r_2)+\frac{3m_Q^2}{\eta_3}\right\}T_1^{*R}(\eta_3,k_1)T_1^{*R}(\eta_3,k_2)\Bigg]\,.
\end{aligned}\tag{3.65}$$

We can similarly evaluate the other two terms in eq. (3.32) contributed from $L_3^{(ii)}$. Taking the super-horizon limit, we obtain (10),

$$k_1^2k_2^2k_3^2B_h^{(ii)}(k_1,k_2,k_3)=4\Xi\epsilon_B e^{\pi(2m_Q+m_Q^{-1})}\left(\frac{H}{M_{\rm Pl}}\right)^4\left[\mathcal{F}^{*2}\tilde{\mathcal{N}}_1+r_2^{-1}|\mathcal{F}|^2\tilde{\mathcal{N}}_2+r_3^{-1}\mathcal{F}^2\tilde{\mathcal{N}}_3\right],\tag{3.66}$$

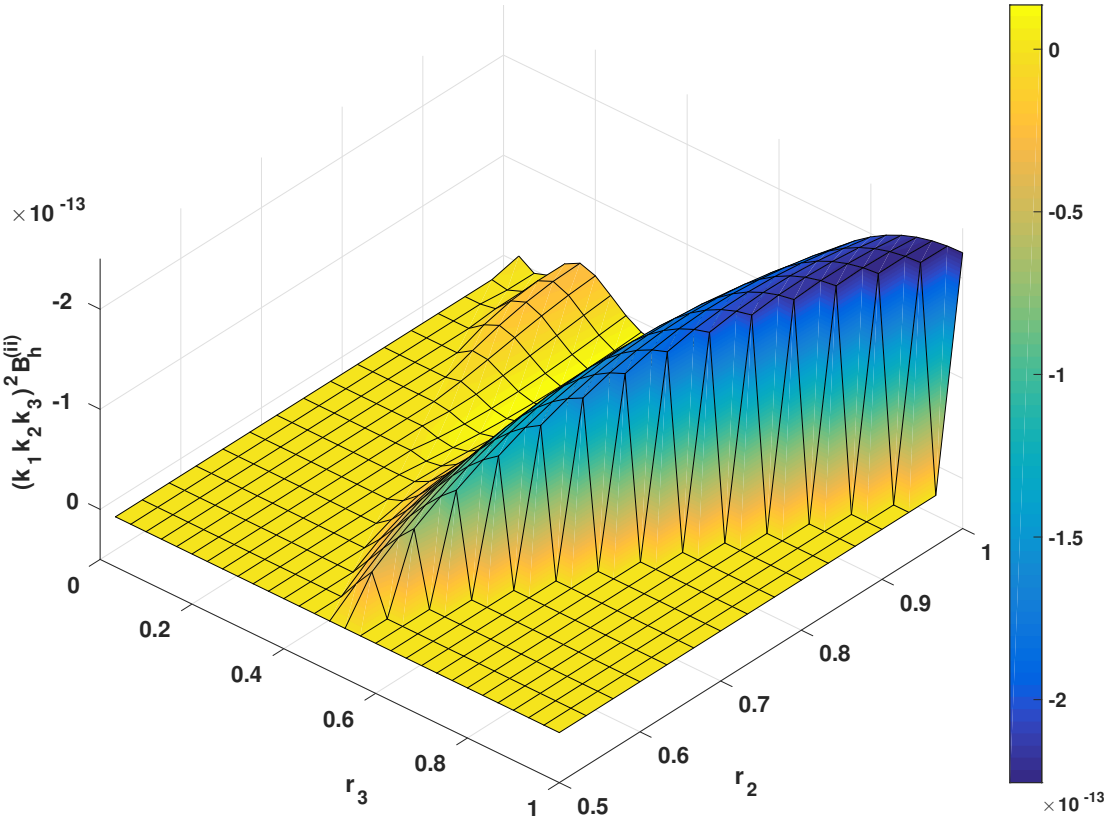

Figure 3.4: 3D plot of $(k_1k_2k_3)^2 B_h^{(ii)}$ for diagram 2. Note that the z-axis has been reversed to show negative values.

with

$$\tilde{\mathcal{N}}_i \equiv \int_0^{x_{\rm max}} \frac{dy}{y} \left[r_i y \cos(r_i y) - \sin(r_i y)\right] \Big[y\tilde{\mathcal{W}}_i(y) + \Big(\frac{r_1 r_2 r_3}{r_i} y - (r_1 + r_2 + r_3 - r_i) m_Q + \frac{3m_Q^2}{y} \Big) \mathcal{W}_i(y) \Big], \tag{3.67}$$

where $\tilde{\mathcal{W}}_1(y) = \partial_y W_{\beta,\alpha}(-2ir_2 y)\partial_y W_{\beta,\alpha}(-2ir_3 y)$, $\tilde{\mathcal{W}}_2(y) = \partial_y W^*_{\beta,\alpha}(-2iy)\partial_y W_{\beta,\alpha}(-2ir_3 y)$, $\tilde{\mathcal{W}}_3(y) = \partial_y W^*_{\beta,\alpha}(-2ir_2 y)\partial_y W^*_{\beta,\alpha}(-2iy)$, and as before, we have introduced $y \equiv -k_1\tau$.

Figure 3.4 shows the gravitational wave bispectrum from the diagram (ii). The magnitude of this bispectrum is smaller than that of the diagram (i) by a factor of a few, and they have the opposite signs. The bispectrum from the diagram (ii) peaks in the equilateral configuration, $r_2 = r_3 = 1$.

3.3.3 Diagram (iii)

For the diagram (iii), we consider the second order gravitational wave $\hat{\psi}_2^R$ sourced by a first order gauge field perturbation $\hat{t}_1^R$ and a first order metric perturbation $\hat{\psi}_1^R$. The EoM for $\hat{\psi}_2^R$ is derived from $L_3^{(iii)}$ to be,

$$\left[\partial_\tau^2 + k^2 - \frac{2}{\tau^2}\right]\hat{\psi}_2^R(\tau,\boldsymbol{k}) = \frac{H}{M_{\rm Pl}}[e_{ij}^R(\boldsymbol{k})]^{-1}\mathcal{S}_{ij}^{(iii)}(\tau,\boldsymbol{k})\,, \tag{3.68}$$

where the source term is again written as the sum of two parts,

$$\begin{aligned}\mathcal{S}_{ij}^{(iii)}(\tau,\boldsymbol{k}) &\equiv \int \mathrm{d}^3x\, e^{-i\boldsymbol{k}\cdot\boldsymbol{x}}\,\frac{\delta L_3^{(iii)}}{\delta\psi_{ij}(\tau,\boldsymbol{x})},\\ &= \int \frac{d^3q_1 d^3q_2}{(2\pi)^6}\delta_D(\boldsymbol{q}_1+\boldsymbol{q}_2-\boldsymbol{k})\,4\sqrt{\epsilon_B}\left[\mathcal{S}_{1ij}^{(iii)}(\tau,\boldsymbol{q}_1,\boldsymbol{q}_2)+\mathcal{S}_{2ij}^{(iii)}(\tau,\boldsymbol{q}_1,\boldsymbol{q}_2)\right]\,. \end{aligned}\tag{3.69}$$

The first part depends on the fields without time derivatives,

$$\begin{aligned}\mathcal{S}_{1ij}^{(iii)}(\tau,\boldsymbol{q}_1,\boldsymbol{q}_2) = -\hat{t}_1^R(\tau,\boldsymbol{q}_1)\hat{\psi}_1^R(\tau,\boldsymbol{q}_2)\Big[&2\,|\boldsymbol{q}_1|\,e_{ai}^R(\boldsymbol{q}_1)e_{aj}^R(\boldsymbol{q}_2)\\ &+ i\epsilon^{apj}e_{ai}^R(\boldsymbol{q}_1)e_{lp}^R(\boldsymbol{q}_2)q_{1l} + i\epsilon^{ajp}e_{al}^R(\boldsymbol{q}_1)e_{lp}^R(\boldsymbol{q}_2)q_{1i}\Big]\,,\end{aligned}\tag{3.70}$$

whereas the second part includes time derivatives of the gauge field perturbation,

$$\mathcal{S}_{2ij}^{(iii)}(\tau,\boldsymbol{q}_1,\boldsymbol{q}_2) = m_Q^{-1}\,e_{ai}^R(\boldsymbol{q}_1)e_{aj}^R(\boldsymbol{q}_2)\,\hat{t}_1^{\prime R}(\tau,\boldsymbol{q}_1)\hat{\psi}_1^R(\tau,\boldsymbol{q}_2)\,. \tag{3.71}$$

However, we find that the first part multiplied by the polarisation factor vanishes: $e_{ij}^L(\boldsymbol{k}_3)\mathcal{S}_{1ij}^{(iii)}(\tau,-\boldsymbol{k}_1,-\boldsymbol{k}_2) = 0$, for all the permutations of $\boldsymbol{k}_1,\boldsymbol{k}_2$, and $\boldsymbol{k}_3$. Hence we consider only the second part. With Green's function, we find the second order gravitational wave as

$$\begin{aligned}\hat{\psi}_2^R(\tau,\boldsymbol{k}) = \frac{4\sqrt{\epsilon_B}}{m_Q}\frac{H}{M_{\rm Pl}}\int_{-\infty}^{\infty}d\eta\,G_\psi(\tau,\eta,k)\int\frac{d^3q_1d^3q_2}{(2\pi)^6}\delta_D(\boldsymbol{q}_1+\boldsymbol{q}_2-\boldsymbol{k})\\ \times\left[\hat{t}_1^{\prime R}(\eta,\boldsymbol{q}_1)\hat{\psi}_1^R(\eta,\boldsymbol{q}_2)\,e_{ij}^L(\boldsymbol{k})e_{ia}^R(\boldsymbol{q}_1)e_{aj}^R(\boldsymbol{q}_2)\right].\end{aligned}\tag{3.72}$$

The first term in eq. (3.32) from the diagram (iii) yields

$$\begin{aligned}\left\langle\hat{\psi}_1^R(\tau,\boldsymbol{k}_1)\hat{\psi}_1^R(\tau,\boldsymbol{k}_2)\hat{\psi}_2^R(\tau,\boldsymbol{k}_3)\right\rangle = \frac{4\sqrt{\epsilon_B}}{m_Q}\frac{H}{M_{\rm Pl}}\int\prod_{i=1}^{2}(\mathrm{d}\eta_i G_\psi(\tau,\eta_i,k_i)\mathcal{D}(\eta_i,k_i))\int\mathrm{d}\eta_3 G_\psi(\tau,\eta_3,k_3)\\ \times\int\frac{d^3q_1d^3q_2}{(2\pi)^6}\delta_D(\boldsymbol{q}_1+\boldsymbol{q}_2-\boldsymbol{k}_3)\left\langle\hat{t}_1^R(\eta_1,\boldsymbol{k}_1)\hat{t}_1^R(\eta_2,\boldsymbol{k}_2)\hat{t}_1^{\prime R}(\eta_3,\boldsymbol{q}_1)\hat{\psi}_1^R(\eta_3,\boldsymbol{q}_2)\right\rangle e_{jl}^L(\boldsymbol{k}_3)e_{ja}^R(\boldsymbol{q}_1)e_{al}^R(\boldsymbol{q}_2)\,.\end{aligned}\tag{3.73}$$

The expected value is calculated as

$$\begin{aligned}\left\langle\hat{t}_1^R(\eta_1,\boldsymbol{k}_1)\hat{t}_1^R(\eta_2,\boldsymbol{k}_2)\hat{t}_1^{\prime R}(\eta_3,\boldsymbol{q}_1)\hat{\psi}_1^R(\eta_3,\boldsymbol{q}_2)\right\rangle = (2\pi)^6(\delta_{\boldsymbol{k}_1\boldsymbol{q}_1}\delta_{\boldsymbol{k}_2\boldsymbol{q}_2}+\delta_{\boldsymbol{k}_1\boldsymbol{q}_2}\delta_{\boldsymbol{k}_2\boldsymbol{q}_1})\\ \times T_1^R(\eta_1,k_1)T_1^R(\eta_2,k_2)T_1^{\prime *R}(\eta_3,q_1)\Psi_1^{*R}(\eta_3,q_2)\,.\end{aligned}\tag{3.74}$$

Then, equation (3.73) reads

$$\left\langle \hat{\psi}_1^R(\tau,\boldsymbol{k}_1)\hat{\psi}_1^R(\tau,\boldsymbol{k}_2)\hat{\psi}_2^R(\tau,\boldsymbol{k}_3)\right\rangle = (2\pi)^3\,\delta_D(\boldsymbol{k}_1+\boldsymbol{k}_2+\boldsymbol{k}_3)\,\Psi_1^R(\tau,k_1)\Psi_1^R(\tau,k_2)$$
$$\frac{4\sqrt{\epsilon_B}\Xi}{m_Q}\frac{H}{M_{\rm Pl}}\int d\eta_3\, G_\psi(\tau,\eta_3,k_3)\Big[T_1^{\prime *R}(\eta_3,k_1)\Psi_1^{*R}(\eta_3,k_2)+T_1^{\prime *R}(\eta_3,k_2)\Psi_1^{*R}(\eta_3,k_1)\Big]\,. \quad (3.75)$$

Combining with the other two terms in eq. (3.32), we obtain the bispectrum from the diagram (iii) as

$$k_1^2k_2^2k_3^2B_h^{(iii)}(k_1,k_2,k_3) = 16\Xi\frac{\epsilon_B^2}{m_Q}e^{\pi(2m_Q+m_Q^{-1})}\left(\frac{H}{M_{\rm Pl}}\right)^4\Big[\mathcal{F}^{*2}\breve{\mathcal{N}}_1+r_2^{-1}|\mathcal{F}|^2\breve{\mathcal{N}}_2+r_3^{-1}\mathcal{F}^2\breve{\mathcal{N}}_3\Big], \quad (3.76)$$

with

$$\breve{\mathcal{N}}_i \equiv \int_0^{x_{\rm max}}\frac{dy}{y}\,[r_iy\cos(r_iy)-\sin(r_iy)]\breve{\mathcal{W}}_i(y), \quad (3.77)$$

where we define $\breve{\mathcal{W}}_1(y)=\partial_yW_{\beta,\alpha}(-2ir_2y)\Phi(-2ir_3y)+\partial_yW_{\beta,\alpha}(-2ir_3y)\Phi(-2ir_2y)$, $\breve{\mathcal{W}}_2(y)=\partial_yW^*_{\beta,\alpha}(-2iy)\Phi(-2ir_3y)+\partial_yW^*_{\beta,\alpha}(-2ir_3y)\Phi(-2iy)$, $\breve{\mathcal{W}}_3(y)=\partial_yW^*_{\beta,\alpha}(-2iy)\Phi^*(-2ir_2y)+\partial_yW^*_{\beta,\alpha}(-2ir_2y)\Phi^*(-2iy)$, $y\equiv-k_1\tau$, and

$$\Phi(-2ir_iy)\equiv\frac{1}{r_iy}\int_{r_iy}^{x_{\rm max}}\frac{dz}{z}\,[(z-r_iy)\cos(z-r_iy)-(1+zr_iy)\sin(z-r_iy)]$$
$$\times\left[\frac{\partial_z}{m_Qz}+\frac{m_Q-z}{z^2}\right]W_{\beta,\alpha}(-2iz). \quad (3.78)$$

Figure 3.5 shows the momentum dependence of the bispectrum from the diagram (iii). We find that the contribution from the diagram (iii) is almost 7 orders of magnitude smaller than that of the diagram (i) and (ii), justifying that we neglected its contribution in our previous work (10). This diagram is also zero in the folded limit and the bispectrum peaks in the equilateral configuration. The contribution from this diagram is so small that we do not compare the templates to it.

3.3.4 Total bispectrum

Combining the three contributions which we have calculated in the previous subsections, eqs. (3.53), (3.66) and (3.76), we obtain the total bispectrum of the sourced GWs in our model as

$$B_h^{RRR}(k_1,k_2,k_3) = B_h^{(i)}+B_h^{(ii)}+B_h^{(iii)},$$
$$= \frac{\epsilon_B\,\Xi(r_2,r_3)}{k_1^2k_2^2k_3^2}\left(\frac{H}{M_{\rm Pl}}\right)^4\Upsilon(m_Q,r_2,r_3), \quad (3.79)$$

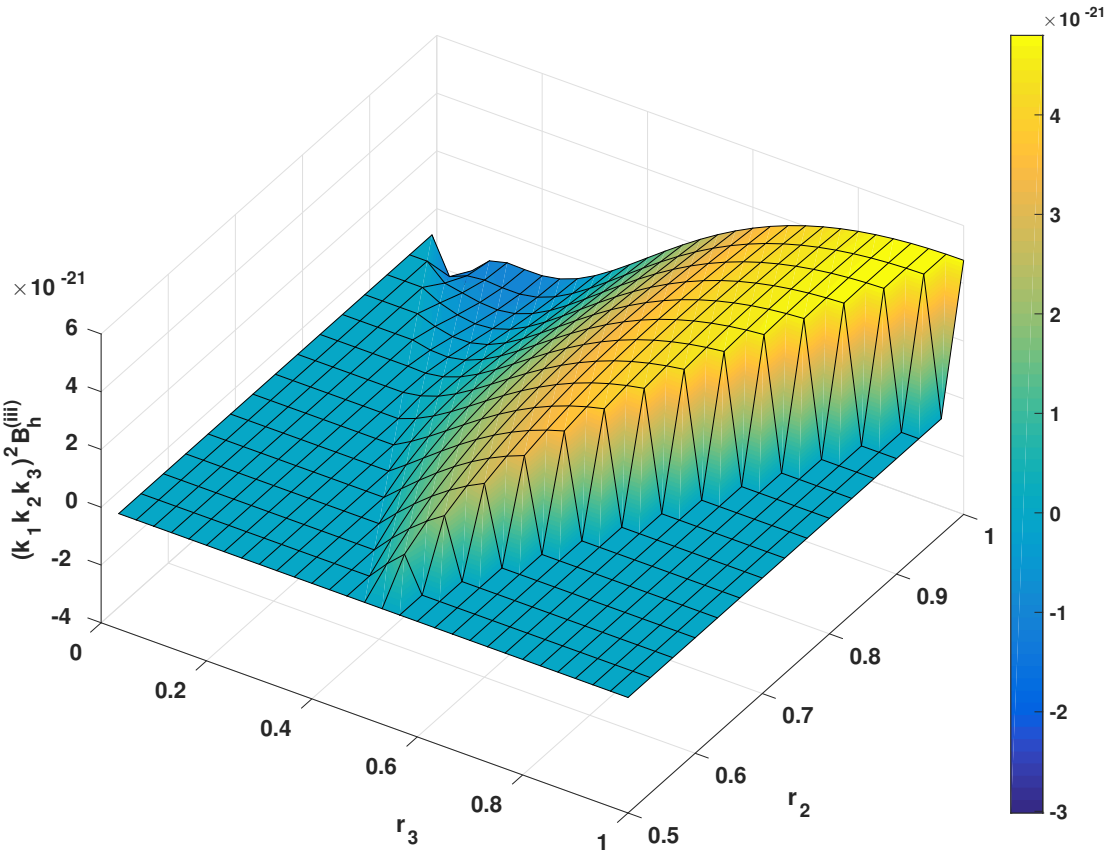

Figure 3.5: 3D plot of $(k_1k_2k_3)^2B_h^{(iii)}$ for diagram 3. Its magnitude is much smaller than the other two contributions, $B_h^{(i)}$ and $B_h^{(ii)}$, shown in figures 3.3 and 3.4, respectively.

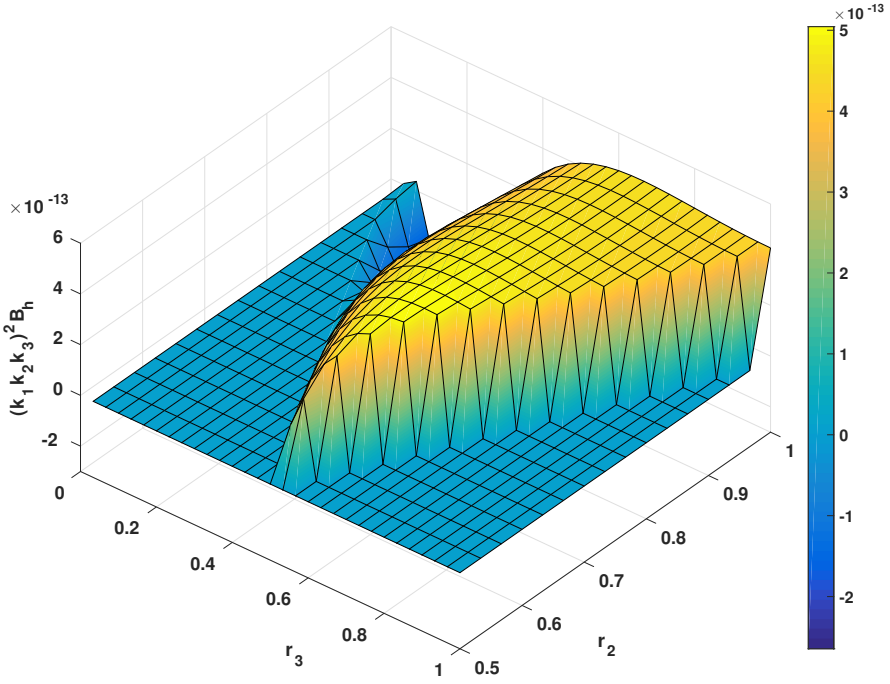

Figure 3.6: 3D plot of the total bispectrum $(k_1k_2k_3)^2B_h^{RRR}$ given in eq. (3.79). It has a peak at $r_2 \simeq r_3 \approx 0.6$ where the brightest yellow is seen.

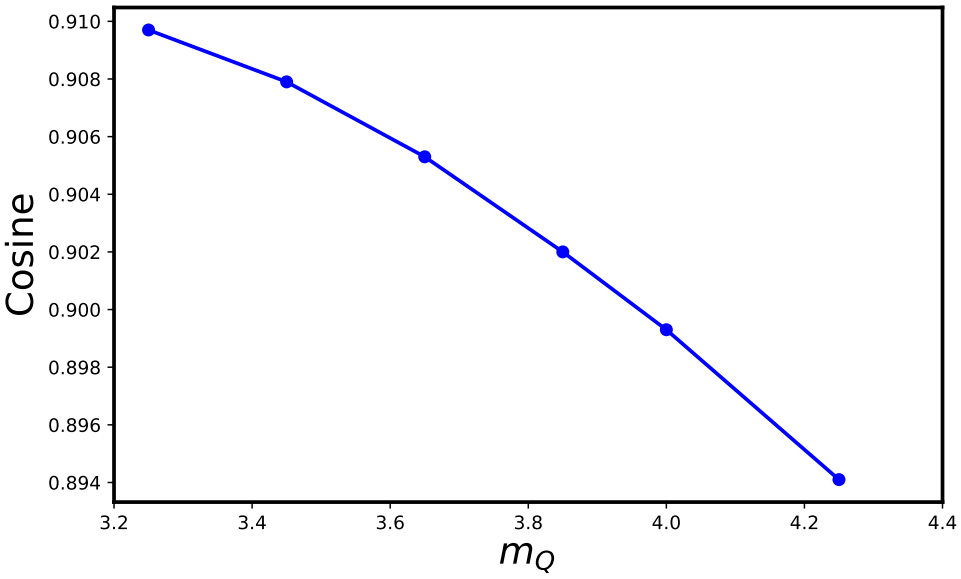

Figure 3.7: Similarity of the shapes of an equilateral bispectrum and our tensor bispectrum B_h^{RRR}, eq. (3.79), which is calculated as the "cosine" (see appendix C for definition).

with

$$\begin{aligned}\Upsilon(m_Q, r_2, r_3) \equiv\ & 8m_Q^2 e^{2\pi(2m_Q+m_Q^{-1})}\left[\mathcal{F}^{*2}\mathcal{N}_1 + r_2^{-2}|\mathcal{F}|^2\mathcal{N}_2 + r_3^{-2}\mathcal{F}^2\mathcal{N}_3\right] \\ & + 4e^{\pi(2m_Q+m_Q^{-1})}\left[\mathcal{F}^{*2}\tilde{\mathcal{N}}_1 + r_2^{-1}|\mathcal{F}|^2\tilde{\mathcal{N}}_2 + r_3^{-1}\mathcal{F}^2\tilde{\mathcal{N}}_3\right] \\ & + 16\frac{\epsilon_B}{m_Q}e^{\pi(2m_Q+m_Q^{-1})}\left[\mathcal{F}^{*2}\check{\mathcal{N}}_1 + r_2^{-1}|\mathcal{F}|^2\check{\mathcal{N}}_2 + r_3^{-1}\mathcal{F}^2\check{\mathcal{N}}_3\right]. \end{aligned} \tag{3.80}$$

The ϵ_B dependence of Υ is weak, since the third line in eq.(3.80) from the diagram (iii) is negligible compared to the others. In figure 3.6, we show the shape of the total bispectrum $(k_1k_2k_3)^2B_h^{RRR}(k_1, k_2, k_3)$. We find a mild peak around $r_2 \simeq r_3 \approx 0.6$ as a result of the combination of the plateau of $B_h^{(i)}$ and the negative slope of $B_h^{(ii)}$ on the $r_2 = r_3$ plane.

Aside from some interesting local features, the shape of our bispectrum B_h^{RRR} looks similar to the equilateral shape shown in figure C.1. To quantitatively measure similarity, we calculate the "cosine" between the shape of our bispectrum and the equilateral shape, $\cos(B_h \cdot F_{\rm eq})$ (17). Definition of the cosine is described in appendix C. In figure 3.7, the cosine is shown as a function of m_Q. Note that the cosine depends only on m_Q, because H and ϵ_B change only the overall amplitude as long as the diagram (iii) is negligible. We find that the cosine is around 0.9 and it varies up to 1% for the parameter range of interest (see section 3.5).

Around 90% similarity to the equilateral shape implies that our gravitational wave bispectrum is reasonably characterized by the amplitude at the equilateral limit, $r_2 = r_3 =$

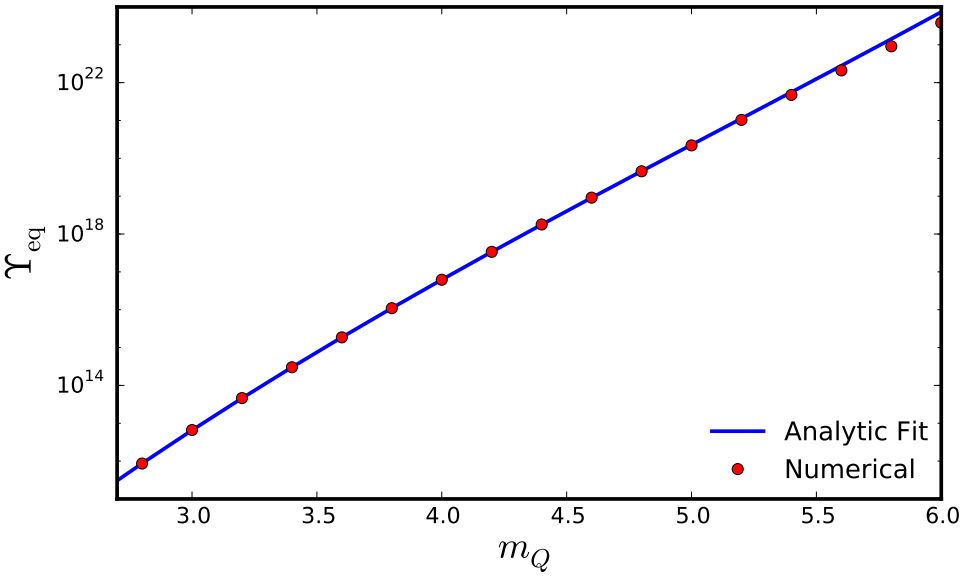

Figure 3.8: $\Upsilon_{\rm eq}(m_Q)$ defined in eq. (3.82) and its fitting formula (eq. (3.83)) are plotted as the red dots and blue line, respectively.

1. In the equilateral limit, the factors in the bispectrum become

$$\Xi(r_2 = r_3 = 1) = \frac{27}{64} \tag{3.81}$$

and

$$\begin{aligned}\Upsilon_{\rm eq}(m_Q) &\equiv \Upsilon(m_Q, 1, 1) \\ &\simeq 8m_Q^2 e^{2\pi(2m_Q + m_Q^{-1})} \left[|\mathcal{F}|^2 \mathcal{N}_2 + 2\,{\rm Re}[\mathcal{F}^2 \mathcal{N}_3]\right] \\ &\quad + 4e^{\pi(2m_Q + m_Q^{-1})} \left[|\mathcal{F}|^2 \tilde{\mathcal{N}}_2 + 2\,{\rm Re}[\mathcal{F}^2 \tilde{\mathcal{N}}_3]\right] ,\end{aligned} \tag{3.82}$$

where ${\rm Re}[z]$ denotes a real part of a complex number z, and the small contribution from the diagram (iii) is ignored. In figure 3.8, we plot $\Upsilon_{\rm eq}$. For $3 \lesssim m_Q \lesssim 5$, $\Upsilon_{\rm eq}$ is well approximated by the following expression:

$$\Upsilon_{\rm eq} \simeq \exp[0.1377 m_Q^3 - 2.128 m_Q^2 + 18.96 m_Q - 12.8], \qquad (2.8 \leq m_Q \leq 4.8). \tag{3.83}$$

Here, the relative error of this fitting formula is less than 1%.

The ratio of the bispectrum to the squared power spectrum of GWs from the vacuum fluctuation of the metric, $B_h^{\rm vac}/(P_h^{\rm vac})^2$, is of order unity (108; 109). The ratio for the sourced GWs can be much greater than unity. From eqs. (3.30) and (3.79), the ratio in the equilateral limit is given by

$$\frac{B_h^{\rm sourced}(k,k,k)}{\left(P_h^{\rm sourced}(k)\right)^2} = \frac{3^3 \Upsilon_{\rm eq}(m_Q)}{2^8 |\mathcal{F}(m_Q)|^4}\, \epsilon_B^{-1} . \tag{3.84}$$

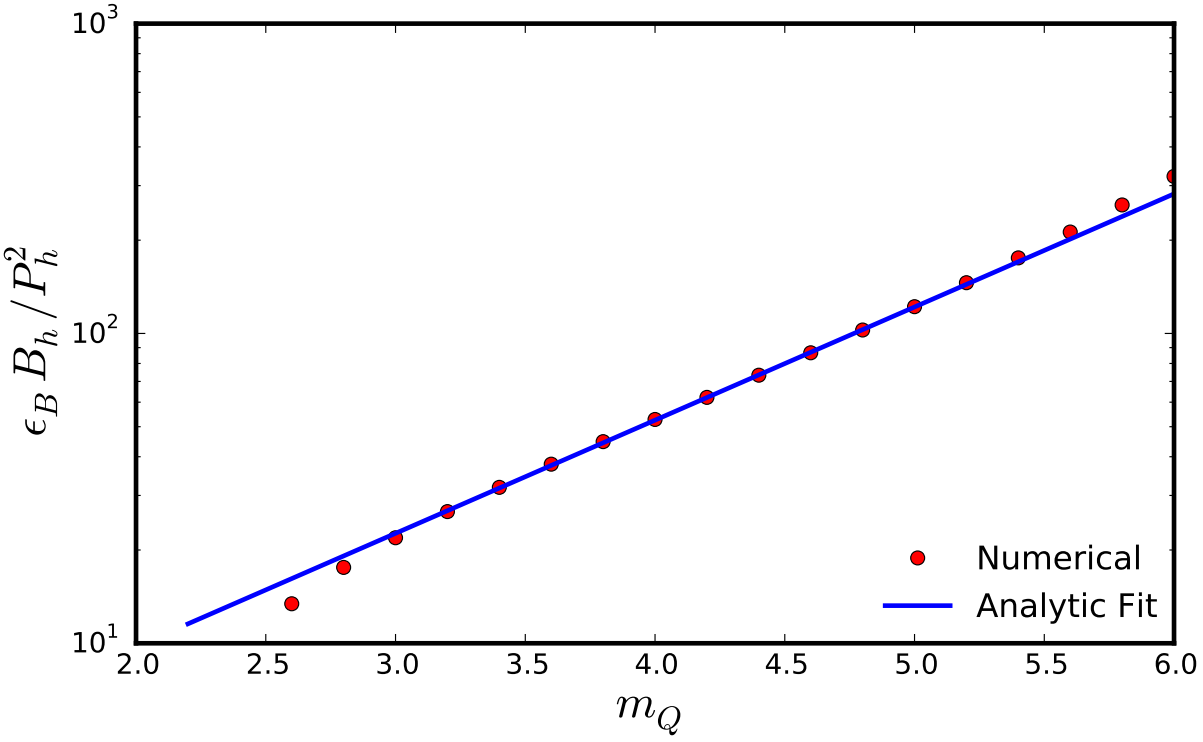

Figure 3.9: Ratio of the sourced tensor bispectrum to the sourced tensor power spectrum squared (normalised by ϵ_B) as a function of the parameter m_Q, along with its fitting formula (eq. (3.85)), plotted as the red dots and blue line respectively. It rises exponentially as m_Q increases. Since the y-axis shows the ratio normalised by the energy density fraction of the gauge field, ϵ_B, the ratio of the correlation functions can be very large for allowed values of ϵ_B.

In figure 3.9, we plot $\epsilon_B\, B_h^{\rm sourced}/(P_h^{\rm sourced})^2$ in which steep exponential dependence of the bispectrum and power spectrum on m_Q cancels out, though milder exponential dependence remains. We find a simple relation for a specific range of m_Q; for instance,

$$\frac{B_h^{\rm sourced}(k,k,k)}{\left(P_h^{\rm sourced}(k)\right)^2} \approx \frac{1.816\, e^{0.841 m_Q}}{\epsilon_B} \simeq \frac{0.908\, e^{0.841 m_Q}}{\Omega_A}, \qquad (3 \lesssim m_Q \lesssim 5), \tag{3.85}$$

where $\Omega_A \equiv (\epsilon_B + \epsilon_E)/2 \simeq (1 + m_Q^{-2})\epsilon_B/2$ (see eq. (3.10)) is the energy density fraction of the background $SU(2)$ gauge field.

Dependence on the energy density fraction of the gauge fields in eq. (3.85) is analogous to the curvaton mechanism (106; 105), where a similar relation holds for the scalar non-Gaussianity parameter, $f_{\rm NL} \sim \Omega_\sigma^{-1}$. Ω_σ is the energy density fraction of the curvaton field at its decay time. Therefore the origin of the dependence in eq. (3.85) may be understood in a similar way as the curvaton case (96): suppose that the metric perturbation h is given by $h = c_1 t$ where t is the mode function of the gauge field. At the same time, t is expanded as $t = t^{(1)} + t^{(2)} + \mathcal{O}(t^{(3)})$ such that $t^{(2)} = c_2 (t^{(1)})^2$. Then $B_h/P_h^2 \sim c_2/c_1$. From equations (3.14) and (3.17), we see that $c_1 \propto \sqrt{\epsilon_B} H/M_{\rm Pl}$. We also see from equation (3.39) that $c_2 \propto g$. Thus $B_h/P_h^2 \sim g M_{\rm Pl}/(\sqrt{\epsilon_B} H) = m_Q^2/\epsilon_B$. It should be noted, however, that this relation only holds when the gauge field has the dominant contribution to both the tensor power spectrum and bispectrum, and thus, is not valid in the limit $\epsilon_B \to 0$.

3.4 Peak of Bispectrum

The total tensor bispectrum given in eq. (3.79) has a peak not at the equilateral limit $r_2 = r_3 = 1$ but at $r_2 = r_3 \approx 0.6$ (see figure. 3.6). In this section, we study why this happens, by looking into the evolution of the tensor perturbations of the $SU(2)$ gauge field t_{ij}.

The shape of the tensor bispectrum is determined by $\mathcal{N}_i(m_Q, r_2, r_3)$ and $\tilde{\mathcal{N}}_i(m_Q, r_2, r_3)$ $(i = 1, 2, 3)$ as well as $\Xi(r_2, r_3)$ in eq. (3.79), while the contributions from $\breve{\mathcal{N}}_i(m_Q, r_2, r_3)$ are negligible. For our current purpose, it suffices to focus on the case with $r_2 = r_3$ in which the three momenta, $\boldsymbol{k}_1, \boldsymbol{k}_2, \boldsymbol{k}_3$, form an obtuse-angled isosceles triangle. In other words, we concentrate on a cross-section surface of the 3D plot, figure 3.6. For $r \equiv r_2 = r_3$, the r dependence of $\mathcal{N}_i(m_Q, r)$ and $\tilde{\mathcal{N}}_i(m_Q, r)$ is shown in figure 3.10. We do not plot $|\mathcal{N}_3|$ and $|\tilde{\mathcal{N}}_3|$ which are the same as $|\mathcal{N}_2|$ and $|\tilde{\mathcal{N}}_2|$ for $r_2 = r_3$, respectively. We find that only $\mathcal{N}_1$ grows significantly as r decreases, while the others have moderate dependences. To understand its behaviour, we look closely at the second line of $\mathcal{N}_1$ in eq. (3.54) for $r_2 = r_3$,

$$\mathcal{I}_1(m_Q, r, y) \equiv \int_y^{x_{\rm max}} \frac{{\rm d}z}{z}\, {\rm Im}[W^*_{\beta,\alpha}(-2iy) W_{\beta,\alpha}(-2iz)] \Big(z(1+2r) - 5m_Q - 2m_Q^{-1} \Big)\, \mathcal{W}_1(z). \tag{3.86}$$

In the integrand of $\mathcal{I}_1$, the first part, ${\rm Im}[W^*_{\beta,\alpha}(-2iy) W_{\beta,\alpha}(-2iz)]$, represents Green's function for t_2^R given in eq. (3.44), and the second part, $\left(z(1+2r) - 5m_Q - 2m_Q^{-1}\right)\, \mathcal{W}_1(z)$,

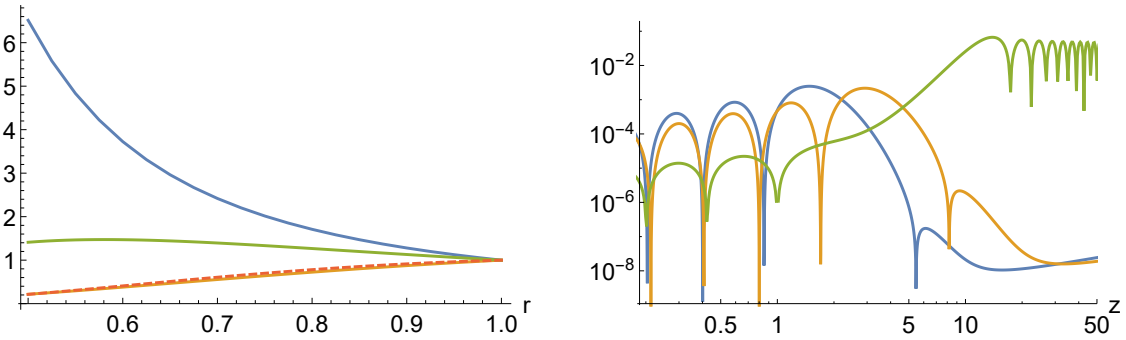

Figure 3.10: **(Left panel)** Absolute values of $\mathcal{N}_i$ and $\tilde{\mathcal{N}}_i$ normalized by their values at $r = 1$ are shown, namely $|\mathcal{N}_1(r)|/|\mathcal{N}_1(r = 1)|$ (blue), $r^{-2}|\mathcal{N}_2(r)|/|\mathcal{N}_2(r = 1)|$ (yellow), $|\tilde{\mathcal{N}}_1(r)|/|\tilde{\mathcal{N}}_1(r = 1)|$ (green) and $r^{-1}|\tilde{\mathcal{N}}_2(r)|/|\tilde{\mathcal{N}}_2(r = 1)|$ (red dashed). **(Right panel)** Absolute value of the source term part in the integrand of $\mathcal{I}_1$, namely $|(z(1+2r) - 5m_Q - 2m_Q^{-1})\mathcal{W}_1(z)|$, is shown for $r = 1$ (blue) and $r = 0.5$ (yellow). Its Green's function part, $|\mathrm{Im}[W^*_{\beta,\alpha}(-2iy)W_{\beta,\alpha}(-2iz)]|$, for $y = 1$ is also plotted as the green line. In both panels we set $m_Q = 3.15$.

represents the non-linear source term from the first order tensor perturbations, $t_1^R \times t_1^R$. They are plotted in figure 3.10 for $r = 1$ and $r = 0.5$. Basically the second part is shifted by a factor of ≈ 2 along the z-axis, as r is reduced to the half. However, Green's function has a bigger amplitude at larger z without oscillations up to $z \simeq 10$. Note that the non-linear source term contains $\mathcal{W}_1(z) \equiv W_{\beta,\alpha}(-2ir_2z)W_{\beta,\alpha}(-2ir_3z)$, indicating that the two sourcing modes t_1^R have momenta $k_2 = k_3 = rk_1$ in the case of $r \equiv r_2 = r_3$, while the momentum of the sourced mode t_2^R is k_1 in the process of $\mathcal{N}_1$. The fact that Green's function for t_2^R is larger on sub-horizon scales implies that the source effect from $t_1^R \times t_1^R$ to t_2^R is more efficient when the sourcing modes $t_1^R(rk_1)$ have lower momenta (i.e. a smaller r) and get amplified before $t_2^R(k_1)$ crosses the horizon. In other words, $\mathcal{N}_1$ becomes larger for a smaller r, because atypical Green's function G_t allows the sourcing effect to be active deep inside the horizon.

This non-linear sourcing process of t_2 through the diagram (i) shows clear contrast from the linear sourcing process from t_1 to ψ_1 discussed in section 3.2. There, Green's function for ψ, G_ψ, rapidly oscillates inside the horizon and does not allow t_1 to induce ψ_1 on sub-horizon scales, as shown in figure 3.1. In cases where only such normal Green's functions are involved, the shape of the bispectrum is typically equilateral, since all the modes are mainly produced around the horizon crossing. Nonetheless, in our case, Green's function for t_R is peculiar due to tachyonic instability, and the peak of the bispectrum deviates from the equilateral limit.

The total contribution to the bispectrum from $\mathcal{N}_i$ and $\tilde{\mathcal{N}}_i$ is maximal in the folded limit $r = 0.5$. However, $\Xi(r_2, r_3)$ arising from the tensor polarisations is also an important factor determining the shape of the tensor bispectrum. Ξ is multiplied to the total bispectrum eq. (3.79) as an overall factor and it vanishes at $r_2 = r_3 = 0.5$. In figure 3.11, we illustrate how Ξ changes the shape of the bispectrum on the $r_2 = r_3$ plane. Ξ suppresses the

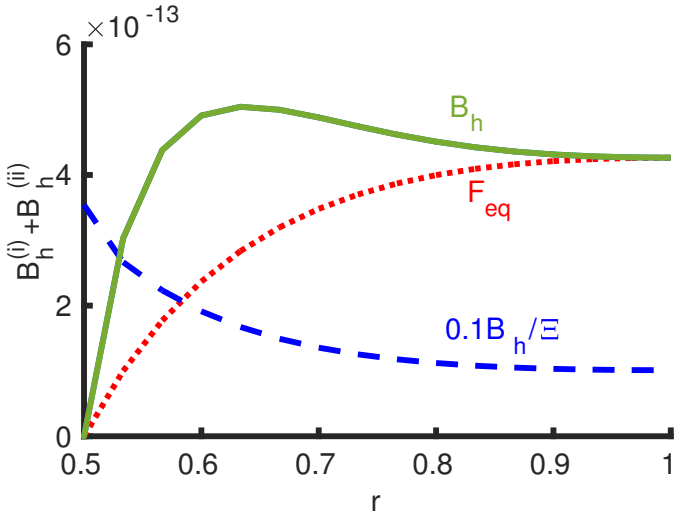

Figure 3.11: $(k_1k_2k_3)^2(B_h^{(i)}+B_h^{(ii)})$ is plotted as solid green line as an function of $r \equiv r_2 = r_3$. The peak is located at $r \approx 0.6$ and the deviation from the equilateral shape (red dotted) is remarkable. The blue dashed line shows the case without Ξ, namely $10^{-1}(k_1k_2k_3)^2(B_h^{(i)} + B_h^{(ii)})/\Xi$ which is multiplied by 0.1 for illustrative purpose. The parameters are given in eq. (3.38).

bispectrum at lower r and vanishes at $r = 0.5$. In fact, Ξ vanishes not only at $r_2 = r_3 = 0.5$, but at all points on the line $r_2 + r_3 = 1$ (i.e. the folded limit), because of conservation of angular momentum. The Feynman diagrams in figure 3.2 can be seen as processes in which two spin-2 particles collide and one spin-2 particle comes out. In particular, in the case of a head-on collision, which corresponds to the folded limit, $k_2 + k_3 = k_1$, the cross-section vanishes, because the angular momentum is contributed only by spins (i.e. no orbital angular momentum) and the spin of the system cannot be conserved as $2 \pm 2 \neq \pm 2$.

In summary, the peak of the tensor bispectrum B_h is located at $r \equiv r_2 = r_3 \approx 0.6$ for the following two reasons - (i) Among several contributions to the sourced tensor bispectrum B_h^{RRR}, the biggest one comes from $\langle \hat{\psi}_2^R(k_1)\hat{\psi}_1^R(k_2)\hat{\psi}_1^R(k_3)\rangle \propto \mathcal{N}_1$ in which the two linear perturbations of $SU(2)$ gauge field $\hat{t}_1^R(k = rk_1)$ non-linearly induce the second order one $\hat{t}_2^R(k_1)$ and subsequently $\hat{t}_2^R(k_1)$ sources the second order GW $\hat{\psi}_2^R(k_1)$. In this process, the amplitude of the second order fluctuations is larger when the momentum of the first order perturbations, rk_1, is smaller, because in this case t_1^R gets amplified when the second order t_2^R is still deep inside the horizon where the source effect is more efficient (i.e. Green's function G_t has a bigger amplitude). Hence, $\mathcal{N}_1$, which dominates the tensor bispectrum, is a decreasing function of r (see figure 3.10). (ii) The polarisation tensors also yield a r dependence as an overall factor $\Xi(r)$ to the total bispectrum. $\Xi(r)$ is a growing function of r and vanishes at $r = 0.5$. Multiplying $\Xi(r)$ changes the blue dashed line into the green line in figure 3.11. As the result of (i) and (ii), we obtain the bispectrum with a peak at $r \simeq 0.6$.

3.5 Parameter Search

In this section, we constrain the parameter regions from present observations and self-consistency of the model. We also clarify the parameter regions where the power spectrum or bispectrum of the sourced GWs will be detectable by upcoming CMB observations. Note that there remain four parameters, H, m_Q, ϵ_B and g, and one relationship $g^2\epsilon_B M_{\rm Pl}^2 = m_Q^4 H^2$. Eliminating g, we are left with three free parameters, H, m_Q and ϵ_B, in our model.

3.5.1 Tensor-to-scalar ratio

Currently the CMB observations put an upper bound on the tensor-to-scalar ratio r as

$$r \equiv \frac{P_h(k_{\rm CMB})}{P_\zeta(k_{\rm CMB})} < 0.07, \qquad (95\%\ \text{C.L.}), \tag{3.87}$$

where P_ζ is the power spectrum of the curvature perturbation and $k_{\rm CMB} = 0.05\,{\rm Mpc}^{-1}$. In our model, not only the vacuum fluctuation of the metric but also the sourced GWs contribute to P_h. Substituting eq. (3.30), the total tensor-to-scalar ratio is given as

$$r = \frac{\Delta^h_{\rm vac}}{\Delta_\zeta}\left(1 + \frac{\epsilon_B}{2}\left|\mathcal{F}(m_Q)\right|^2\right), \tag{3.88}$$

where the dimensionless scalar power spectrum, $\Delta_\zeta \equiv k^3 P_\zeta/2\pi^2 \approx 2.2\times10^{-9}$ (5), and that of the tensor metric vacuum fluctuation, $\Delta^h_{\rm vac} \equiv k^3 P_h^{\rm vac}/2\pi^2 = 2H^2/\pi^2 M_P^2$, are introduced. Translating the upper bound on r into the constraint on our model parameters, we obtain

$$\epsilon_B < \left(\frac{0.07}{r_{\rm vac}} - 1\right)\frac{2}{|\mathcal{F}(m_Q)|^2}, \tag{3.89}$$

where the conventional tensor-to-scalar ratio contributed only from the tensor metric vacuum fluctuation is defined by

$$r_{\rm vac} \equiv \frac{\Delta^h_{\rm vac}}{\Delta_\zeta} \approx \frac{1}{2.2\times10^{-9}}\frac{2H^2}{\pi^2 M_{\rm Pl}^2}. \tag{3.90}$$

Since the upcoming CMB B-mode polarisation observation missions aim to achieve a sensitivity $r \approx 10^3$, the parameter region predicting $r \geq 10^{-3}$ is particularly interesting. In our model, we find

$$r \geq 10^{-3} \quad \Longleftrightarrow \quad \epsilon_B \geq \left(\frac{10^{-3}}{r_{\rm vac}} - 1\right)\frac{2}{|\mathcal{F}(m_Q)|^2}. \tag{3.91}$$

3.5.2 Tensor bispectrum

The constraint on the tensor bispectrum in the equilateral limit is also reported as a bound on $f_{\rm NL}^{\rm tens}$ (5);[4]

$$-1100 < f_{\rm NL}^{\rm tens} \equiv \frac{B_h^{RRR}(k,k,k)}{2\sqrt{2}F_\zeta^{\rm eq}(k)} < 1900\,, \qquad (68\%\ \text{C.L.}), \tag{3.92}$$

where $B_h^{RRR}(k_1,k_2,k_3)$ is defined in eq. (3.31) and $F_\zeta^{\rm eq}(k) \equiv (18/5)P_\zeta^2(k)$, evaluated at the pivot scale, $k_{\rm CMB} = 0.05\,{\rm Mpc}^{-1}$ (5). Our model should satisfy these two observational constraints.

From the constraint on $f_{\rm NL}^{\rm tens}$ we find,

$$\epsilon_B \geq \frac{64\,M_{\rm Pl}^4}{27\,H^4}\frac{1100\cdot 18\cdot\Delta_\zeta^2\cdot 4\pi^4\cdot 2\sqrt{2}}{-5\cdot\Upsilon_{\rm eq}(m_Q)}\,, \tag{3.93}$$

$$\epsilon_B \leq \frac{64\,M_{\rm Pl}^4}{27\,H^4}\frac{1900\cdot 18\cdot\Delta_\zeta^2\cdot 4\pi^4\cdot 2\sqrt{2}}{5\cdot\Upsilon_{\rm eq}(m_Q)}\,, \tag{3.94}$$

where the first constraint applies when $\Upsilon_{\rm eq} < 0$ and the second when $\Upsilon_{\rm eq} > 0$.

3.5.3 Consistency of the model

In addition to these observational constraints, we discuss the restriction imposed by self-consistency of the model. Scalar perturbations of the spectator sector have a fatal instability on sub-horizon scale if $m_Q < \sqrt{2}$ (53). Hence we demand $m_Q > \sqrt{2}$ in our model. Since ϵ_B approximately indicates the energy density fraction of the background SU(2) gauge field,

$$\Omega_A \equiv \frac{\rho_Q}{3M_{\rm Pl}^2H^2} = \frac{(\dot{Q}+HQ)^2+g^2Q^4}{2M_{\rm Pl}^2H^2} \simeq \frac{1+m_Q^2}{2m_Q^2}\,\epsilon_B, \tag{3.95}$$

ϵ_B is positive and small. As found in (63), if ϵ_B is too large, its effect on the evolution of the inflaton perturbation significantly alters the spectral index n_s, because ϵ_B contributes to $\dot{H}$ through eq. (3.11). To keep this effect negligible, it is required

$$\epsilon_B(t_*) < 2\times 10^{-2}\,, \tag{3.96}$$

where t_* is the time at which CMB modes leave the horizon. On the other hand, since ϵ_B can be rewritten as $\epsilon_B = m_Q^4H^2/(g^2M_{\rm Pl}^2)$, if one lowers ϵ_B by fixing m_Q and H, one would confront a large self-coupling constant g of the SU(2) gauge fields which leads to a non-negligible backreaction from $SU(2)$ tensor perturbations to the background dynamics. In order to avoid large backreaction, we need to have (52)

$$\epsilon_B > \frac{m_Q^2[\mathcal{B}+\tilde{\mathcal{B}}/(m_Q+m_Q^{-1})]}{24\pi^2}\Big(\frac{H}{M_{\rm Pl}}\Big)^2\,, \tag{3.97}$$

[4]The factor of $2\sqrt{2}$ in the denominator comes from the difference of the normalisation of the polarisation tensors. In (5), $e_{ij}^R(\boldsymbol{k})e_{ij}^R(-\boldsymbol{k}) = 2$ is adopted.

where $\mathcal{B}$ and $\tilde{\mathcal{B}}$ are functions of m_Q given by

$$\mathcal{B}(m_Q) = \int_0^{x_{\rm max}} dx\, x \left|i^\beta W_{\beta,\alpha}(-2ix)\right|^2 , \quad \tilde{\mathcal{B}}(m_Q) = \int_0^{x_{\rm max}} dx\, x^2 \left|i^\beta W_{\beta,\alpha}(-2ix)\right|^2 . \quad (3.98)$$

We also find that equation (3.97) ensures $g \ll 1$ as well, which is preferred for validity of the perturbation series.[5]

3.5.4 Allowed parameter regions

Equations (3.87)–(3.97), together with $m_Q > \sqrt{2}$, give the set of constraints we employ to define the regions in ϵ_B-m_Q plane that are interesting for future CMB experiments. Figures (3.12)–(3.14) show the allowed regions for 3 different choices of H or equivalently $r_{\rm vac} = 10^{-4}$, 10^{-3} and 10^{-2}. As $r_{\rm vac}$ increases, the allowed parameter space shrinks. This is because the upper bound on r implies that the power in the sourced tensor modes cannot be very large if $r_{\rm vac}$ is large.

The bottom right corners in these figures (i.e. regions with a large m_Q and small ϵ_B) are shaded as the parameter spaces with non-negligible backreaction, although this does not mean that these regions are excluded. Rather, it indicates that one needs to perform numerical calculations to take into account backreaction, to study this parameter space (52) (see ref. (63) where the backreaction is numerically incorporated).

We find that there's a general trend in the constraining power of tensor power spectrum and bispectrum. While the power spectrum is better at constraining small m_Q regions, the bispectrum is better at constraining large m_Q regions. This happens because B_h is exponentially more sensitive to m_Q (it has an extra factor of $e^{2\pi(2m_Q+m_Q^{-1})}$ compared to r), and so, a small change in m_Q can easily change B_h by a large factor ($\sim e^{4\pi\Delta m_Q}$). This also has interesting consequences for detectability of the tensor bispectrum, as a large range of bispectra can be generated even for the small range of values of interest, $\sqrt{2} < m_Q \lesssim 4$, making a detection of the tensor bispectrum (in this model) possible in the near future, even if r is small (see figures (3.12)–(3.14)). While even the current constraints on $f_{\rm NL}^{\rm tens}$ are useful for ruling out the top right corners in the figures (i.e. regions with a large m_Q and large ϵ_B), there remains parameter space in which the tensor bispectrum can be observed in the future. It is then natural to ask what range of parameters can be probed in upcoming CMB missions.

To that end we also plot the line for $\sigma(f_{\rm NL}^{\rm tens}) = 1$ in figures (3.12)–(3.14), which is expected to be the target sensitivity of LiteBIRD (M. Shiraishi, private communication). We see that this improved sensitivity will allow us to probe a significant portion of the parameter space with large m_Q and small ϵ_B, which is inaccessible to measurements of r, even if we can measure $r = 10^{-4}$ (figure 3.12, bottom right). Although our present calculation does not ensure that this conclusion stays unchanged when we account for

[5]Strictly speaking, since our setup does not include any $SU(2)$ charged particle, a large g itself is not necessarily problematic. However, if one considers a charged particle, $g \gtrsim 1$ causes a strong coupling problem in that loop effects would alter dynamics of the SU(2) gauge fields.

the backreaction, it might still be true when backreaction is included. We also show the line corresponding to $r_{\rm source} = r_{\rm vac}$. Regions to the left of this line denote regions where the amplitude of the sourced tensor modes is smaller than the amplitude of vacuum tensor of the metric. From figure 3.14 we see that if $r_{\rm vac} = 10^{-2}$, there is a region of intermediate ϵ_B and m_Q values for which $f_{\rm NL}^{\rm tens} > 1$, also if $r_{\rm source} < r_{\rm vac}$. This regime is particularly interesting because one can learn about both vacuum fluctuations of the metric and spectator fields during inflation, by combining the power spectrum and bispectrum. On the other hand, if $r_{\rm vac}$ is smaller, a small $r_{\rm source}$ is accompanied by a small tensor bispectrum as well.

3.6 Scalar perturbations

The SU(2) field can also contribute to ζ. In flat gauge ζ is given by

$$\zeta = \frac{\sum_i \delta\rho_i}{3\sum_i(\rho_i + P_i)} \approx \frac{\Omega_\phi \delta\rho_\phi/\rho_\phi + \Omega_\chi \delta\rho_\chi/\rho_\chi + \Omega_A \delta\rho_A/\rho_A}{2\epsilon}\,, \tag{3.99}$$

where ρ_i, P_i, $\delta\rho_i$, and $\Omega_i = \rho_i/3H^2M_{\rm Pl}^2$ are the energy density, pressure, energy density perturbation, and energy density fraction of $i = (\phi, \chi, A)$. We have used $\rho_\phi + P_\phi = \dot\phi^2 = 2\epsilon H^2 M_{\rm Pl}^2$ and ignored the terms related to the axion and gauge fields in the denominator. The third term in the numerator is suppressed by Ω_A and will be negligible once χ settles into the potential minimum and stops producing SU(2), i.e., $\Omega_A \to 0$. The SU(2) field produces axion perturbations via $t_{ij}+t_{ij} \to \delta\chi$ which, in turn, produces ζ in two ways. One is via the second term in the numerator, and is negligible after inflation as $\Omega_\chi \to 0$. Another channel is production of $\delta\phi$ from $\delta\chi$, producing ζ via the first term in the numerator. This can in principle make a sizeable contribution if m_Q is large; however, for our choice of $3 < m_Q < 4$ the contribution is several orders of magnitude smaller than the vacuum contribution of inflaton. A rough order estimate can be given as below.

Considering the exponential dependence $t_{ij} \approx e^{2m_Q}$ (which includes m_Q dependence of the Whittaker function) and a vertex $g\Lambda/2(\partial_\eta\delta\chi)t_{ij}t_{ij}$ (where $\Lambda \equiv \lambda Q/f$ (129; 52)), the power spectrum of χ is evaluated as $k^3P_{\delta\chi}^{tt}/H^2 \approx g^2(\Lambda/2)^2e^{8m_Q}$. (The vertices that are not proportional to g do not involve one $\delta\chi$ and two tensors.) In addition, the gravitational coupling between $\delta\phi$ and $\delta\chi$ is suppressed by $\sqrt{\epsilon_\phi\epsilon_\chi}$. Then we obtain $k^3P_{\delta\phi}^{tt}/H^2 \approx \epsilon_\phi\epsilon_\chi g^2(\Lambda/2)^2e^{8m_Q} \approx 7.5\times10^{-3}$, where $\epsilon_\phi = 10^{-4}$, $\epsilon_\chi = 10^{-8}$, $g = 10^{-2}$, and $m_Q = 3.45$ ((52), see eq.(3.2) and Fig.2). Therefore this model can produce a significant amount of GWs over a wide range in wavenumbers, while simultaneously satisfying stringent observational constraints on the scalar curvature power spectrum.

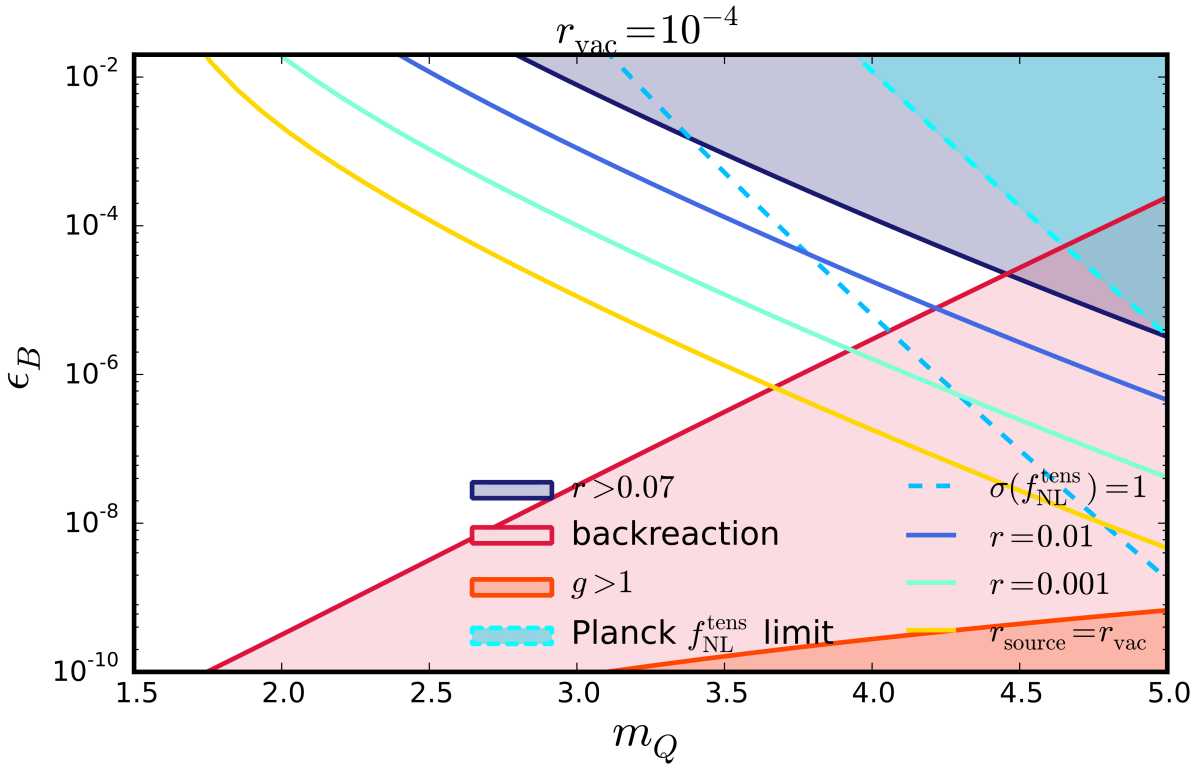

Figure 3.12: Parameter space for gravitational wave production in our model, for $r_{\rm vac} = 10^{-4}$, and for scale-invariant GWs. The blue and magenta shaded regions are excluded by the current upper bound on $f_{\rm NL}^{\rm tens}$ and r (5), respectively. The light red shaded region is not necessarily ruled out but a significant backreaction requires a dedicated numerical treatment to obtain the predictions. In the orange shaded region, the system confronts a strong coupling problem, if one considers $SU(2)$ charged particle. We also show $f_{\rm NL}^{\rm tens} = 1$ as the dashed blue line, because an error of order unity $\sigma(f_{\rm NL}^{\rm tens}) \sim 1$ would be achieved by upcoming CMB B-mode missions. The solid lines denote $r = 10^{-2}$ (blue), 10^{-3} (green) and 10^{-4} (yellow).

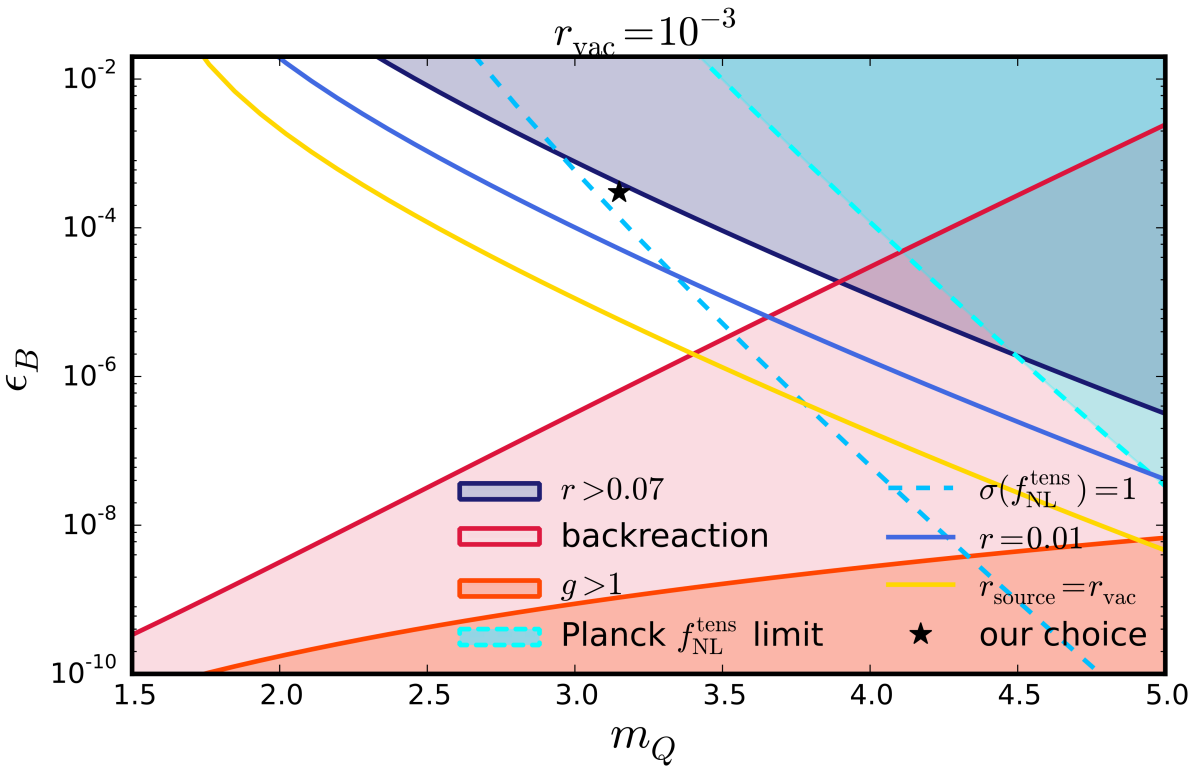

Figure 3.13: Same as figure 3.12 but for $r_{\rm vac} = 10^{-3}$. The black star denotes the parameter choice given in eq. (3.38).

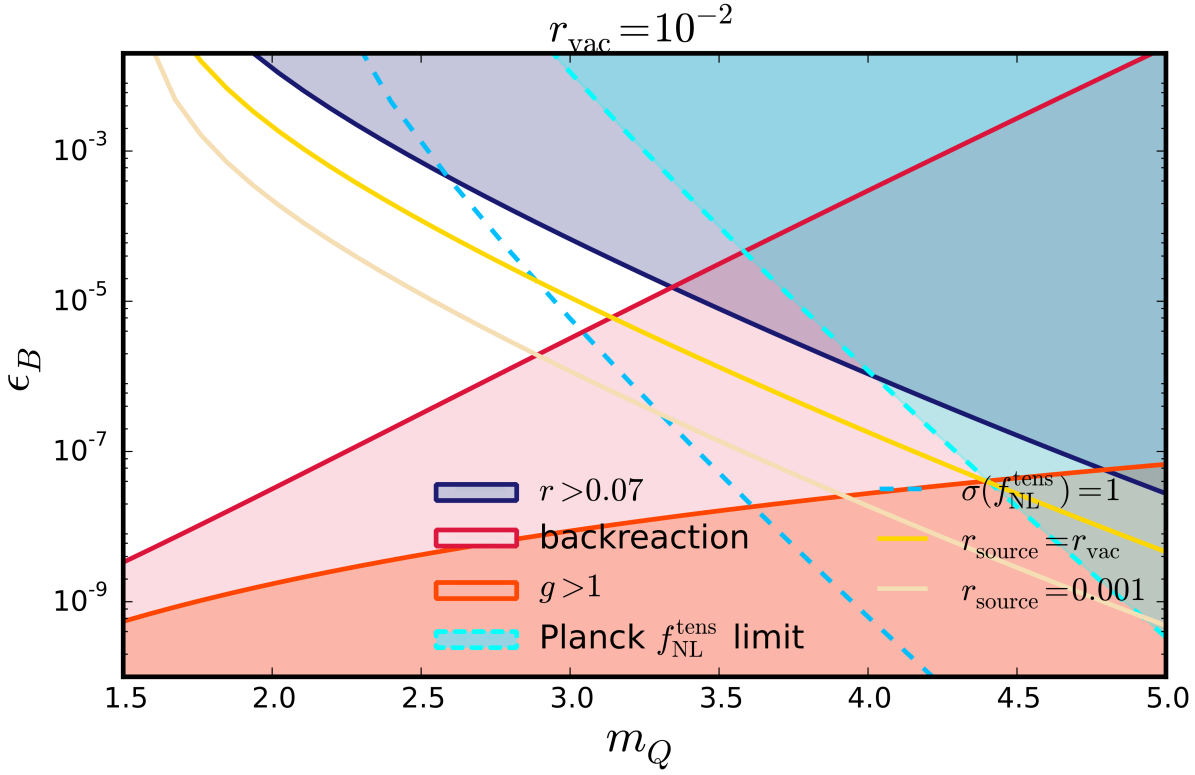

Figure 3.14: Same as figure 3.12 but for $r_{\rm vac} = 10^{-2}$.

3.7 Conclusion

Unification of gravity with the Standard Model has been one of the most sought-after goals of physics for decades now (144). The hope is that all fundamental forces can be subsumed into one grand unified theory (GUT) at high energies, which, in the low-energy limit, reduces to the four different interactions. Such a theory though, is still missing (179) owing to our inability to quantize gravity, in contrast to the three other forces - strong, weak and electromagnetic, which have been successfully quantized. A theory of quantum gravity has been elusive because of various issues, including non-renormalizability (for QFT-like quantum gravity) or other theoretical issues (string theory or loop quantum gravity (35)). Cosmology presents a very powerful (and probably the only) probe of quantum gravity, in the cosmic microwave background (CMB).

Although, we do not yet know how to quantize gravity over an entire spacetime, as detailed in chapter 2, we can quantize its perturbations around a specified background. In this case, the degrees of freedom of the gravitational field, including the transverse traceless tensor modes of the metric, should have ground state vacuum fluctuations (69; 166). These can be found in B-mode polarisation of the cosmic microwave background (CMB) (152; 86); thus, a detection of non-zero (primordial) B-modes is evidence for tensor fluctuations of the metric.

So far, no such evidence has been found (4). CMB experiments provide constraints on the tensor-to-scalar ratio r, which is defined as the ratio of the power in tensor modes ($P_h(k_0)$) to the power in scalar modes ($P_\zeta(k_0)$), at some wavenumber k_0, $r \equiv P_h(k_0)/P_\zeta(k_0)$. Currently, this ratio is constrained to be $r < 0.07$ (95 % C.L.) (4) at $k_0 = 0.05$ Mpc^{-1}.

In this chapter we showed that a detection of B-mode polarisation in the CMB is evidence for primordial tensor perturbations, but is not necessarily evidence for the vacuum fluctuation in the tensor metric. For the standard scenario of single-field slow-roll inflation, the tensor fluctuations of the metric, h_{ij}, obey the equation

$$\Box h_{ij}(t, \boldsymbol{x}) = 0\,, \tag{3.100}$$

where $\Box$ is the d'Alembertian operator in 4-dimensions. Equation (3.100) shows that if we find evidence for tensor fluctuations, in the absence of anything that can source them, they have to be necessarily quantum.

However, there is no *a priori* reason to ignore sources in the right hand side of Equation (3.100). It is reasonable to think that there are (many) more than one field during inflation. While their energy density may be much smaller than that of the dominant inflaton field, they can still act as sources of perturbations. In general, we write

$$\Box h_{ij}(t, \boldsymbol{x}) = \Pi_{ij}(t, \boldsymbol{x})\,, \tag{3.101}$$

and tensor perturbations are sourced by the anisotropic stress-energy Π_{ij}, which is provided by quantum fluctuations of a field other than the metric. These sourced tensor fluctuations can be much larger than the vacuum one and can generate observable B-modes, invalidating the claim that B-modes are evidence for vacuum fluctuations of the metric. Consequently,

there have been intense efforts to build inflation models where a sizeable r can be generated from sources, without violating stringent observational constraints on the scalar perturbation. The sources include scalars (46; 36; 32; 154), U(1) gauge fields (162; 15; 20; 19; 136), and SU(2) gauge fields (112; 54; 8; 7; 110; 52).

In particular, in this chapter we have calculated the bispectrum of tensor perturbations sourced by spectator SU(2) gauge fields during inflation (52). The primary contribution to the bispectrum comes from the self-interaction of the SU(2) gauge fields; thus, it is unique to non-Abelian gauge theory. We find that the amplitude of the bispectrum parametrised by its ratio to the (squared) power spectrum, B_h/P_h^2, is very large, $\sim 1/\epsilon_B$ (10). Since $\epsilon_B \ll 1$, this is much larger than ~ 1 which is predicted for quantum fluctuations of the metric (108; 109).

We also explored parameter space of the model relevant to future CMB missions. Even with an $r_{\rm vac}$ as low as 10^{-4}, large parameter space remains consistent theoretically as well as with the current CMB observations. However, the exponential sensitivity of the power spectrum and bispectrum on model parameters makes it difficult to completely eliminate all the parameter space of the model on the basis of just these observations.

Upcoming CMB missions such as LiteBIRD (117) will measure the CMB polarisation to unprecedented accuracy. This will allow us to not only detect B-modes but also to characterise them, hence testing one of our most ambitious claims about our origins. Vacuum fluctuations of the metric are usually almost scale invariant, with a slightly red tilt (see (87) for the latest review). On the other hand, B-modes from sources can have a red or blue tilt or completely non-power-law spectra such as bumps, depending upon model parameters. Moreover, the tensor fluctuations produced by sources can be chiral (see section 3.2), and so can be seen as a non-vanishing TB/EB correlation in the CMB (145; 127; 171; 104; 68; 65), whereas vacuum fluctuations produce parity-even B-modes. Finally, these modes can be highly non-Gaussian (10). Because tensor modes from vacuum fluctuations of the metric are almost Gaussian (108; 109), non-Gaussianity provides strong evidence for sourced tensor modes. Therefore, if the primordial B-modes arise from quantum fluctuations of the metric, we will find them to be parity invariant, near scale-invariant, and weakly non-Gaussian. If not, we will use the deviations to constrain the fraction of energy density in spectator gauge fields in the inflationary Universe (47; 127; 156; 10).

Chapter 4

Generating Log-normal Mocks in Redshift Space

4.1 Introduction

Deducing robust cosmological constraints from galaxy surveys requires an accurate modelling of the observed two-point correlation function and power spectrum along with their covariance matrices. This is a challenging task because of non-linearity and non-Gaussianity of the galaxy density field. First, non-linear gravitational evolution transforms a nearly Gaussian initial density field into a non-Gaussian one (28), and the galaxy density field is related non-linearly to this non-Gaussian matter density field (*galaxy bias*; see (51) for a review). In addition, the observed galaxy density field differs from the underlying one because of systematics due to peculiar velocity (RSD) and variations in observing conditions across the survey area (window function effect).

Due to these various non-linearities, unlike for the CMB analysis, the Gaussian approximation is no longer valid for computing the covariance matrix of the galaxy two-point statistics. Going beyond the Gaussian approximation, a method based on non-linear perturbation theory including contributions from connected four-point functions can model the non-linear covariance matrix on quasi-linear scales (120; 21). Perturbative approaches break down on small scales where non-linearities are too strong. The gravitational amplification and galaxy bias in these non-linear scales may be fitted by a number of free parameters of effective field theory (24; 37). However, treatment of the mode-coupling effect due to the survey window function (for example, due to sparse sampling of the survey area (39)) requires a full account of modes down to the resolution scale of the survey, set by the number density of the sample: $\bar{n}_g \gtrsim 1/P(k)$, $P(k) \equiv |\delta(\boldsymbol{k})|^2$ being the power spectrum of the overdensity field $\delta(\boldsymbol{x})$.

Cosmological N-body simulations have been the gold standard in modelling non-linearity in the large-scale structure. As phenomena in a wide range of scales are involved in the formation and evolution of galaxies, simulating all the relevant physics of the formation and evolution of galaxies is impractical. Instead, the usual practice is to "paint" galaxies

onto the halos in matter-only simulations by using the halo-occupation distribution (HOD) function estimated from, for example, the angular clustering of the survey (e.g., (70)), or by using Subhalo Abundance Matching (SHAM) with the observed stellar mass function (e.g., (146). With these *mock* galaxy samples from the simulation at hand, the galaxy correlation functions and their covariance matrices can be measured directly from a suite of N-body simulations including various selection effects of the surveys. Even for these matter-only N-body simulations, however, a robust cosmological parameter estimation may demand too large computational resources. This is because estimating the covariance matrix from N-body simulations hampers the cosmological parameter estimation by a factor of $1 + N_b/N_s$, where N_s is the number of N-body simulations and N_b is the number of independent bins used for the estimation of parameters (55). If we were to achieve a percent precision on the covariance matrix, we would need $N_b/N_s = 10^{-2}$. As $N_b \approx 10^2$ for typical survey data, $N_s \approx 10^4$ would be required. This requirement would become more severe in estimating the inverse covariance matrix and its associated errors (see e.g., (75; 137; 153)).

One pragmatic way of bypassing this problem is to simulate gravitational evolution by adopting a set of simplified assumptions. In this approach, one trades accuracy for speed of simulations, especially on small scales. For example, the Zel'dovich simulation (184) captures correct density and velocity fields on large scales where non-linearities are modest; the higher order Lagrangian perturbation theory (LPT (122; 34; 38)) simulations capture non-linearities on progressively smaller scales (44; 119; 89; 170; 128; 90). We refer the readers to Ref. (121) for a recent review and to Refs. (118; 40; 126) for comparisons between different approaches.

In this chapter, we shall take a different approach: instead of modelling the non-linear density evolution, we exploit statistical properties of the non-linear galaxy density field. Specifically, we generate a mock galaxy catalog with the assumption that the probability density function (PDF) of galaxy density fields follows a log-normal distribution. This assumption is based upon the observation that the PDF of log-transformed density fields, $\ln(1+\delta)$ with $\delta \equiv n/\bar{n} - 1$ being the density contrast, measured from N-body simulations roughly matches a Gaussian PDF (43; 45; 91; 29; 173; 155). The evidence for a log-normal PDF does not only come from the matter density fields in simulations, but also from the Dark Energy Survey (DES) science verification data (41) and earlier measurements (79; 181).

Note that log-normality is not merely a statement about the one-point PDF, but it means that the log-transformed field $\ln(1+\delta)$ is a multi-variate Gaussian random field whose statistics are completely specified by its two-point correlation function. For this, the N-body simulation of Ref. (88) has confirmed that the two-point correlation function of matter density fields also roughly matches the prediction of log-normality well into fairly non-linear regime.

In addition, the log-normal mock generator presents the following practical advantages that further motivate our pursuing this approach:

1. It is fast. Since the relation between the density fields and the Gaussian (log-transformed) fields is given by a local transformation (see section 4.3 for more de-

tails), the log-normal mock generator is almost as fast as generating three-dimensional Gaussian random fields. This allows us to quickly generate a large number of mock galaxy distributions.

2. It is direct. The log-normal mock generator takes the observed galaxy two-point correlation function as an input so that we can avoid post-processing steps (halo finding, HOD, for example) connecting the non-linear density field to mock galaxies.

3. It is instructive. Upon assuming log-normal PDF of the galaxy density field, all higher-order correlation functions are given in terms of the two-point correlation function of the log-transformed field (43). This allows us to quantitatively study highly non-linear mode-coupling effects in both the signal and covariance matrix that demand knowledge about the density field on non-linear scales. One such example is mode-coupling due to the survey window function. By using a thousand log-normal mock catalogs, Ref. (39) has quantified the effect from a duplicated, sparse (instead of contiguous) angular selection function, and deduced the optimal analysis strategy.

In this chapter, we extend the real-space log-normal mock generator presented in Ref. (39) by including the velocity field in a consistent manner. We then generate the log-normal mock in redshift space by applying the real-to-redshift space mapping. Again, equipped with perfect knowledge about the statistical properties of the galaxy density and velocity fields, such a mock catalog serves as an excellent test bed for modelling RSD due to this non-linear mapping (148). To test the RSD effect on the two-point statistics of the log-normal mock catalog, we begin with the real-space galaxy two-point correlation function as an input. We use a log-normal PDF to generate a three-dimensional galaxy density field, as well as a matter density field. Finally, we generate a velocity field consistent with the matter density field by using the linearised continuity equation (see section 4.3 for more details). We then measure the galaxy two-point statistics (correlation function and power spectrum) both in real and redshift space, and the pairwise line-of-sight velocity PDFs from the log-normal mock catalog. We also calculate the mean pairwise velocity using log-normal statistics and show that it agrees with the measurement from the catalog.

Our implementation of log-normal galaxy density and velocity fields differs from other log-normal codes such as FLASK (182), CoLoRe (14) and (134). FLASK does not have a prescription for producing a velocity field; hence one has to provide an anisotropic power spectrum when generating density fields in redshift space. CoLoRe generates a velocity field by using linear theory velocities corresponding to the log-transformed field, so the resulting velocities follow a Gaussian PDF. Note that the fact that the velocity field follows a Gaussian PDF does not imply that the pairwise line-of-sight velocity PDF is Gaussian because the pairwise line-of-sight velocity PDF is a pair-weighted quantity (see section 4.2 for more details). In contrast, in this chapter, we use the linearised continuity equation to ensure mass conservation with little additional computing cost compared to the CoLoRe method.

The rest of the chapter is organized as follows. In section 4.2 we present an overview of redshift-space statistics including the two-point correlation function and the pairwise

line-of-sight velocity PDF. In section 4.3 we introduce our method to generate log-normal density and velocity fields. In section 4.4 we present measurements from our log-normal mock catalogs, including two-point statistics in real space (sec. 4.4.1), the cross-correlation coefficient between matter and galaxy fields (sec. 4.4.1), two-point statistics in redshift space (sec. 4.4.2), and pairwise line-of-sight velocity PDFs (sec. 4.4.3); in sec. 4.4.4 we discuss how the streaming model reduces to the Kaiser limit at large separations. We summarize the results in section 4.5. In appendix D, we present a derivation of the streaming model for RSD. In appendix E, we lay out the method that we use to correct for the binning effect when measuring power spectra. In appendix F, we present the details of calculating the mean pairwise line-of-sight velocity from the log-normal mock catalogs. Throughout, we use the following Fourier convention:

$$f(\boldsymbol{k}) = \int d^3x f(\boldsymbol{x}) e^{-i\boldsymbol{k}\cdot\boldsymbol{x}},\ f(\boldsymbol{x}) = \int \frac{d^3k}{(2\pi)^3} f(\boldsymbol{k}) e^{i\boldsymbol{k}\cdot\boldsymbol{x}}\,. \tag{4.1}$$

In this chapter, the term *real* space refers to the contrast with redshift space, and the term *configuration* space refers to the contrast with Fourier space.

4.2 Review of RSD

In spectroscopic galaxy redshift surveys, radial distances to galaxies are inferred from observed spectral shifts containing both the Hubble expansion and peculiar velocities of galaxies along the line-of-sight. The observed positions (redshift space) of galaxies are related to the true positions (real space) of galaxies by

$$\boldsymbol{s} = \boldsymbol{x} + \frac{1}{\mathcal{H}}\boldsymbol{v}(\boldsymbol{x})\cdot\hat{\ell}\,. \tag{4.2}$$

Here, $\boldsymbol{x}$ and $\boldsymbol{s}$ are the comoving coordinates, respectively, in real and redshift space, $\mathcal{H}$ is defined by $\mathcal{H} \equiv aH$ with H being the Hubble expansion rate and a being the scale factor of the universe, $\boldsymbol{v} = d\boldsymbol{x}/d\eta$ is the peculiar velocity of the galaxy with η being the conformal time (related to the time coordinate by $d\eta = dt/a(t)$), and $\hat{\ell}$ is the line-of-sight direction of the galaxy. In this chapter, we shall take the plane-parallel (distant-observer) approximation such that $\hat{\ell} \equiv \hat{z}$ is fixed for all galaxies in the survey.

As a result of the shift in the line-of-sight distance given by equation (4.2), the observed galaxy distribution in redshift space is anisotropically distorted from the underlying real-space distribution. It is anisotropic because the distortion happens only along the line-of-sight direction. Since the number of galaxies in real and redshift space must be the same, we have

$$[1 + \delta_g^s(\boldsymbol{s})]d^3s = [1 + \delta_g(\boldsymbol{x})]d^3x\,, \tag{4.3}$$

where $\delta_g \equiv n_g/\bar{n}_g - 1$ and $\delta_g^s \equiv n_g^s/\bar{n}_g^s - 1$ are the galaxy density contrasts in real and redshift space, respectively. Here, we ignore the time evolution of the mean number density of galaxies so that $\bar{n}_g = \bar{n}_g^s$; this would induce the evolution bias (b_e) contribution in Ref. (83)

which is small for $kr \gg 1$. We then relate the redshift-space density contrast δ_g^s to the real space one δ_g as

$$\delta_g^s(\boldsymbol{s}) = [1 + \delta_g(\boldsymbol{x})]J(\boldsymbol{x}) - 1, \tag{4.4}$$

with the Jacobian of the coordinate transformation

$$J(\boldsymbol{x}) = \left|\frac{d^3x}{d^3s}\right| = \left[1 + \frac{1}{\mathcal{H}}\frac{\partial v_z(\boldsymbol{x})}{\partial z}\right]^{-1}, \tag{4.5}$$

where z refers to the line-of-sight coordinate. Note that the relation above only works when the distant-observer approximation is valid and when the real-to-redshift coordinate mapping [equation (4.2)] is one-to-one; otherwise, the Jacobian would be infinite.

There are two sources of non-linearity in the relationship between real- and redshift-space density contrasts. First, the Jacobian of the mapping, equation (4.5), is a non-linear function of the velocity field. Second, the velocity field itself is non-linear due to gravitational evolution at late times. Ignoring the velocity bias (51) that only affects at galaxy formation scales, we assume that the peculiar velocity is sourced by the underlying matter density fluctuation and that galaxies are moving with the same velocity as matter. With this assumption, the peculiar velocity field is governed by the continuity equation for matter density contrast

$$\frac{\partial \delta_m(\boldsymbol{x})}{\partial \eta} + \nabla \cdot \{[1 + \delta_m(\boldsymbol{x})]\, \boldsymbol{v}(\boldsymbol{x})\} = 0\,, \tag{4.6}$$

and the Euler equation,

$$\frac{\partial \boldsymbol{v}(\boldsymbol{x})}{\partial \eta} + \mathcal{H}\boldsymbol{v}(\boldsymbol{x}) + \boldsymbol{v}(\boldsymbol{x}) \cdot \nabla \boldsymbol{v}(\boldsymbol{x}) = -\frac{3}{2}\mathcal{H}^2\nabla^{-1}\delta(\boldsymbol{x})\,. \tag{4.7}$$

In the large-scale limit, in which the density contrast and the peculiar velocity are small, we can linearise both the Jacobian and the continuity equation to obtain

$$\delta_g^s(\boldsymbol{s}) = b\delta_m^L(\boldsymbol{x}) - \frac{1}{\mathcal{H}}\frac{\partial v_z(\boldsymbol{x})}{\partial z}\,, \quad \boldsymbol{v}(\boldsymbol{k}) = i\mathcal{H}f\frac{\boldsymbol{k}}{k^2}\delta_m^L(\boldsymbol{k})\,, \tag{4.8}$$

where δ_m^L is the linear matter density contrast, $f = \mathrm{d}\ln D/\mathrm{d}\ln a$ is the logarithmic growth rate with D being the linear growth factor, and b is the linear bias factor. Then the linear redshift-space galaxy power spectrum $P_{gg}^s(k, \mu_k)$ becomes

$$P_{gg}^s(k, \mu_k) = \left(b + f\mu_k^2\right)^2 P_m^L(k)\,, \tag{4.9}$$

where $\mu_k = \hat{k} \cdot \hat{z}$ is the cosine of the angle between the line-of-sight and the wave vector $\boldsymbol{k}$, and P_m^L is the linear matter power spectrum. This is the so-called Kaiser formula (85). It is useful to expand the redshift-space power spectrum using the Legendre polynomials $\mathcal{L}_\ell(\mu_k)$,

$$P_{gg}^s(k, \mu_k) = \sum_\ell P_{gg,\ell}^s(k)\mathcal{L}_\ell(\mu_k). \tag{4.10}$$

Non-zero components are monopole, quadrupole, and hexadecapole, which are given respectively by

$$\begin{aligned} P^s_{gg,\ell=0}(k) &= \left(b^2 + \frac{2}{3}bf + \frac{1}{5}f^2\right) P^L_m(k)\,, \\ P^s_{gg,\ell=2}(k) &= \left(\frac{4}{3}bf + \frac{4}{7}f^2\right) P^L_m(k)\,, \\ P^s_{gg,\ell=4}(k) &= \frac{8}{35}f^2 P^L_m(k)\,. \end{aligned} \tag{4.11}$$

The corresponding galaxy two-point correlation function is given in a similar manner as (73; 74):

$$\xi^s_{gg}(s,\mu) = \left(b^2 + \frac{2}{3}bf + \frac{1}{5}f^2\right)\xi_0(s) - \left(\frac{4}{3}bf + \frac{4}{7}f^2\right)\mathcal{L}_2(\mu)\xi_2(s) + \frac{8}{35}f^2\mathcal{L}_4(\mu)\xi_4(s), \tag{4.12}$$

with

$$\xi_\ell(s) \equiv \int \frac{dk}{2\pi^2} k^2 P^L_m(k) j_\ell(ks)\,. \tag{4.13}$$

On very small scales, corresponding to the interior of virialized objects such as galaxy clusters, peculiar velocities are randomly oriented. As a result, the clustering amplitude is reduced along the line-of-sight; this effect is called Fingers-of-God (FoG; (80)), as clusters appear elongated along the line-of-sight direction. The small-scale damping of the power spectrum due to FoG is often modelled by introducing an exponential or a Lorentzian damping factor motivated by the pairwise line-of-sight velocity PDF measured from N-body simulations (148).

On intermediate scales, the Jacobian and the continuity equation cannot be linearised, and galaxies are not in random motion in virialised objects. We thus need to take into account the non-linear effects in the velocity field as well as in the Jacobian. Modelling non-linear RSD has been studied extensively in the literature for the past decade including, for example, standard (Eulerian) perturbation theory (76; 28), Lagrangian perturbation theory (114; 113; 115; 116; 167), effective field theory (101; 138), and the distribution function approach (151; 132; 131; 175; 176; 130). All these methods are based on non-linear perturbation theory and treat both non-linearities in the velocity field and the Jacobian perturbatively. The resummation approaches (169; 177), and the streaming model (135; 49; 60; 148; 174), on the other hand, can accommodate the full non-linearities in the Jacobian. Here, we focus on the streaming model.

The streaming model describes RSD in the galaxy two-point correlation function as a mapping between galaxy pairs in real and redshift space. This method aligns well with the interpretation that the galaxy two-point correlation function is the excess number of pairs over the cosmic mean. Mathematically, denoting the pairwise line-of-sight velocity PDF as $\mathcal{P}(s_\parallel - r_\parallel, \boldsymbol{r})$, that is, in terms of the change in the line-of-sight separation $r_\parallel - s_\parallel \equiv -\Delta v_z/\mathcal{H}$, the redshift-space galaxy two-point correlation function ξ^s_{gg} can be written as

$$1 + \xi^s_{gg}(s_\parallel, s_\perp) = \int dr_\parallel \; [1 + \xi_{gg}(r)]\, \mathcal{P}(s_\parallel - r_\parallel, \boldsymbol{r})\,, \tag{4.14}$$

where ξ_{gg} is the real-space galaxy correlation function. We show a derivation of the streaming model in appendix D, assuming only number conservation and statistical homogeneity of the Universe. Once the pairwise line-of-sight velocity PDF $\mathcal{P}(s_\parallel - r_\parallel, \boldsymbol{r})$ is known accurately, one can map the real-space correlation function into redshift space by equation (4.14). Of course, the linearised streaming model reproduces the linear theory result (60; 82).

The key characteristic of the pairwise line-of-sight velocity PDF is that it is a *pair-weighted* quantity. Ref. (148) (also see appendix D) shows the moment generating function of the pairwise line-of-sight velocity PDF as

$$\mathcal{P}(s_\parallel - r_\parallel, \boldsymbol{r}) = \int \frac{d\gamma}{2\pi} e^{i\gamma(s_\parallel - r_\parallel)} \mathcal{M}(-i\gamma, \boldsymbol{r}), \tag{4.15}$$

$$\mathcal{M}(\lambda, \boldsymbol{r}) = \frac{\left\langle e^{\lambda(v_z(\boldsymbol{x}_1) - v_z(\boldsymbol{x}_2))/\mathcal{H}} \left[1 + \delta_g(\boldsymbol{x}_1)\right] \left[1 + \delta_g(\boldsymbol{x}_2)\right] \right\rangle}{1 + \xi_{gg}(r)}, \tag{4.16}$$

where $\boldsymbol{r} = \boldsymbol{x}_1 - \boldsymbol{x}_2$. We show in figure 4.1 the pairwise line-of-sight velocity PDF of dark matter halos averaged over 160 N-body simulations (141). The box size is 2400 h^{-1} Mpc on a side, and the redshift is $z = 0$. We find that the PDF has a negative mean (vertical dotted lines) and a negative skewness, and the trend is more obvious for smaller separations. In our sign convention, this means that there are more approaching pairs than recessing pairs, which is a consequence of the attractive nature of gravity. For larger separations, linear theory applies so that both the mean pairwise velocity and the skewness get smaller, and the distribution becomes more symmetric. We also find that the mean of the PDF is more negative for larger mass halos.

Several attempts have been made in the literature (33; 174; 178; 142) to model the redshift-space galaxy two-point correlation function by calculating $\mathcal{P}(s_\parallel - r_\parallel, \boldsymbol{r})$ analytically. It is still difficult to predict redshift-space two-point correlation function on all scales without the aid of free parameters. The key issue in modelling the pairwise line-of-sight velocity PDF is its non-Gaussianity; as shown in Ref. (148; 60), the PDF is non-Gaussian even when the density and velocity field follow a Gaussian distribution. As discussed in section 4.4.3, we also find this non-Gaussianity in the log-normal mock catalogs. The pairwise line-of-sight velocity PDFs that we measure from the log-normal catalogs show qualitatively the same features as those from N-body simulations. In both cases we recover the Kaiser limit on large scales. In section 4.4.4 we quantitatively discuss how the streaming model reduces to the Kaiser limit at large separations, for our log-normal mocks, making use of the moments of the measured pairwise line-of-sight velocity PDF.

4.3 Log-normal Catalog Generation

The log-normal distributed density contrast $\delta(\boldsymbol{x})$ is related to a Gaussian (log-transformed) field $G(\boldsymbol{x}) \equiv \ln\left[1 + \delta(\boldsymbol{x})\right] - \langle \ln\left[1 + \delta(\boldsymbol{x})\right] \rangle$ as

$$\delta(\boldsymbol{x}) = e^{-\sigma_G^2 + G(\boldsymbol{x})} - 1\,, \tag{4.17}$$

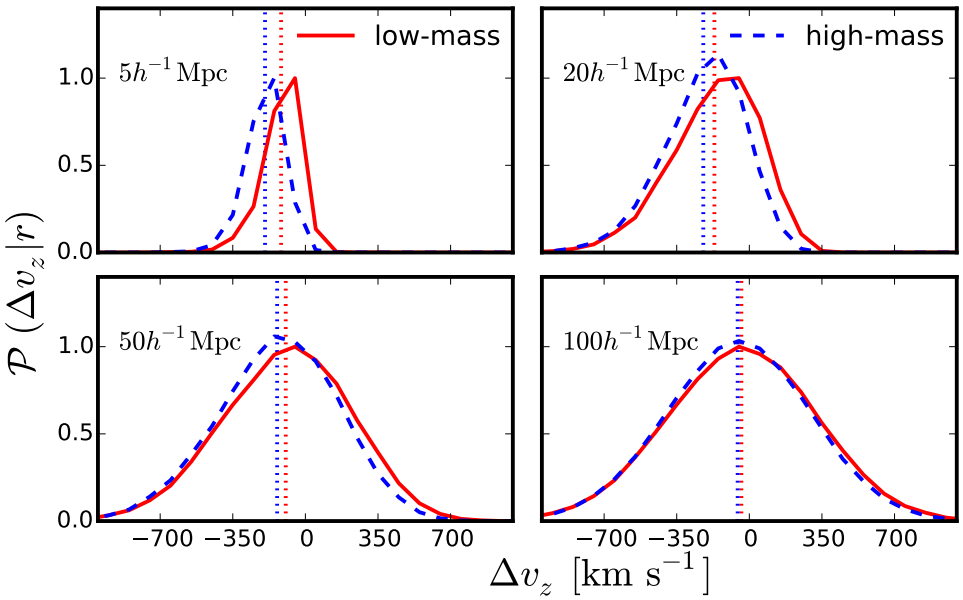

Figure 4.1: Pairwise line-of-sight velocity PDFs averaged over 160 N-body simulations along the line-of-sight ($0.99 \leq \mu \leq 1.0$) for four separations of galaxy pairs: 5.25 h^{-1} Mpc (top left), 20.25 h^{-1} Mpc (top right), 50.25 h^{-1} Mpc (bottom left), and 100.25 h^{-1} Mpc (bottom right). The simulation volume is (2400 h^{-1} Mpc)^3 and the output is at $z = 0$. The red solid and blue dashed lines denote the PDFs for low-mass ($5 \times 10^{13} - 6.5 \times 10^{13}$ $h^{-1}\,M_\odot$) and high-mass ($1 \times 10^{14} - 2.5 \times 10^{14}$ $h^{-1}\,M_\odot$) halos, for which the average halo biases are $b = 1.8$ and 2.5, respectively. Negative (positive) velocities denote galaxy pairs moving towards (away from) each other. The red and blue dashed vertical lines denote the mean pairwise line-of-sight velocity for low-mass and high-mass halos respectively. The PDFs have been normalised to unity, and rescaled such that the maximum of the red lines is unity. For small separations (top panels), there is a small but significant shift towards more negative values for PDFs with a higher mass; for larger separations (bottom panels), the PDFs become more symmetric. However, the mean velocity is still not zero even at separations of $\sim 100h^{-1}$ Mpc.

where the pre-factor with the variance of the Gaussian field $\sigma_G^2 \equiv \langle G^2 \rangle$ ensures that the mean of $\delta(\boldsymbol{x})$ vanishes. Note that the log-normal density fields follow the natural constraint $\delta(\boldsymbol{x}) \geq -1$ of density contrasts by definition. This is not the case for simulations that generate the linear density contrast from Gaussian realisations, although the violation rarely occurs when the variance is small at, e.g., high redshift for setting up the initial conditions of simulations. Applying equation (4.17), one can relate the two-point correlation function of the Gaussian field $\xi^G(r)$ to the two-point correlation function of the density field $\xi(r)$ as (43)

$$\xi^G(r) = \ln\left[1 + \xi(r)\right] . \tag{4.18}$$

Since Gaussian fields of different Fourier modes are uncorrelated, we generate G in Fourier space. To generate a log-normal density field with a given power spectrum $P(k)$, we first Fourier transform the power spectrum to get the target two-point correlation function $\xi(r)$. We then calculate the two-point correlation function of the Gaussian field $\xi^G(r)$ by equation (4.18), and Fourier transform $\xi^G(r)$ to get the power spectrum $P^G(k)$ of G. The Fourier space Gaussian field $G(\boldsymbol{k})$ is generated with (81)

$$G(\boldsymbol{k}) = \sqrt{\frac{P^G(k)V}{2}}\,(\theta_r + i\theta_i) , \tag{4.19}$$

where θ_r and θ_i are Gaussian random variables with unit variance and zero mean, and V is the volume of the simulation. We also enforce $G(-\boldsymbol{k}) = G^*(\boldsymbol{k})$ so that the Gaussian field in configuration space $G(\boldsymbol{x})$ is real. After $G(\boldsymbol{k})$ is generated at each point in the Fourier grid, we use FFTW library (1) to Fourier-transform $G(\boldsymbol{k})$ and obtain $G(\boldsymbol{x})$ on regular cells in configuration space. We then use equation (4.17) to transform $G(\boldsymbol{x})$ into the desired log-normal density contrast $\delta(\boldsymbol{x})$ on each cell, with the variance σ_G measured from $G(\boldsymbol{x})$ in all cells. The resulting density fluctuation $\delta(\boldsymbol{x})$ follows a log-normal distribution with the target power spectrum $P(k)$.

At each cell in configuration space, we calculate the expectation value for the number of galaxies $N_g(\boldsymbol{x}) = \bar{n}_g[1+\delta(\boldsymbol{x})]V_{\rm cell}$, where $\bar{n}_g$ is the global mean galaxy number density and $V_{\rm cell}$ is the volume of the cell. As $N_g(\boldsymbol{x})$ is not an integer, we draw a Poisson random number with the mean $N_g(\boldsymbol{x})$ to obtain the integer number of galaxies in the cell and populate galaxies randomly within the cell. This discretisation is consistent with the nearest-grid-point (NGP) density assignment in the sense that the galaxies are equally spread over the cell.

We next assign velocities to galaxies. For our mock catalogs, we estimate velocities by using the linearised continuity equation of the matter fields:

$$\frac{\partial \delta_m(\boldsymbol{x})}{\partial \eta} + \nabla \cdot \boldsymbol{v}(\boldsymbol{x}) = 0 , \quad \text{or} \quad \boldsymbol{v}(\boldsymbol{k}) = i\mathcal{H}f\frac{\boldsymbol{k}}{k^2}\delta_m(\boldsymbol{k}) . \tag{4.20}$$

As the velocity bias can be ignored at the leading order (51), the velocity of a galaxy follows the local matter velocity. We implement this equation as follows. We take the target matter power spectrum to compute $\delta_m(\boldsymbol{k})$ on Fourier cells following the procedures described above, use equation (4.20) to compute $\boldsymbol{v}(\boldsymbol{k})$ on each Fourier grid, and then

Fourier-transform $\boldsymbol{v}(\boldsymbol{k})$ back into configuration space to obtain $\boldsymbol{v}(\boldsymbol{x})$ on each cell. To ensure that the galaxy overdensities and velocities are correlated, we use the same random seed for G of galaxies and matter. Namely, the phases of $G_g(\boldsymbol{k})$ and $G_m(\boldsymbol{k})$ are identical; however, this does not imply that the phases of $\delta_g(\boldsymbol{k})$ and $\delta_m(\boldsymbol{k})$ are identical, as we show in section 4.4.1. Finally, we assign the same velocity to all galaxies within one cell.

The target galaxy and matter power spectra can be chosen freely. We need a galaxy bias model (51) to find the matter power spectrum that is consistent with the chosen galaxy power spectrum. In this chapter, we use a linear bias relation between the matter and galaxy power spectra, $P_{gg}(k) = b^2 P_{mm}(k)$, with the linear bias parameter b. One important feature of the log-normal catalogs is that even though the target galaxy and matter power spectra are linearly related, the density fields are not proportional to each other (see section 4.4.1). Also, while the galaxy power spectrum and the matter power spectrum are linearly related, the power spectra of their corresponding Gaussian fields are not proportional to each other because

$$\ln[1 + b^2\xi(r)] \neq b^2 \ln[1 + \xi(r)]\,. \tag{4.21}$$

We generate 50 log-normal mock catalogs in a cubic volume with $L_{\rm box} = 1000\ h^{-1}$ Mpc, and 1024^3 grids for the Fourier transformation. This corresponds to the Nyquist frequency of $k_{Ny} = 3.22\ h$ Mpc^{-1}. The catalogs are generated at $z = 1.3$, and each catalog contains roughly 2.1 million galaxies. We compute the input galaxy power spectrum from the linear matter power spectrum using Eisenstein and Hu's fitting function (57) and the linear galaxy bias $b = 1.455$. We assume a flat ΛCDM model with $\Omega_m = 0.272$, $n_s = 0.963$, $A = 2.1 \times 10^{-9}$. The outcome of this mock generator is a set of positions and velocities of galaxies in three-dimensional space with the target galaxy power spectrum. We shall present detailed tests on the output catalogs in section 4.4.

4.4 Validation of the Log-normal Mocks

In this section, we present the results of the log-normal mock generator. We start from the two-point statistics in real space (section 4.4.1) and then move onto the redshift space correlation function (section 4.4.2), the pairwise velocity PDF (section 4.4.3) and recovery of the Kaiser limit on large scales (section 4.4.4).

4.4.1 Real-space density statistics

Two-point Statistics

We first measure the real-space two-point statistics: power spectrum and two-point correlation function. As we have pointed out earlier, our log-normal catalogs populate galaxies randomly in each cell, and this is equivalent to adopting the NGP mass assignment scheme. To be consistent, we use NGP with the same grid number to estimate the galaxy density contrast for Fast Fourier Transform (FFT). In this way, we recover the input target power

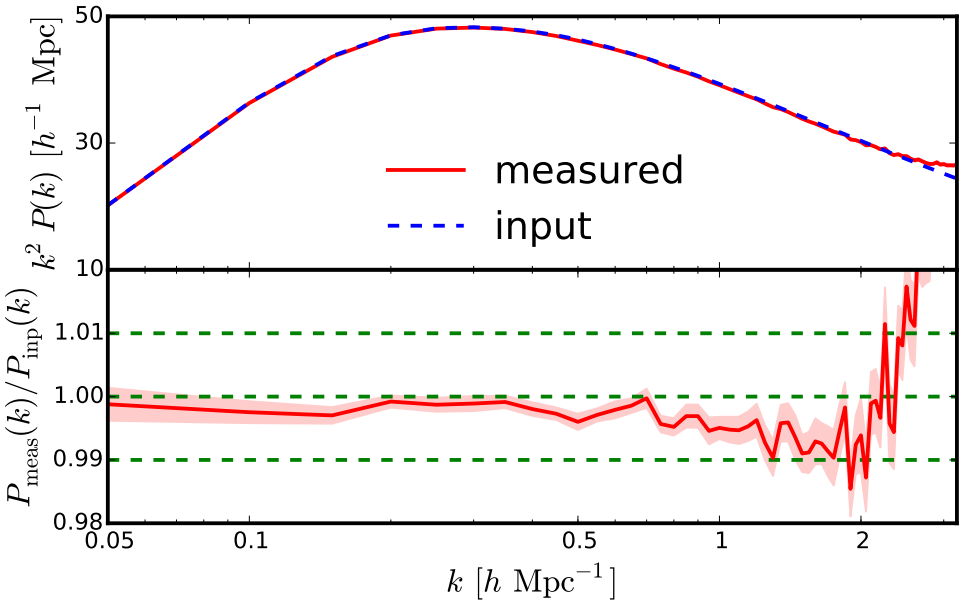

Figure 4.2: (*Top*) Mean of the real-space galaxy power spectrum measured from 50 log-normal catalogs (solid) and the input power spectrum (dashed). We show $k^2P(k)$. (*Bottom*) Ratio of the two. The band shows the error on the mean estimated from 50 realisations. The Nyquist frequency for these measurements is $k_{\rm Ny} = 3.22\,h$ Mpc^{-1}.

spectrum (having subtracted a constant shot noise $= 1/\bar{N}$, $\bar{N}$ denoting the number density of galaxies), without needing to deconvolve the window function due to the density assignment (84). Should we use a different mesh number or density assignment scheme (such as Cloud-In-Cell), we would have to correct for the window function effects by applying an appropriate deconvolution.

Figure 4.2 shows the comparison between the input power spectrum and the power spectrum averaged over 50 log-normal realisations (top), and the ratio of the two (bottom). The band shows the error on the mean estimated from 50 realisations. We find an excellent agreement between the measured and input power spectra for $k \lesssim 2\ h$ Mpc^{-1}. Note that, when comparing the measurement and prediction we need to take special care to calculate the correct *effective* wavenumber by which each bin of the measured power spectrum is represented; this is because the binned power spectrum is averaged over many different wavenumbers that fall into the binning criteria. This effect is particularly important on large scales where the number of Fourier modes is small. We present the details of this correction in appendix E.

We measure the galaxy two-point correlation function by using the Landy-Szalay estimator (97)

$$\xi(\boldsymbol{r}) = \frac{DD(\boldsymbol{r}) - 2DR(\boldsymbol{r}) + RR(\boldsymbol{r})}{RR(\boldsymbol{r})}\,, \tag{4.22}$$

where $DD(\boldsymbol{r})$, $DR(\boldsymbol{r})$, and $RR(\boldsymbol{r})$ are the number of galaxy-galaxy, galaxy-random, and

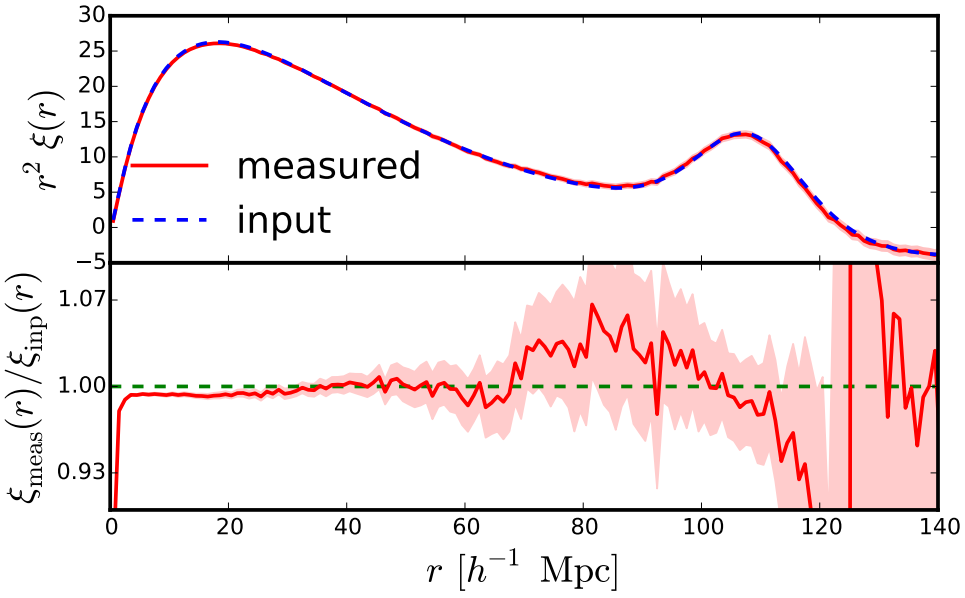

Figure 4.3: Same as figure 4.2 but for the correlation function. We show $r^2\xi(r)$. The spikes at $r \approx 120 - 130\ h^{-1}$ Mpc in the bottom panel corresponds to the zero crossing of the correlation function so a small deviation in the mean of the measured correlation function leads to a large ratio. We use a bin size of $1\,h^{-1}$ Mpc.

random-random pairs, respectively. The Landy-Szalay estimator cancels the leading order uncertainties in estimating the mean number density. Figure 4.3 shows the average of the measured correlation function (top) and the ratio to the input (bottom). We also find an excellent agreement between the measured and input correlation functions over a wide range of scales.

Cross-Correlation Coefficient

We next examine the cross-correlation coefficient

$$r(k) = \frac{P_{gm}(k)}{\sqrt{P_{gg}(k)P_{mm}(k)}}\,, \tag{4.23}$$

between matter and galaxy density contrasts in real space. Here, $P_{gm}(k)$ denotes the cross power spectrum of galaxy and matter. In figure 4.4, the red solid line in the top panel shows the measured cross-correlation coefficient $r(k)$ from the log-normal mock catalogs. The measured cross-correlation coefficient approaches unity on large scales, but decreases on small scales with high significance, despite the fact that we have imposed a linear bias relation between the galaxy and matter power spectra, $P_{gg}(k) = b^2 P_{mm}(k)$, and that the random realisations of G_g and G_m have been drawn from an identical random seed. This result is a generic feature of log-normal fields that the proportionality relation in power spectra does not guarantee the proportionality of the fields (182).

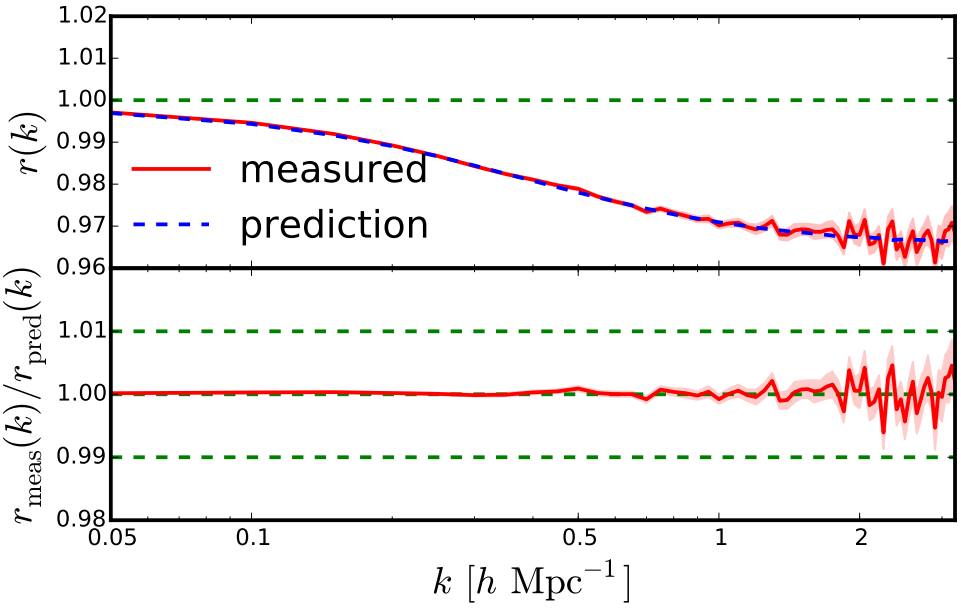

Figure 4.4: (Top) Measured (red solid) and predicted (blue dashed) cross-correlation coefficient as a function of the wavenumber. The red band shows the error on the mean measured from 50 log-normal mock catalogs. (Bottom) Ratio of the measured to the predicted cross-correlation coefficients.

Because, in our mock, the Gaussian (log-transformed) fields of galaxy and matter have the same random numbers ($\theta_r + i\theta_i$ in equation (4.19)), they are related to each other in every Fourier cell as

$$\frac{G_g(\boldsymbol{k})}{G_m(\boldsymbol{k})} = \sqrt{\frac{P^G_{gg}(k)}{P^G_{mm}(k)}}\,, \tag{4.24}$$

where $P^G_{mm}(k)$ and $P^G_{gg}(k)$ are the power spectra of G_m and G_g, respectively. Indeed, it is the cross-correlation coefficient between G_m and G_g that is equal to unity. On the other hand, the galaxy and matter density fields $\delta_g(\boldsymbol{x})$ and $\delta_m(\boldsymbol{x})$ are exponentially related to $G_g(\boldsymbol{x})$ and $G_m(\boldsymbol{x})$. That is, $\delta_g(\boldsymbol{k})$ and $\delta_m(\boldsymbol{k})$ are not linearly related to each other so that the cross-correlation coefficient must deviate from one (182). On large scales where the correlation functions are small, the cross-correlation approaches unity because δ's are approximately the same as G's.

We can compute $r(k)$ analytically for log-normal density fields. Specifically, using the one-dimensional Fourier transform we first compute the galaxy-matter cross spectrum as

$$P_{gm}(k) = \int dr\; r^2 \xi_{gm}(r) j_0(kr) = \int dr\; r^2 \left[e^{\xi^G_{gm}(r)} - 1\right] j_0(kr)\,, \tag{4.25}$$

where $j_0(x)$ is the spherical Bessel function of the zeroth order, and $\xi_{gm}(r) = \langle \delta_g(\boldsymbol{x} + \boldsymbol{r})\delta_m(\boldsymbol{x})\rangle$ and $\xi^G_{gm}(r) = \langle G_g(\boldsymbol{x} + \boldsymbol{r})G_m(\boldsymbol{x})\rangle$. The relation between $\xi_{gm}(r)$ and $\xi^G_{gm}(r)$ is

analogous to equation (4.18). We then compute $\xi^G_{gm}(r)$ as

$$\begin{aligned}\xi^G_{gm}(r) &= \int \frac{d^3k_1}{(2\pi)^3}\frac{d^3k_2}{(2\pi)^3}\langle G_g(\boldsymbol{k}_1)G^*_m(\boldsymbol{k}_2)\rangle e^{i[\boldsymbol{k}_1\cdot(\boldsymbol{x}+\boldsymbol{r})-\boldsymbol{k}_2\cdot\boldsymbol{x}]} \\ &= \int \frac{d^3k_1}{(2\pi)^3}\frac{d^3k_2}{(2\pi)^3}\sqrt{\frac{P^G_{gg}(k_1)}{P^G_{mm}(k_1)}}\langle G_m(\boldsymbol{k}_1)G^*_m(\boldsymbol{k}_2)\rangle e^{i[(\boldsymbol{k}_1-\boldsymbol{k}_2)\cdot\boldsymbol{x}+\boldsymbol{k}_1\cdot\boldsymbol{r}]} \\ &= \int \frac{dk}{2\pi^2}k^2\sqrt{P^G_{gg}(k)P^G_{mm}(k)}j_0(kr)\,. \end{aligned} \tag{4.26}$$

Combining equations (4.25)–(4.26), $r(k)$ can be evaluated. The blue dashed line in the top panel of figure 4.4 shows the prediction, whereas the bottom panel shows the ratio between the measurement and the prediction. We find an excellent agreement between the measurement and the prediction.

4.4.2 Redshift-space density statistics

We now present the measurements of the two-point statistics in redshift space. We obtain the redshift-space mock catalogs from the real-space ones by mapping real-space positions of galaxies to redshift-space positions by equation (4.2). We use the periodic boundary condition along the z-direction for galaxies that move out of the box by this mapping. Measurements of the power spectrum or correlation function for these redshift-space catalogs proceed in the same manner as in real space.

As described in section 4.2, when linearising the Jacobian, the redshift-space power spectrum is given by

$$P^s_{gg}(k,\mu_k) = P_{gg}(k) + 2\mu_k^2 f P_{gm}(k) + \mu_k^4 f^2 P_{mm}(k). \tag{4.27}$$

When using linear theory (that we shall call "Kaiser"), we relate the galaxy-galaxy power spectrum and galaxy-matter power spectrum to the matter-matter power spectrum as $P_{gg}(k) = b^2 P_{mm}(k)$ and $P_{gm}(k) = bP_{mm}(k)$. We stress, however, that the galaxy-matter cross power spectrum $P_{gm}(k)$ is not equal to $bP_{mm}(k)$ for the log-normal density fields, as shown in section 4.4.1. Therefore, in order to highlight the effect from non-linearity in the Jacobian, we calculate the redshift-space galaxy power spectrum with equation (4.27) but use the cross power spectrum in section 4.4.1 (that we call "linear Jacobian").

Figures (4.5)–(4.6) show the measured monopole and quadrupole power spectra, compared with the Kaiser (with $P_{gm}(k) = bP_{mm}(k)$) and the linear Jacobian (with measured $P_{gm}(k)$) predictions. On large scales (small k), we find a good agreement for all three cases as expected. On small scales, the linear Jacobian calculation deviates from the Kaiser value due to the non-unity cross-correlation between the matter and galaxy (section 4.4.1). The deviation is smaller than what we find in figure 4.4 because $f/b = 0.616$ is less than unity.

Both the Kaiser and linear Jacobian calculations fail to model the measured monopole and quadrupole power spectra on small scales. As we use the real-space power spectrum

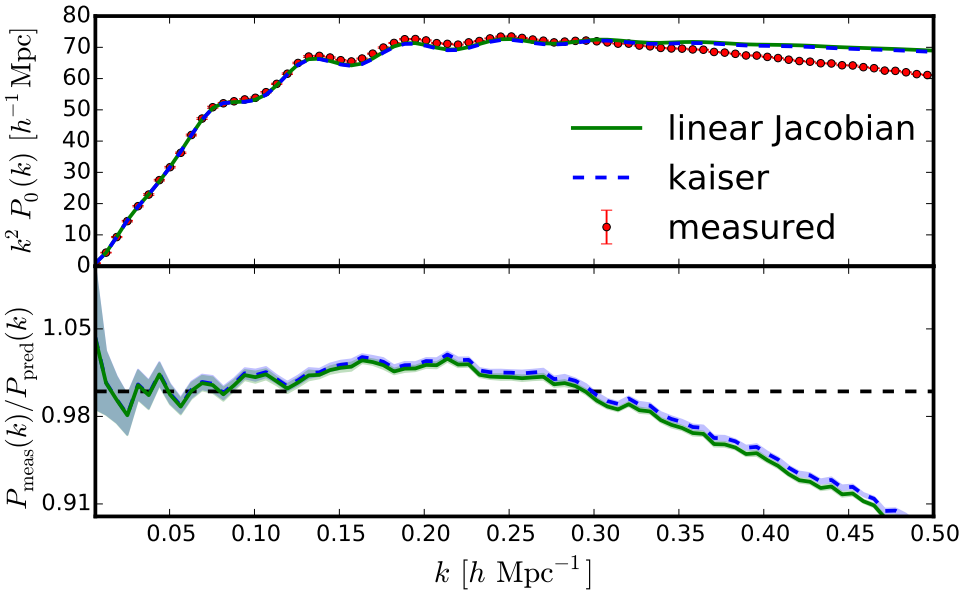

Figure 4.5: (Top) Monopole redshift-space power spectrum. The red solid line shows the measurement averaged over 50 log-normal mock catalogs. The blue dashed line shows the Kaiser prediction while the green dash-dotted line shows the linear Jacobian prediction. We show $k^2P_0(k)$ to enhance differences at large k. (Bottom) Ratio of the measured monopole power to the Kaiser and linear Jacobian predictions. The band shows the error on the mean estimated from 50 realisations. We find a sub-1% agreement on scales $k \lesssim 0.1\ h\ \mathrm{Mpc}^{-1}$.

used to generate the log-normal catalog in each term in equation (4.27), any discrepancy that we find in figures (4.5)–(4.6) is due to non-linearity in the mapping between real and redshift space. That is, when densities and velocities become large, the Jacobian cannot be linearised, and so the linear Jacobian approximation is no longer valid. For example, the measured monopole power spectrum in figure 4.5 is smaller than the linear Jacobian calculation on small scales ($k > 0.3\,h\,\mathrm{Mpc}^{-1}$). This behaviour is qualitatively similar to the FoG damping effect, which is usually attributed to RSD of random motion within bigger halos. In our log-normal mock catalog, however, the damping cannot be the FoG effect because we do not include any random component when generating peculiar velocities. Rather, the power suppression we see here originates solely from non-linearity in the Jacobian of real-to-redshift mapping due to *coherent* peculiar velocity fields given by the continuity equation.

Mathematically, combining equations (4.4)–(4.5) yields the the non-linear mapping between the real- and redshift-space density contrasts

$$1 + \delta_g^s(\boldsymbol{s}) = \frac{1 + \delta_g(\boldsymbol{x})}{\left|1 + \frac{1}{\mathcal{H}}\frac{\partial v_z(\boldsymbol{x})}{\partial z}\right|}\,, \tag{4.28}$$

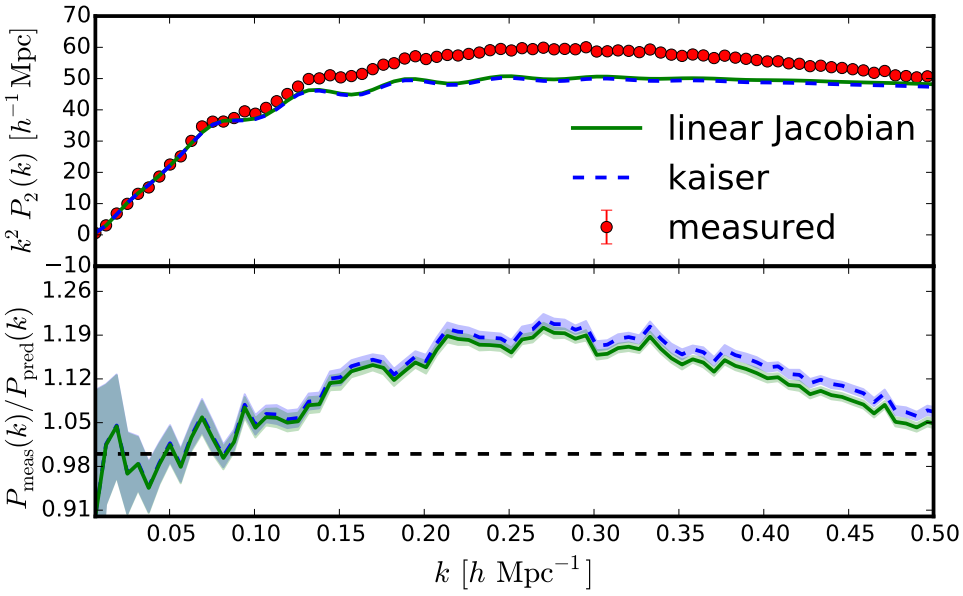

Figure 4.6: Same as figure 4.5, but for the quadrupole power spectrum.

which turns to, in Fourier space (169),

$$\delta_g^s(\boldsymbol{k}) = \int d^3x\, e^{-i\boldsymbol{k}\cdot\boldsymbol{x}} \left[\delta_g(\boldsymbol{x}) - \frac{1}{\mathcal{H}}\frac{\partial v_z(\boldsymbol{x})}{\partial z}\right] e^{ik_z v_z(\boldsymbol{x})/\mathcal{H}}\,. \tag{4.29}$$

As long as velocities are small, i.e. $k_z v_z \ll 1$, the exponential factor in equation (4.29) can be approximated to unity, leading to the linear Jacobian formula. However, on small scales, this approximation breaks down, and the exponential factor leads to the non-linear Jacobian effects (169).

We show the configuration-space two-point correlation function in figures (4.7)–(4.8), and compare them with the linearised Jacobian prediction:

$$\delta_g^s(\boldsymbol{s}) = \delta_g(\boldsymbol{x}) - \frac{1}{\mathcal{H}}\frac{\partial}{\partial z} v_z(\boldsymbol{x})\,. \tag{4.30}$$

Combining with the linear continuity equation that we use to generate the velocity field,

$$\boldsymbol{v}(\boldsymbol{x}) = -\mathcal{H} f \nabla\left[\nabla^{-2}\delta_m(\boldsymbol{x})\right], \tag{4.31}$$

we find the configuration space expression for the redshift-space density contrast:

$$\delta_g^s(\boldsymbol{s}) = \delta_g + f\left(\frac{\partial}{\partial z}\right)^2\left[\nabla^{-2}\delta_m(\boldsymbol{x})\right], \tag{4.32}$$

from which we calculate

$$\begin{aligned}\xi_{gg}^s(s,\mu) \;&=\; \left[\xi_{gg}(s) + \frac{2}{3}f\xi_{gm}(s) + \frac{1}{5}f^2\xi_{mm}(s)\right] \\ &- \left[\frac{4}{3}f\xi_{gm,2}(s) + \frac{4}{7}f^2\xi_{mm,2}(s)\right]\mathcal{L}_2(\mu) + \frac{8}{35}f^2\xi_{mm,4}(s)\mathcal{L}_4(\mu).\end{aligned} \tag{4.33}$$

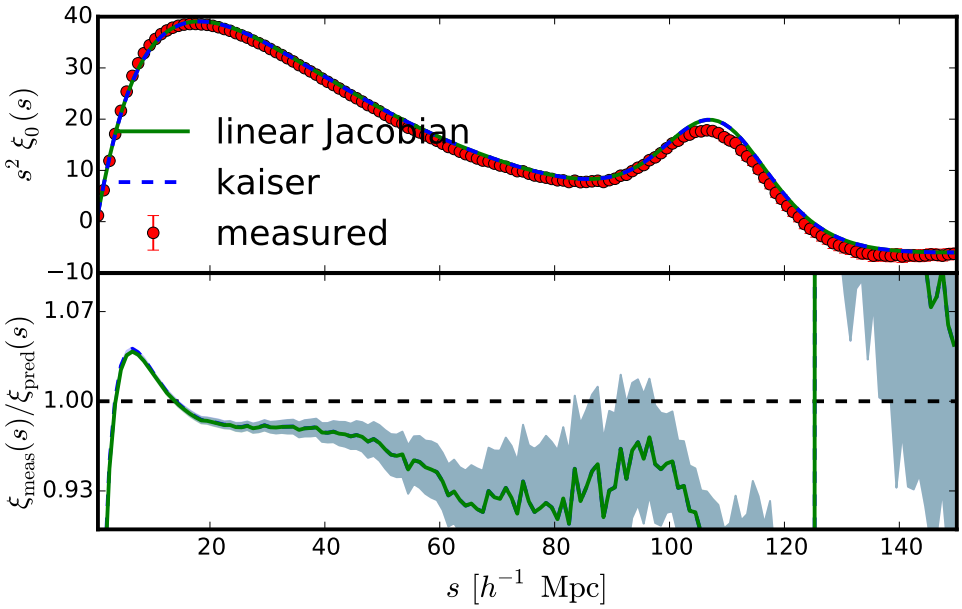

Figure 4.7: (Top) Monopole redshift-space two-point correlation function. The meaning of the lines is the same as in figure 4.5. We show $s^2\xi_0(s)$ to enhance differences on large separations. (Bottom) Ratio of the measured monopole correlation function to the Kaiser and linear Jacobian predictions.

Just like the case for the power spectrum, the expression reduces to the linear Kaiser prediction (equation (4.13)) when we set $\xi_{gm}(r) = b\xi_{mm}(r)$, but we must take into account non-unity cross-correlation function for the log-normal catalog.

While the Kaiser and linear Jacobian models are reproduced in the power spectrum at $k \lesssim 0.1\ h\ \mathrm{Mpc}^{-1}$, they are not well reproduced in the correlation functions at all separations. This indicates that the correlation functions at large separations are sensitive to non-linearity in the Jacobian.

4.4.3 Pairwise Line-of-Sight Velocity PDFs

How do we incorporate non-linearity in the Jacobian into the model? As discussed in section 4.2, the pairwise line-of-sight velocity PDF fully describes the mapping from the real-space two-point correlation function to the redshift-space one.

We show in figure 4.9 the PDFs of pairwise line-of-sight velocity averaged over 50 log-normal mock catalogs, for four different separations between galaxy pairs (*From top left to bottom right*, 5.25, 20.25, 50.25, and 100.25 h^{-1} Mpc) along the line-of-sight direction ($0.99 \leq \mu \leq 1$). We show the pairwise line-of-sight velocity PDFs along the line-of-sight direction because the relative peculiar velocities are at their maximum (i.e., no perpendicular component). For the streaming model, we need the relative velocity PDFs for galaxy pairs along all directions.

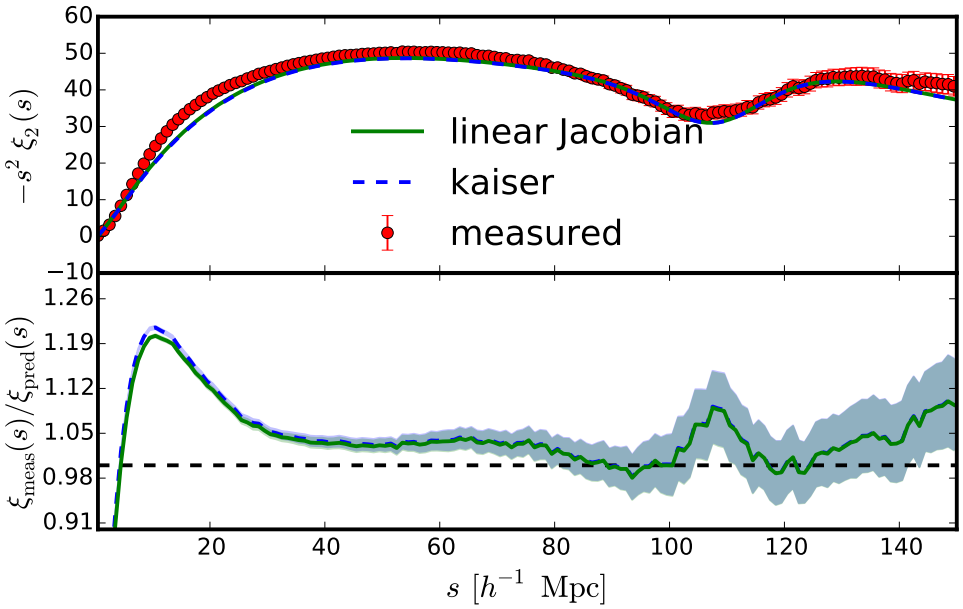

Figure 4.8: Same as figure 4.7, but for the quadrupole two-point correlation function. We show $-s^2\xi_2(s)$.

We show the measured pairwise line-of-sight velocity PDFs for two different linear biases $b = 1.455$ (low-mass) and 2 (high-mass) as, respectively, the blue dashed lines and the red solid lines. Note that we use the same phases (that is, the same sequence of random numbers) for generating velocity fields for both cases; thus, galaxies in the same cell have identical velocities regardless of the assumed bias parameter. Overall, we find that the pairwise line-of-sight velocity PDFs from our log-normal mock catalogs capture qualitative features that we have seen in N-body simulations (figure 4.1). Namely, both PDFs have negative mean velocity and negative skewness for smaller separations (top panels of figure 4.9 and figure 4.1) and approach a symmetric PDF for larger separations. Also, the tendency is more obvious for high-mass (high-bias) galaxies. The log-normal catalogs show larger velocity dispersion than N-body simulations especially at small separations.

Our results show that the coherent irrotational velocity given by the linearised continuity equation can explain a part of the non-linear features in the pairwise line-of-sight velocity PDF. We stress, again, that we do not include any random velocities. Also note that we have assigned the same velocity to all galaxies in the same cell, and the velocity field is exactly the same for the high-mass and low-mass samples. Nevertheless, the pairwise line-of-sight velocity PDF for galaxies with different biases are still different due to pair weighting: velocities of galaxies with high (low) bias are weighted higher (lower) density regions.

While successful at a qualitative level, the PDFs from log-normal catalogs and those from N-body simulations are different in detail. For example, the velocity field in our log-normal mock catalogs only reflects non-Gaussianity of the log-normal density fields, which

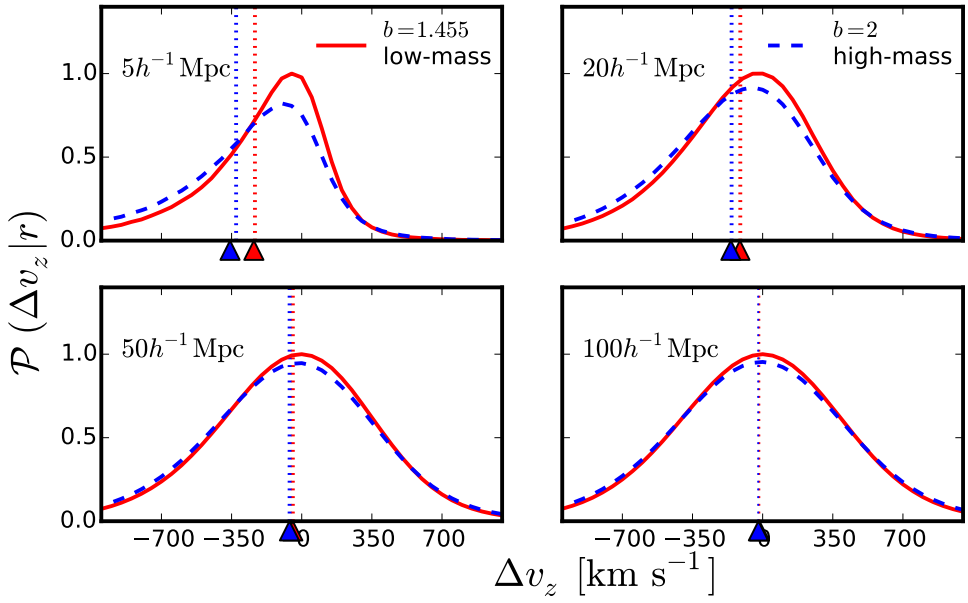

Figure 4.9: Same as figure 4.1, but for PDFs averaged over 50 log-normal mock catalogs. The simulation volume is (1000 h^{-1} Mpc)^3 and the output is at $z = 1.3$. The biases of low- and high-mass catalogs are $b = 1.455$ (red) and 2 (blue), respectively. The triangles on the horizontal axes show the calculations from equation (4.35).

is not the same as that in N-body simulations where the complete non-linear gravitational evolution is encoded.

Strong non-Gaussianity in the pairwise line-of-sight velocity PDF makes it challenging to analytically compute its full moments, even if the velocity field is assumed to follow the linear continuity equation. Nevertheless, we can still compute the mean pairwise line-of-sight velocity (that is, the first moment) as follows. Using the linearised continuity equation (equation (4.8)), the parallel component of relative velocity for galaxies separated by r is given by

$$v_{1z} - v_{2z} = i\mathcal{H}f \int \frac{d^3k}{(2\pi)^3} \frac{k_z}{k^2} \delta_m(\boldsymbol{k}) \left(e^{i\boldsymbol{k}\cdot\boldsymbol{x}_1} - e^{i\boldsymbol{k}\cdot\boldsymbol{x}_2} \right) . \tag{4.34}$$

Because the parallel relative velocity is the exponent in the velocity generating function (equation (4.15)), the mean pairwise line-of-sight velocity can be calculated from

$$\begin{aligned} \langle \Delta v_z \rangle = \mathcal{H} \left. \frac{\partial M(\lambda, \boldsymbol{r})}{\partial \lambda} \right|_{\lambda=0} &= \frac{\langle (v_{1z} - v_{2z}) \left[1 + \delta_{g1}\right] \left[1 + \delta_{g2}\right] \rangle}{1 + \xi_{gg}(r)} \\ &= i\mathcal{H}f \frac{\int d^3x' q(\boldsymbol{x}'_1, \boldsymbol{x}'_2) \left\langle \left[1 + \delta_{g1}\right] \left[1 + \delta_{g2}\right] \delta_{m3} \right\rangle}{1 + \xi_{gg}(r)} , \end{aligned} \tag{4.35}$$

where $\boldsymbol{x}'_i \equiv \boldsymbol{x}_i - \boldsymbol{x}'$, $\delta_{m3} = \delta_m(\boldsymbol{x}')$, and

$$q(\boldsymbol{x}'_1, \boldsymbol{x}'_2) \equiv \int \frac{d^3k}{(2\pi)^3} \frac{k_z}{k^2} \left(e^{i\boldsymbol{k}\cdot\boldsymbol{x}'_1} - e^{i\boldsymbol{k}\cdot\boldsymbol{x}'_2} \right) . \tag{4.36}$$

The triangles on the horizontal axes in figure 4.9 show the predictions computed from equation (4.35). We find that they are in an excellent agreement with the measurements. As shown in equation (4.35) the mean of the pairwise line-of-sight velocity depends on the integral of the three-point function of the log-normal fields. We present the details of this calculation in appendix F.

Likewise, in order to compute the nth-order moments of the pairwise line-of-sight velocity we need to integrate over $(n+2)$-point correlation functions of the log-normal fields. Thus, it is impractical to compute all the moments of the pairwise line-of-sight velocity PDF, even though the statistics of log-normal fields are known. On the other hand, should we assume a Gaussian PDF for the pairwise line-of-sight velocity distribution, all the higher-order moments but the first two would be ignored; thus, we miss the non-Gaussian effects coming from non-linear evolution of the Universe as well as the pair weighting effect.

4.4.4 Recovery of Kaiser limit

Even though the pairwise velocity PDF in our log-normal mocks does not precisely reproduce the velocity PDF from N-body simulations, the redshift space power spectrum from both matches the Kaiser prediction on large scales ($k \lesssim 0.1\,h$ Mpc^{-1}). To understand why this happens, we now consider the redshift space two-point correlation function in the large-scale limit, i.e. separations such that only the linear order terms contribute.

The large-scale limit of the redshift space two-point correlation function (to linear order) is given as (60)

$$\xi^s_{gg}(s_\parallel, s_\perp) = \xi_{gg}(s) - \frac{\mathrm{d}}{\mathrm{d}r_\parallel}\left[v_{12}(r)\frac{r_\parallel}{r}\right]\Big|_{r_\parallel=s_\parallel} + \frac{1}{2}\frac{\mathrm{d}^2}{\mathrm{d}r_\parallel^2}\left[\sigma^2_{12}(r,\mu)\right]\Big|_{r_\parallel=s_\parallel}, \tag{4.37}$$

where $s^2 \equiv s_\parallel^2 + s_\perp^2$, $r^2 \equiv s_\perp^2 + r_\parallel^2$, $v_{12}(r)$ is the mean of the radial pairwise velocity (which is the relative velocity projected along the line joining the pair of particles; we call the remaining component tangential pairwise velocity), and $\sigma^2_{12}(r,\mu)$ is the variance of the line-of-sight pairwise velocities, with $\mu \equiv r_\parallel/r$.

In linear theory, the mean and variance can be calculated as

$$v_{12}(r) = -\frac{\mathcal{H}fb}{\pi^2}\int dk k P_{\rm mm}(k) j_1(kr)\,, \tag{4.38}$$

$$\sigma^2_{12}(r,\mu) = 2[\sigma_v^2 - \mu^2\Psi_\parallel - (1-\mu^2)\Psi_\perp]\,, \tag{4.39}$$

$$\Psi_\parallel(r) = \frac{\mathcal{H}^2 f^2}{2\pi^2}\int dk P_{\rm mm}(k)\left[j_0(kr) - \frac{2j_1(kr)}{kr}\right], \tag{4.40}$$

$$\Psi_\perp(r) = \frac{\mathcal{H}^2 f^2}{2\pi^2}\int dk P_{\rm mm}(k)\frac{j_1(kr)}{kr}\,, \tag{4.41}$$

where $\sigma_v^2 \equiv \langle \boldsymbol{v}(\boldsymbol{x})\cdot\boldsymbol{v}(\boldsymbol{x})\rangle/3$ is the one-dimensional velocity variance, $P_{\rm mm}(k)$ is the matter power spectrum in real space, $\Psi_\parallel$ is the variance of the radial pairwise velocities, $\Psi_\perp$ is the

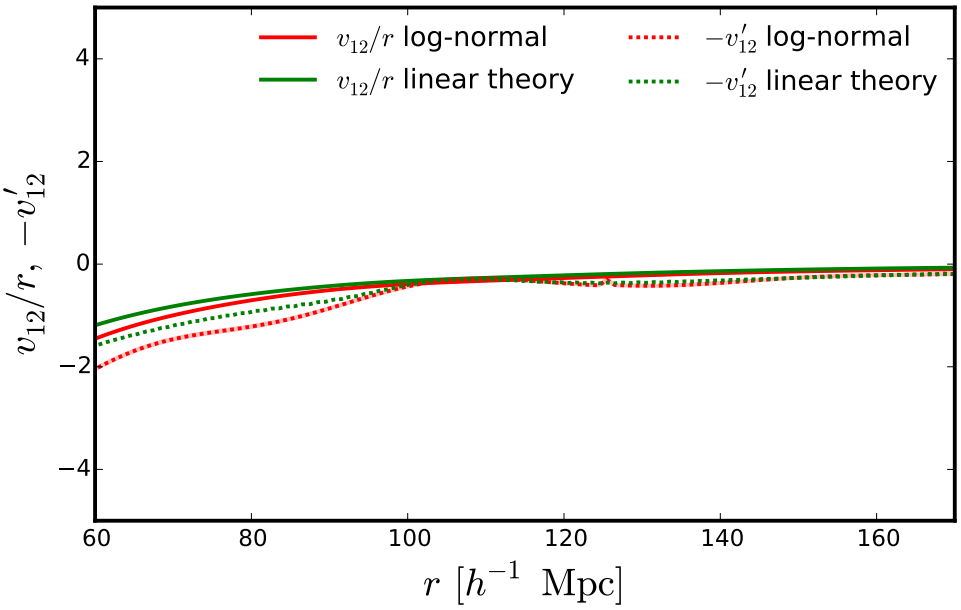

Figure 4.10: Mean radial pairwise velocity (solid) measured from our log-normal mocks (red) as well as that predicted by linear theory (green). Derivative w.r.t. separation r (dotted). Red band denotes the error on the mean measured from 50 realisations. They agree at separations $\gtrsim 140\,h^{-1}$ Mpc.

variance of the tangential pairwise velocities, and j_n denotes the spherical Bessel function of the n^{th} order. As shown in refs. (60; 142),

$$-\frac{\mathrm{d}}{\mathrm{d}r_\parallel}\left[v_{12}(r)\frac{r_\parallel}{r}\right]\Big|_{r_\parallel=s_\parallel} = \frac{v_{12}(r)}{r}(\mu^2-1) - v'_{12}(r)\mu^2\,, \tag{4.42}$$

$$\frac{1}{2}\frac{\mathrm{d}^2}{\mathrm{d}r_\parallel^2}\left[\sigma^2_{12}(r,\mu)\right]\Big|_{r_\parallel=s_\parallel} = (2-10\mu^2+8\mu^4)\frac{\Psi_\perp-\Psi_\parallel}{r^2} + (5\mu^4-5\mu^2)\frac{\Psi'_\parallel}{r} + (-1+6\mu^2-5\mu^4)\frac{\Psi'_\perp}{r} - \mu^4\Psi''_\parallel + (\mu^4-\mu^2)\Psi''_\perp\,, \tag{4.43}$$

so that the Kaiser limit of the redshift space two-point correlation function does not depend on any constant or the isotropic dispersion of the pairwise line-of-sight velocities. In this section $'$ denotes d/dr.

In figures (4.10)–(4.12) we show the different terms that contribute to the Kaiser limit of the two-point correlation function, namely, v_{12}/r, v'_{12}, $(\Psi_\perp-\Psi_\parallel)/r^2$, $\Psi'_\parallel/r$, $\Psi'_\perp/r$, $\Psi''_\parallel$, and $\Psi''_\perp$ for our log-normal mocks (we choose $b=1.8$ which is the average linear bias for halos in the mass range $5\times10^{13}-6.5\times10^{13}\ h^{-1}\,M_\odot$ at $z=0$), and linear theory predictions. They agree at large separations, which ensures that the Kaiser limit is attained. This is because only the spatial derivatives of the first two moments of the pairwise velocity PDF contribute to the lowest-order redshift space correlation function in the large-scale limit (60; 148; 142), as we confirm. So, even though the PDF from our log-normal mocks shows

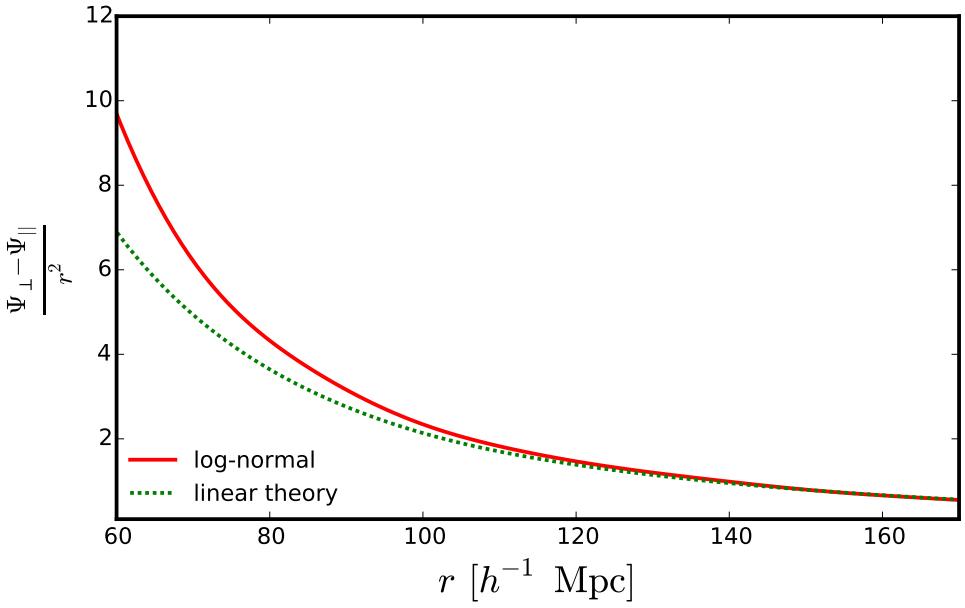

Figure 4.11: Same as figure 4.10 but for difference of radial ($\Psi_\parallel$) and tangential ($\Psi_\perp$) pairwise velocity variances. They agree at separations $\gtrsim 140\,h^{-1}$ Mpc.

a non-zero excess kurtosis on large scales and the dispersion is larger than the one from the N-body simulations (by a scale-independent constant), we find agreement with the Kaiser prediction on large scales.

4.5 Conclusions

In this chapter, we have presented a new public code for generating log-normal realisations including velocity fields satisfying the linear continuity equation. The log-normal realisations provide not only a fast and easy way to generate mock galaxy catalogs but also an excellent test bed for studying non-linear effects such as the window function and RSD.

We have verified that the real-space two-point correlation functions measured from our log-normal mock galaxy catalogs are in excellent agreement with the input. We find that the cross-correlation coefficients between the matter and galaxy density fields are not unity (182). Non-linear (exponential, to be specific) transformation of perfectly correlated Gaussian fields induces a deviation of the cross-correlation coefficient from unity. We analytically compute the cross-correlation coefficient that matches the measurement to a sub-percent level.

We have also shown measurements from our log-normal mock catalogs in redshift space. The redshift-space power spectrum is commonly modelled as a combination of a "squashing" term (in the Kaiser limit, arising from coherent large-scale flows) and a damping term (FoG from random virial motion on small scales). Using our log-normal mock catalogs, we have investigated the redshift-space power spectrum and found a good agreement with the

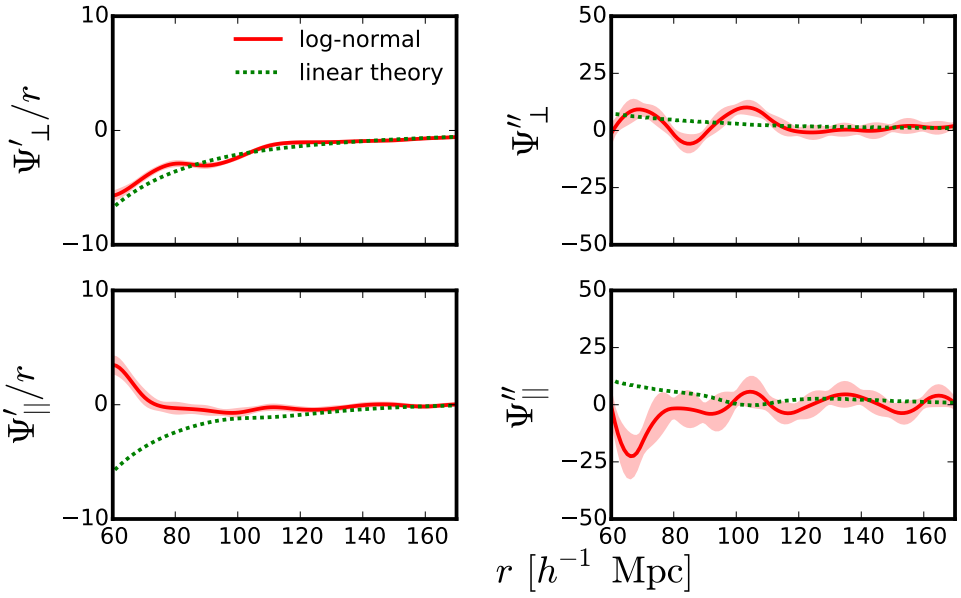

Figure 4.12: Same as figure 4.10 but for first and second derivatives of tangential and radial pairwise velocity variances. The second derivatives are noisy but they seem to agree with linear theory predictions at separations $\gtrsim 120\,h^{-1}$ Mpc.

squashing term on large scales ($k \lesssim 0.1\,h^{-1}$ Mpc) as expected. On small scales, we find a damping which is qualitatively similar to the FoG; the damping we observe, however, does not come from random motion, as we do not include any random virial motion in our mock generator. Rather, the damping comes from non-linearity in the Jacobian of the real-to-redshift space mapping, and from the coherent peculiar velocity field. Attributing all of the damping to the FoG, as commonly done in the literature, is thus misleading. The configuration space two-point correlation function calculated with the linear Jacobian approximation cannot reproduce the measurement at all separations; thus, the correlation function is sensitive to non-linearity in the Jacobian even at large separations.

The streaming model can take into account the full non-linearity of the real-to-redshift space mapping. In this model a fundamental entity in predicting the redshift-space two-point statistics is the pairwise line-of-sight velocity PDF, which is notoriously hard to predict owing to its *pairwise* nature. We find that the problem persists even with our, rather simpler, setting: the PDF of the density field is exactly known to be log-normal, and the velocity is linearly related to the density field. We nevertheless have made some progress in a couple of areas in modelling the pairwise line-of-sight velocity PDF. First, we show that the pairwise line-of-sight velocity PDF from our log-normal mock catalogs qualitatively captures features of the PDF from full N-body simulations, such as a negative skewness for small separations and the shift of the PDF towards more negative velocities for higher mass halos. We find these features even when the same coherent velocity field is assigned to galaxy fields with different biases, i.e., galaxies with different biases move with

the same velocities, but pair-weighting makes the pairwise velocity PDF depend on the galaxy bias. Second, for the log-normal setting, one can in principle predict the moments of the pairwise line-of-sight velocity PDF, as we explicitly demonstrate for the mean pairwise line-of-sight velocity. We have compared the predicted mean velocity to the one measured from the catalogs, and find an excellent match between the two. Likewise, although very demanding, we envisage that the analytical calculation can also be done for the higher order moments.

Our log-normal generator has been used extensively to help design the on-going and planned galaxy redshift surveys such as HETDEX (Hobby-Eberly Telescope Dark Energy Experiment) (77), PFS (Prime Focus Spectrograph) (168), and WFIRST-AFTA (Wide Field Infrared Survey Telescope Astrophysics-Focused Telescope Assets) (163). It should also be equally useful for DESI (Dark Energy Spectroscopic Instrument) (100), LSST (Large Synoptic Survey Telescope) (3), and Euclid (98).

Chapter 5

Summary and Outlook

The central theme of this thesis has been non-Gaussianity. As we discussed in chapter 1, most of our current understanding of the Universe comes from analysis of the power spectrum of primordial (via their imprint on CMB temperature), and late-time (via their imprint on galaxy clustering) density fields. However, we also saw that the power spectrum is not sufficient to characterise non-Gaussian fields. In fact, it does not capture any information arising from the non-linear evolution of density and velocity fields under gravity. To constrain the nature of gravity on length and time scales of the size and age of the Universe, we simply *cannot* do without measurement of non-Gaussian statistics. Given this importance of studying non-Gaussianity, we studied the first non-zero statistic for a non-Gaussian distribution, the bispectrum, for primordial GWs, and considered an approximate non-Gaussian model for matter and galaxy density fields in the Universe.

In chapter 2, we laid out the current paradigm for structure formation in the Universe, starting from quantum fluctuations during an inflationary stage of the Universe, and ending at formation of dark matter halos, into which galaxies, stars, planets, etc. form. We discussed the origin of primordial GWs and their characteristics, such as scale-independence and mild non-Gaussianity. We then used the initial conditions set by these quantum fluctuations to solve for the density and velocity fields at later time in the Universe. Because the field equations for gravity are non-linear, the Gaussian primordial fields become non-Gaussian, under the action of gravity.

The inflationary Universe might have contained other fields, which have sub-dominant contributions to the energy density, so that they do not affect the background evolution. We considered the possible imprints of such fields on present-day observables in chapter 3. In particular, if the spectator sector consists of a pseudoscalar axion, and SU(2) gauge fields, such that the two are coupled to each other via a Chern-Simons like interaction, the gauge field experiences a tachyonic instability. Because the SU(2) gauge field has a tensor degree of freedom as well, it can linearly source GWs. These sourced GWs can be strongly scale-dependent, or scale-independent like those from vacuum fluctuations of the metric. In contrast to vacuum fluctuations however, they are chiral, since the pseudoscalar axion violates parity, and they are highly non-Gaussian. We also showed that the non-Gaussianity, characterised by the ratio of the bispectrum to the square of the

power spectrum, is inversely proportional to the energy density fraction of the gauge fields. Since the gauge fields are spectator fields, this fraction can be quite small, leading to a large non-Gaussianity. As a consequence, we argued that non-Gaussianity is a definitive test for the origin of primordial GWs. We also showed that the tensor non-Gaussianity can be easily observed in upcoming CMB missions such as LiteBIRD (117).

The non-linear gravitational evolution of Gaussian fluctuations, sourced during inflation, makes them non-Gaussian. In chapter 4, we presented a public code to generate log-normal realisations of matter and galaxy density fields. Non-Gaussian peculiar velocities were generated from the log-normal matter field using the linear continuity equation. We showed that the redshift space power spectra agree with the Kaiser predictions on large scales as expected. We also computed the cross correlation coefficient, and measured the pairwise velocity PDFs. These PDFs show a non-zero skewness and kurtosis, as has been seen previously in pairwise velocity PDFs from N-body simulations. Our code has been used to also model lensing, and to study covariance matrices for future surveys such as PFS, WFIRST and Euclid.

Looking ahead, the era of precision cosmology using the power spectrum is mature. Planck (5) has obtained a cosmic variance limited map of the CMB temperature anisotropies. Polarisation is undoubtedly the next frontier for CMB experiments. There, a non-zero detection of primordial B-modes will be exciting, but we would still need to ensure that the bispectrum is small, in accordance with the estimates presented in chapter 2, before claiming vacuum fluctuations of the metric, or "first evidence for quantum gravity". Large scale structure surveys have recently also started coming of age, and now match the CMB in their precision. For galaxy redshift surveys, the bispectrum is definitely the observable to look for, as the constraining power is greatly enhanced and it is an important signature of non-linear gravitational evolution.

From a mathematical perspective, it is a bit unsatisfactory that we need to rely on moments of the distribution to characterize non-Gaussian distributions. As argued in chapter 1, if the bispectrum is non-zero we can claim that a distribution is non-Gaussian, but if it is zero we cannot claim that the distribution is Gaussian. This would necessitate us having to measure the trispectrum, the 5-point function, and so on. There are an infinite number of moments which are non-zero for non-Gaussian distributions, and it is not clear where to stop. To that end, it would be interesting to consider other methods of parametrizing non-Gaussianity (such as Minkowski functionals), and understand if a finite set of observables that capture the most essential features of non-Gaussianity can be developed. At any rate, non-Gaussianity is here to stay!

Appendix A

Source Function at Second-Order

In this appendix, we present the source function at second-order, in terms of the contributions from different polarisations of the first-order modes. The source function is given by the right hand side of equation (2.32),

$$S_{pq}(\tau,\boldsymbol{x}) = \frac{H}{M_P}\,\tau\,\Big[2\psi_{pl,qr}(\tau,\boldsymbol{x})\psi_{lr}(\tau,\boldsymbol{x}) + 2\psi_{pr,l}(\tau,\boldsymbol{x})\psi_{ql,r}(\tau,\boldsymbol{x}) + \psi_{lr,q}(\tau,\boldsymbol{x})\psi_{lr,p}(\tau,\boldsymbol{x}) - 2\psi_{pq,lr}(\tau,\boldsymbol{x})\psi_{lr}(\tau,\boldsymbol{x}) - 2\psi_{lr,q}(\tau,\boldsymbol{x})\psi_{lp,r}(\tau,\boldsymbol{x})\Big]\,, \quad \text{(A.1)}$$

which in Fourier space gives,

$$S_{pq}(\tau,\boldsymbol{k}) = \frac{H}{M_P}\,\tau\int\frac{d^3p_1\,d^3p_2}{(2\pi)^6}\delta_D(\boldsymbol{p}_1+\boldsymbol{p}_2-\boldsymbol{k})\Big[2p_{1q}p_{1r}\psi_{pl}(\tau,\boldsymbol{p}_1)\psi_{lr}(\tau,\boldsymbol{p}_2) + 2p_{1l}p_{2r}\psi_{pr}(\tau,\boldsymbol{p}_1)\psi_{ql}(\tau,\boldsymbol{p}_2) + p_{1q}p_{2p}\psi_{lr}(\tau,\boldsymbol{p}_1)\psi_{lr}(\tau,\boldsymbol{p}_2) - 2p_{1l}p_{1r}\psi_{pq}(\tau,\boldsymbol{p}_1)\psi_{lr}(\tau,\boldsymbol{p}_2) - 2p_{1q}p_{2r}\psi_{lr}(\tau,\boldsymbol{p}_1)\psi_{lp}(\tau,\boldsymbol{p}_2)\Big]\,, \quad \text{(A.2)}$$

where we have defined (c.f. equation (**??**))

$$\psi_{ij}(\tau,\boldsymbol{p}_n) \equiv \Big[e^R_{ij}(\boldsymbol{p}_n)\psi^R_{\boldsymbol{p}_n}(\tau) + e^L_{ij}(\boldsymbol{p}_n)\psi^L_{\boldsymbol{p}_n}(\tau)\Big] = \sum_{c=L,R} e^c_{ij}(\boldsymbol{p}_n)\psi^c_{\boldsymbol{p}_n}(\tau)\,, \quad \text{(A.3)}$$

with $n = 1$ or 2. Substituting this in equation (A.2) we find

$$S_{pq}(\tau,\boldsymbol{k}) = \frac{H}{M_P}\,\tau\int\frac{d^3p_1\,d^3p_2}{(2\pi)^6}\delta_D(\boldsymbol{p}_1+\boldsymbol{p}_2-\boldsymbol{k})\Big[S^{LL}_{pq} + S^{LR}_{pq} + S^{RL}_{pq} + S^{RR}_{pq}\Big]\,, \quad \text{(A.4)}$$

with the different parts given as

$$S_{pq}^{LL} = \psi^L_{\boldsymbol{p}_1}\psi^L_{\boldsymbol{p}_2}\Big[2e^L_{pl}(p_1)e^L_{lr}(p_2)p_{1q}p_{1r} + 2e^L_{pr}(p_1)e^L_{ql}(p_2)p_{1l}p_{2r} + e^L_{rl}(p_1)e^L_{rl}(p_2)p_{1p}p_{2q} - 2e^L_{pq}(p_1)e^L_{lr}(p_2)p_{1l}p_{1r} - 2e^L_{lr}(p_1)e^L_{lp}(p_2)p_{1q}p_{2r}\Big] \equiv \psi^L_{\boldsymbol{p}_1}\psi^L_{\boldsymbol{p}_2}Q^{LL}_{pq}\,, \tag{A.5}$$

$$S_{pq}^{LR} = \psi^L_{\boldsymbol{p}_1}\psi^R_{\boldsymbol{p}_2}\Big[2e^L_{pl}(p_1)e^R_{lr}(p_2)p_{1q}p_{1r} + 2e^L_{pr}(p_1)e^R_{ql}(p_2)p_{1l}p_{2r} + e^L_{rl}(p_1)e^R_{rl}(p_2)p_{1p}p_{2q} - 2e^L_{pq}(p_1)e^R_{lr}(p_2)p_{1l}p_{1r} - 2e^L_{lr}(p_1)e^R_{lp}(p_2)p_{1q}p_{2r}\Big] \equiv \psi^L_{\boldsymbol{p}_1}\psi^R_{\boldsymbol{p}_2}Q^{LR}_{pq}\,, \tag{A.6}$$

$$S_{pq}^{RL} = \psi^R_{\boldsymbol{p}_1}\psi^L_{\boldsymbol{p}_2}\Big[2e^R_{pl}(p_1)e^L_{lr}(p_2)p_{1q}p_{1r} + 2e^R_{pr}(p_1)e^L_{ql}(p_2)p_{1l}p_{2r} + e^R_{rl}(p_1)e^L_{rl}(p_2)p_{1p}p_{2q} - 2e^R_{pq}(p_1)e^L_{lr}(p_2)p_{1l}p_{1r} - 2e^R_{lr}(p_1)e^L_{lp}(p_2)p_{1q}p_{2r}\Big] \equiv \psi^R_{\boldsymbol{p}_1}\psi^L_{\boldsymbol{p}_2}Q^{RL}_{pq}\,, \tag{A.7}$$

$$S_{pq}^{RR} = \psi^R_{\boldsymbol{p}_1}\psi^R_{\boldsymbol{p}_2}\Big[2e^R_{pl}(p_1)e^R_{lr}(p_2)p_{1q}p_{1r} + 2e^R_{pr}(p_1)e^R_{ql}(p_2)p_{1l}p_{2r} + e^R_{rl}(p_1)e^R_{rl}(p_2)p_{1p}p_{2q} - 2e^R_{pq}(p_1)e^R_{lr}(p_2)p_{1l}p_{1r} - 2e^R_{lr}(p_1)e^R_{lp}(p_2)p_{1q}p_{2r}\Big] \equiv \psi^R_{\boldsymbol{p}_1}\psi^R_{\boldsymbol{p}_2}Q^{RR}_{pq}\,, \tag{A.8}$$

where we have separated the factors containing the polarisation tensors as $Q^{c_1c_2}_{pq}$, since they are not quantized. Then, in order to obtain correlation functions of GWs generated from quantum fluctuations, we quantize the fields $\psi^c_{\boldsymbol{p}}(\tau) \to \hat{\psi}^c_1(\tau, \boldsymbol{p})$, and use the condition of Gaussianity on $\hat{\psi}_1$ so that Wick's theorem can be used, and that at first-order, different polarisations are uncorrelated, $\left\langle \hat{\psi}^L_1\hat{\psi}^R_1 \right\rangle = \left\langle \hat{\psi}^R_1\hat{\psi}^L_1 \right\rangle = 0$. As a consequence of this, we see that whenever we want to evaluate a bispectrum with two other first-order modes, the only non-zero contributions arise from parts of S_{pq} containing the same number of left- and right-handed modes as the other two.

Appendix B

Polarisation Tensor

In this appendix, we construct the left and right-handed transverse and traceless polarisation tensors. We start with the left and right-handed polarisation vector whose wave number is parallel to the z-axis,

$$\boldsymbol{\epsilon}^{L/R}(\hat{\boldsymbol{z}}) = \frac{1}{\sqrt{2}} \begin{pmatrix} 1 \\ \pm i \\ 0 \end{pmatrix}. \tag{B.1}$$

The plus and minus signs are for left- (L) and right-handed (R) polarisation vectors, respectively. From now on, $\pm$ means $+$ for L and $-$ for R, whereas $\mp$ means $-$ for L and $+$ for R. To obtain the polarisation vector with a general wave number $\hat{\boldsymbol{k}}$ which points in the direction of (θ, φ) in polar coordinate, we use the following rotation matrix which transforms $\hat{\boldsymbol{z}}$ into $\hat{\boldsymbol{k}}$:

$$S(\hat{\boldsymbol{k}}) = \begin{pmatrix} \cos\theta\cos\varphi & -\sin\varphi & \sin\theta\cos\varphi \\ \cos\theta\sin\varphi & \cos\varphi & \sin\theta\sin\varphi \\ -\sin\theta & 0 & \cos\theta \end{pmatrix}. \tag{B.2}$$

Then we find

$$\boldsymbol{\epsilon}^{L/R}(\hat{\boldsymbol{k}}) = S(\hat{\boldsymbol{k}})\boldsymbol{\epsilon}^{L/R}(\hat{\boldsymbol{z}}) = \frac{1}{\sqrt{2}} \begin{pmatrix} \cos\theta\cos\varphi \mp i\sin\varphi \\ \cos\theta\sin\varphi \pm i\cos\varphi \\ -\sin\theta \end{pmatrix}. \tag{B.3}$$

These polarisation vectors satisfy

$$\begin{aligned} &\boldsymbol{k}\cdot\boldsymbol{\epsilon}^{L/R}(\hat{\boldsymbol{k}}) = 0, \qquad \boldsymbol{\epsilon}^{L/R*}(\hat{\boldsymbol{k}}) = \boldsymbol{\epsilon}^{R/L}(\hat{\boldsymbol{k}}) = \boldsymbol{\epsilon}^{L/R}(-\hat{\boldsymbol{k}}), \\ &\boldsymbol{\epsilon}^{L/R}(\hat{\boldsymbol{k}})\cdot\boldsymbol{\epsilon}^{R/L}(\hat{\boldsymbol{k}}) = 1, \qquad \boldsymbol{\epsilon}^{L/R}(\hat{\boldsymbol{k}})\cdot\boldsymbol{\epsilon}^{L/R}(\hat{\boldsymbol{k}}) = 0. \end{aligned} \tag{B.4}$$

The polarisation tensor $e_{ij}^{L/R}(\hat{\boldsymbol{k}})$ can be constructed from the polarisation vectors,

$$e_{ij}^{L/R}(\hat{\boldsymbol{k}}) = \epsilon_i^{L/R}(\hat{\boldsymbol{k}})\,\epsilon_j^{L/R}(\hat{\boldsymbol{k}}). \tag{B.5}$$

These polarisation tensors are transverse and traceless and satisfy

$$e^L_{ij}(-\hat{\boldsymbol{k}}) = e^{L*}_{ij}(\hat{\boldsymbol{k}}) = e^R_{ij}(\hat{\boldsymbol{k}}), \quad i\epsilon_{ijk}k_i e^{L/R}_{jl}(\hat{\boldsymbol{k}}) = \pm k e^{L/R}_{kl}(\hat{\boldsymbol{k}}), \quad e^L_{ij}(\hat{\boldsymbol{z}}) = \frac{1}{2}\begin{pmatrix} 1 & i & 0 \\ i & -1 & 0 \\ 0 & 0 & 0 \end{pmatrix}. \tag{B.6}$$

Although the general expression for $e^{L/R}_{ij}(\hat{\boldsymbol{k}})$ is rather complicated, we can fix θ in the current case. This is because we calculate three polarisation tensors with three different wavenumbers, $e^R_{ij}(\hat{\boldsymbol{k}}_1)e^R_{kl}(\hat{\boldsymbol{k}}_2)e^R_{nm}(\hat{\boldsymbol{k}}_3)$ whose indices are somehow contracted, and these wave vectors are on the same plane due to momentum conservation, $\delta(\boldsymbol{k}_1+\boldsymbol{k}_2+\boldsymbol{k}_3)$. In that case, we can set $\theta = \pi/2$ and let these vectors, $\boldsymbol{k}_1, \boldsymbol{k}_2, \boldsymbol{k}_3$, move only on the x-y plane. For $\theta = \pi/2$, the polarisation tensors become

$$e^{L/R}_{ij}\left(\theta = \frac{\pi}{2}, \varphi\right) = \frac{1}{2}\begin{pmatrix} -\sin^2\varphi & \cos\varphi\sin\varphi & \pm i\sin\varphi \\ \cos\varphi\sin\varphi & -\cos^2\varphi & \mp i\cos\varphi \\ \pm i\sin\varphi & \mp i\cos\varphi & 1 \end{pmatrix}. \tag{B.7}$$

Now we have three angles, $\varphi_1, \varphi_2, \varphi_3$, associated with wavenumbers, $\boldsymbol{k}_1, \boldsymbol{k}_2, \boldsymbol{k}_3$, respectively. Without loss of generality, we can set $\varphi_1 = 0$. Furthermore, these trigonometric functions of φ_2 and φ_3 can be rewritten as functions of $r_2 \equiv k_2/k_1$ and $r_3 \equiv k_3/k_1$. Using $\boldsymbol{k}_1+\boldsymbol{k}_2+\boldsymbol{k}_3 = 0$, we find

$$k_3^2 = |\boldsymbol{k}_1+\boldsymbol{k}_2|^2 = k_1^2+k_2^2+2k_1k_2\cos\varphi_2 \quad \Longrightarrow \quad \cos\varphi_2 = \frac{r_3^2-r_2^2-1}{2r_2}. \tag{B.8}$$

In the same way, we also find $\cos\varphi_3 = (r_2^2-r_3^2-1)/(2r_3)$. With this notation, we find

$$\sum_{\{I,J,K\}}^{\{1,2,3\}} i\epsilon^{abc}\, k^i_K e^R_{ai}(\hat{\boldsymbol{k}}_I)e^R_{bj}(\hat{\boldsymbol{k}}_J)e^R_{cj}(\hat{\boldsymbol{k}}_K) = -2k_1\Xi\tilde{\Xi}\,, \tag{B.9}$$

$$e^R_{ij}(\hat{\boldsymbol{k}}_1)e^R_{jl}(\hat{\boldsymbol{k}}_2)e^R_{li}(\hat{\boldsymbol{k}}_3) = \Xi, \qquad \epsilon^{abc}\epsilon^{ijk}\, e^R_{ai}(\hat{\boldsymbol{k}}_1)e^R_{bj}(\hat{\boldsymbol{k}}_2)e^R_{ck}(\hat{\boldsymbol{k}}_3) = 2\,\Xi\,, \tag{B.10}$$

where

$$\Xi \equiv \frac{(1+r_2+r_3)^3}{64r_2^2r_3^2}(r_2+r_3-1)(1+r_2-r_3)(1+r_3-r_2)\,, \tag{B.11}$$

$$\tilde{\Xi} \equiv 1+r_2+r_3. \tag{B.12}$$

$\sum_{\{I,J,K\}}^{\{1,2,3\}}$ denotes summation of all the permutation, $\{I,J,K\} = \{\mathrm{Perm}(1,2,3)\}$.

Appendix C

Equilateral Shape

To measure similarity of the shapes of bispectra, the cosine between two shapes is introduced as (17),

$$\cos(B_h, F_{\rm ref}) \equiv \frac{B_h \cdot F_{\rm ref}}{\sqrt{(B_h \cdot B_h)(F_{\rm ref} \cdot F_{\rm ref})}}\,, \tag{C.1}$$

where the dot product is defined as

$$X \cdot Y \equiv \int_0^1 dr_2 \int_0^1 dr_3 (r_2 r_3)^4 X(1, r_2, r_3) Y(1, r_2, r_3). \tag{C.2}$$

Here $F_{\rm ref}$ is the reference template to which the similarity is measured. In chapter 3 we have used the equilateral template (48)

$$F_{\rm eq}(k_1, k_2, k_3) = \left[-\frac{1}{k_1^3 k_2^3} - \frac{1}{k_1^3 k_3^3} - \frac{1}{k_2^3 k_3^3} - \frac{2}{k_1^2 k_2^2 k_3^2} + \frac{1}{k_1 k_2^2 k_3^2} + (5\,\text{perm}) \right]. \tag{C.3}$$

Figure C.1 shows the shape of this template as a function of r_2 and r_3.

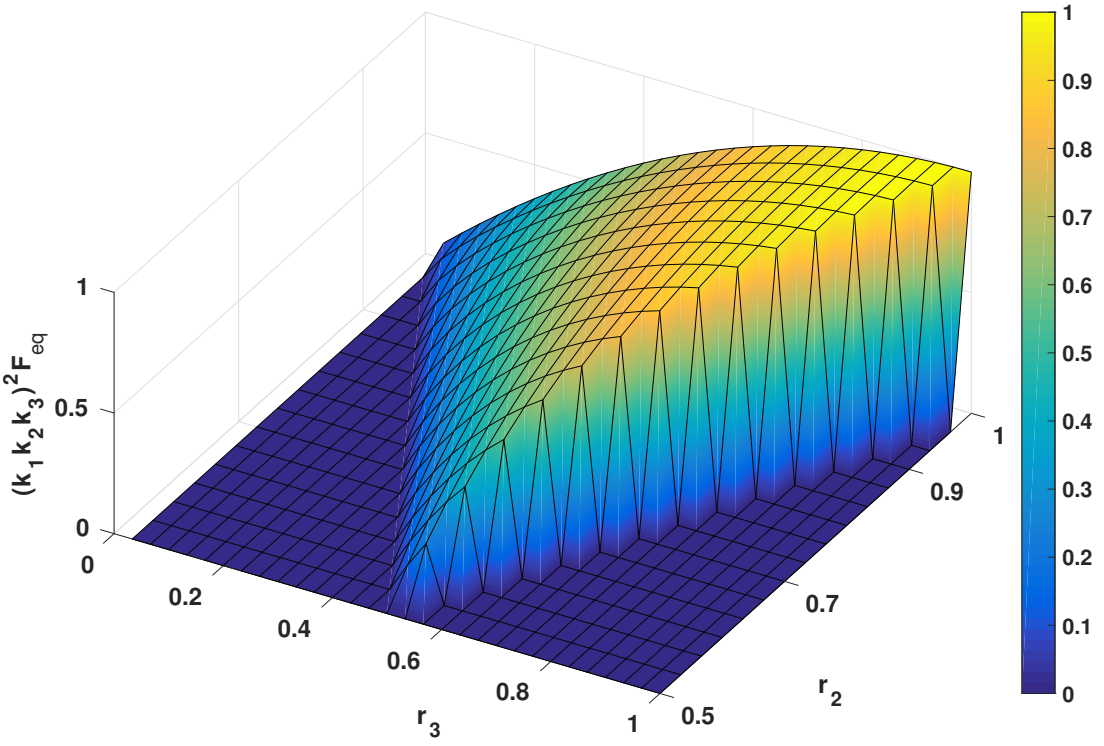

Figure C.1: 3D plot of $(k_1k_2k_3)^2F_{\rm eq}$, equation (C.3).

Appendix D

Derivation of the streaming model in configuration space

In this appendix, we re-derive the streaming model (135; 49; 60; 148; 174), which equates the redshift-space two-point correlation function ξ^s_{gg} to the real-space two-point correlation function ξ_{gg} re-mapped by the pairwise line-of-sight velocity PDF $\mathcal{P}$ as

$$1 + \xi^s_{gg}(\boldsymbol{s}) = \int dr_\parallel \mathcal{P}\left(s_\parallel - r_\parallel; \boldsymbol{r}\right) \left[1 + \xi_{gg}(\boldsymbol{r})\right] . \tag{D.1}$$

Here, $\boldsymbol{s}$ and $\boldsymbol{r}$ are, respectively, the separations in redshift space and real space. To the best of our knowledge, the streaming model in the form of equation (D.1) has first appeared in (135), and the later studies (49; 60; 148; 174) have improved the modelling and interpretation of the pairwise line-of-sight velocity PDF. For example, Ref. (60) incorporates the scale-dependence of the velocity dispersion to reproduce the Kaiser (85) prediction; Ref. (148) finds the expression for the pairwise line-of-sight velocity PDF and its moment generating function with an assumption that the velocity field $\boldsymbol{v}(\boldsymbol{r})$ is a single-valued function of positions (we shall call this *single-stream* case). More recently, Ref. (174) generalizes the results to the *multi-stream* case where there are multiple velocity components (streams) at a single position; this is, for example, the case for the shell crossing in the spherical collapse. Here, we shall closely follow the result of Ref. (174) so that derivation we present here works for the multi-streaming case.

Starting from the galaxy number conservation between the real and redshift space (equation (4.3)), and using the general phase space function $f(\boldsymbol{x}, \boldsymbol{v})$, we may write the redshift-space density contrast as (151):

$$1 + \delta^s_g(\boldsymbol{s}) = \int d^3x \int d^3v \; f(\boldsymbol{x}, \boldsymbol{v}) \delta^D \left(\boldsymbol{x} + \frac{v_\parallel}{\mathcal{H}} \hat{\ell} - \boldsymbol{s}\right) , \tag{D.2}$$

where δ^D is the Dirac-delta operator. The redshift-space two-point correlation function is

then given as

$$\left\langle \left[1+\delta_g^s(\boldsymbol{s}_1)\right]\left[1+\delta_g^s(\boldsymbol{s}_2)\right]\right\rangle = \int d^3\boldsymbol{x}_1 \int d^3\boldsymbol{x}_2 \int d^3\boldsymbol{v}_1 \int d^3\boldsymbol{v}_2 \\ \left\langle \delta^D\left(\boldsymbol{x}_1 - \boldsymbol{s}_1 + \frac{v_{1,\parallel}}{\mathcal{H}}\hat{\ell}\right)\delta^D\left(\boldsymbol{x}_2 - \boldsymbol{s}_2 + \frac{v_{2,\parallel}}{\mathcal{H}}\hat{\ell}\right) f(\boldsymbol{x}_1,\boldsymbol{v}_1) f(\boldsymbol{x}_2,\boldsymbol{v}_2)\right\rangle . \tag{D.3}$$

As is apparent from equation (4.2), the RSD only applies to the line-of-sight quantities, so it is helpful to explicitly indicate the line-of-sight quantities with the subscript $\parallel$ and perpendicular quantities with the subscript $\perp$. Then, equation (D.3) becomes

$$\left\langle \left[1+\delta_g^s\left(s_{1,\parallel}, s_{1,\perp}\right)\right]\left[1+\delta_g^s\left(s_{2,\parallel}, s_{2,\perp}\right)\right]\right\rangle = \int dx_{1,\parallel} \int dx_{2,\parallel} \int d^3\boldsymbol{v}_1 \int d^3\boldsymbol{v}_2 \\ \left\langle \delta^D\left(x_{1,\parallel} - s_{1,\parallel} + \frac{v_{1,\parallel}}{\mathcal{H}}\right)\delta^D\left(x_{2,\parallel} - s_{2,\parallel} + \frac{v_{2,\parallel}}{\mathcal{H}}\right) f(x_{1,\parallel}, s_{1,\perp}, \boldsymbol{v}_1) f(x_{2,\parallel}, s_{2,\perp}, \boldsymbol{v}_2)\right\rangle . \tag{D.4}$$

Here, we keep the Dirac-delta operators inside the ensemble average as they contain the peculiar velocity field. We then use the definition of the Dirac-delta $\delta^D(x) = (2\pi)^{-1}\int_{-\infty}^{\infty} d\gamma e^{-i\gamma x}$, to transform equation (D.4) as

$$\left\langle \left[1+\delta_g^s\left(s_{1,\parallel}, s_{1,\perp}\right)\right]\left[1+\delta_g^s\left(s_{2,\parallel}, s_{2,\perp}\right)\right]\right\rangle = \int dx_{1,\parallel} \int dx_{2,\parallel} \int \frac{d\gamma_1}{2\pi} \int \frac{d\gamma_2}{2\pi} e^{-i\gamma_1\left(x_{1,\parallel} - s_{1,\parallel}\right)} \\ e^{-i\gamma_2\left(x_{2,\parallel} - s_{2,\parallel}\right)} \times \int d^3\boldsymbol{v}_1 \int d^3\boldsymbol{v}_2 \left\langle e^{-i\gamma_1\frac{v_{1,\parallel}}{\mathcal{H}}} e^{-i\gamma_2\frac{v_{2,\parallel}}{\mathcal{H}}} f(x_{1,\parallel}, s_{1,\perp}, \boldsymbol{v}_1) f(x_{2,\parallel}, s_{2,\perp}, \boldsymbol{v}_2)\right\rangle . \tag{D.5}$$

Because of statistical homogeneity of the Universe, the ensemble average must depend only on the separation. We make it explicit by introducing new variables $R_\parallel = (x_{1,\parallel} + x_{2,\parallel})/2$ and $r_\parallel = x_{1,\parallel} - x_{2,\parallel}$, with which the right-hand side of the equation above becomes

$$\begin{aligned} &\left\langle \left[1+\delta_g^s\left(s_{1,\parallel}, s_{1,\perp}\right)\right]\left[1+\delta_g^s\left(s_{2,\parallel}, s_{2,\perp}\right)\right]\right\rangle \\ &= \int dr_\parallel \int \frac{d\gamma_1}{2\pi} \int d\gamma_2 \left[\int \frac{dR_\parallel}{2\pi} e^{-iR_\parallel(\gamma_1+\gamma_2)}\right] e^{-\frac{i}{2}r_\parallel(\gamma_1-\gamma_2)} e^{i\left(\gamma_1 s_{1,\parallel} + \gamma_2 s_{2,\parallel}\right)} \\ &\quad \times \int d^3\boldsymbol{v}_1 \int d^3\boldsymbol{v}_2 \left\langle e^{-i\gamma_1\frac{v_{1,\parallel}}{\mathcal{H}}} e^{-i\gamma_2\frac{v_{2,\parallel}}{\mathcal{H}}} f(x_{1,\parallel}, s_{1,\perp}, \boldsymbol{v}_1) f(x_{2,\parallel}, s_{2,\perp}, \boldsymbol{v}_2)\right\rangle \\ &= \int dr_\parallel \int \frac{d\gamma_1}{2\pi} \int d\gamma_2 \delta^D(\gamma_1+\gamma_2) e^{-\frac{i}{2}r_\parallel(\gamma_1-\gamma_2)} e^{i\left(\gamma_1 s_{1,\parallel} + \gamma_2 s_{2,\parallel}\right)} \\ &\quad \times \int d^3\boldsymbol{v}_1 \int d^3\boldsymbol{v}_2 \left\langle e^{-i\gamma_1\frac{v_{1,\parallel}}{\mathcal{H}}} e^{-i\gamma_2\frac{v_{2,\parallel}}{\mathcal{H}}} f(x_{1,\parallel}, s_{1,\perp}, \boldsymbol{v}_1) f(x_{2,\parallel}, s_{2,\perp}, \boldsymbol{v}_2)\right\rangle . \end{aligned} \tag{D.6}$$

Finally, integrating the Dirac-delta yields

$$1 + \xi_{gg}^s(s_\parallel, s_\perp) = \int dr_\parallel \int \frac{d\gamma_1}{2\pi} e^{-i\gamma_1(r_\parallel - s_\parallel)} \int d^3\boldsymbol{v}_1 \int d^3\boldsymbol{v}_2 \left\langle e^{-i\gamma_1\frac{\Delta v_\parallel}{\mathcal{H}}} f(x_{1,\parallel}, s_{1,\perp}, \boldsymbol{v}_1) f(x_{2,\parallel}, s_{2,\perp}, \boldsymbol{v}_2)\right\rangle , \tag{D.7}$$

with $\Delta v_\parallel = v_{1,\parallel} - v_{2,\parallel}$. Again, note that the ensemble average must depend only on the separation. Following Ref. (148), we define the pairwise line-of-sight velocity PDF as

$$\mathcal{P}(r_\parallel - s_\parallel, \boldsymbol{r}) = \int \frac{d\gamma}{2\pi} e^{-i\gamma(r_\parallel - s_\parallel)} \mathcal{M}(-i\gamma, \boldsymbol{r}), \tag{D.8}$$

where $\boldsymbol{r} = \boldsymbol{x}_1 - \boldsymbol{x}_2$ and $\mathcal{M}(\lambda, \boldsymbol{r})$ is the generating function associated with the pairwise line-of-sight velocity PDF:

$$\left[1 + \xi_{gg}(\boldsymbol{r})\right] \mathcal{M}(\lambda, \boldsymbol{r}) \equiv \int d^3\boldsymbol{v}_1 \int d^3\boldsymbol{v}_2 \left\langle e^{\lambda \frac{\Delta v_\parallel}{\mathcal{H}}} f(\boldsymbol{x}_1, \boldsymbol{v}_1) f(\boldsymbol{x}_2, \boldsymbol{v}_2) \right\rangle . \tag{D.9}$$

This leads to the streaming model:

$$1 + \xi^s_{gg}(s_\parallel, s_\perp) = \int dr_\parallel \mathcal{P}(r_\parallel - s_\parallel; \boldsymbol{r}) \left[1 + \xi_{gg}(\boldsymbol{r})\right], \tag{D.10}$$

where $\boldsymbol{r}_\perp = \boldsymbol{s}_\perp$, and the real space two-point correlation function is given as

$$1 + \xi_{gg}(\boldsymbol{r}) \equiv \int d^3\boldsymbol{v}_1 \int d^3\boldsymbol{v}_2 \left\langle f(\boldsymbol{x}_1, \boldsymbol{v}_1) f(\boldsymbol{x}_2, \boldsymbol{v}_2) \right\rangle . \tag{D.11}$$

Along the course of the derivation, we have only used the homogeneity of the Universe. We, therefore, conclude that the streaming model is an *exact* expression for the redshift-space two-point correlation function, following from the number conservation and the statistical homogeneity.

Note that for the single streaming case, where the distribution function may be written as $f(\boldsymbol{x}, \boldsymbol{v}) = \left[1 + \delta_g(\boldsymbol{x})\right] \delta^D(\boldsymbol{v} - \bar{\boldsymbol{v}}(\boldsymbol{x}))$ with the bulk velocity $\bar{\boldsymbol{v}}(\boldsymbol{x})$ uniquely defined at the position $\boldsymbol{x}$, equation (D.9) reduces to the the result of (148):

$$\left[1 + \xi_{gg}(\boldsymbol{r})\right] \mathcal{M}(\lambda, \boldsymbol{r}) \overset{\text{single stream}}{=} \left\langle e^{\lambda \Delta \bar{v}_\parallel / \mathcal{H}} \left[1 + \delta_g(\boldsymbol{x}_1)\right] \left[1 + \delta_g(\boldsymbol{x}_2)\right] \right\rangle . \tag{D.12}$$

The general formula, equation (D.9), must be used whenever multiple velocities are assigned to single spatial elements. That happens, for example, when coarse-graining the galaxy density field.

Appendix E

Binning effect of the power spectrum measurement

For a density field in a cubic volume of $V = L^3$, we estimate the power spectrum at $k = nk_F$ (n is an integer and $k_F \equiv 2\pi/L$ is the fundamental wavenumber) by taking the average over the amplitudes of Fourier modes around k (59; 81):

$$P(k_F n) = \frac{V}{N^6} \left(\frac{1}{N_k} \sum_{|n_k - n| \leq 1/2} |\delta_{\mathrm{FFTW}}(\mathbf{n}_k)|^2 \right) , \tag{E.1}$$

where δ_{FFTW} is the density field in Fourier space, N is the number of one-dimensional grid so that $H^3 = V/N^3$ becomes the volume of one grid Fourier cell, and N_k is the number of discrete Fourier modes falling into the bin. Because of the binning, the estimated power spectrum at k in equation (E.1) may differ from the true power spectrum $P(nk_F)$; we call it a binning effect. This effect is particularly important on large scales, where the number of Fourier modes is small. To make accurate comparison between the measurement and prediction, we need to take this effect into account. In the following, we explore three methods to account for the binning effect.

1. Compute the prediction by volume-averaging the input power spectrum $P_{\mathrm{inp}}(k)$, i.e.,

$$P_{\mathrm{smooth}}(k) = \frac{\int_{k_{\mathrm{min}}}^{k_{\mathrm{max}}} dk k^2 \; P_{\mathrm{inp}}(k)}{\left(k_{\mathrm{max}}^3 - k_{\mathrm{min}}^3\right)/3} , \tag{E.2}$$

   where k_{max} and k_{min} denote the boundaries of the particular k bin. We shall refer to this as "smoothed".

2. Volume-average the wavenumber to compute an *effective* wavenumber for each k bin

$$k_{\mathrm{eff}} = \frac{\int_{k_{\mathrm{min}}}^{k_{\mathrm{max}}} dk k^2 \; k}{\left(k_{\mathrm{max}}^3 - k_{\mathrm{min}}^3\right)/3} = \frac{3}{4} \frac{\left(k_{\mathrm{max}}^4 - k_{\mathrm{min}}^4\right)}{\left(k_{\mathrm{max}}^3 - k_{\mathrm{min}}^3\right)} , \tag{E.3}$$

and interpolate the input power spectrum at this effective wavenumber $P(k_{\rm eff})$. We shall refer to this as "k-smoothed".

3. Interpolate the input power spectrum on each $\boldsymbol{k}$ grid, and then bin this interpolated power spectrum. Namely,

$$P_{\rm discrete}(k_F\mathbf{n}_1) = \frac{V}{N^6}\left(\frac{1}{N_k}\sum_{|n_k-n_1|\leq 1/2} P_{\rm inp}(\mathbf{n}_k k_F)\right) , \tag{E.4}$$

and we shall refer to this as "discrete".

Figure E.1 shows the ratio of the measured power spectrum to the input power spectrum computed using the above three methods. The top and bottom panels show binning sizes of 0.05 and $= 0.006\ h\ {\rm Mpc}^{-1}$ (which is the fundamental frequency), respectively. For the large k bin, the smoothed method is inaccurate but the k-smoothed and discrete methods agree well with the measurement; for the small k bin, all methods perform similarly, with the discrete method performing slightly better at $k \lesssim 0.02\ h\ {\rm Mpc}^{-1}$. Thus, in chapter 4 we have used the discrete method for computing the prediction.

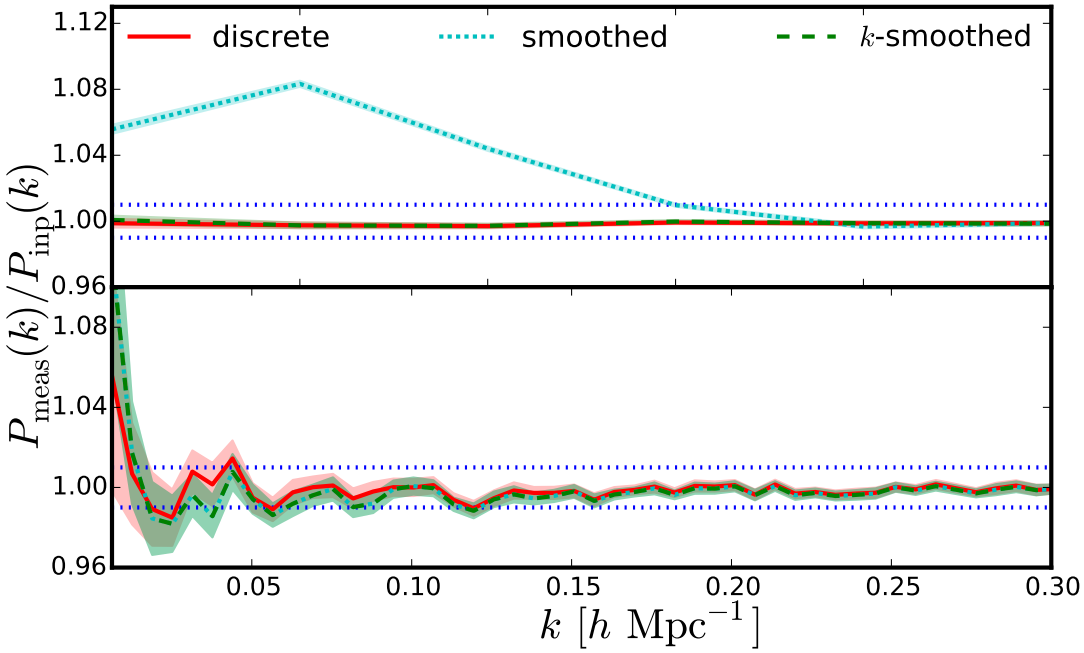

Figure E.1: Ratio of the measured power spectrum to the input for three different methods of accounting for the binning effect. (Top) Bin size of 0.05 h Mpc^{-1}. (Bottom) Bin size of 0.006 h Mpc^{-1}, which is the fundamental frequency in our mock catalog. The three methods are shown in the red solid (discrete), cyan dotted (smoothed), and green dashed (k-smoothed) lines. The band denotes the error on the mean measured from 50 realisations. The cyan and green bands overlap in the bottom panel.

Appendix F

Mean pairwise line-of-sight velocity in log-normal mock catalog

From equation (4.35), we find that the mean of the pairwise line-of-sight velocity is given by

$$[1+\xi_{gg}(r)]\,\langle \Delta v_z\rangle = \langle v_{1z}\delta_{g2}\rangle - \langle v_{2z}\delta_{g1}\rangle + \langle v_{1z}\delta_{g1}\delta_{g2}\rangle - \langle v_{2z}\delta_{g2}\delta_{g1}\rangle \ , \tag{F.1}$$

where we use $\langle v_{1z}\rangle = \langle v_{2z}\rangle$ and $\langle v_{1z}\delta_{g1}\rangle = \langle v_{2z}\delta_{g2}\rangle$ from homogeneity and isotropy. Thus, to compute the mean of the pairwise line-of-sight velocity, we need the contributions from both two- and three-point functions.

The two-point function contribution is given by

$$\langle v_{iz}\delta_{gj}\rangle = i\mathcal{H}f\int\frac{d^3k}{(2\pi)^3}\frac{k_z}{k^2}P_{gm}(k)e^{i\boldsymbol{k}\cdot\boldsymbol{r}_{ij}} = i\mathcal{H}f\mu\int\frac{dk}{2\pi^2}kP_{gm}(k)j_1(kr_{ij})\,, \tag{F.2}$$

where $\boldsymbol{r}_{ij}\equiv\boldsymbol{x}_i-\boldsymbol{x}_j$, $\mu\equiv\hat{z}\cdot\hat{r}_{ij}$ and $j_1(x)$ is the spherical Bessel function of the first order. Note that this product is anti-symmetric under the exchange of i and j, hence $\langle v_{1z}\delta_{g2}\rangle - \langle v_{2z}\delta_{g1}\rangle = 2\,\langle v_{1z}\delta_{g2}\rangle$. Using equations (4.25)–(4.26), equation (F.2) can be evaluated numerically as a function of r and μ. The blue dashed line in figure F.1 shows its contribution to the mean pairwise line-of-sight velocity for $\mu = 0.995$. We find that as the separation approaches to zero, this contribution drops to zero since $j_1(x)\to 0$ for $x\to 0$. The contribution also decreases with increasing separation, which is a generic feature following the trend of the density two-point correlation function.

For the three-point function contribution, we have

$$\langle v_{iz}\delta_{gi}\delta_{gj}\rangle = i\mathcal{H}f\int d^3x_p\frac{d^3k}{(2\pi)^3}\frac{k_z}{k^2}e^{i\boldsymbol{k}\cdot\boldsymbol{r}_{ij}}\,\langle\delta_m(\boldsymbol{x}_p)\delta_g(\boldsymbol{x}_i)\delta_g(\boldsymbol{x}_j)\rangle \ , \tag{F.3}$$

which is an integral over the three-point function of the (matter and galaxy) density fields. As the velocity field is linearly related to the density field in Fourier space and the three-point function is only calculated easily in configuration space, we need to introduce another vector variable $\boldsymbol{x}_p$ to evaluate this contribution.[1] If the density fields are Gaussian, then

[1]It follows that for each power of velocity in the moment, we need to introduce one vector variable and integrate over this variable, which makes this calculation impractical for higher moments.

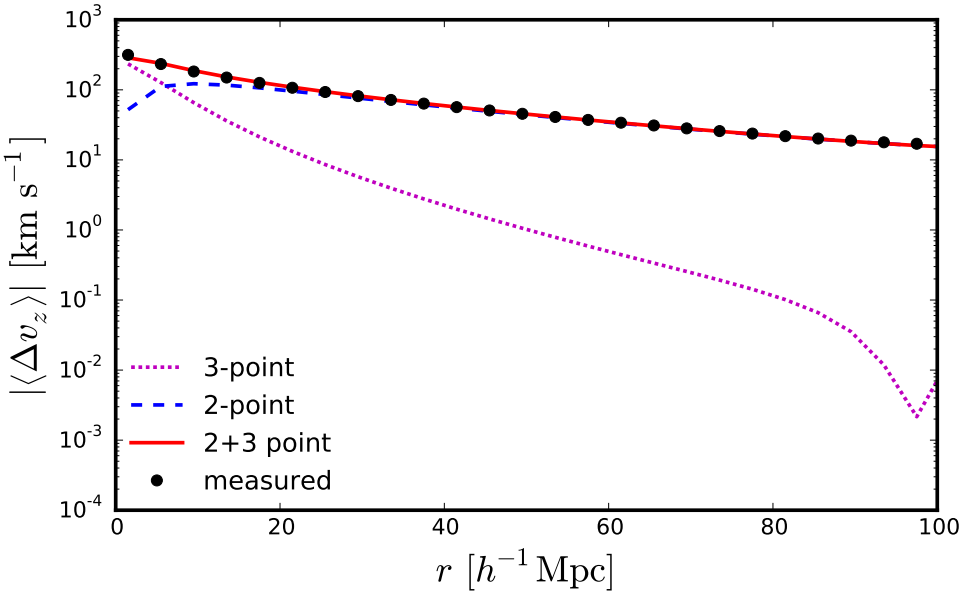

Figure F.1: Calculation of the mean pairwise line-of-sight ($\mu = 0.995$) velocity in our log-normal mock catalogs. The magenta dotted, blue dashed, and red solid lines show the contributions from three-point function alone, two-point function alone, and two- and three-point functions, respectively. The black points show the measurement from the log-normal mock catalogs.

this term vanishes and we do not get any contribution. However, for log-normal fields this term is non-zero and is given by (43)

$$\begin{aligned}\langle \delta_m(\boldsymbol{x}_p)\delta_g(\boldsymbol{x}_i)\delta_g(\boldsymbol{x}_j)\rangle = \xi_{gm}(r_{pi})\xi_{gm}(r_{pj})\xi_{gg}(r_{ij}) + \\ \xi_{gm}(r_{pi})\xi_{gg}(r_{ij}) + \xi_{gm}(r_{pj})\xi_{gg}(r_{ij}) + \xi_{gm}(r_{pi})\xi_{gm}(r_{pj})\,,\end{aligned} \tag{F.4}$$

which can be evaluated for our mock catalogs. The magenta dotted line in figure F.1 shows this contribution. We find that the contribution decreases with increasing separation, with an upturn at around the BAO scale. The two-point function contribution dominates on most scales except on very small scales.

Combining the contributions from both two- and three-point functions, we find good agreement between the analytic prediction and the measurement in the log-normal mock catalogs, as demonstrated in figure 4.9.

Bibliography

[1] Fastest Fourier Transform in the West. Available at `http://www.fftw.org/`.

[2] T.M.C. Abbott et al. , ArXiv e-prints (2017).

[3] P.A. Abell, J. Allison, S.F. Anderson, J.R. Andrew, J.R.P. Angel, L. Armus, D. Arnett, S.J. Asztalos, T.S. Axelrod, S. Bailey et al. , Arxiv e-print (2009).

[4] P.A.R. Ade et al. , Phys. Rev. Lett. **116** (2016), 031302.

[5] P.A.R. Ade et al. , Astron. Astrophys. **594** (2016), A13.

[6] P.A.R. Ade et al. , Astron. Astrophys. **594** (2016), A17.

[7] P. Adshead, E. Martinec und M. Wyman, Phys. Rev. **D88** (2013), 021302.

[8] P. Adshead, E. Martinec und M. Wyman, JHEP **09** (2013), 087.

[9] P. Adshead und M. Wyman, Phys. Rev. Lett. **108** (2012), 261302.

[10] A. Agrawal, T. Fujita und E. Komatsu, Arxiv e-print (2017).

[11] A. Agrawal, T. Fujita und E. Komatsu, (2018).

[12] S. Alam et al. , Submitted to: Mon. Not. Roy. Astron. Soc. (2016).

[13] A. Albrecht und P.J. Steinhardt, Phys. Rev. Lett. **48** (1982), 1220.

[14] D. Alonso, P.G. Ferreira und M.G. Santos, Mon. Not. Roy. Astron. Soc. **444** (2014), 3183.

[15] M.M. Anber und L. Sorbo, Phys. Rev. **D85** (2012), 123537.

[16] L. Anderson et al. , Mon. Not. Roy. Astron. Soc. **441** (2014), 24.

[17] D. Babich, P. Creminelli und M. Zaldarriaga, JCAP **0408** (2004), 009.

[18] J.S. Bagla, Curr. Sci. **88** (2005), 1088.

[19] N. Barnaby, J. Moxon, R. Namba, M. Peloso, G. Shiu und P. Zhou, Phys. Rev. **D86** (2012), 103508.

[20] N. Barnaby und M. Peloso, Phys. Rev. Lett. **106** (2011), 181301.

[21] A. Barreira und F. Schmidt, Arxiv e-print (2017).

[22] N. Bartolo, E. Komatsu, S. Matarrese und A. Riotto, Phys. Rept. **402** (2004), 103.

[23] D. Baumann. Lecture notes on Cosmology. Available at `http://cosmology.amsterdam/education/cosmology/`.

[24] D. Baumann, A. Nicolis, L. Senatore und M. Zaldarriaga, JCAP **7** (2012), 051.

[25] D. Baumann, P.J. Steinhardt, K. Takahashi und K. Ichiki, Phys. Rev. **D76** (2007), 084019.

[26] C.L. Bennett, A. Banday, K.M. Gorski, G. Hinshaw, P. Jackson, P. Keegstra, A. Kogut, G.F. Smoot, D.T. Wilkinson und E.L. Wright, Astrophys. J. **464** (1996), L1.

[27] C.L. Bennett et al. , Astrophys. J. Suppl. **208** (2013), 20.

[28] F. Bernardeau, S. Colombi, E. Gaztanaga und R. Scoccimarro, Phys. Rept. **367** (2002), 1.

[29] F. Bernardeau und L. Kofman, Astrophys. J. **443** (1995), 479.

[30] F. Beutler et al. , Mon. Not. Roy. Astron. Soc. **443** (2014), 1065.

[31] F.L. Bezrukov und M. Shaposhnikov, Phys. Lett. **B659** (2008), 703.

[32] M. Biagetti, M. Fasiello und A. Riotto, Phys. Rev. **D88** (2013), 103518.

[33] D. Bianchi, W. Percival und J. Bel, Arxiv e-print (2016).

[34] T. Buchert und J. Ehlers, Mon. Not. Roy. Astron. Soc. **264** (1993).

[35] S. Carlip, Rept. Prog. Phys. **64** (2001), 885.

[36] D. Carney, W. Fischler, E.D. Kovetz, D. Lorshbough und S. Paban, JHEP **11** (2012), 042.

[37] J.J.M. Carrasco, M.P. Hertzberg und L. Senatore, JHEP **9** (2012), 82.

[38] P. Catelan, Mon. Not. Roy. Astron. Soc. **276** (1995), 115.

[39] C.T. Chiang et al. , JCAP **1312** (2013), 030.

[40] C.H. Chuang et al. , Mon. Not. Roy. Astron. Soc. **452** (2015), 686.

[41] L. Clerkin et al. , Submitted to: Mon. Not. Roy. Astron. Soc. (2016).

[42] S. Cole et al. , Mon. Not. Roy. Astron. Soc. **362** (2005), 505.

[43] P. Coles und B. Jones, Mon. Not. Roy. Astron. Soc. **248** (1991), 1.

[44] P. Coles, A.L. Melott und S.F. Shandarin, Mon. Not. Roy. Astron. Soc. **260** (1993), 765.

[45] S. Colombi, Astrophys. J. **435** (1994), 536.

[46] J.L. Cook und L. Sorbo, Phys. Rev. **D85** (2012), 023534. [Erratum: Phys. Rev.D86,069901(2012)].

[47] J.L. Cook und L. Sorbo, JCAP **1311** (2013), 047.

[48] P. Creminelli, A. Nicolis, L. Senatore, M. Tegmark und M. Zaldarriaga, JCAP **0605** (2006), 004.

[49] M. Davis und P.J.E. Peebles, Astrophys. J. **267** (1982), 465.

[50] W. Dehnen und J.I. Read, European Physical Journal Plus **126** (2011), 55.

[51] V. Desjacques, D. Jeong und F. Schmidt, Arxiv e-print (2016).

[52] E. Dimastrogiovanni, M. Fasiello und T. Fujita, JCAP **1701** (2017), 019.

[53] E. Dimastrogiovanni und M. Peloso, Phys. Rev. **D87** (2013), 103501.

[54] E. Dimastrogiovanni und M. Peloso, Phys. Rev. **D87** (2013), 103501.

[55] S. Dodelson und M.D. Schneider, Phys. Rev. **D88** (2013), 063537.

[56] A.R. Duffy, J. Schaye, S.T. Kay, C. Dalla Vecchia, R.A. Battye und C.M. Booth, Mon. Not. Roy. Astron. Soc. **405** (2010), 2161.

[57] D.J. Eisenstein und W. Hu, Astrophys. J. **496** (1998), 605.

[58] D.J. Eisenstein et al. , Astrophys. J. **633** (2005), 560.

[59] H.A. Feldman, N. Kaiser und J.A. Peacock, Astrophys. J. **426** (1994), 23.

[60] K.B. Fisher, Astrophys. J. **448** (1995), 494.

[61] K. Freese, J.A. Frieman und A.V. Olinto, Phys. Rev. Lett. **65** (1990), 3233.

[62] J.N. Fry, A.L. Melott und S.F. Shandarin, **412** (1993), 504.

[63] T. Fujita, R. Namba und Y. Tada, Phys. Lett. **B778** (2018), 17.

[64] X. Gao, T. Kobayashi, M. Yamaguchi und J. Yokoyama, Phys. Rev. Lett. **107** (2011), 211301.

[65] M. Gerbino, A. Gruppuso, P. Natoli, M. Shiraishi und A. Melchiorri, JCAP **1607** (2016), 044.

[66] H. Gil-Marn, J. Norea, L. Verde, W.J. Percival, C. Wagner, M. Manera und D.P. Schneider, Mon. Not. Roy. Astron. Soc. **451** (2015), 539.

[67] H. Gil-Marn, W.J. Percival, L. Verde, J.R. Brownstein, C.H. Chuang, F.S. Kitaura, S.A. Rodrguez-Torres und M.D. Olmstead, Mon. Not. Roy. Astron. Soc. **465** (2017), 1757.

[68] V. Gluscevic und M. Kamionkowski, Phys. Rev. **D81** (2010), 123529.

[69] L.P. Grishchuk, Sov. Phys. JETP **40** (1975), 409. [Zh. Eksp. Teor. Fiz.67,825(1974)].

[70] H. Guo et al. , Mon. Not. Roy. Astron. Soc. **453** (2015), 4368.

[71] A.H. Guth, Phys. Rev. **D23** (1981), 347.

[72] O. Hahn, R.E. Angulo und T. Abel, Mon. Not. Roy. Astron. Soc. **454** (2015), 3920.

[73] A.J.S. Hamilton, Astrophys. J. Lett. **385** (1992), L5.

[74] A.J.S. Hamilton: Linear Redshift Distortions: a Review. Linear Redshift Distortions: a Review, In The Evolving Universe, herausgegeben von D. Hamilton, Band 231 von Astrophysics and Space Science Library. (1998) Seite 185.

[75] J. Hartlap, P. Simon und P. Schneider, Astron. Astrophys. (2006). [Astron. Astrophys.464,399(2007)].

[76] A.F. Heavens, S. Matarrese und L. Verde, Mon. Not. Roy. Astron. Soc. **301** (1998), 797.

[77] G.J. Hill et al. , ASP Conf. Ser. **399** (2008), 115.

[78] G. Hinshaw et al. , Astrophys. J. Suppl. **208** (2013), 19.

[79] E. Hubble, Astrophys. J. **79** (1934), 8.

[80] J.C. Jackson, Mon. Not. Roy. Astron. Soc. **156** (1972), 1P.

[81] D. Jeong: Cosmology with high (z>1) redshift galaxy surveys. The University of Texas at Austin, Dissertation, 2010. Available at `http://www.personal.psu.edu/duj13/documents.htm`.

[82] D. Jeong, L. Dai, M. Kamionkowski und A.S. Szalay, Mon. Not. Roy. Astron. Soc. **449** (2015), 3312.

[83] D. Jeong, F. Schmidt und C.M. Hirata, Phys. Rev. **D85** (2012), 023504.

[84] Y.P. Jing, Astrophys. J. **620** (2005), 559.

[85] N. Kaiser, Mon. Not. Roy. Astron. Soc. **227** (1987), 1.

[86] M. Kamionkowski, A. Kosowsky und A. Stebbins, Phys. Rev. Lett. **78** (1997), 2058.

[87] M. Kamionkowski und E.D. Kovetz, Ann. Rev. Astron. Astrophys. **54** (2016), 227.

[88] I. Kayo, A. Taruya und Y. Suto, Astrophys. J. **561** (2001), 22.

[89] F.S. Kitaura und S. Heß, Mon. Not. Roy. Astron. Soc. **435** (2013), L78.

[90] J. Koda, C. Blake, F. Beutler, E. Kazin und F. Marin, Mon. Not. Roy. Astron. Soc. **459** (2016), 2118.

[91] L. Kofman, E. Bertschinger, J.M. Gelb, A. Nusser und A. Dekel, Astrophys. J. **420** (1994), 44.

[92] E. Komatsu: The pursuit of non-gaussian fluctuations in the cosmic microwave background. Tohoku U., Astron. Inst., Dissertation, 2001.

[93] E. Komatsu, Class. Quant. Grav. **27** (2010), 124010.

[94] E. Komatsu und D.N. Spergel, Phys. Rev. **D63** (2001), 063002.

[95] E. Komatsu et al. , Astrophys. J. Suppl. **148** (2003), 119.

[96] E. Komatsu et al. , Astrophys. J. Suppl. **148** (2003), 119.

[97] S.D. Landy und A.S. Szalay, Astrophys. J. **412** (1993), 64.

[98] R. Laureijs et al. , Arxiv e-print (2011).

[99] A. Le Tiec und J. Novak. In An Overview of Gravitational Waves: Theory, Sources and Detection, herausgegeben von G. Auger und E. Plagnol (2017), Seiten 1–41.

[100] M. Levi et al. , Arxiv e-print (2013).

[101] M. Lewandowski, L. Senatore, F. Prada, C. Zhao und C.H. Chuang, Arxiv e-print (2015).

[102] A.D. Linde, Phys. Lett. **B108** (1982), 389.

[103] J. Loveday und J. Pier, Arxiv e-print (1998).

[104] A. Lue, L.M. Wang und M. Kamionkowski, Phys. Rev. Lett. **83** (1999), 1506.

[105] D.H. Lyth, C. Ungarelli und D. Wands, Phys. Rev. **D67** (2003), 023503.

[106] D.H. Lyth und D. Wands, Phys. Lett. **B524** (2002), 5.

[107] D. Maity, Nucl. Phys. **B919** (2017), 560.

[108] J.M. Maldacena, JHEP **05** (2003), 013.

[109] J.M. Maldacena und G.L. Pimentel, JHEP **09** (2011), 045.

[110] A. Maleknejad, JHEP **07** (2016), 104.

[111] A. Maleknejad und E. Erfani, JCAP **1403** (2014), 016.

[112] A. Maleknejad und M.M. Sheikh-Jabbari, Phys. Lett. **B723** (2013), 224.

[113] T. Matsubara, Phys. Rev. **D78** (2008), 083519. [Erratum: Phys. Rev.D78,109901(2008)].

[114] T. Matsubara, Phys. Rev. **D77** (2008), 063530.

[115] T. Matsubara, Phys. Rev. **D83** (2011), 083518.

[116] T. Matsubara, Phys. Rev. **D90** (2014), 043537.

[117] T. Matsumura et al. , J. Low. Temp. Phys. **176** (2014), 733.

[118] A.L. Melott, Astrophys. J. Lett. **426** (1994).

[119] A.L. Melott, T. Buchert und A.G. Weib, Astron. Astrophys. **294** (1995), 345.

[120] I. Mohammed, U. Seljak und Z. Vlah, Mon. Not. Roy. Astron. Soc. **466** (2017), 780.

[121] P. Monaco, Galaxies **4** (2016), 53.

[122] F. Moutarde, J.M. Alimi, F.R. Bouchet, R. Pellat und A. Ramani, Astrophys. J. **382** (1991), 377.

[123] V. Mukhanov: Physical Foundations of Cosmology. Cambridge University Press, 2005.

[124] V.F. Mukhanov und G.V. Chibisov, JETP Lett. **33** (1981), 532. [Pisma Zh. Eksp. Teor. Fiz.33,549(1981)].

[125] V.F. Mukhanov, H.A. Feldman und R.H. Brandenberger, Phys. Rept. **215** (1992), 203.

[126] E. Munari, P. Monaco, J. Koda, F.S. Kitaura, E. Sefusatti und S. Borgani, ArXiv e-prints (2017).

[127] R. Namba, M. Peloso, M. Shiraishi, L. Sorbo und C. Unal, JCAP **1601** (2016), 041.

[128] M.C. Neyrinck, Mon. Not. Roy. Astron. Soc. **455** (2016), L11.

[129] I. Obata und J. Soda, Phys. Rev. **D93** (2016), 123502.

[130] T. Okumura, N. Hand, U. Seljak, Z. Vlah und V. Desjacques, Phys. Rev. **D92** (2015), 103516.

[131] T. Okumura, U. Seljak und V. Desjacques, JCAP **1211** (2012), 014.

[132] T. Okumura, U. Seljak, P. McDonald und V. Desjacques, JCAP **1202** (2012), 010.

[133] J.A. Peacock und S.J. Dodds, Mon. Not. Roy. Astron. Soc. **280** (1996), L19.

[134] D.W. Pearson, L. Samushia und P. Gagrani, Mon. Not. Roy. Astron. Soc. **463** (2016), 2708.

[135] P.J.E. Peebles: The large-scale structure of the universe, 1980.

[136] M. Peloso, L. Sorbo und C. Unal, JCAP **1609** (2016), 001.

[137] W. Percival: The Invisible Universe: Dark Matter and Dark Energy. Springer Berlin Heidelberg, Berlin, Heidelberg, 2007.

[138] A. Perko, L. Senatore, E. Jennings und R.H. Wechsler, Arxiv e-print (2016).

[139] S. Perlmutter et al. , Astrophys. J. **517** (1999), 565.

[140] M.E. Peskin und D.V. Schroeder: An Introduction To Quantum Field Theory (Frontiers in Physics). CRC Press, 1995.

[141] R. de Putter, C. Wagner, O. Mena, L. Verde und W. Percival, JCAP **1204** (2012), 019.

[142] B.A. Reid und M. White, Mon. Not. Roy. Astron. Soc. **417** (2011), 1913.

[143] A.G. Riess et al. , Astron. J. **116** (1998), 1009.

[144] C. Rovelli: Notes for a brief history of quantum gravity. Notes for a brief history of quantum gravity, In Recent developments in theoretical and experimenta (2000) Seiten 742–768.

[145] S. Saito, K. Ichiki und A. Taruya, JCAP **0709** (2007), 002.

[146] S. Saito et al. , Mon. Not. Roy. Astron. Soc. **460** (2016), 1457.

[147] J.J. Sakurai und J.J. Napolitano: Modern Quantum Mechanics (2nd Edition). Pearson, 2010.

[148] R. Scoccimarro, Phys. Rev. **D70** (2004), 083007.

[149] D. Seery, K.A. Malik und D.H. Lyth, JCAP **0803** (2008), 014.

[150] E. Sefusatti, M. Crocce, S. Pueblas und R. Scoccimarro, Phys. Rev. **D74** (2006), 023522.

[151] U. Seljak und P. McDonald, JCAP **1111** (2011), 039.

[152] U. Seljak und M. Zaldarriaga, Phys. Rev. Lett. **78** (1997), 2054.

[153] E. Sellentin und A.F. Heavens, Mon. Not. Roy. Astron. Soc. **464** (2017), 4658.

[154] L. Senatore, E. Silverstein und M. Zaldarriaga, JCAP **1408** (2014), 016.

[155] J. Shin, J. Kim, C. Pichon, D. Jeong und C. Park, ArXiv e-prints (2017).

[156] M. Shiraishi, C. Hikage, R. Namba, T. Namikawa und M. Hazumi, Phys. Rev. **D94** (2016), 043506.

[157] E. Sirko, Astrophys. J. **634** (2005), 728.

[158] Z. Slepian et al. , Arxiv e-print (2016).

[159] Z. Slepian et al. , Mon. Not. Roy. Astron. Soc. **469** (2017), 1738.

[160] R.E. Smith und K. Markovic, Phys. Rev. **D84** (2011), 063507.

[161] G.F. Smoot et al. , Astrophys. J. **396** (1992), L1.

[162] L. Sorbo, JCAP **1106** (2011), 003.

[163] D. Spergel et al. , Arxiv e-print (2015).

[164] D.N. Spergel und P.J. Steinhardt, Phys. Rev. Lett. **84** (2000), 3760.

[165] V. Springel, Mon. Not. Roy. Astron. Soc. **364** (2005), 1105.

[166] A.A. Starobinsky, JETP Lett. **30** (1979), 682. [Pisma Zh. Eksp. Teor. Fiz.30,719(1979)].

[167] N.S. Sugiyama, Astrophys. J. **788** (2014), 63.

[168] N. Tamura et al. , Proc. SPIE Int. Soc. Opt. Eng. **9908** (2016), 99081M.

[169] A. Taruya, T. Nishimichi und S. Saito, Phys. Rev. **D82** (2010), 063522.

[170] S. Tassev, M. Zaldarriaga und D.J. Eisenstein, "JCAP" **6** (2013), 036.

[171] B. Thorne, T. Fujita, M. Hazumi, N. Katayama, E. Komatsu und M. Shiraishi, Arxiv e-print (2017).

[172] S. Tulin, H.B. Yu und K.M. Zurek, Phys. Rev. D **87** (2013), 115007.

[173] C. Uhlemann, S. Codis, C. Pichon, F. Bernardeau und P. Reimberg, Mon. Not. Roy. Astron. Soc. **460** (2016), 1529.

[174] C. Uhlemann, M. Kopp und T. Haugg, Phys. Rev. **D92** (2015), 063004.

[175] Z. Vlah, U. Seljak, P. McDonald, T. Okumura und T. Baldauf, JCAP **1211** (2012), 009.

[176] Z. Vlah, U. Seljak, T. Okumura und V. Desjacques, JCAP **1310** (2013), 053.

[177] L. Wang, B. Reid und M. White, Mon. Not. Roy. Astron. Soc. **437** (2014), 588.

[178] L. Wang, B. Reid und M. White, Mon. Not. Roy. Astron. Soc. **437** (2014), 588.

[179] S. Weinberg: Dreams of a final theory: The Search for the fundamental laws of nature, 1992.

[180] S. Weinberg, Phys. Rev. **D72** (2005), 043514.

[181] V. Wild et al. , Mon. Not. Roy. Astron. Soc. **356** (2005), 247.

[182] H.S. Xavier, F.B. Abdalla und B. Joachimi, Mon. Not. Roy. Astron. Soc. **459** (2016), 3693.

[183] N. Yoshida, V. Springel, S.D.M. White und G. Tormen, Astrophys. J. Lett. **544** (2000), L87.

[184] Y.B. Zel'dovich, Astron. Astrophys. **5** (1970), 84.

Acknowledgement

First and foremost, I would like to thank my supervisor Prof. Eiichiro Komatsu. He has been the best mentor I could ask for, and it's been a great experience to know him and learn from him over the last 5 years. His knowledge and understanding of physics amazes me to this day, and I look up to him as an ideal. Needless to say, everything that this thesis contains, I learnt from him. I am extremely grateful to him for providing me the opportunity to work with him, and for all that he has done for me. I am particularly obliged for his request to people at NORDITA to allow me to attend a conference on inflation there and talk about my work, and for the pains that he had to go through to make my drafts tolerable. His enthusiasm has always kept me inspired and excited about my work, even through the hard times. He has taught me as much about life as about physics, through his curiosity and commitment to things (one of the most impressionable memories I have is of waking up at 8 am to see Eiichiro and Donghui in an email exchange at 3am!!). It was a pleasure to join him for a couple of baseball games and all the group dinners. They were among the most fun times of my life in Munich, and I owe a lot to him for all that. I hope I can one day be even half of him.

Next I would like to thank my collaborator Tomohiro Fujita profusely. He is one of the most intelligent people I know, and his speed of working is unparalleled. He was always there to help me through difficult bits of calculations, and extremely patient when I made careless mistakes. I learnt a great deal about inflation from him. It was fun to work with him (at least for me!) and sincerely hope we can work together in future as well. I am also highly grateful to Shun Saito who has been immensely resourceful both for scientific and academic advice pertaining to postdoc applications. His insistence on improving my terrible plots helped me greatly in understanding the importance of good plots, and will be useful forever. Besides that, he was really helpful in understanding some aspects of RSD and I thank him for that. I also thank Ryu Makiya for his great work in optimizing my horrible version of the log-normal code and making it easier to use. He also gave me some good advice regarding my applications for which I am grateful.

I worked with Prof. Donghui Jeong only for a short while, but he impressed me quite a lot by his way of checking results. I learnt some cool tricks from him and one of the most useful things he told me was to not be afraid of asking stupid questions - this is perhaps the last time in my academic life that this is possible. I benefit a lot from this advice and hopefully made a good use of it. Lastly, I also want to thank him for writing a reference letter for me. I would also like to thank Prof. Supratik Pal, with whom I started

my inflation work. He was always ready to help me with my stupid questions, and was instrumental in guiding the first stages of those projects. I also thank him profusely for writing me a reference letter.

Life in Munich would have been a nightmare without the support of the cosmology group at MPA and a number of friends I made. I would like to thank Tsz Yan Lam, Christian Wagner, Jaiseung Kim, Xun Shi, and Kari Helgason for being such cool and accessible post-docs so that I could easily ask them silly questions and to whom I owe a large part of what I know about cosmology. Special thanks to Xun also for taking care of my plant when I was away. I also made a lot of good friends over the years. I am thankful to all of them, in particular Titouan, Sam, Alex, Leila, Kaloian, Aoife, Azadeh, Inh, Minh, Virginia, and Christina. They are all wonderful people, and provided much needed laughter throughout the years. Titouan inspired me a lot on how to live and helped me particularly through the depressing months of rejections. I wish him all the best for Trieste. Sam has been one of my closest friends through these years, and I hope she will be happy wherever she is. I also met friends from back home who were my go-to people when I missed home and Hindi - special "dhanyavaad" to Darshan, Shweta, Samarth and Viraj. I wish them all a life full of fun and adventure for the rest of their stay in Chile and in Munich.

Finally, I would like to thank my parents who believed in me, and provided constant support and encouragement. I would also like to thank Arohi, who was a wonderful partner for a big part of my life in Munich, and hope she will be happy, always.